Power System Dynamics Enhancement Through Phase Unbalanced and Adaptive Control Schemes in Series FACTS devices

A Thesis
Submitted to the College of Graduate Studies and Research
in Partial Fulfillment of the Requirements
for the PhD Degree
in the Department of Electrical and Computer Engineering
University of Saskatchewan
Saskatoon

by
Dipendra Rai

Saskatoon, Saskatchewan, Canada

Permission to Use

In presenting this thesis in partial fulfilment of the requirements for a Ph. D. degree from the University of Saskatchewan, I agree that the Libraries of this University may make it freely available for inspection. I further agree that permission for copying of this thesis in any manner, in whole or in part, for scholarly purposes may be granted by the professors who supervised my thesis work or, in their absence, by the Head of the Department or the Dean of the College of Engineering. It is also understood that due recognition shall be given to me and to the University of Saskatchewan in any scholarly use which may be made of any material in my thesis. Copying or publication or any other use of this thesis for financial gain without approval by the University of Saskatchewan and my written permission is prohibited.

Requests for permission to copy or to make other use of material in this thesis in whole or part should be addressed to:

Head of the Department of Electrical and Computer Engineering
University of Saskatchewan
57 Campus Drive
Saskatoon, Saskatchewan, Canada S7N 5A9

Abstract

This thesis presents novel series compensation schemes and adaptive control techniques to enhance power system dynamics through damping Subsynchronous Resonance (SSR) and low-frequency power oscillations: local and inter-area oscillations. Series capacitive compensation of transmission lines is used to improve power transfer capability of the transmission line and is economical compared to the addition of new lines. However, one of the impeding factors for the increased utilization of series capacitive compensation is the potential risk of SSR, where electrical energy is exchanged with turbine-generator shaft systems in a growing manner which can result in shaft damage. Furthermore, the fixed capacitor does not provide controllable reactance and does not aid in the low-frequency oscillations damping.

The Flexible AC Transmission System (FACTS) controllers have the flexibility of controlling both real and reactive power which could provide an excellent capability for improving power system dynamics. Several studies have investigated the potential of using this capability in mitigating the low-frequency (electromechanical) as well as the subsynchronous resonance (SSR) oscillations. However, the practical implementations of FACTS devices are very limited due to their high cost.

To address this issue, this thesis proposes a new series capacitive compensation concept capable of enhancing power system dynamics. The idea behind the concept is a series capacitive compensation which provides balanced compensation at the power frequency while it provides phase unbalance at other frequencies of oscillations. The compensation scheme is a combination of a single-phase Thyristor Controlled Series Capacitor (TCSC) or Static Synchronous Series Compensator (SSSC) and a fixed series capacitors in series in one phase of the compensated transmission line and fixed capacitors on the other two phases. The proposed scheme is economical compared to a full three-phase FACTS counterpart and improves reliability of the device by reducing number of switching components.

The phase unbalance during transients reduces the coupling strength between the mechanical and the electrical system at asynchronous oscillations, thus suppressing the build-up of torsional stresses on the generator shaft systems. The SSR oscillations damping capability of the schemes is validated through detailed time-domain electromagnetic transient simulation studies on the IEEE first and second benchmark models. Furthermore, as the proposed schemes provide controllable reactance through TCSC or SSSC, the supplementary controllers can be implemented to damp low-frequency power oscillations as well. The low-frequency damping capability of the schemes is validated through detail time-domain electromagnetic transient simulation studies on two machines systems connected to a very large system and a three-area, six-machine power system. The simulation studies are carried out using commercially available electromagnetic transient simulation tools (EMTP-RV and PSCAD/EMTDC).

An adaptive controller consisting of a robust on-line identifier, namely a robust Recursive Least Square (RLS), and a Pole-Shift (PS) controller is also proposed to provide optimal damping over a wide range of power system operations. The proposed identifier penalizes large estimated errors and smooth-out the change in parameters during large power system disturbances. The PS control is ideal for its robustness and stability conditions. The combination results in a computationally efficient estimator and a controller suitable for optimal control over wider range of operations of a non-linear system such as power system. The most important aspect of the controller is that it can be designed with an approximate linearized model of the complete power system, and does not need to be re-tuned after it is commissioned. The damping capability of such controller is demonstrated through detail studies on a three-area test system and on an IEEE 12-bus test system.

Finally, the adaptive control algorithm is developed on a Digital Signal Processing Board, and the performance is experimentally tested using hardware-in-the-loop studies. For this purpose, a Real Time Digital Simulator (RTDS) is used, which is capable of simulating power system in real-time at 50 μs simulation time step. The RTDS facilitates the performance evaluation of a controller just like testing on a real power system. The experimental results match closely with the simulation results; which demonstrated the practical applicability of the adaptive controller in power systems. The proposed controller is computationally efficient and simple to implement in DSP hardware.

Acknowledgements

This dissertation was carried out at the Department of Electrical and Computer Engineering, University of Saskatchewan, during 2008 – 2012 under the kind supervision of Dr. Ramakrishna Gokaraju and Dr. Sherif O. Faried.

First and the foremost, I would like to express my sincere gratitude to my academic supervisors, Dr. Gokaraju and Dr. Faried. Their guidance, encouragement, and thoughtful discussions have been extremely valuable source of inspiration and motivation for my study, which paved the way for completion of this thesis.

I would like to acknowledge Dr. Abdel-Aty Edris for his valuable suggestions on phase unbalanced compensations. I owe my sincere thanks to all the Advisory Committee members for their constructive critics, and all the professors of the Department of Electrical and Computer Engineering for their course supervision and strengthening my knowledge on various aspects of Electrical Engineering. I would like to thank Dr. Dharshana Muthumuni, Manitoba HVDC Research Centre, for his valuable inputs relating to the PSCAD/EMTDC simulations, Dr. Kalyan Sen for his helpful inputs on FACTS devices, Dr. Antal Soos for his helpful suggestions on recursive algorithm code development in Texas Instrument Digital Signal Processor, and Dr. Ahmed M. El-Serafi for his useful advices on synchronous machine modelling. I would also like to thank Prof. A.M. Gole for giving an opportunity to visit the Power System Simulations Laboratory at the University of Manitoba from January-April, 2010.

I gratefully acknowledge the financial support provided by the College of Graduate Studies and Research in the form of Dean's Scholarship (2008-2010), the Natural Sciences and Engineering Research Council of Canada in the form of Alexander Graham Bell Canada Graduate Scholarships (NSERC CGS D2, 2010-2012), the Department of Electrical and Computer Engineering in the form of Devolved Scholarship (2010-2011) and the College of Engineering in the form of top-up scholarship (2010-2012). Research of this kind could not have been completed without these financial assistances.

The journey toward my graduate study would not have been enjoyable one without my friends and their support. I wish to thank my colleagues in the University: Eli Pajuelo, Binod Shrestha, Mohamed Elsamahy, Irfan Unal, Sushan Pan, Urvi Malhotra, and several other friends for their help and technical suggestions.

DEDICATION

My precious wife *Ms. Suchitra Shrestha* for her endless encouragement and unconditional love

&

My late father *Mr. Jaya B. Rai* and my mother *Ms. Raj K. Rai* who never left my side and are always very special to me

I owe you all I have ever accomplished

Table of Contents

List of Tables

List of Figures

List of Abbreviations

ω_0	System Fundamental Frequency
kB	TCSC Boost Factor
kB_{ref}	TCSC Reference Boost Factor
ANSI	American National Standards Institute
ARMA	Auto-Regressive Moving Average
ARX	Autoregressive External Input
BtB	Back-to-Back
CFAD	Constant Firing Angle Delay
DFT	Discrete Fourier Transform
EMT	Electromagnetic Transient
EXC	Exciter
FACTS	Flexible AC Transmission Systems
FFT	Fast Fourier Transform
GTO	Gate Turn-off Thyristor
HP	High Pressure Turbine
HVDC	High Voltage Direct Current
IEC	International Electrotechnical Commission
IGBT	Insulated Gate-Bipolar Transistor
IGCT	Insulated Gate-Commutated Transistor
IP	Intermediate Pressure Turbine

IPFC	Interline Power Flow Controller
LPA/LPB	Low Pressure Turbine A/B
LVUR	Line Voltage Unbalance Rate
p.u.	per unit
PI	Proportional-Integral
PLL	Phase Locked Loop
PMU	Phasor Measurement Unit
PRBS	Pseudo Random Binary Sequence
PSS	Power System Stabilizer
PWM	Pulse Width Modulation
RLS	Recursive Least Square
SMIB	Single-Machine Infinite Bus
SPWM	Sinusoidal Pulse Width Modulation
SSR	Subsynchronous Resonance
SSSC	Static Synchronous Series Compensator
STATCOM	Static Synchronous Compensator
SVC	Static Var Compensator
SVR	Synchronous Voltage Reversal
T(GEN-EXC)	GEN-EXC shaft torsional torque
T(HP-IP)	HP-IP shaft torsional torque
T(IP-LPA)	IP-LPA shaft torsional torque
T(LPA-LPB)	LPA-LPB shaft torsional torque
T(LPB-GEN)	LPB-GEN shaft torsional torque
TCPAR	Thyristor Controlled Phase Angle Regulator

TCR	Thyristor-Controlled Reactor
TCSC	Thyristor Controlled Series Capacitor
TSC	Thyristor-Switched Capacitor
TSSC	Thyristor Switched Series Capacitor
UPFC	Unified Power Flow Controller
VCO	Voltage-Controlled Oscillator
VSC	Voltage Source Converter

List of Publications

Following publications resulted from the work reported in this thesis.

List of Journal Papers:

[J1] D. Rai, S. O. Faried, R. Gokaraju and A. Edris, "An SSSC-Based Hybrid Series Compensation Scheme Capable of Damping Subsynchronous Resonance," *IEEE Transaction on Power Delivery*, Vol. 27, issue 2, pp. 531-540, April 2012.

[J2] D. Rai, S. O. Faried, R. Gokaraju, and A. A. Edris, "Damping Inter-Area Oscillations using Phase Imbalanced Series Compensation Schemes," *IEEE Transactions on Power Systems*, Vol. 26, No. 3, pp. 1753-1761, Aug. 2011, also presented at the *IEEE Power and Energy Society General Meeting*, Detroit, USA, July 24-29, 2011.

[J3] D. Rai, R. Gokaraju, S. O. Faried, and A. Edris, "Enhancement of Power System Dynamics Using a Phase Imbalanced Series Compensation Scheme," *IEEE Transactions on Power Systems*, vol. 25, no. 2, pp. 966-974, 2010, also presented at the *IEEE Power and Energy Society General Meeting*, Minneapolis, USA, July 25-29, 2010.

[J4] D. Rai, S. O. Faried, R. Gokaraju, and A. Edris, "Hybrid Series Compensation Scheme Capable of Damping Subsynchronous Resonance," *IET Generation, Transmission & Distribution*, vol. 4, pp. 456-466, 2010.

List of Conference Papers [Acceptance based on full paper review]:

[C1] D. Rai, S. O. Faried, R. Gokaraju, and A. A. Edris, "Impact of Imbalanced Phase Operation of SSSC on Damping Subsynchronous Resonance," *Presented at the IEEE Power and Energy Society General Meeting*, Detroit, USA, July 24-29, 2011.

[C2] D. Rai, R. Gokaraju, and S. O. Faried, "Model Reference Adaptive Control of FACTS," *Presented at the* 16th *National Power System Conference*, Hyderabad, India, Dec 15-17, 2010.

[C3] D. Rai, R. Gokaraju, S. O. Faried, and A. A. Edris, "Damping Subsynchronous Resonance Using a STATCOM Operating in a Phase Imbalanced Mode," *Presented at the IEEE Power and Energy Society General Meeting*, Calgary, Canada, July 26-30, 2009.

[C4] D. Rai, R. Gokaraju, S.O. Faried, A. Edris, "A Novel Approach for Damping Subsynchronous Resonance Using a STATCOM", *15th National Power System Conference*, IIT Bombay, India, 16-18 Dec. 2008.

List of Poster Presentation [Acceptance based on 1 page abstract]:

[P1] D. Rai, R. Gokaraju, and S. O. Faried, "Model Reference Adaptive Control for FACTS" *IEEE Power and Energy Society General Meeting*, Minneapolis, Minnesota, 25-29 July 2010.

Chapter 1

Introduction

1.1 Background

Today's electrical networks are highly interconnected for the economical sharing of resources. Power generating sites are usually located far from load centers and the power needed to be transmitted through transmission lines. Growth of electric power transmission facilities is restricted despite the fact that bulk power transfers and use of transmission systems by third parties are increasing. Transmission system expansion is needed, but not easily accomplished. Factors that contribute to this situation include a variety of environmental, land-use and regulatory requirements. Transmission bottlenecks, non-uniform utilization of facilities and unwanted parallel-path or loop flows are not uncommon. As a result, the utility industry is facing the challenge of the efficient utilization of the existing AC transmission lines. The transmission systems are being pushed to operate closer to their stability and thermal limits. Although electricity is a highly engineered product, it is increasingly being considered and handled as a commodity. Thus, the focus on the quality of power delivered is also greater than ever.

Series capacitive compensation of transmission lines is an important and the most economical way to improve power transfer capability, especially when large amounts of power must be transmitted through long transmission lines. However, one of the impeding factors for the increased utilization of series capacitive compensation is the potential risk of Subsynchronous Resonance (SSR), where electrical energy is exchanged with turbine-generator shaft systems in a growing manner which can result in shaft damage [1]. Figure 1.1 shows a typical time response of a turbine-generator shaft torsional torque during and after clearing a fault on a series capacitive compensated transmission line in the presence of the SSR phenomenon. It is worth noting here that this shaft is designed to withstand a maximum torsional torque of 2 *per unit* (p.u.). Two successive shaft failures were reported in the Mohave generating station in 1970 and 1971 in Nevada, USA because of this problem [2].

Another limitation of series capacitive compensation is its inability to provide adequate damping to power system oscillations after clearing system faults. Figure 1.2 shows a typical time response of a generator load angle, measured with respect to a reference generator load angle, during and after clearing a three-phase fault on a series capacitive compensated transmission line. As it can be seen from this figure, the oscillations are not completely damped after the first few seconds from fault clearing, resulting in degrading the power quality of the system.

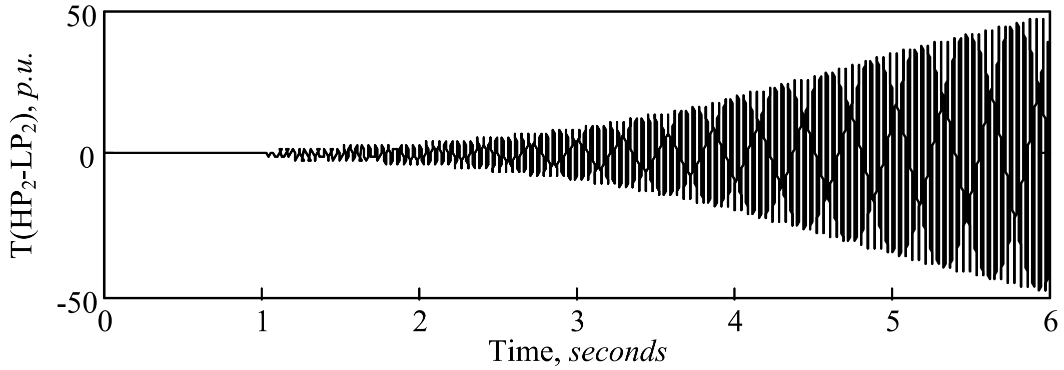

Figure 1.1: Transient time response of a turbine-generator shaft torsional torque during and after clearing a system fault on a series capacitive compensated transmission line.

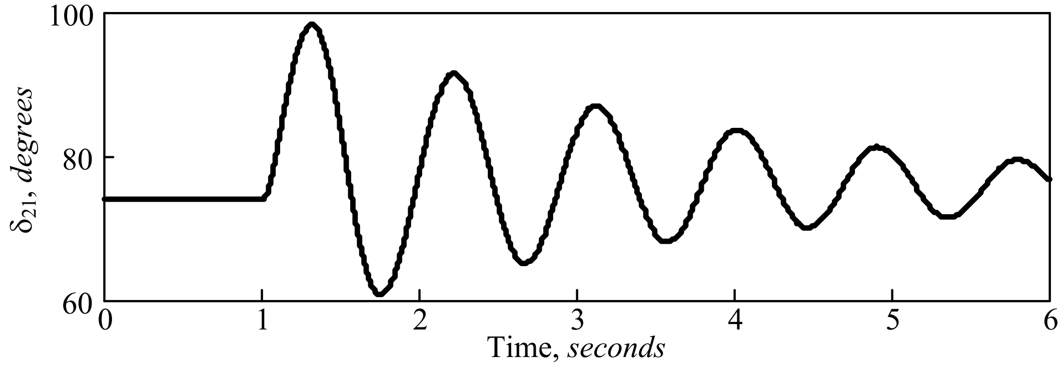

Figure 1.2: Transient time response of a generator load angle, measured with respect to a reference generator load angle, during and after clearing a system fault on a series capacitive compensated transmission line.

Flexible AC transmission system (FACTS) is an emerging technology whose principal role is to enhance the controllability and the power transfer capability in ac systems. FACTS technologies use switching power electronic devices to control the power flow in the range of a few tens to a few hundreds of megawatts. The potential benefits of these FACTS controllers are now widely recognized by the power system engineering and the transmission and distribution communities. The FACTS devices have shown to be attractive and very effective in damping SSR torsional oscillations and low frequency oscillations [3–5]. However, the practical implementations of FACTS devices are very limited due to their high cost. In comparison to traditional series capacitor compensation, the costs of Thyristor Controlled Series Capacitor (TCSC) and Static Synchronous Series Compensator (SSSC) are almost two and three times higher, respectively [6].

This thesis presents new types of series compensation schemes capable of improving power system dynamics by damping subsynchronous resonance and low frequency oscillations. The proposed schemes use a combination of traditional fixed capacitors and modern single-phase FACTS devices. These schemes are economical compared to full three-phase FACTS devices and use lower numbers of switching components. Furthermore, the thesis proposes a robust recursive least-square (RLS) identification based adaptive pole-shift controller to enhance system damping for the wide range of power system operating conditions. A *Sigmoid* like nonlinear function is proposed for RLS parameter update equation; which makes the estimation procedure robust for large disturbances i.e. prevents parameter blowout during such conditions.

The electromagnetic transient (EMT) type time-domain simulation softwares have been used to develop detail models of power system components and the proposed devices. The EMT studies presented in this thesis use detailed transient models of the various power system components, and therefore give an accurate representation of the power system operation. Experimental verification of the performance of the robust RLS-based adaptive pole-shift controller is also presented using hardware-in-the-loop test on RTDS platform.

1.2 Transmission Line Series Compensation

The main purpose of series compensation in a power system is virtual reduction of line reactance in order to enhance power system stability and increase the loadability of transmission corridors [7]. The principle is based on the compensation of the distributed line reactance by the insertion of a series capacitor. Figure 1.3 shows a typical series compensated transmission system equivalent seen from a generator, where X_T, X_L and X_{sys} represents transformer, transmission line and system equivalent reactances, R represents transmission line resistance, and X_C represents reactance of the series capacitor. The ratio of the capacitive reactance of the series capacitors to the total equivalent inductive reactance of the line is known as *degree of compensation.* This is often written as:

$$\text{Degree of compensation, } k(\%) = \frac{X_C}{X_L} \times 100\ \%. \tag{1.1}$$

Typical values for the degree of compensation range from about 0.2 to 0.8. The compensation values greater than about 0.7 require careful study [8]. In the power systems, only degrees of compensation less than unity are considered, even though the capacitive compensation larger than line inductive reactance ($k > 1$) is possible in theory.

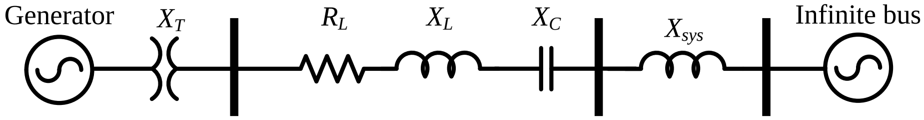

Figure 1.3: The system equivalent of a series compensated system from a generator.

The reactive power generated by the capacitor is continuously proportional to the square of the line current. This means that the series capacitor has a self-regulating effect. When the system loading increases, the reactive power generated by the series capacitor increases as well. The response of the series capacitor is automatic, instantaneous and continuous as long as the capacitor current remains within the specified operating limits. The following are some of the major benefits of incorporating series capacitors in transmission systems:

- **Steady-state voltage regulation:** During light loading, the voltage drop on the series capacitor is low. When the load increases and the voltage drop on the line becomes larger, the contribution of the series capacitor increases, and therefore the system voltage at the receiving end will be regulated.

- **Load sharing between parallel transmission lines:** When two transmission lines are connected in parallel, the natural power sharing between them is determined by their respective impedances. The two lines could have different thermal ratings, but their impedances could still be very close. In such situation, the power transmitted in each line will be similar [9]. In this case, if overloading the lower thermal rating line is to be avoided, then the full power capacity of the other line will never be reached. However, if a series capacitor is installed in the higher thermal rating line, both transmission lines can operate at their maximum capacity when the appropriate degree of compensation is provided (50% in this case) [10].

- **Increase in power transfer capability:** The series compensation will improve the power transfer capability in two ways. It will decrease the initial generator load angle corresponding to a specific power transfer, and it will also shift the power-load angle ($P - \delta$) characteristic curve upwards. These changes will result in increasing the transient stability margin.

The increase in the power transfer capability as a function of the degree of compensation for a transmission line can be illustrated using a two-bus system shown in Fig. 1.4(a) and corresponding phasor diagram in Fig. 1.4(b). The power transfer on the transmission line is given by:

$$P = \frac{|V_S||V_R|}{X_L - X_C}\sin\delta = \frac{|V_S||V_R|}{X_L(1-k)}\sin\delta \tag{1.2}$$

where $|V_S|$ and $|V_R|$ are sending end and receiving end voltage magnitudes, δ is phase angle difference between sending and receiving end voltages, and $k = X_C/X_L$ is the degree of compensation.

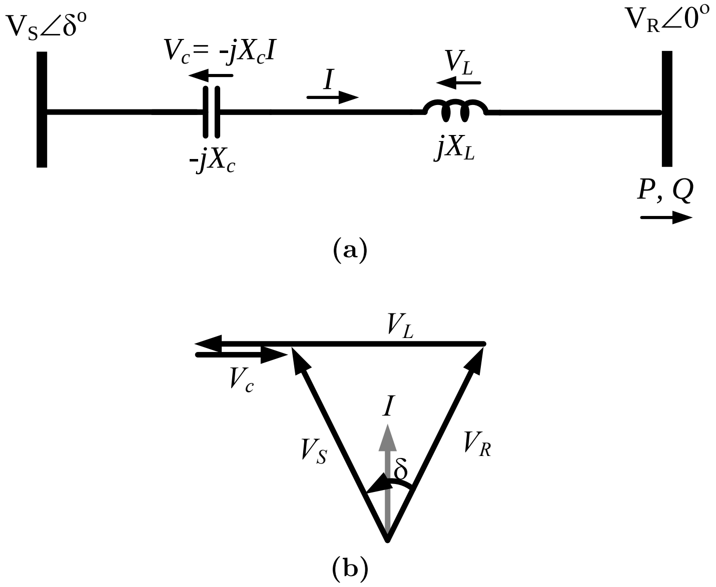

Figure 1.4: (a) A series capacitor compensated transmission line, and (b) corresponding voltage and current phasors.

The effect of the degree of series compensation on power transfer capability of the line is shown in power versus angle curve ('$P - \delta$ curve') in Fig. 1.5(a). The power transfer through the transmission line at different compensations for a constant angle difference of 40^o are marked in Fig. 1.5(a). From the plot in Fig. 1.5(a), it can be observed that the 40% compensated line transfers 1.07 *p.u.* power compared to 0.64 *p.u.* during no compensation

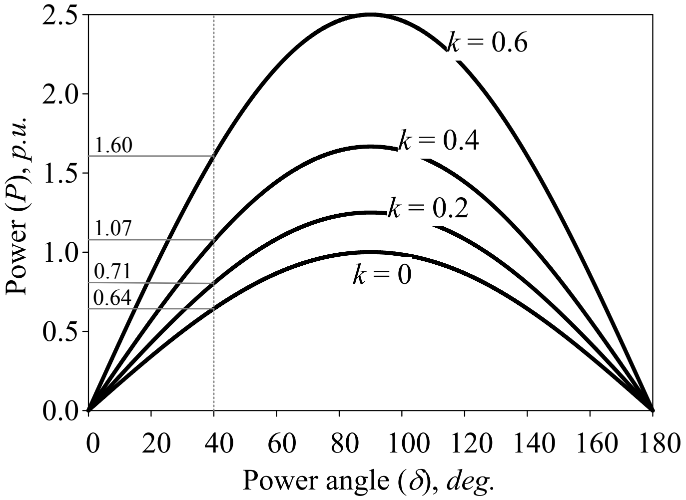

(a) $P - \delta$ curve

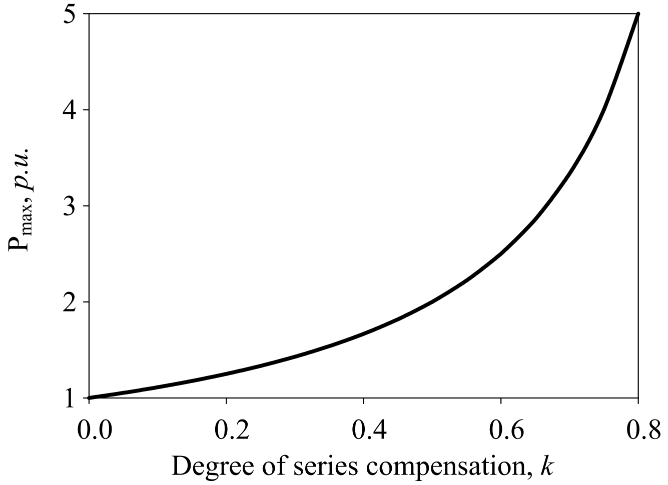

(b) P_{max} vs. k curve

Figure 1.5: (a) Power vs. δ plot, and, (b) maximum power transfer capability as a function of compensation degree k.

when operating at $\delta = 40^o$. As mentioned before, the practical compensation degree ranges from 20 to 80 percent, and the transmission capability increase of more than two times can be obtained in practice. Similarly, Fig. 1.5(b) shows the maximum power transfer capability of the line as a function of compensation degree.

1.3 Flexible AC Transmission Systems

All of the above discussed advantages of series compensation can be achieved without the risks of SSR phenomena, if series Flexible AC Transmission Systems (FACTS) devices are used instead of series capacitors. These devices are also able to provide adequate and fast damping to power system oscillations. FACTS devices are power electronic based controllers which can influence transmission system voltages, currents, impedances and/or phase angles rapidly [5]. These controllers have the flexibility of controlling both real and reactive power, which could provide an excellent capability for improving power system dynamics.

FACTS controllers may be based on thyristor switching devices with no gate turn-off (only with gate turn-on) known as '*line commutated*' devices, or switching devices with gate turn-off capability (GTO, IGBT or IGCT) also known as '*self commutated*' devices. In general, the self-commutated controllers are based on dc to ac converters, which can exchange active and/or reactive power with the *ac* system. The line-commutated controllers are either reactive compensators, which are unable to exchange real power with the ac system, or regulators, which can exchange real (and reactive) power, but are unable to generate reactive power and thus cannot provide reactive compensation. The FACTS devices can be classified into the following categories based on their applications.

1. **Series FACTS device:** The series FACTS devices are used to control power flow through transmission line. The series FACTS devices can be used to replace fixed series capacitor compensation or in combination with the fixed series capacitor. Thyristor switch based series FACTS devices are Thyristor Controlled Series Compensator (TCSC), Thyristor Switched Series Capacitor (TSSC) and Thyristor Controlled Phase Angle Regulator (TCPAR). Similarly, Static Synchronous Series Compensator (SSSC) is a gate turn-on/off based series FACTS device.

2. **Shunt FACTS device:** Shunt compensation is used in a transmission system to supply reactive power to increase the transmittable power and voltage profile along the line. Thus, the shunt compensator should be able to minimize the line overvoltage under light load conditions, and maintain voltage levels under heavy load conditions [5]. Static Var Compensator (SVC), Thyristor-Switched Capacitor (TSC) and Thyristor-Controlled Reactor (TCR) are thyristor switch based shunt FACTS devices, whereas Static Synchronous Compensator (STATCOM) is a gate turn-on/off based shunt FACTS device.

3. **Combined FACTS device:** The multiple converter based FACTS devices can be operated in three possible arrangements. In the first arrangement, one converter is in series and the other is in shunt with the transmission line. One of the such combination device is know as Unified Power Flow Controller (UPFC) which combines a STATCOM and an SSSC. In the second arrangement, multiple converters are connected in series with, usually, a different line. This arrangement is know as Interline Power Flow

Controller (IPFC). In the third arrangement, converters are connected in shunt, each with a different power system. This arrangement functions as an asynchronous tie, sometimes referred to as a back-to-back (BtB) STATCOM tie.

In the studies conducted in this thesis, the series FACTS controller based on thyristor switches, namely Thyristor Controlled Series Capacitor (TCSC) and IGBT based FACTS controller namely Static Synchronous Series Compensator (SSSC), are considered. Brief descriptions of the TCSC and SSSC devices are given in the following subsections.

1.3.1 Thyristor Controlled Series Capacitor

Thyristor Controlled Series Capacitor is a series-controlled reactance that can provide continuous control of power on the ac line over a wide range. A schematic of the TCSC is shown in Fig. 1.6. By appropriately controlling thyristor firing angle, increase or decrease in fundamental-frequency voltage across the fixed capacitor can be achieved [11]. This change in voltage changes the effective value of the TCSC reactance. Minimum series capacitive compensation is reached when the reactor branch is turned off.

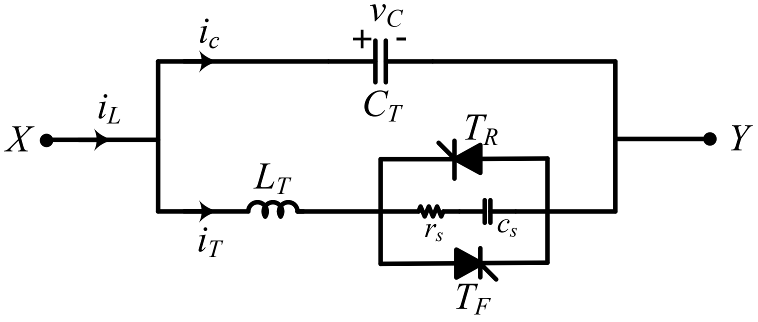

Figure 1.6: A schematic diagram of a TCSC.

The TCSC has been installed and operated successfully by utilities in several countries. One example of this installation is the Brazilian North-South interconnection (a 500 kV, 1020 km transmission line with a rated transmitted power of 1300 MW), where a hybrid three-phase TCSC connects the North and South systems [12]. Such a hybrid three-phase TCSC, shown in Fig. 1.7, consists of six fixed capacitors distributed equally along the line length and two TCSC modules located at the sending and receiving ends. The degree of compensation of the interconnection is 66% (1100 $MVar$ capacitive), where the fixed capacitors provide 54% and each TCSC module provides 6%. The task of the TCSC modules is purely damping the low-frequency inter-area power oscillations between the two systems.

These oscillations would otherwise provide a hazard to the stability of the interconnected system.

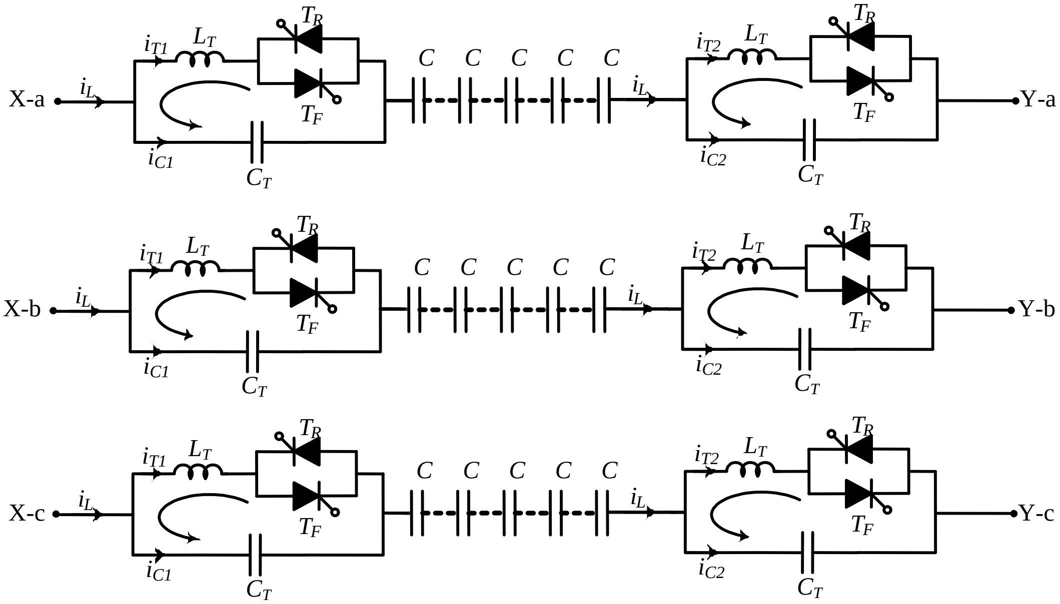

Figure 1.7: A schematic diagram of a hybrid three-phase TCSC.

Often the TCSC is combined with fixed capacitor to provide series compensation in order to increase the transient stability in the most cost-effective way. The operating principle and modelling of the TCSC will be discussed in detail in Chapter 2.

1.3.2 Static Synchronous Series Compensator

Static Synchronous Series Compensator (SSSC) is a series-controlled FACTS device and uses a voltage-source converter to inject series voltage in quadrature phase lead or lag with the line current. The converter output is arranged to appear in series with the transmission line via the use of a series coupling transformer. The converter output voltage V_{inj} can be set to any relative phase, and any magnitude within its operational limits. The injected voltage can be either adjusted to appear to lag the line current by 90^o, thus behaving as a capacitor, or lead the line current by 90^o so as to act as an inductor. If the converter dc side is connected to dc energy source such as battery, the device can also inject active power to the line and vice versa. The schematic of the SSSC is shown in Fig. 1.8(a), and the phasor diagram for inductive/capacitive operation is shown in Fig. 1.8(b).

This type of device can provide a wide range of series compensation by varying the magnitude and phase angle of the injected voltage. For example, reversal of the phase of V_{inj} from capacitive to inductive region increases overall line reactance; this may be desirable to

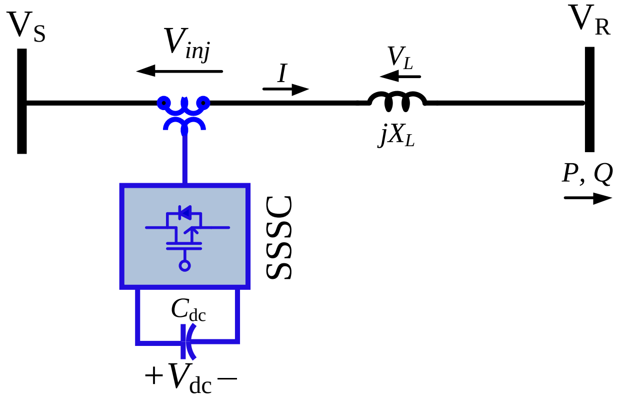

(a) SSSC compensation.

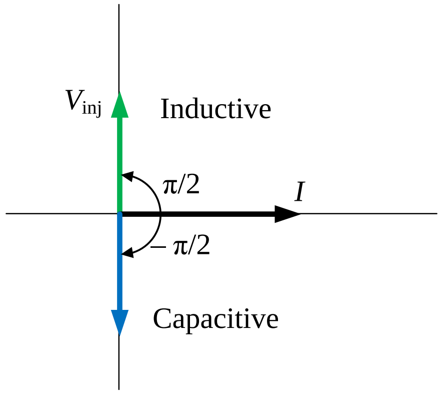

(b) Phasor diagram.

Figure 1.8: An SSSC compensation schematic and respective phasor diagram.

limit fault current, or to dampen power system oscillations. More details on SSSC operating principle and modelling are provided on Section 2.4 of Chapter 2.

There are many types of converter topologies within the voltage-sourced converter category that can be considered for the SSSC operation – for example, multi-pulse, multi-level, and cascade topology. As all the converter topologies operate by turn-on and turn-off of power electronic gates, they require some sort of switching circuitry. The inverter switching strategies being used in practice at present can be classified into two main categories [13]:

1. *Fundamental frequency switching:* In this technique, the switching of each semiconductor device is limited to one turn-on and one turn-off per power cycle. A six-pulse converter topology produces a quasi-square-wave output with this switching method, which has an unacceptably high harmonic content. In practice, a number of six-pulse units are combined in series and/or parallel to achieve a better waveform quality and higher power ratings.

2. *Pulse-Width Modulation (PWM):* In this technique, the semiconductor switches are turned '*on*' and '*off*' at a rate considerably higher than the power frequency. The output waveform has multiple pulses per half-cycle. This shifts the undesirable harmonics in the output to higher frequencies and filtering is possible with smaller components. This method suffers, however, from higher switching losses compared to the fundamental frequency switching technique. The PWM method has certain advantages such as faster response and capability for harmonic elimination [14] compared to the fundamental frequency switching method, and hence this technique is implemented in the design of SSSC in this thesis. Brief descriptions of voltage source converter and PWM switching methods are provided in the following subsection.

A. Voltage Source Converter

Figure 1.9 shows a three-phase six-valve Voltage Source Converter (VSC) topology. The VSC topology provides a three-phase ac voltage, where the amplitude, phase, and frequency of the voltages can be controllable. Two valves in one leg (1 and 4, 3 and 6, 5 and 2) cannot be switched on simultaneously because this would result in a short circuit across the dc link. On the other hand, the valves of a leg of the inverter cannot be switched off simultaneously as this will result in indeterminate ac voltage output. Similarly, turning on upper switches 1, 3 and 5 and turning off lower switches 4, 6 and 2 or vice versa will lead to zero output voltages. In this case, the ac line currents freewheel through either the upper or lower components and should be avoided [15]. Various switching techniques can be implemented for turning *on* and *off* the valves [13]. One such method used in this thesis is Pulse Width Modulation technique.

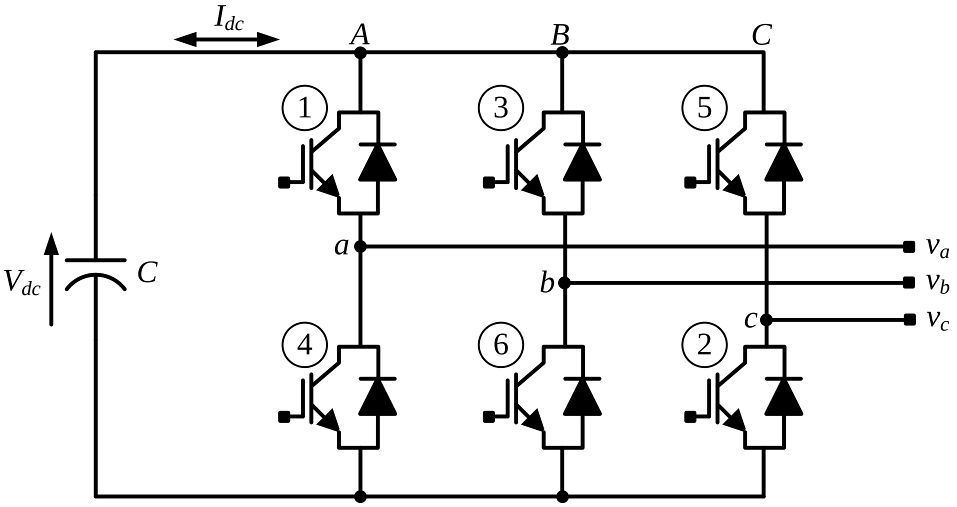

Figure 1.9: Three-phase converter topology.

B. Pulse Width Modulation

A Pulse Width Modulation (PWM) based switching scheme creates a train of switching pulses at a rate considerably higher than the power frequency. The *ac* output voltage of the converter consists of multiple pulses per half-cycle, and the width of the pulses can be varied to change the amplitude of the fundamental frequency of the output voltage. The PWM converter related basic terms that are used throughout this thesis are as follows:

v_{ref} = Reference sinusoidal signal, volts.
f_r = Reference sinusoidal wave frequency, Hz, 60 Hz in general.
v_{cr} = Triangular carrier signal, volts.
f_c = Triangular carrier wave frequency, Hz.
$m_a = V_{ref}/V_{carrier},$ amplitude modulation ratio, or modulation index.
$m_f = f_c/f_r,$ frequency modulation ratio.

For a three-phase ac voltage output, modulating reference signals that are 120^o out of phase are used. Figure 1.10(a) shows the three-phase reference and a carrier waveforms. Frequency of reference signal is chosen as 1 Hz and that of carrier is chosen as 9 Hz for the demonstration purpose. Figure 1.10(b) shows the switching signal generated for upper valves of leg B and C, and corresponding output voltage. The fundamental frequency component is marked as v_1 in Fig. 1.10(b). Switching pulses are generated by comparing the triangular carrier waveform and the modulating reference waveforms. For example, when the rising slope of the triangular wave crosses the sinusoidal wave $v_{ref,b}$, ③ switches '*off*', and when the negative slope of the triangular wave crosses the $v_{ref,b}$, ③ turns '*on*'. This type of switching technique uses sinusoidal reference waveform and is known as Sinusoidal Pulse Width Modulation (SPWM).

The magnitude of the PWM converter output voltage can be controlled from zero to the maximum value and the phase angle and/or frequency can be controlled by controlling the reference wave phase and/or frequency almost instantaneously [5].

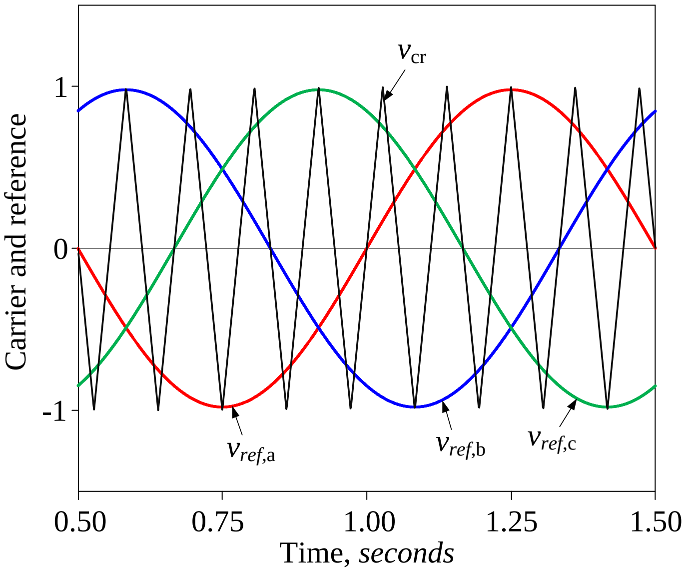

(a) SPWM reference and carrier waveforms

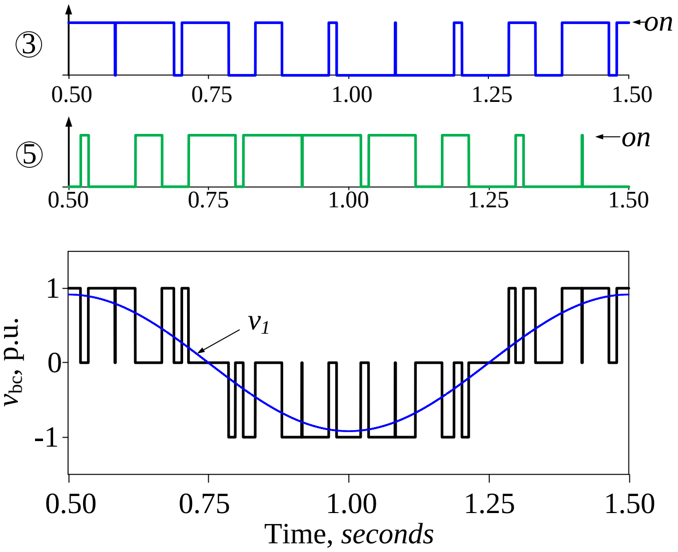

(b) Switching signals and output voltage

Figure 1.10: Three-phase VSC ideal waveforms: (a) SPWM reference and carrier waveforms, and (b) Switching signals for ③ and ⑤, and output voltage v_{bc} in per unit of dc voltage, $m_a = 0.98$, $m_f = 9$.

1.4 Subsynchronous Resonance in Power Systems

The IEEE definition of subsynchronous oscillation is [16]:

> "an electric power system condition where the electric network exchanges significant energy with a turbine-generator at one or more of the natural frequencies of the combined system below the synchronous frequency of the system following

a disturbance from equilibrium".

Subsynchronous resonance is a phenomenon associated with the energy exchanged between the turbine-generator mechanical and electrical systems. A number of mechanical masses of the turbine-generator shaft (e.g. turbine stages and generator) oscillate at some frequencies known as torsional oscillations which are characterized by their mechanical properties like stiffness, mass and inertia. The frequencies of these oscillations range from 10 to 55 Hz for 60 Hz system [1, 17].

The series capacitive compensation is known to cause self-excited oscillations at subsynchronous frequencies in the electrical network [17]. If the torsional oscillation frequency is close to the electrical resonance frequency due to the presence of a series capacitor, the torsional oscillation will amplify, resulting in a shaft fatigue or damage. This kind of interaction between the electrical and mechanical systems at subsynchronous frequencies has been termed as "Subsynchronous Resonance" or "SSR". Two successive shaft failures were reported at Mohav Generating station in Western USA in December 1970 and October 1971 due to the SSR phenomenon [2]. Before that incident, the SSR was being treated as strictly an electrical phenomenon. These incidents alerted utilities to plan ahead to avoid SSR problems during system operation.

Various SSR mitigation techniques have been proposed after Mohav incidents and continues to be a subject of research and development aiming at developing effective SSR countermeasures [18]. There are two basic techniques to mitigate SSR; (*i*) the first is to artificially detune the natural frequencies of the transmission and generation systems; (*ii*) the second is to add an artificially generated stabilizing torque. Detuning may be achieved by continuously filtering the subsynchronous currents as they enter the turbine-generators using static blocking filters [19]. Artificially generated stabilizing torque can be achieved through many ways such as supplementary excitation damping controllers (SEDC) [20], static var compensator (SVC) [21] and super conducting magnetic energy storage (SMES) [22].

Several studies have investigated the potential of using FACTS devices capability in mitigating subsynchronous resonance of series capacitive compensated transmission grids [23–29]. The use of Thyristor Controlled Series Capacitor (TCSC), Static Synchronous Compensator (STATCOM), and Static Synchronous Series Compensator (SSSC) in their balanced mode of operations have been implemented and/or studied as means for damping SSR.

1.5 Power System Oscillations

The stable operation of a power system requires a continuous match between energy input from the prime movers and load demands. Load demand continuously changes and must be accompanied by a corresponding change in the input to the prime movers of the generators. If the mechanical input does not rapidly match the electrical load, system tends to oscillate, and system frequency and voltage will deviate from normal operating conditions. More severe oscillations will occur if the system experiences faults, generation losses, switching of lines or loss of a large load. In an inter-connected system, if one machine deviates from its synchronous speed, power is transferred from the other generators in the system in such a way so as to reduce the speed deviation. The moments of inertia of the generator also come into play, and result in the speed over-correcting in an analogous manner to a pendulum swing, leading to generator rotor oscillation. Since these oscillations are related with moment of inertia of the machines, the frequency of the oscillations is very low, in the range of $0.1 - 2\ Hz$. These oscillations are classified into two groups based on the participation of the machines [30].

1.5.1 Local Oscillations

Local oscillations are associated with single generator or a single plant oscillating against the rest of the power system. Such oscillations are called *local plant mode* oscillations. The stability problems related to such oscillations are similar to those of a single-machine infinite bus (SMIB) system. The oscillation of a machine connected to infinite bus system (Fig. 1.11a) can be observed by comparing with a pendulum swing [31] as shown in Fig. 1.11(b) and (c). When the pendulum is disturbed from equilibrium point, it oscillates around the equilibrium point in the case of stable equilibrium point as shown in Fig. 1.11(b). On the other hand, the pendulum loses stability if it is disturbed in the case of unstable equilibrium point as shown in Fig. 1.11(c). In similar fashion, the machine returns to pre-disturbance equilibrium point if it is operating at stable point, and loses synchronism with rest of the system if it is disturbed during an unstable equilibrium point.

Local oscillations may also be associated with few machines close to each other. Such oscillations are called *inter-machine* or *inter-plant mode* of oscillations. The frequency of oscillations for local modes, both local plant or inter-plant, have values in the range of $0.5\ Hz - 2.0\ Hz$.

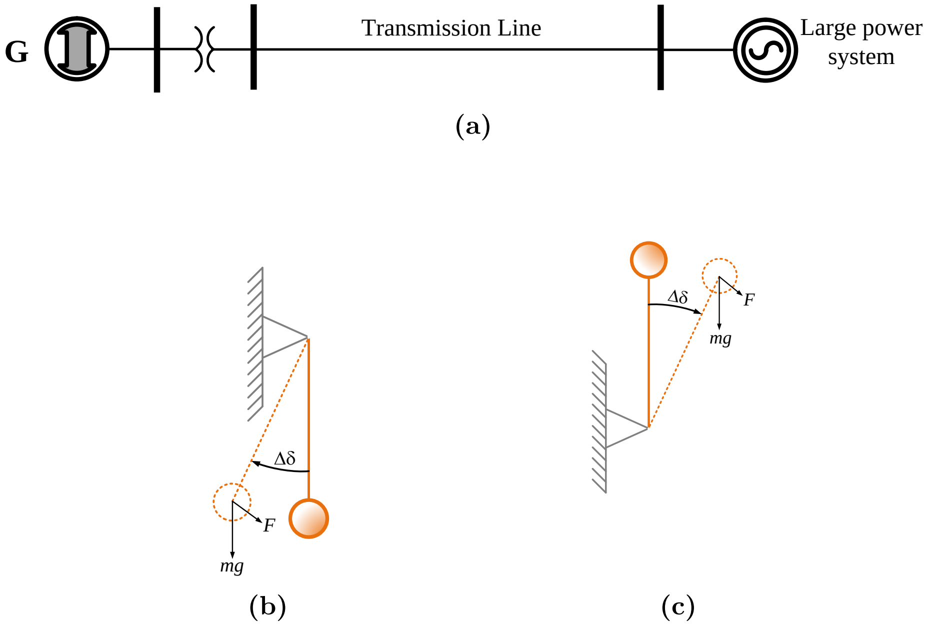

Figure 1.11: (a) A generator-infinite bus system and mechanical analogues: a pendulum at (b) stable and (c) unstable equilibrium points.

1.5.2 Inter-Area Oscillations

Modern power systems have well-developed transmission networks covering large geographical areas. In these circumstances, a disturbance near one of the power stations will also distort the power balance at neighbouring stations and may trigger widespread oscillations. The oscillations involves group of generators in one area swinging against a group of generators in another area. Such oscillations are called inter-area mode of oscillations. A typical large interconnected system is shown in Fig. 1.12. Such system usually have two distinct forms of inter-area oscillations [30]:

1. An oscillation mode involving all interconnected generators. The system is essentially split into two areas, with generators in one area swinging against generators in the other area. The oscillation frequency is very low, in the order of 0.1 to 0.3 Hz.

2. Oscillations involving subgroups of generators swinging against each other. Such oscillations have frequency in the range of 0.4 to 0.7 Hz.

A multi-mass mechanical system as shown in Fig 1.13 [32] can be used to understand the basics of the electromechanical swings resulting in multi-machine power systems. The generators can be compared with the masses suspended from a network consisting of elastic strings representing the transmission lines. In the steady state, each of the strings is loaded below its breaking point (steady-state stability limit). If one of the strings is suddenly cut

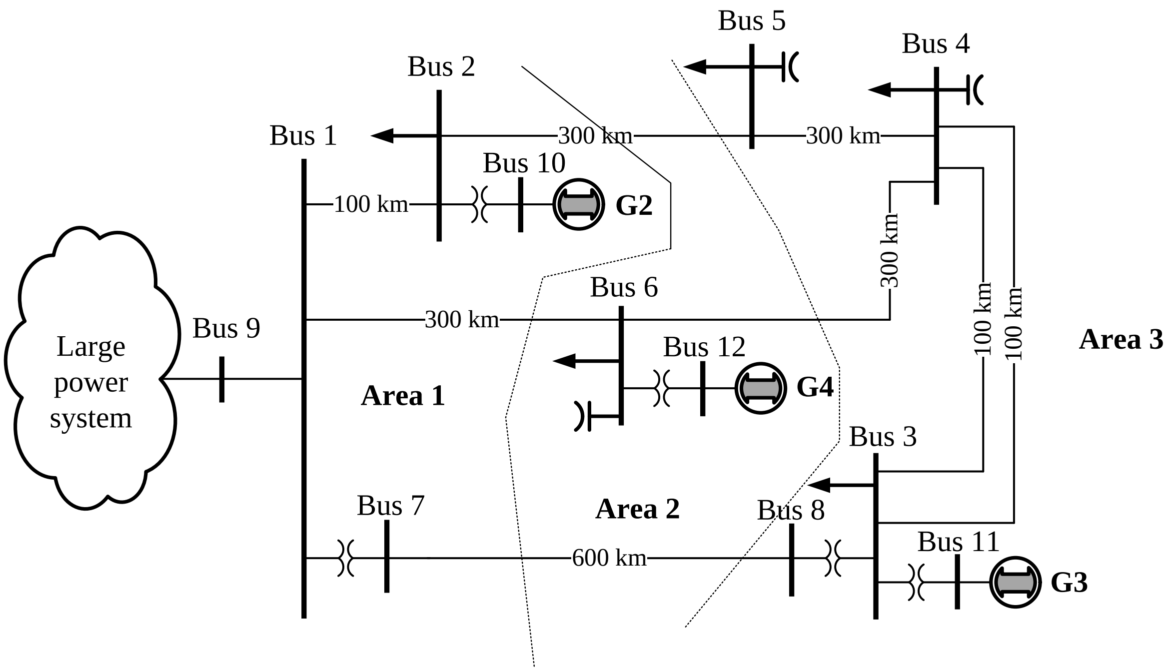

Figure 1.12: A typical multi-machine power system.

(representing a line tripping), the masses will experience coupled transient motion (swinging of the rotors) with fluctuations in the forces in the strings (line powers). Such a sudden disturbance may result in the system reaching a new equilibrium state characterized by a new set of string forces (line powers) and string extensions (rotor angles) or, due to the transient forces involved, one string may break, so weakening the network and producing a chain reaction of broken strings and eventual total system collapse.

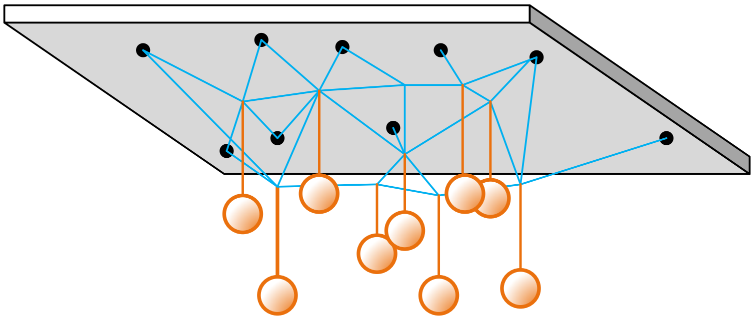

Figure 1.13: Mechanical analogue of swings in a multi-machine system.

Many electric utilities world-wide are experiencing increased loads on portions of their transmission systems, which can, and sometimes do, lead to poorly damped, low-frequency oscillations. These oscillations can severely restrict system operations by requiring the curtailment of electric power transfers as an operational measure. They can also lead to widespread system disturbances if cascading outages of transmission lines occur due to oscillatory power swings, like during the blackout in Western US/Canada interconnected system on August 10, 1996 [33]. A record of power flow on a major transmission line during this event is shown in Fig. 1.14 [34]. In this case, system experienced near zero damping low frequency oscillation, which grows due to sequences of incidents. This growing oscillation eventually splits the system into a number of disconnected regions, with the loss of power to a considerable number of customers.

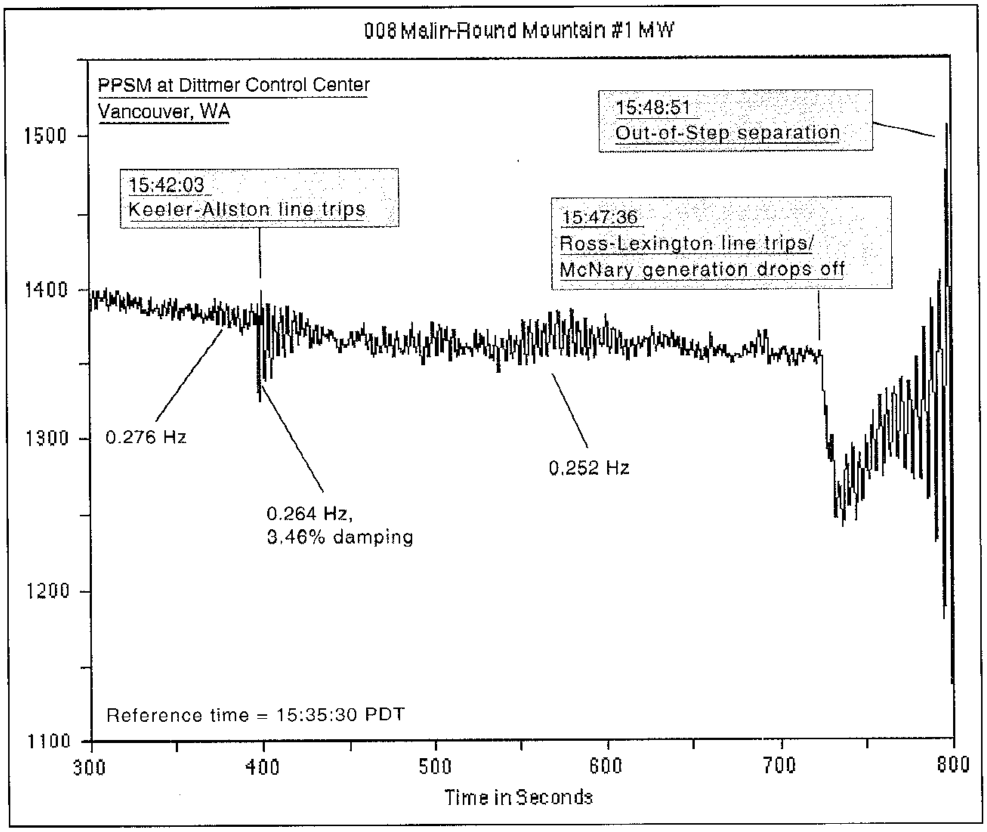

Figure 1.14: Oscillations on the WSCC system, August 10, 1996.

The power system oscillations can be damped, when extra energy is injected into the system which is instantaneously decelerated, and/or when extra energy is consumed in the system which is instantaneously accelerated. The damping energy is obtained by the modulation of load or generation for a period of time, typically in the range of five to ten seconds. The damping energy must have the correct phase shift relative to the accelerated/decelerated system, as incorrect phase angles can excite the oscillations.

Several studies have investigated the potential of using FACTS Controllers' capability in damping inter-area oscillations. The use of Thyristor Controlled Series Capacitor (TCSC), Static Var Compensator (SVC), Static Synchronous Compensator (STATCOM), Unified

Power Flow Controller (UPFC), Thyristor Controlled Phase Angle Regulator (TCPAR), and Static Synchronous Series Compensator (SSSC) have been the subjects of several studies evaluating their respective effectiveness in enhancing power system dynamics [35–42].

1.6 Impact of Phase Unbalance Operation on SSR damping

The coupling between the electrical and mechanical sides in a synchronous generator occurs through an interaction between the driving mechanical torque and the developed electromagnetic torque. The electromagnetic torque is developed by the interaction of the machine currents with the magnetic fields, namely the interaction of the armature currents with the rotor magnetic field and the interaction of the rotor currents with the armature magnetic field. The three-phase currents in the armature windings have their full capability of developing interacting electromagnetic torque when they are balanced in the time and space domains. In this balanced condition, the three-phase currents create a circular rotating magnetic field, of a constant amplitude and speed. Unbalanced currents, on the other hand, create an elliptic rotating field which has time-varying amplitude and rotating speed. The elliptic field, however, is equivalent to a circular rotating field component, and a pulsating field component, of comparatively lower magnitude than if the currents are balanced. This means that phase imbalance weakens the electromechanical coupling and, as a result, reduces the energy exchange between the generator electrical and mechanical sides.

An effective SSR countermeasure based on creating phase unbalance was introduced in [43–45]. The author demonstrated the effectiveness of the phase imbalance in damping SSR using passive elements: inductors and capacitors. The presence of phase imbalance weakens the electromechanical coupling, which will result in reduction of the energy exchanged between the electrical and mechanical sides of turbine generators.

1.7 Adaptive Control Applications in Power Systems

Power systems are complex, dynamic systems and are subjected to unpredictable disturbances such as change in loads, and faults, for example, single-phase to ground faults, three-phase faults, etc. To enhance the dynamic stability of such complex systems, various kind of controllers, such as power system stabilizer for generators and supplementary damping controller for FACTS devices, are being used. The traditional approach is to use fixed-parameter controllers such as lead-lag controllers. Over time, the operating conditions change and fixed-parameter controllers designed for a specific operating point generally cannot provide the same optimal performance at new operating conditions. It is for this reason that the control method that can adapt to wide range of operating conditions, known as adaptive controller, is preferred to improve the power system performance [46–49]. The adaptive control application in power system dynamic enhancement has been a topic of research since 1970's [50]. Several techniques for adaptive identification have been proposed in literature – neural networks, neuro-fuzzy, particle swarm optimization, robust H_∞ based controllers, and pole-shift controllers [42, 46–49, 51–53].

Adaptive controllers has been proposed and used for Power System Stabilizer (PSS) applications successfully in the past. Extending such a control algorithm to transmission line devices, such as FACTS devices, is limited due to the fact that the identification procedure becomes inaccurate for large disturbance conditions in power system, such as three-phase faults. This explains the reason why there are number of works published in technical journals related to PSS applications, but, only a very few applications for transmission line controls. The least-square type of identifiers are optimal if the disturbances are Gaussian and the error is a white noise. In practice, these errors may not be white noise type. It is a direct consequence of the least-square formulation that a single large error will have a drastic influence on the result, because the errors are squared in the least-square criterion [54]. In power systems, especially during large disturbances, parameter identification using least squares procedures is a real challenge. The parameters identified during such conditions have rapid fluctuations due to the large estimation error, leading to poor controller performance. So, a computationally efficient identification algorithm capable of handling large estimation errors is desirable in practical power system applications.

To address the above problem with identification, Sadikovic et.al. [55] in 2006 increased the order of the model to a $12th$ order and proposed the use of regularized constant trace algorithm [54] to keep the correlation matrix symmetrical during the identification procedure. They also proposed use of Kalman filter instead of recursive least-square to improve estimation accuracy.

Domahidi et. al. [56] used a $10th$ order plant model and proposed a random-walk term for updating the covariance matrix in RLS algorithm for pre-specified duration following a large disturbance to achieve smoother variations in the identified coefficients. The authors of the paper also implemented a controller dead-zone following large disturbances to give sufficient time to stabilize the estimator. They reported that the variable forgetting factor based RLS causes large variation in estimated parameters during transients, leading to noisy control that takes a longer time to settle down.

Malik et. al. [48] did some pioneering work in adaptive control for PSS applications.

Later, Rahim, Nowicki and Malik extended the adaptive controller for FACTS application [57]. They showed that the initial transients were the cause of inaccurate estimation, and therefore, the output response was poor for the initial transients. Once the estimation errors reduced (for subsequent disturbances), a better output response was achieved.

Similarly, Chaudhuri et. al [58] reported that the adaptive controller loses stability due to inaccurate estimation, for small time windows, just after clearing faults in the system. Authors used noise covariance matrix in Kalman filter to tackle sudden parameter changes in the system.

This thesis addresses the above discussed problems with the identifiers for adaptive control of FACTS devices. More specifically, it proposes a solution using the RLS technique to handle large disturbances. In the proposed method, a simple *Sigmoid* like nonlinear function is used in parameter update equation, which imposes penalty on error magnitude, i.e. a larger error will have less effect on parameter update. This method helps in smoothing out the parameter variations effectively during major disturbances, and thus produces a stable control response without the need of controller dead-zone.

In this work, it is found that it is not necessary to increase the order of the model or create a controller dead-zone or do a parameter freezing during large disturbance conditions. A simple third-order model with a Sigmoid like nonlinear function proposed in the thesis increases the accuracy of the RLS algorithm during large disturbances. A simple modification to the RLS algorithm as proposed in the thesis is sufficient to generate an effective adaptive control action.

1.8 Electromagnetic Transient Simulation (EMT) Modelling

Electromagnetic transient modelling is a very detailed three-phase representation of the power system. It differs from phasor domain solution, such as load-flow and transient stability programs. The transient stability programs utilize positive sequence representation of the power system and steady-state equations to represent entire electrical systems and can output only fundamental frequency magnitude and phase information. The order of simulation step will be in milliseconds and can be used to study large systems. The stability programs rely on phasor-type solutions and simplified models and do not provide an accurate representation of the behaviour for the switching level transients, whereas the EMT type programs solve instantaneous differential equations and produces results as instantaneous values in time, yet can be converted into phasor magnitudes, and angles. The EMT programs can accurately model physical devices, including non-linearity and harmonics.

Certain phenomena, such as sub-synchronous resonance and device switching, require detailed three-phase representation of machines and systems. So, the EMT type of software is being used for various applications: switching and lightning surge analysis, insulation coordination, shaft torsional oscillation studies, protective relay modeling, harmonic and power quality studies, and HVDC and FACTS device modelling. The simulation time step is usually set in microsecond intervals to capture the transient behaviour of the system. The EMT simulation requires huge computing resources and may need hours to run the models due to the detailed representation of the system. To speed up the simulation process, it is a usual practice to model non essential devices by their average models.

For the proper assessment of performance of the FACTS devices, a great effort has to be spent in detailed modelling. In this thesis, commercially available EMT simulation tools, namely EMTP-RV$^{\text{TM}1}$, PSCAD$^{\text{TM}2}$/EMTDC, and RTDS$^{\text{TM}3}$/RSCAD, are used to develop SSSC and TCSC models. The SSSC and TCSC models are developed in switching level detail and validated against analytical models.

1.9 Motivation and Research Objectives

The practical implementation of FACTS devices is very limited due to their high cost. In comparison to traditional series capacitor compensation, the cost of TCSC and SSSC are almost three to four times higher [6]. A combination of a three-phase TCSC and fixed capacitors or a three-phase SSSC and fixed capacitors (proposed in [28]) for series compensation is still uneconomical compared to the traditional capacitor compensation.

Thus, the idea of developing a robust low-cost controller without degrading reliability has motivated to investigate the use of a mix of conventional technology and the FACTS technology in series capacitive compensation schemes which have the potential of enhancing power system dynamics by damping the low-frequency as well as the subsynchronous oscillations. The basic idea is a spin-off of the phase unbalanced series capacitive compensation schemes introduced in [43–45], which has proven to be an effective SSR countermeasure.

The basic idea of the proposed hybrid series compensation schemes is to use a single-phase TCSC/SSSC in conjunction with fixed capacitors to create a phase imbalance during system disturbances. This can be achieved with the following arrangement: two phases are compensated by traditional series capacitors in each phase and the third phase is compen-

---

[1] EMTP-RV is registered trademark of POWERSYS Solutions Inc.

[2] PSCAD is registered trademark of Manitoba HVDC Research Centre Inc., Manitoba, Canada.

[3] RTDS is registered trademark of RTDS Technologies Inc., Manitoba, Canada.

sated by a combination of a fixed capacitor and a single-phase TCSC/SSSC. This three-phase arrangement is balanced at the power frequency and unbalanced at any other frequency.

The main objectives of the research work are:

1. Damping of subsynchronous resonance using the new proposed hybrid series compensation schemes.

2. Damping of the low-frequency local and inter-area oscillations using the proposed hybrid series compensation schemes.

3. Design of robust adaptive supplementary controllers for TCSC/SSSC using modern optimization techniques to improve low frequency power system oscillation damping.

4. Real-time Hardware-in-the-Loop testing of the proposed adaptive controller.

To achieve above objectives, the electromagnetic transient programs, EMTP-RV$^{\text{TM}}$, PSCAD$^{\text{TM}}$/EMTDC and RTDS$^{\text{TM}}$/RSCAD, are used to develop the detailed models of single-phase TCSC and SSSC and power system. In order to investigate and demonstrate the effectiveness of the proposed schemes in damping SSR oscillations, the IEEE first and second benchmark models for computer simulations of subsynchronous resonance are considered. These computer models were thoroughly tested and have been used to study many SSR related problems in the past.

Similarly, two multi-machine power systems, a three-area, six-machine power system and an IEEE 12-bus system [59], are considered for the studies related to low frequency power system oscillations. A Real-Time Digital Simulator is used for experimental verification of the controller in hardware-in-the-loop testing.

1.10 Scope of the Thesis

One of the aims of this thesis is to study the capability of the single-phase TCSC or SSSC based hybrid series compensation schemes on damping subsynchronous resonance oscillations and low-frequency local and inter-area oscillations in power systems. Another aim is to investigate the effectiveness of the adaptive controller to achieve optimal performance for a wide operating range and different disturbances. Finally, experimental verification of the functioning of adaptive controller in the hardware-in-the-loop is conducted.

1.11 Outline of the Thesis

The thesis consists of seven chapters. In Chapter 1, brief introduction of the fixed capacitor series compensation in power system and its advantages are presented. Furthermore, various types of FACTS devices are briefly introduced. The subsynchronous resonance and low frequency power system oscillations phenomenon are discussed. Brief literature reviews on damping these oscillations are presented. Finally, the motivation behind the thesis and the objectives of the thesis are presented.

Chapter 2 presents details of proposed hybrid series compensation schemes. The detailed description of operating principles and modelling of the single-phase TCSC and SSSC are presented. Furthermore, the validation of the developed TCSC and SSSC model against analytical model are discussed.

In Chapter 3, subsynchronous resonance damping capability of the proposed hybrid TCSC and SSSC schemes are presented. To demonstrate the effectiveness of the hybrid schemes, time-domain simulations results under different disturbance scenarios are presented. The voltage unbalance introduced by the hybrid schemes are also shown.

The power system low-frequency local and inter-area oscillations damping using hybrid TCSC and SSSC compensation schemes are presented in Chapter 4. The time-domain simulation results are presented to demonstrate the effectiveness of the schemes in damping low-frequency oscillations.

Chapter 5 presents robust recursive least square identification based pole-shift control technique to damp the inter-area oscillations. The studies are conducted on two multi-area power systems, and time-domain simulation results are presented.

Chapter 6 presents hardware-in-the-loop test studies of the adaptive pole-shift controller conducted using Real-Time Digital Simulator. The adaptive pole-shift controller algorithm is developed on a DSP board and effectiveness of the controller in damping inter-area oscillations are evaluated using closed loop testing. The experimental results are reported in this chapter.

Chapter 7 presents a summary and the contributions of the thesis.

PART - I

Phase Unbalanced Hybrid Series Compensation

Chapter 2

The Phase Unbalanced Hybrid Series Compensation Schemes

2.1 Introduction

In order to perform the theoretical investigations outlined in Section 1.9, it is necessary, as a first step, to model the two series FACTS controllers. This chapter provides detailed modelling of the single-phase TCSC and SSSC in the electromagnetic transient programs. Moreover, the developed models are validated through step changes in some of their variables.

2.2 Proposed Concept

Figure 2.1 shows the schematics of the proposed schemes for the phase unbalanced series capacitive compensation. In these compensation schemes, hereafter referred to as *hybrid series compensation*, two phases (a, b in Fig. 2.1) are compensated by fixed series capacitors (C) and the third phase (phase c in Fig. 2.1) is compensated using a single-phase TCSC or SSSC in series with a fixed capacitor (C_c).

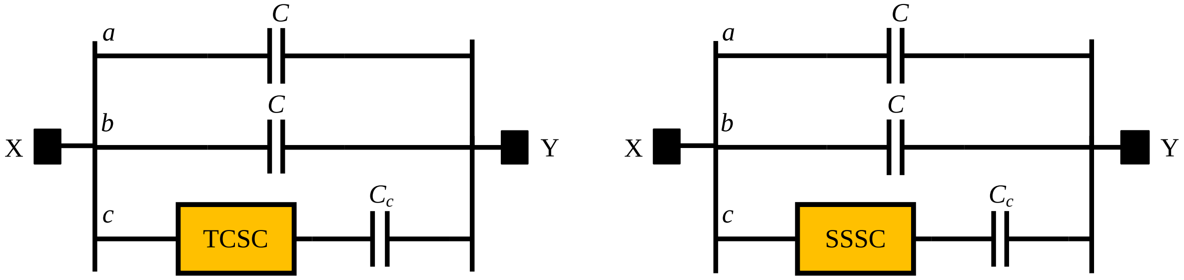

(a) Scheme - I **(b)** Scheme - II

Figure 2.1: Schematics of the hybrid series compensation schemes.

The TCSC and SSSC controls are initially set such that the equivalent reactance at the power frequency combined with the fixed capacitor C_c yields a value equal to the reactance of the fixed capacitor 'C' in the other two phases. Thus, a phase balance is maintained at the power frequency. Since the impedance of the TCSC and the SSSC is independent of the frequency, a phase unbalance is created at any frequency other than the fundamental frequency.

Mathematically, this can be explained as follows - at power frequency, the reactance per phase between X and Y (Fig. 2.1) is given by:

$$X_a = X_b = -j\frac{1}{\omega_0 C} \tag{2.1}$$

$$X_c = -j\frac{1}{\omega_0 C_c} - jX_{S0} \tag{2.2}$$

where ω_0 is the system frequency and jX_{S0} is the effective steady-state capacitive reactance introduced by the TCSC or SSSC such that the reactance of each line is equal, i.e. $X_a = X_b = X_c$.

At any other frequency, f_e, including subsynchronous frequencies, the reactance of the third phase where the FACTS device is present will be:

$$X_c = -j\frac{1}{\omega_e C_c} - j(X_{S0} + \Delta X_s) \tag{2.3}$$

and $X_a = X_b \neq X_c$. The small deviation in the reactance ΔX_s accounts for the action of a supplementary controller.

The proposed schemes have following advantages over the traditional fixed series capacitor compensation:

1. They have inherent capability to suppress the build up of torsional oscillations as the schemes cause the operation of the network in an unbalanced mode at subsynchronous frequencies [43, 44].

2. Since the schemes include FACTS controllers, control methodologies can be applied to further improve subsynchronous resonance oscillations damping.

3. The low frequency oscillations (local and inter-area) can also be damped through implementing an additional supplementary controller in the two FACTS devices.

2.3 Thyristor Controlled Series Capacitor

Thyristor Controlled Series Capacitor (TCSC) is a series-connected device that can provide continuous control of a variable reactance. It consists of a series capacitor, C_T, in parallel with a thyristor-controlled reactor, L_T in each phase (for a three-phase system) as shown in Fig. 2.2. A snubber circuit, denoted by a series resistor (r_s) - capacitor (c_s) connection, is used to limit the rate of rise in the thyristor valve voltage. The thyristor firing angle 'α' (measured from voltage zero crossing), also known as the delay angle, is used to control the current flowing through the reactor branch. The total impedance seen by the system is the parallel combination of the capacitor and the partially conducting inductor. At some firing angles, the reactances of the inductor and capacitor branches become equal, which leads to a resonance condition. During resonance, the impedance across the TCSC becomes very large and results in a significant voltage drop. This situation should be avoided by limiting the thyristor firing angle. The susceptance of the inductor branch ($1/X_L$) is selected as greater or equal to the susceptance of the capacitor branch ($1/X_C$), where, X_L and X_C are the fundamental frequency of the TCSC inductor and capacitor reactances. This brings the operating range of the firing angle (slightly above the resonance zone) above 90^o and is always a practical choice (Fig. 2.3).

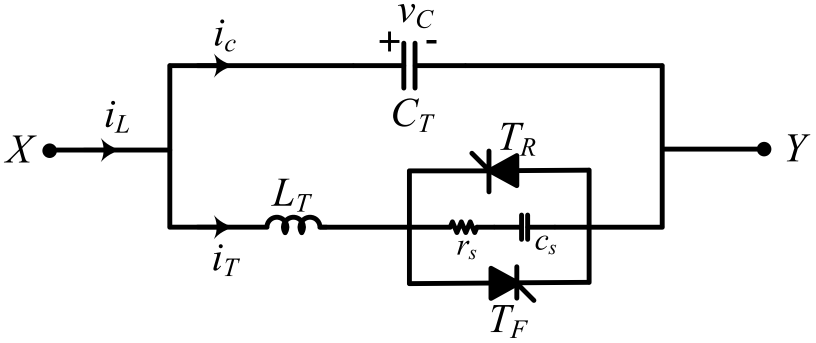

Figure 2.2: Schematic of a thyristor controlled series capacitor.

2.3.1 Basic Operating Principle

The TCSC impedance depends on the firing angle 'α' of the thyristor pairs $\{T_R, T_F\}$. Based on the conduction of T_R and T_F, the operation of the TCSC can be classified into the following three modes [6].

1. ***Bypassed mode***: In this mode, thyristors are made to conduct fully with a conduction angle (σ) of 180^o (Fig. 2.3a). The TCSC module behaves like a parallel capacitor-

inductor combination and the total impedance is $X_{TCSC} = X_C||X_L$. The net TCSC impedance is inductive for the susceptance $1/X_L \geq 1/X_C$. This mode is employed for control proposes and also for initiating certain protective functions.

2. ***Blocked mode***: In this mode, the firings of the thyristors are blocked, and hence no current flows through the thyristor valves (i.e. in the inductor branch). In this case, the TCSC module behaves like a fixed series capacitor with an impedance equal to $X_{TCSC} = X_C$.

3. ***Vernier mode***: In this mode, the TCSC impedance (capacitive or inductive reactance) can be continuously controlled by controlling the thyristor firing angles. However, the smooth transition from capacitive to inductive and vice versa is not possible due to the resonant region between the two modes of operation. This mode can be further divided into (i) *capacitive-vernier mode*, and (ii) *inductive-vernier mode*. The TCSC mainly operates in this mode to create a variable impedance and the details of such an operation is as follows:

In *Vernier mode* of operation, the current passing through the capacitor C_T is expressed as:

$$C_T \frac{dv_C}{dt} = i_L(t) - i_T(t) \tag{2.4}$$

and the apparent TCSC impedance is given by the expression [6]:

$$X_{TCSC} = X_C - \frac{X_C^2}{(X_C - X_L)} \frac{2\beta + \sin 2\beta}{\pi} + \frac{4X_C^2}{(X_C - X_L)} \frac{\cos^2\beta}{k^2 - 1} \frac{(k \tan k\beta - \tan \beta)}{\pi} \tag{2.5}$$

where, $k = \omega_r/\omega_0$ is the ratio of the resonance frequency to the system frequency (ω_0), ω_r is TCSC resonance frequency, and β is the angle of advance, i.e. before the forward capacitor voltage, and,

$X_C = \dfrac{1}{2\pi f C_T}$ is fundamental frequency TCSC capacitor reactance,

$X_L = 2\pi f L_T$ is fundamental frequency TCSC inductor reactance,

$k = \sqrt{\dfrac{X_C}{X_L}}$ is the ratio of the resonance frequency ω_r to the system frequency,

$\omega_r = \dfrac{1}{\sqrt{L_T C_T}}$ is TCSC resonance frequency,

$\beta = \pi - \alpha$ is the angle of advance, i.e. before the forward capacitor voltage becomes zero, f is the system fundamental frequency, and α is the thyristor firing angle.

The TCSC series impedance is usually expressed in terms of a boost factor kB given as:

$$kB = \frac{X_{TCSC}}{X_C} \tag{2.6}$$

A positive value of kB is considered for capacitive operation and a negative value for inductive operation.

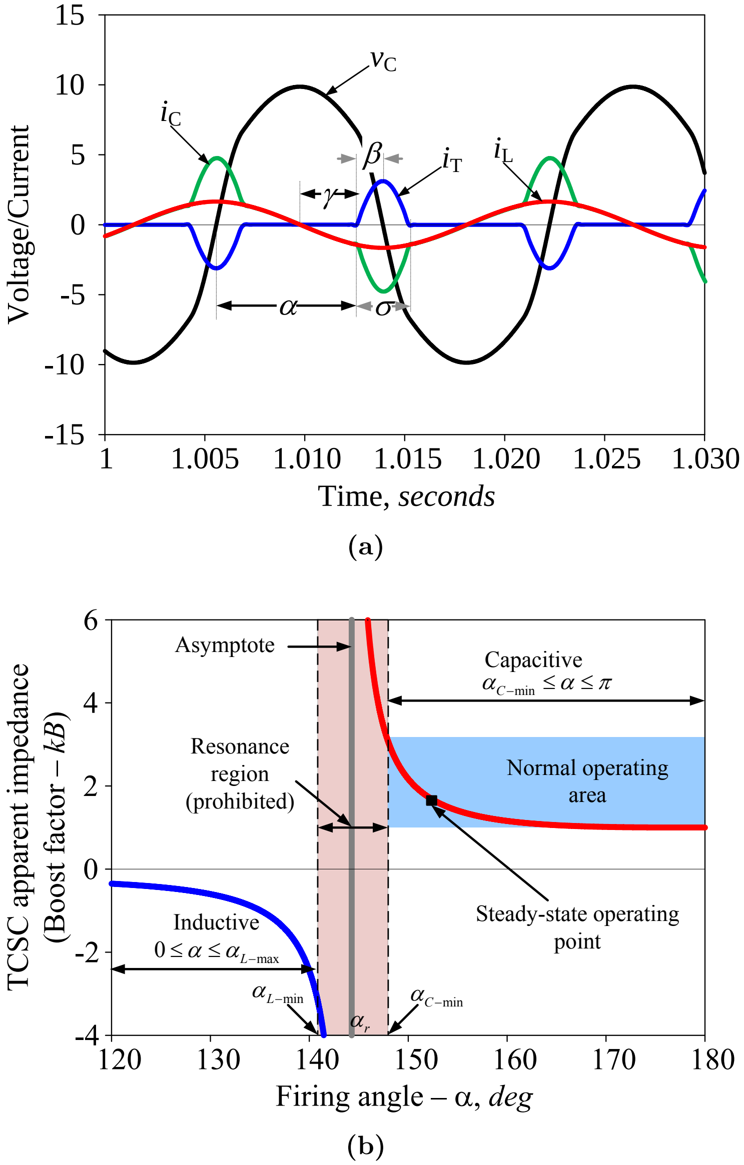

(a)

(b)

Figure 2.3: Steady-state power frequency characteristics of TCSC: (a) trigger angle definition, (b) apparent impedance characteristics.

Various TCSC trigger angles are shown in Fig. 2.3(a). The angle σ is the conduction angle and $\gamma = \alpha - \pi/2$ is the firing angle with respect to current zero crossing. The non-linear relationship between the boost factor and the thyristor firing angle is shown in Fig. 2.3(b) where the capacitive and the inductive operating regions are also shown. At a certain firing angle α_r, the internal resonance condition occurs at a resonance frequency given by the relation $\omega_r = 1/\sqrt{L_T C_T}$. At this condition, the impedance of the TCSC is indefinite. To avoid this situation, the maximum and the minimum firing angles boundaries for the the inductive operation (α_{L-max}) and capacitive operation (α_{C-min}) should be clearly identified.

Capacitive-vernier-control mode: The capacitive-vernier-control mode is a variant of the *Vernier mode.* In this mode, the thyristors are fired when the the capacitor voltage and the current have opposite polarities. This condition causes the reactor current to flow through the capacitor, which increases the voltage across it. The increase in the voltage across the capacitor increases the equivalent reactance of the TCSC. The line current, TCSC inductor voltage and current, and TCSC capacitor voltage and current for the capacitive-varnier mode of operation are shown in Fig. 2.4(a).

Inductive-vernier-control mode: In the inductive-vernier-control mode, the thyristors are fired when the capacitor voltage and current have the same polarity. This condition causes high level of thyristor conduction, resulting in a net inductive reactance of the branch. The line current, TCSC inductor voltage and current and TCSC capacitor voltage and current for the capacitive-varnier mode of operation are shown in Fig. 2.4(b).

From the waveform plots in Fig. 2.4, it can be seen that the *Inductive-vernier* mode introduces a significant distortion to the currents and voltages. For to this reason, the inductive-vernier mode of operation is generally avoided in practice. In the investigations conducted in this thesis, only the capacitive-vernier operation of the TCSC is considered.

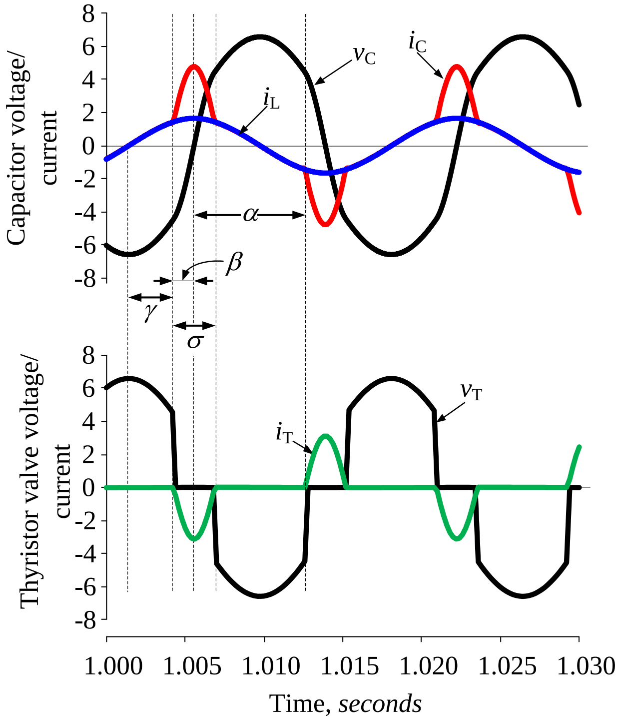

(a) *Capacitive-vernier* ($\gamma = \alpha - \pi/2 = 61.97^o$)

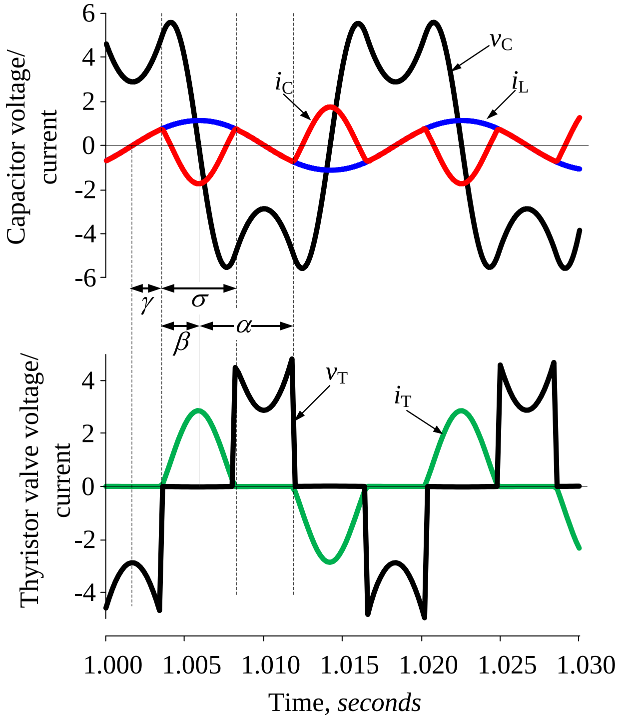

(b) *Inductive-vernier* ($\gamma = 45^o$)

Figure 2.4: Steady-state voltage and current waveforms of capacitor and thyristor valves for: (a) *Capacitive-vernier* ($\gamma = \alpha - \pi/2 = 61.97^o$), and (b) *Inductive-vernier* ($\gamma = 45^o$) modes of operation.

2.3.2 Modelling of TCSC Control

A single-phase TCSC is modelled in the electromagnetic transient simulation software tools (EMTP-RV$^{\text{TM}}$, PSCAD$^{\text{TM}}$/EMTDC and RSCAD/RTDS$^{\text{TM}}$) as a single module, using ideal thyristor pairs and an RC snubber circuit. The schematic of the single-phase TCSC and its control is shown in Fig. 2.5. For three-phase TCSC studies, three units of single-phase TCSC are utilized. A Phase Locked Loop (PLL) is used to extract the phase information of the fundamental frequency line current, which is then used to synchronize the TCSC operation with system. The Phasor Evaluation unit is used to extract the voltage and current phasors. The Boost Measure block calculates the apparent TCSC impedance in terms of a boost factor kB. A positive value of kB is considered for capacitive operation.

A proportional-integral (PI) control based Error Controller is implemented to achieve the desired TCSC boost level. The firing block generates the thyristor firing pulses by comparing the reference phase angle (θ) to the thyristor firing angle (α). In Fig. 2.5, kB_{ref} is the TCSC boost level set point and U_S is the supplementary control signal. The supplementary signal may come from either the SSR damping controller block (discussed in Chapter 5) or power oscillations damping controller block (discussed in Chapter 6). The details of the control blocks are provided in the subsequent sections.

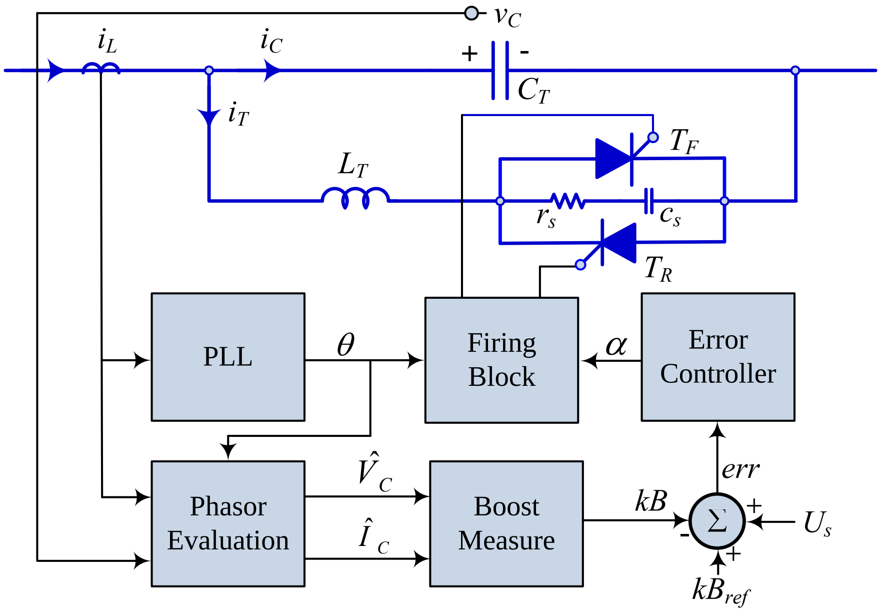

Figure 2.5: Block diagram of a TCSC controller.

A. Phase Locked Loop (PLL)

A Phase Locked Loop is used to estimate the phase angle of the fundamental frequency component of the line current or voltage. The estimated phase angle is used to synchronize the TCSC operation. The PLL consists of a phase detection block, a loop filter, and a voltage-controlled oscillator (VCO). The simulation tools, PSCAD$^{\text{TM}}$/EMTDC and RTDS$^{\text{TM}}$/RSCAD, provide library components for the PLL tracking. In the EMTP-RV$^{\text{TM}}$ studies, the PLL shown in Fig. 2.6 is implemented [60].

In Fig. 2.6, the rate of convergence of the PLL increases with the increase of the gain values K and $(K_P \times K_I \times K_V)$ [60]. The speed of the response increases with the increase in K; however, it creates oscillations in the response. The proper choice of the gain values is a compromise between speed and accuracy. For FACTS applications, fast start-up period and zero steady-state error are desired [61]. The following parameters are found to give satisfactory response and are used for the studies conducted in this thesis: $K_P = 1$, $K_I = 200$, $K_V = 100$ and $K = 200$.

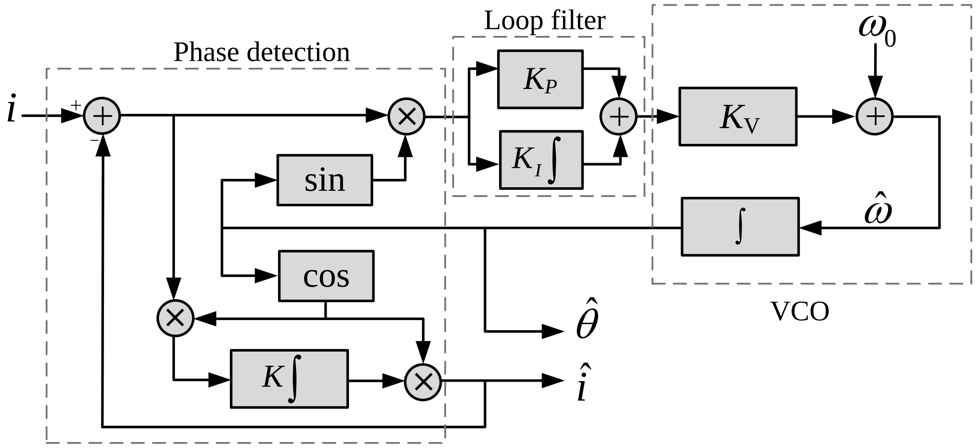

Figure 2.6: Block diagram of a phase locked loop.

Example: PLL tracking

A sinusodial current signal of a peak amplitude 1.0 *Amps* and 60 Hz frequency is passed to the PLL shown in Fig. 2.6 to examine its tracking behaviour. The actual current signal, estimated current signal and the estimated phase information are shown in Fig. 2.7. The amplitude and phase angle tracking during the startup are shown in Figs. 2.7(a) and (b) respectively. Similarly, the tracking response for a step change in the amplitude from 1.0 to 0.5 *Amps* (at $t = 0.3$ *sec*) are shown in Figs. 2.7(c) and (d), respectively. These responses show that the PLL is able to track the signal phase angle within 0.05 *sec* from the startup.

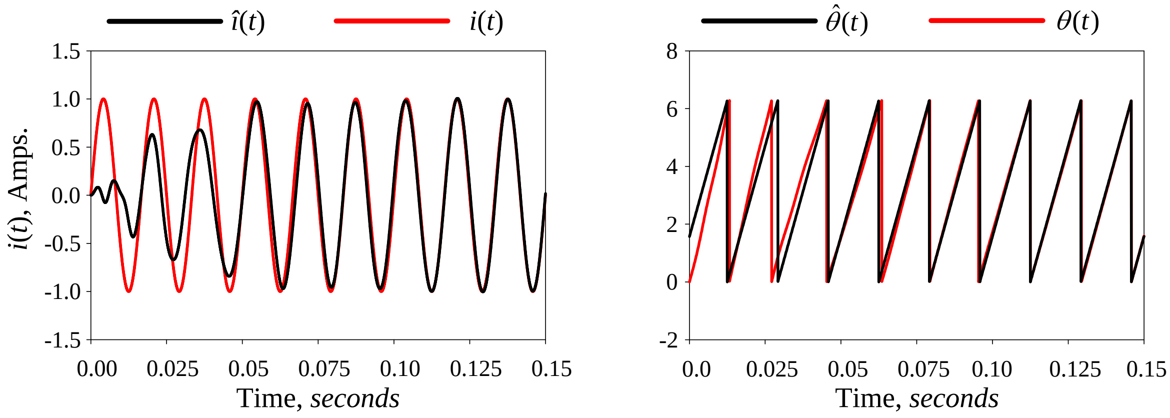

(a) PLL tracking - startup **(b)** PLL phase angle tracking - startup

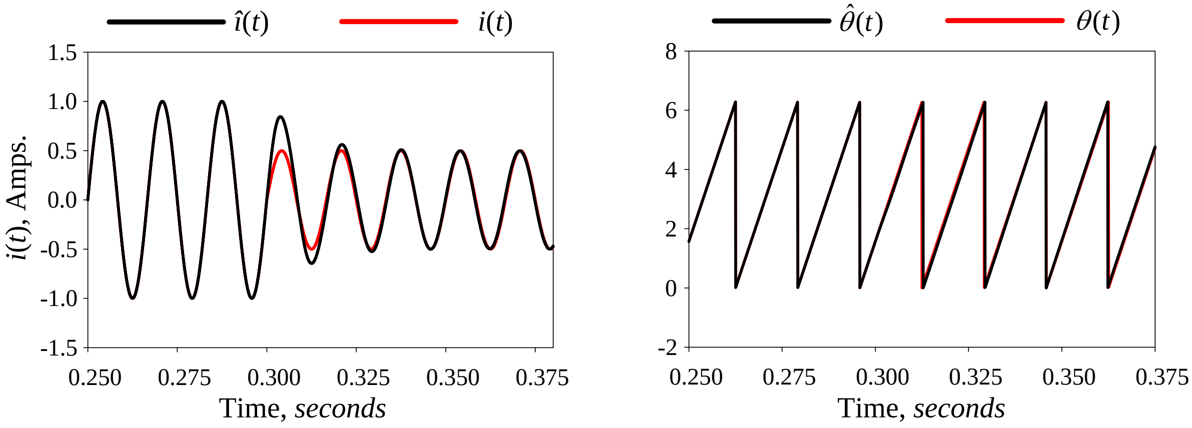

(c) PLL tracking - sudden change in amplitude **(d)** Phase angle tracking for **(c)**

Figure 2.7: PLL tracking response plots.

During steady-state condition, although the magnitude tracking is taking almost one and half cycles to converge, the phase angle tracking error is insignificant.

B. Phasor Evaluation

The Phasor Evaluation unit extracts phasors from the instantaneous voltage or current signals. The PSCAD$^{\mathrm{TM}}$/EMTDC provides Fast Fourier Transform (FFT) tool [62] for the phasor extraction, and, RTDS$^{\mathrm{TM}}$/RSCAD provides Discrete Fourier Transform (DFT) tool [63]. In the EMTP-RV$^{\mathrm{TM}}$, a low-pass filter based phasor estimation algorithm [64] is implemented. This method is easy to implement on the EMTP type of simulation tools. The details of the algorithm are presented in Appendix A.1.

The block diagram shown in Fig. 2.8 represents the low-pass filter based phasor estimation algorithm. Here, $e(t)$ represents the instantaneous input signal, $\hat{E_R}$ represents the real part

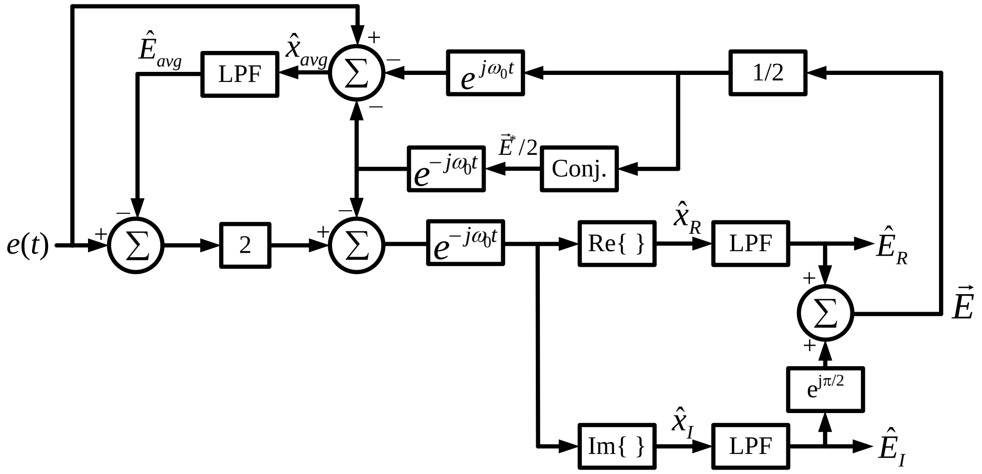

Figure 2.8: Low-pass filter based phasor estimation.

and $\hat{E}_I$ represents the imaginary part of the phasor.

Example: Low-pass filter based phasor estimation

A low-pass filter based estimation algorithm is used to estimate the following signal

$$e(t) = \begin{cases} e^{-10t} + A_0\ \cos(2\pi ft) & \text{if } t < 0.2\ secs \\ e^{-10t} + \frac{1}{2}A_0\ \cos(2\pi ft) & \text{if } t >= 0.2\ secs \end{cases} \tag{2.7}$$

where $A_0 = 1$ and $f = 60\ Hz$.

A second-order low-pass filter is used for the estimation algorithm. The cut-off frequency for the filter is chosen to be 0.2 Hz. The transfer function of the filter is given in Eq. (2.8). The performance of the low-pass filter estimation algorithm is presented in Fig. 2.9. The algorithm is found to be able to track the DC component and the real-imaginary phasors at high speed and accuracy.

$$H_{LPF}(s) = \frac{5684.8921}{1 + 106.6291s + 5684.8921s^2} \tag{2.8}$$

C. Boost Measure

A Boost Measurement block performs complex TCSC boost factor calculations as

$$kB = Imag\left\{\frac{\hat{V_c}/\hat{I_C}}{X_{C\ TCSC}}\right\} \tag{2.9}$$

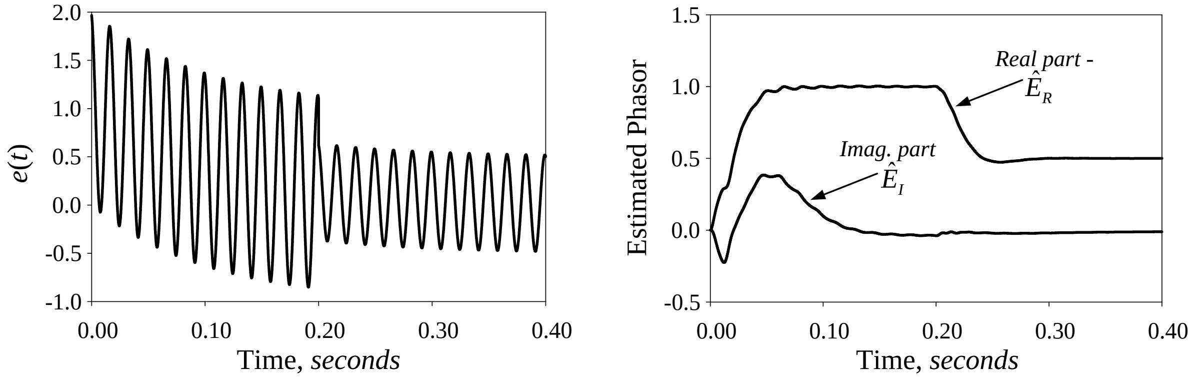

(a) Composite signal $e(t)$ - Eq. (2.7) **(b)** Estimated real-imag part

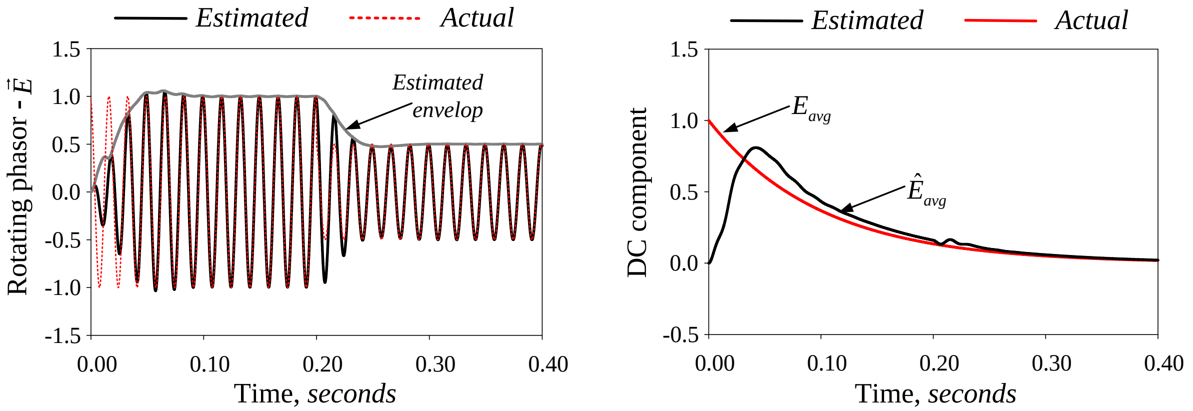

(c) Rotating phasor $\hat{E}$ **(d)** Average component estimate

Figure 2.9: Performance of the low-pass filter based estimation algorithm.

where $\hat{V_c}$ and $\hat{I_C}$ are the estimated phase voltage and current at the fundamental frequency, and $X_{C\,TCSC}$ is the capacitive reactance of the TCSC capacitor branch at the fundamental frequency.

D. Error Controller

A PI control based Error Controller is used, as shown in Fig. 2.10, to maintain the TCSC boost level at a desired value. The controller minimizes the error between the reference boost factor kB_{ref} and the actual boost factor kB. The output of the controller is added to the initial boost factor (kB_0). The thyristor firing angle is calculated using the non-linear TCSC characteristic (Fig 2.3b). The output α is then compared with reference phase angle θ from PLL to generate appropriate firing pulses for thyristor pairs. The boost factor vs. firing angle lookup method (using non-linear characteristic curve) to control the TCSC impedance is called the constant firing angle delay (CFAD).

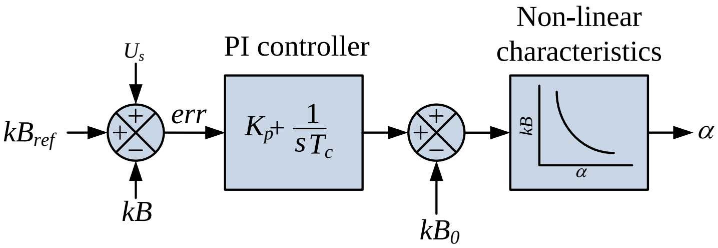

Figure 2.10: TCSC error controller.

The increase in the proportional gain increases the rising time, while the decrease in the integral time constant decreases the settling time. However, if the proportional gain is too high, the system may go to an unstable state, and if it is too low, the system response may be sluggish. Similarly, lower integral time constant increases the peak amplitude of the oscillations in the response. So the proper values of the PI controller gains are a compromise between the rise and settling times.

Subsynchronous resonance studies: For the subsynchronous resonance studies, to improve the SSR damping, Synchronous Voltage Reversal (SVR) firing control algorithm is implemented [64, 65]. The impedance control (PI control in Fig. 2.10) is upper level control and constant firing angle delay (CFAD) is lower level control. When implementing such a control scheme, the upper-level controls may influence the behavior of TCSC under subsynchronous frequency range [66]. However, in SVR control methodology, the firing instants of the TCSC thyristors are determined by adjusting the capacitor voltage zero crossing, which eliminates non-linearity in boost control and the TCSC apparent impedance at subsynchronous frequencies appears as inductive [67]. Furthermore, at low boost factor, SVR controlled TCSC can provide much better SSR damping than conventional CFAD control [64]. Such advantages have motivated the use of the SVR firing method in the SSR studies conducted in this thesis.

The Synchronous Voltage Reversal block solves for the angle β from the non-linear relation given as:

$$u_{CZ} = X_0 i_{LM} \left[\lambda\beta - \tan(\alpha\lambda)\right] \tag{2.10}$$

where u_{CZ} is the estimated capacitor voltage at the desired instant when the capacitor voltage zero crossing occurs, i_{LM} is the measured value of the line current i_L, X_0 is the TCSC capacitor reactance at the TCSC resonance frequency, λ is the ratio between the TCSC resonance frequency and the system fundamental frequency and β is the angle difference between the firing time and the voltage zero-crossing. The value of β is used to calculate the exact firing instants of the individual thyristors. The details of the SVR algorithm are given in [64, 65].

2.3.3 TCSC Model Validation

The detailed TCSC model is developed in the Electromagnetic Transient Simulation Software tools - EMTP-RV^{TM}, PSCAD^{TM}/EMTDC and RTDS^{TM}/RSCAD for various studies. The model is validated for a step changes in thyristor firing angle and the reference reactance against the analytical model of Eq. (2.5). The TCSC model validation results in PSCAD^{TM}/EMTDC are presented in this section. A similar procedure is followed in other software platforms as well. The following parameters are used for the validation:

$$C_T = 175.53\ \mu F, \qquad L_T = 6.40\ mH, \qquad \text{Simulation time step} = 25\ \mu s.$$

The characteristics curve for the TCSC (from Eq. 2.5) is shown in Fig. 2.11(b) for the above TCSC parameters.

A. Step change in the firing angle

A step change in firing angle (from $\alpha = 151^o$ to 156^o) at $t = 5\ sec$ is applied. The TCSC impedance (boost factor) obtained from the simulation is shown in Fig. 2.11(a). The firing angles obtained from the analytical solution (Eq. 2.5) for the same boost factors are 151.5^o and 155.5^o respectively (Fig. 2.11b). It can be seen from Fig. 2.11(a) that the simulated final values are very close to the analytical solution. The very small difference between the simulation and analytical results ($\approx 0.5^o$) could be due to the simulation time step resolution. A simulation time step of 25 μs corresponds to the thyristor firing angle of 0.54^o resolution.

B. Step change in the boost factor

A step change in boost factor from $kB_{ref} = 1.50$ to $kB_{ref} = 1.75$ is applied at $t = 5\ sec$. The TCSC impedance (boost factor) obtained from the simulation is shown in Fig. 2.12(a). The firing angles obtained from the simulation are 154.22^o and 151.66^o and are shown in Fig. 2.12(b). The firing angles obtained from the analytical solution for the same boost factors are 153.9^o and 152^o respectively. It can be seen from these results that the simulated steady-state values are very close to the analytical solution.

In conclusion, the developed TCSC model in PSCAD^{TM}/EMTDC is performing as desired.

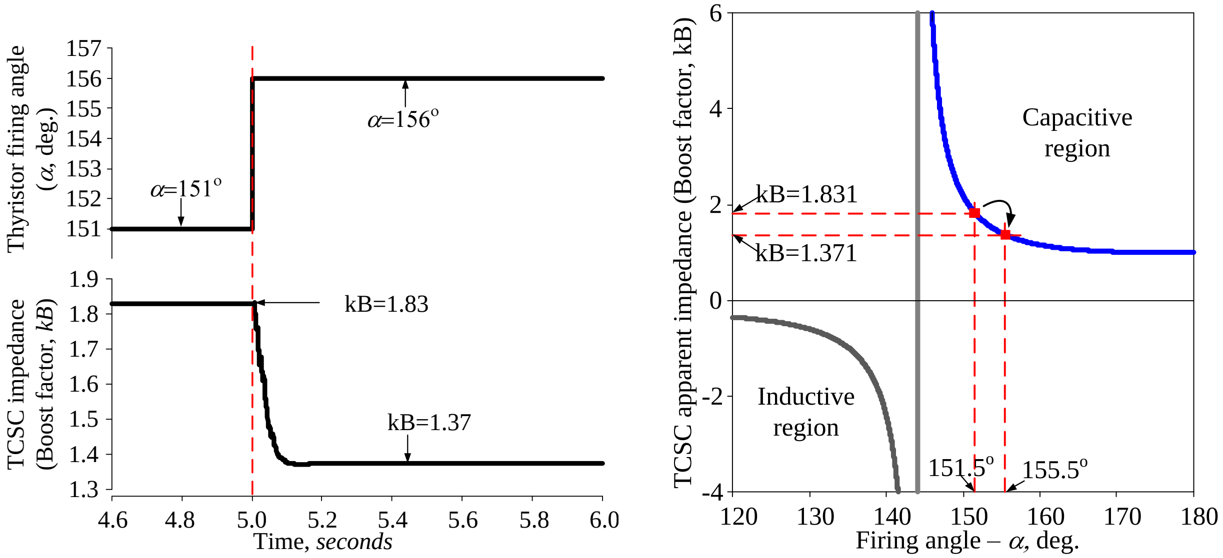

(a) Step change in firing angle **(b)** TCSC characteristic curve

Figure 2.11: (a) Step change in firing angle and corresponding change in boost factor, and (b) operating points marked on TCSC characteristics curve.

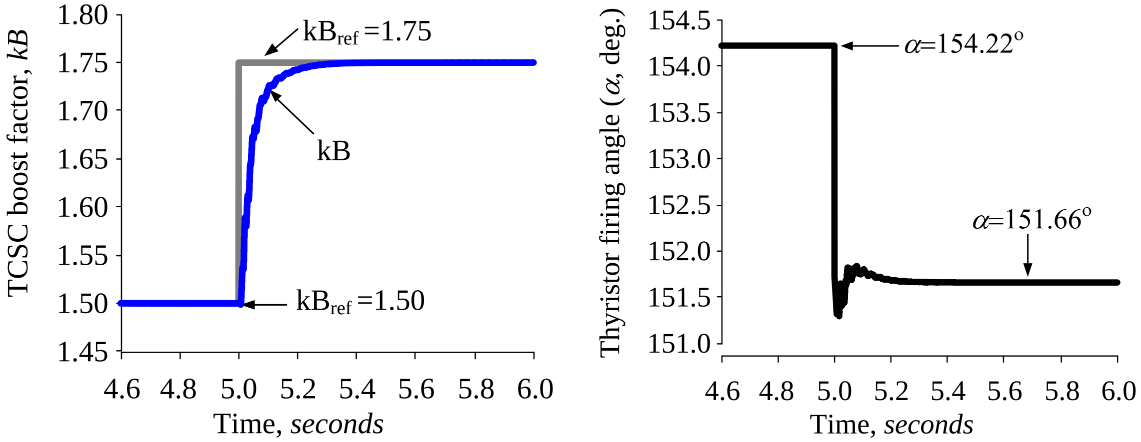

(a) **(b)**

Figure 2.12: (a) Step change in boost factor and (b) corresponding change in firing angle.

2.4 Static Synchronous Series Compensator (SSSC)

A Static Synchronous Series Compensator is a series connected voltage-source converter (VSC). It can vary the effective impedance of the transmission line by injecting series voltage at the fundamental frequency in quadrature phase with the line current. The output of the VSC can be controlled in amplitude as well as in phase. By controlling the injected voltage phase angle, the SSSC can be used as a reactive power compensating device or a real power compensating device, provided an energy storage is attached to the DC side of the converter [5]. For example, if the injected series voltage leads or lags the transmission line current by 90^o, then reactive power, either absorbed or generated, would be exchanged. On the other hand, if the injected voltage is in phase with the line current, then real power would be exchanged with the attached energy storage. The SSSC is a more beneficial controller than the TCSC because of its ability to modulate not only the line reactance but also the line resistance [6].

2.4.1 Basic Operating Principle

The basic operating principle of the SSSC can be explained with reference to a conventional fixed series capacitive compensation as shown in Fig. 2.13. The fixed series capacitor presents a lagging quadrature voltage with respect to the line current, which opposes the leading voltage across the inductance of the transmission line, as shown in the phasor diagram in Fig. 2.13(b). Thus, the series capacitive compensation works by increasing the voltage across the impedance of the given physical line, which in turn increases the corresponding line current and transmitted power.

In the similar manner, the same steady-state power transmission can be established if the series compensation is provided by a synchronous ac voltage-source as shown in Fig. 2.14, where the VSC output voltage (V_{inj}) precisely matches the voltage of the series capacitor, i.e.

$$V_{inj} = V_c = -jX_c\, I = -jk\, X_L\, I \tag{2.11}$$

where V_c is voltage across the capacitor, I is the line current, X_L is the transmission line reactance, and $k = X_c/X_L$ is the degree of series compensation.

By making the output voltage of the VSC a function of the line current as shown in Eq. (2.11), the same compensation provided by the fixed capacitor in Fig. 2.13 can be accomplished. However, in contrast to the fixed capacitor, the voltage-source converter is able to maintain a constant compensating voltage even in the presence of a variable line current.

Figure 2.14(b) shows the phasor diagram when the VSC output voltage is lagging the line current by $\pi/2$ and is acting as a capacitor while Fig. 2.14(d) shows the VSC output voltage leading the line current by $\pi/2$ and results an inductive effect. The output voltage of a VSC can be smoothly varied by a simple control action to make it lead or lag the line current by 90^o and increase or decrease the magnitude.

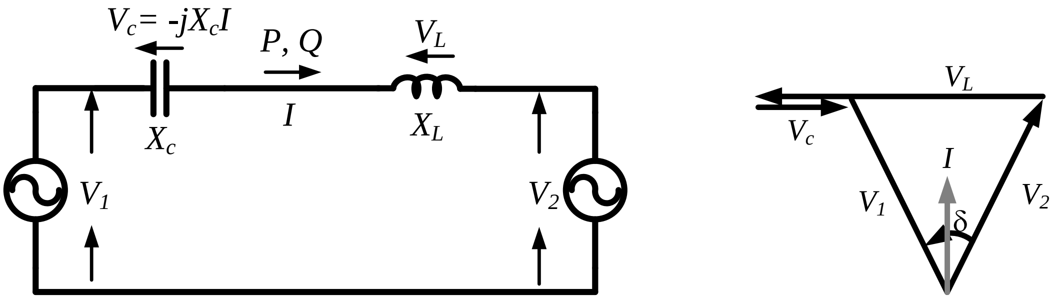

(a) **(b)**

Figure 2.13: A basic two machine system with (a) a series capacitor compensated line and (b) associated phasor diagram.

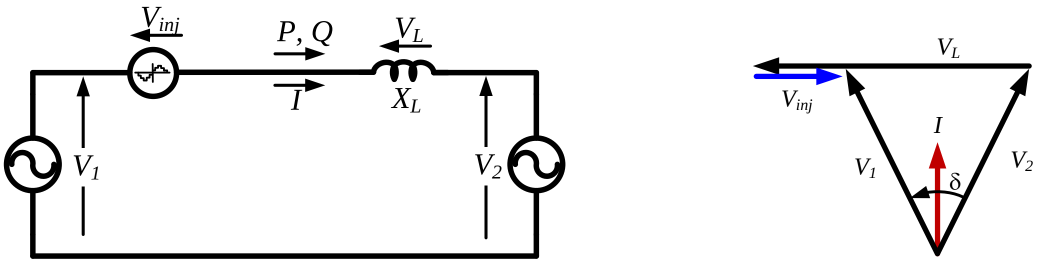

(a) Two-machine system **(b)** Capacitive

(c) No comp. **(d)** Inductive

Figure 2.14: Two-machine system with a VSC compensated line and phasor diagrams for various compensations.

2.4.2 Modelling of SSSC Controller

For the studies related to the hybrid SSSC series compensation scheme, a detailed single-phase SSSC model is developed in the electromagnetic transient simulation software packages using a three-level Insulated-Gate Bipolar Transistor (IGBT) based Sinusodial Pulse Width Modulation (SPWM) converter modules. The schematic diagram of an SSSC connected to the transmission system is shown in Fig. 2.15. The line voltage and current as well as other controllable variables are measured and passed to a controller. A coupling transformer is used to integrate the SSSC with the ac system. An LC filter is used to filter out the high-frequency switching noises.

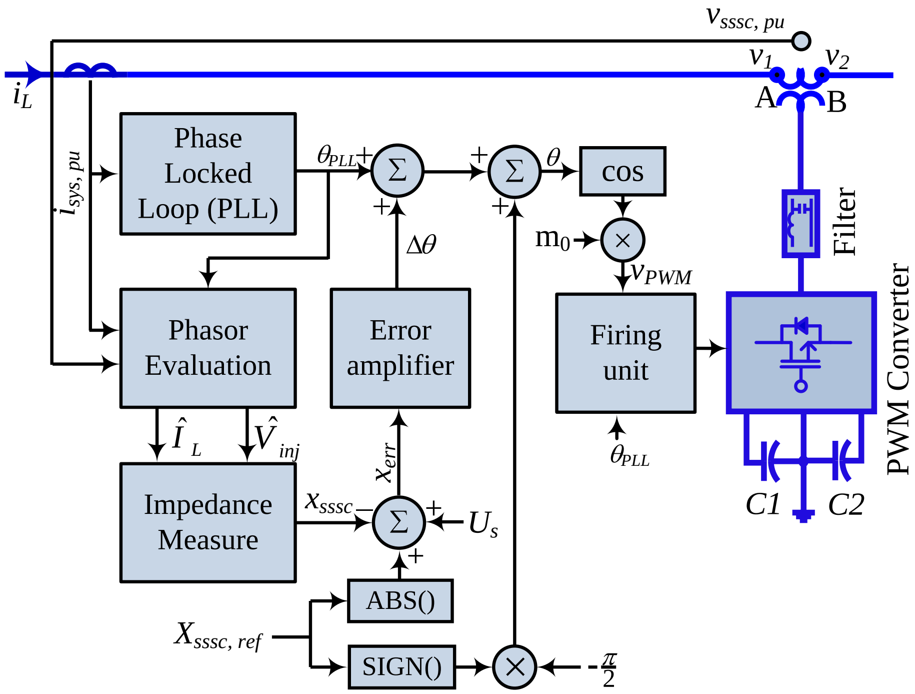

Figure 2.15: SSSC implementation block diagram.

The injected voltage ($v_{sssc} = v_2 - v_1$ in p.u.) and the line current (i_{sys} in p.u.) are used to calculate the injected impedance to the line. The damping signal U_s (for SSR or power oscillation damping) obtained from the supplementary controller is added to the difference between the actual impedance and the reference impedance and then processed in a PI controller based error amplifier. A constant modulation index of near unity ($m_a = 0.99$) is used for PWM firing scheme to minimize the harmonic content of the converter output. The DC link capacitor voltage is dynamically regulated in relationship with the compensating reactance demand ($X_{sssc} + U_s$). If the measured SSSC impedance is less than the reference value, error (x_{err}) will be positive, and the phase shift between the carrier and the reference waveform increases. The increase in the phase shift increases the active power flow from the ac to dc system, which in turn charges the capacitor. On the other hand, an opposite process takes place if the measured SSSC impedance is higher than the reference value. A positive value of x_{ref} is assumed for capacitive compensation while a negative value is taken for inductive compensation.

Some of the SSSC control blocks are similar to the TCSC control blocks discussed in Section 2.3.2. The single-phase voltage source converter, Pulse Width Modulation technique and the switching logics used in the studies conducted in this thesis are additional components and are presented in the rest of this sub-section.

A. Single-Phase Voltage Source Converter (VSC)

Figure 2.16 shows the schematic of a single-phase voltage source converter. This type of structure is referred as a full-bridge (H-bridge) converter. It uses two single-phase legs of a three-phase converter (Fig. 1.9) to convert a single-phase *ac* energy into a *DC* energy and vice versa. In this type of arrangement, the full DC voltage appears on the *ac* side, and is preferred for high power applications compared to the half-bridge topology in which half of the DC voltage appears in the *ac* side [15].

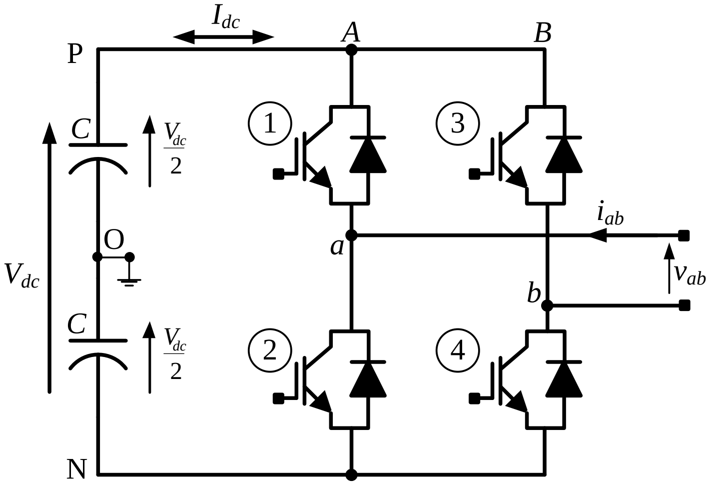

Figure 2.16: Schematic of a single-phase IGBT based voltage-source converter.

The switching nodes 1 & 2 (or 3 & 4) of each leg cannot be turned *on* simultaneously to avoid DC capacitor short circuit. Furthermore, if all the switches are turned *off*, the output ac voltage will have undefined state. Hence, to avoid DC capacitor short circuit and undefined output voltage conditions, either the top or the bottom switch of each leg should be *on* at any instant. Table 2.1 summarizes the switching states and the corresponding output of a single-phase full-bridge voltage source converter [15].

Table 2.1: Switch states and output for a full-bridge single-phase VSC.

Switch state		State	Voltage outputs		
on	*off*		v_a	v_b	v_{ab}
1 & 4	2 & 3	1	$V_{dc}/2$	$-V_{dc}/2$	V_{dc}
2 & 3	1 & 4	2	$-V_{dc}/2$	$V_{dc}/2$	$-V_{dc}$
1 & 3	2 & 4	3	$V_{dc}/2$	$V_{dc}/2$	0
2 & 4	1 & 3	4	$-V_{dc}/2$	$-V_{dc}/2$	0
-	(1 & 2)	5	$-V_{dc}/2$	$V_{dc}/2$	V_{dc}
	(3 & 4)		$V_{dc}/2$	$-V_{dc}/2$	$-V_{dc}$

B. Pulse Width Modulation for Single-Phase VSC

A unipolar Sinusoidal Pulse Width Modulation (SPWM) technique is used to switch *on/off* the IGBTs of the converter legs. This technique takes advantage of four switching states (states 1 to 4, Table 2.1) to generate three output voltage levels. The generated *ac* output voltage can take one of three values, namely, V_{dc}, 0, and $-V_{dc}$ respectively.

Two sinusoidal modulating signals (v_{ref} and $-v_{ref}$) are compared with a triangular carrier waveform to generate the switching signals for leg A (v_a) and leg B (v_b) respectively, as shown in Fig. 2.17. For demonstration purposes, 1 Hz sinusoidal reference signal and 11 Hz triangular carrier signal are used. The leg and terminal voltages of the converter are shown in Fig. 2.18. The three output voltage levels 1, 0, and −1 (scaled to dc voltage V_{dc}) appear on the ac terminal based on the switching state. The magnitude of the fundamental frequency component depends on the modulation ratio m_a and the output phase depends on the phase displacement between the carrier and the reference signal.

The ac voltage harmonic components are given as [13]:

$$\begin{aligned} v_{ab}(t) &= m_a V_{dc}\cos(\omega_0 t) \\ &\quad + \frac{4V_{dc}}{\pi}\sum_{i=1}^{\infty}\sum_{j=-\infty}^{\infty}\frac{1}{2i}J_{2j-1}(i\pi m_a)\cos([i+j-1]\pi)\cos(2i\omega_c t+[2j-1]\omega_0 t) \end{aligned} \tag{2.12}$$

where m_a is the modulation index, ω_0 is the fundamental frequency, ω_c is the carrier frequency and J is the Bessel function. For the linear operating region, i.e. $0 \leq m_a \leq 1$, the fundamental frequency component of the output voltage is proportional to the modulation index.

C. Firing Unit

The carrier and reference waveforms are generated from the estimated angle obtained from the PLL as shown in Fig. 2.19. The angle is multiplied by the desired frequency modulation ratio 'm_f' and then modulo operation is performed to limit the signal between $0 - 360^o$ range. The result is then passed to a non-linear transform block which converts saw-tooth signal into a triangular waveform. For reference waveform generation, small angle shift (θ_{shift} - from PI controller) is added to the angle that is obtained from the PLL. The resultant angle is then passed to a '*sin*' function. The resultant signal is then multiplied with a modulation ratio m_a to generate the required reference waveform. The modulation ratio is generally chosen near unity to suppress harmonics. The firing signals are generated using the comparison logic shown in Fig. 2.20.

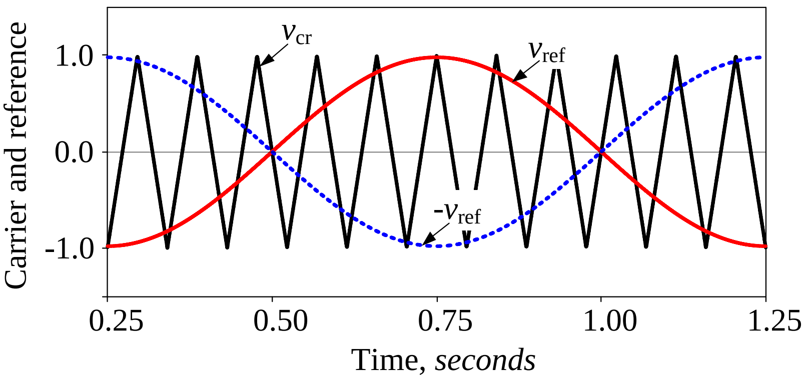

Figure 2.17: SPWM reference and carrier waveforms ($m_f = 11$, $m_a = 0.98$).

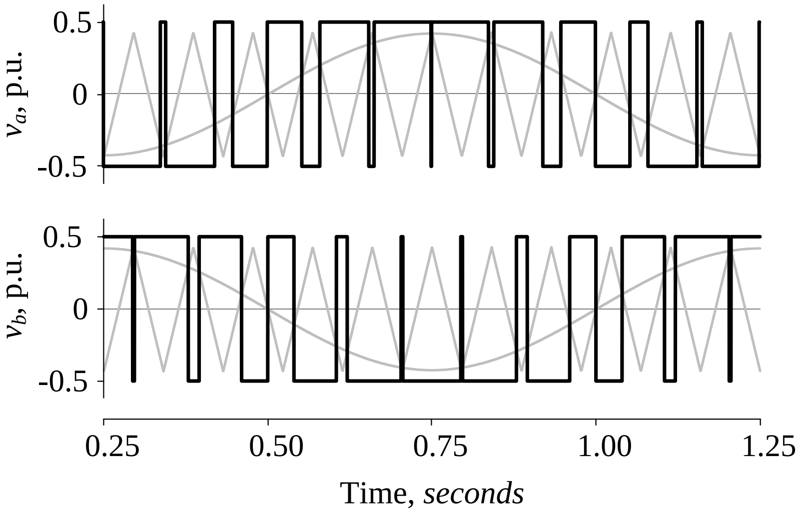

(a) Leg voltages.

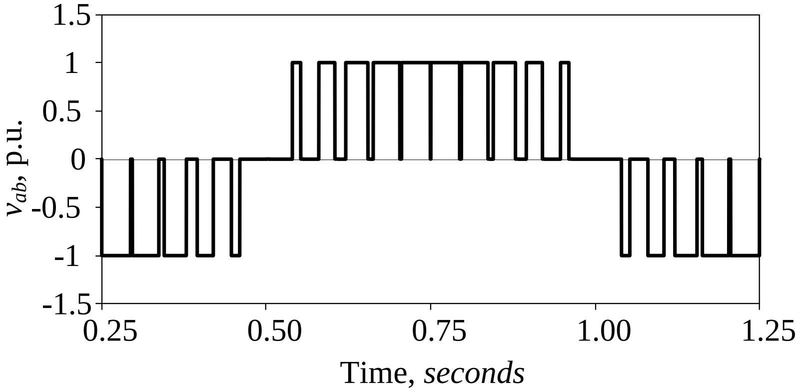

(b) Terminal voltage.

Figure 2.18: Single-phase VSC *ac* voltage output (in p.u. of V_{dc}).

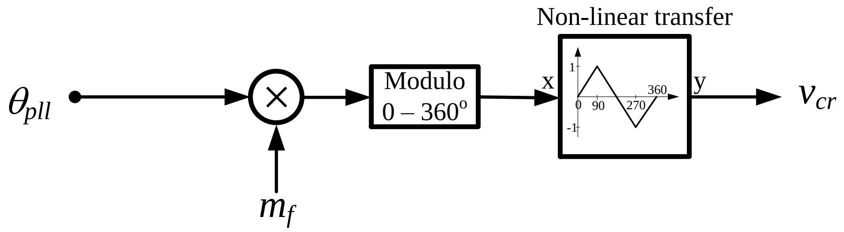

Figure 2.19: Carrier waveforms generation.

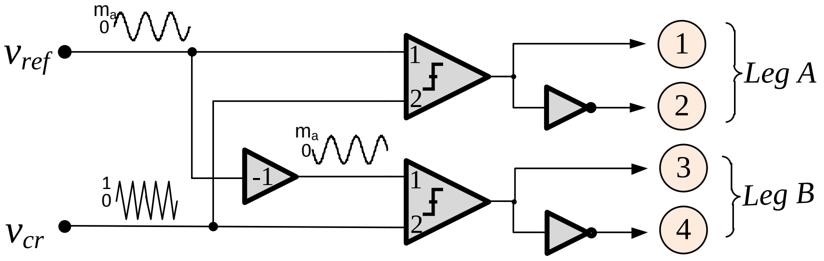

Figure 2.20: Firing logic for full bridge single-phase VSC.

2.4.3 SSSC Model Validation

The system shown in Fig. 2.21 is used for the validation of the SSSC operation. The sending end voltage source supplies power to the receiving end voltage source through an SSSC compensated loss-less transmission line. The parameters used for the design of the SSSC are given in Table 2.2.

Table 2.2: SSSC data.

Coupling Transformer: 25 MVA, 11/33 kV, $x_t = 0.05$ p.u.
Carrier frequency: 1.26 kHz
Steady-state reactance: 22 Ω, capacitive

A step change in the SSSC impedance demand from 1.0 $p.u.$ inductive to 1.0 $p.u.$ capacitive is applied at $t = 4.5$ sec and is reverted back to 1.0 $p.u.$ inductive at $t = 9.5$ $sec.$ This test is used to verify the steady-state inductive and capacitive series compensation operation of the single-phase SSSC. The results are verified against analytical network sending/receiving end power-flow results.

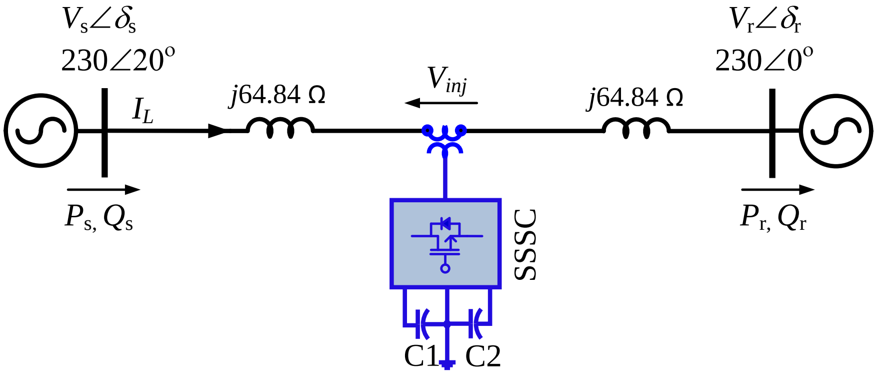

Figure 2.21: The SSSC test system: two ac-source connected via an SSSC compensated loss-less transmission line.

A. Network power flow validation

The steady-state line current and sending and receiving end real and reactive powers for the two operating conditions are calculated analytically using a series capacitive impedance representation of the SSSC (and presented in Appendix B.1.1). The responses from the detail SSSC model developed in EMTDC/PSCAD simulation are illustrated in the Fig. 2.22. Table 2.3 summarizes the sending and receiving end powers obtained for the test system for the analytical calculation and detailed EMT model of the SSSC. It can be seen from this Table 2.3 that the results from EMT simulation and analytical calculation are very close, a fact which verifies the very good accuracy of the developed model of the SSSC. The very small difference between the simulated real power at the sending and receiving ends represents the switching and resistive loss in the SSSC.

B. Capacitor DC Voltage Validation

The calculated dc capacitor voltages for inductive and capacitive operations of the SSSC are 5.81 kV and 10.33 kV respectively (Appendix B.1.2). The average measured dc-voltage of the capacitor for the inductive and the capacitive operating conditions in the simulations are found to be $V_{dc} = 5.97\ kV$ and $V_{dc} = 10.16\ kV$ respectively. The small discrepancy between the measured and the calculated values is due to the simplification of the magnetizing branch of the coupling transformer in analytical calculations.

C. PWM Operation Validation

The detailed PWM waveforms for the inductive and the capacitive operating conditions are shown in the Fig. 2.23. It can be seen from these responses that the simulated PWM waveforms are similar to the ideal PWM waveforms shown in Figs. 2.17 and 2.18.

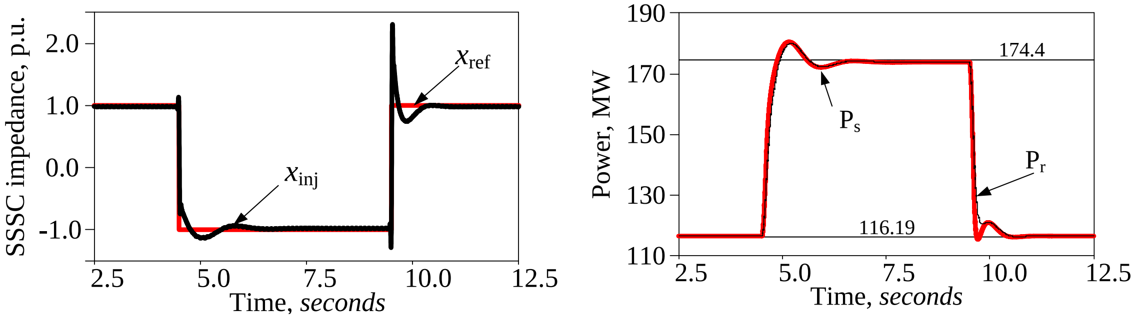

(a) SSSC reactance **(b)** Active power flow

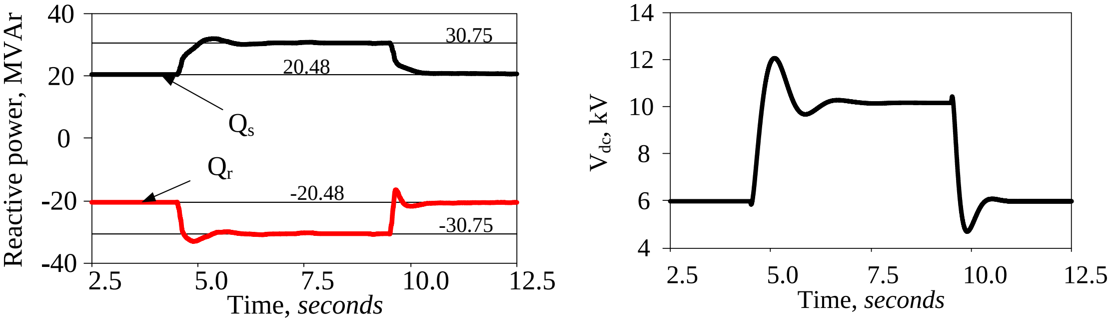

(c) Reactive power flow **(d)** DC voltage

Figure 2.22: SSSC validation: response plots for step change in reactance order.

Table 2.3: Steady-state power comparison.

Real and reactive power	Compensation			
	Inductive		Capacitive	
	Analytical calculation	Detail EMT model	Analytical calculation	Detail EMT model
Sending-end power (MW)	116.197	116.518	174.409	173.894
Receiving-end power (MW)	116.197	116.481	174.409	173.812
Sending-end reactive power (MVAr)	20.488	20.515	30.753	30.489
Receiving-end reactive power (MVAr)	-20.488	-20.489	-30.753	-30.575

2.5 Summary

In this chapter, the proposed phase unbalanced hybrid series compensation schemes are presented and their main components are discussed. Moreover, detailed computer modelling

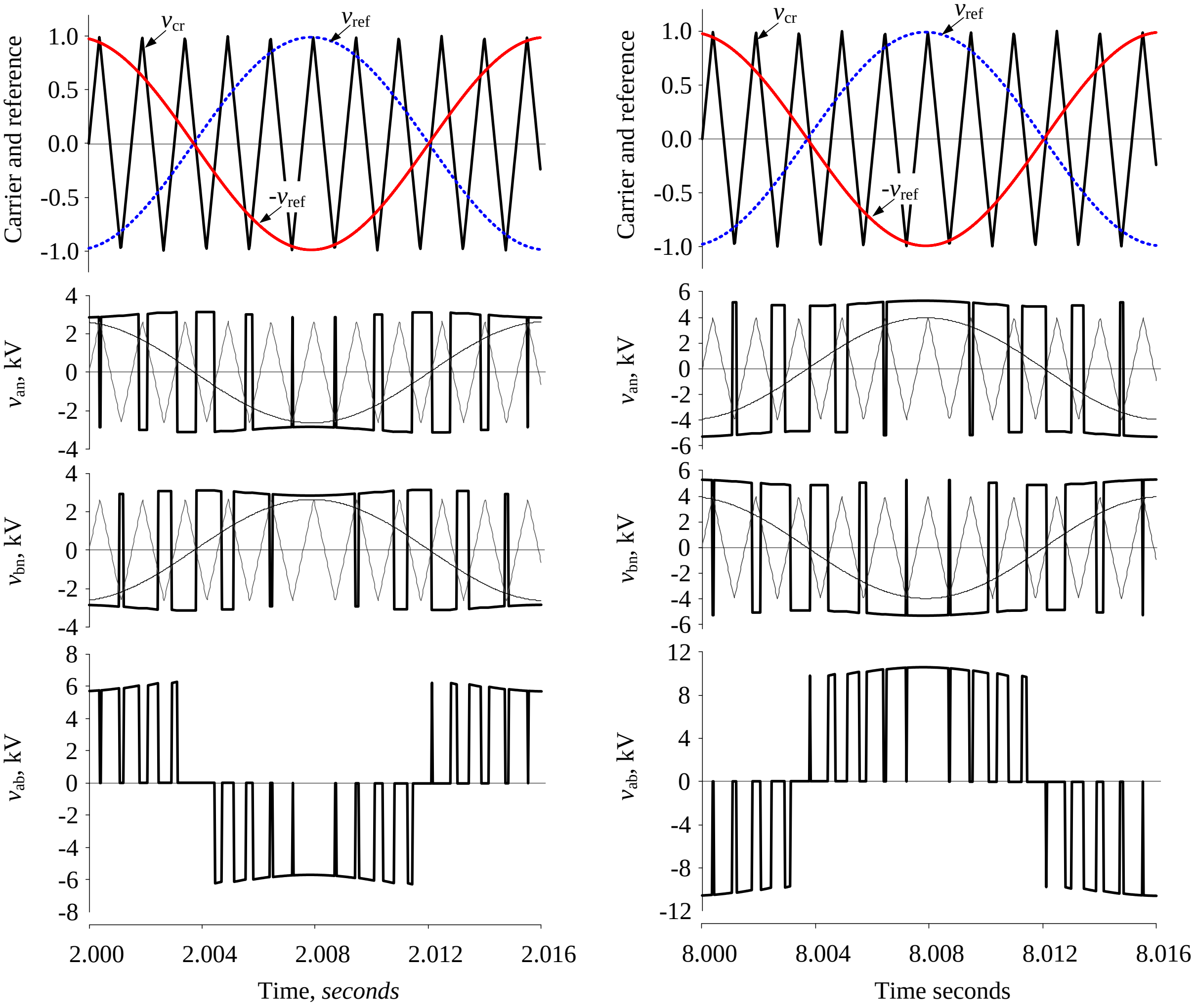

(a) Inductive operation **(b)** Capacitive operation

Figure 2.23: SSSC validation: PWM signals and converter output voltages.

of the single-phase TCSC and SSSC are developed in the electromagnetic transient simulation package PSCAD^{TM}/EMTDC and validated against their analytical mathematical models. Similar method is followed for the model development in EMTP-RV^{TM}and and RTDS^{TM}/RSCAD. The results of these validations demonstrate very good accuracy of the developed models.

Chapter 3

Damping of Subsynchronous Resonance

3.1 Introduction

In this chapter, investigations are carried out to explore the capability of the proposed phase unbalanced hybrid compensation schemes in damping subsynchronous resonance in series capacitor compensated transmission systems. In this context, studies are conducted on both the IEEE first and second benchmark models for computer simulations of subsynchronous resonance. The impact of the proposed phase unbalanced hybrid compensation schemes on the voltage unbalance induced in the system is also investigated.

3.2 Subsynchronous Resonance in Power Systems

Subsynchronous resonance is a condition that can exist on a power system where the network has natural frequencies that fall below the fundamental frequency of the generated voltages [68]. Transient currents flowing in the ac network have two components; one component at the frequency of the driving voltages and another component at a frequency that depends entirely on the network elements. For a network with only series resistance (R) and inductance (L), an isolated transient, such as switching a load, will consist of a fundamental component and a dc component that decays with a time constant that depends on the L/R ratio of the equivalent impedance between the source and the load. Since loads are frequently switched on and off, the transient currents usually appear as random noise, superimposed on the fundamental frequency currents. The addition of shunt capacitors to the network result in new natural frequencies of oscillation that are always greater than the fundamental frequency. In networks containing series capacitors, the currents will include oscillatory components with frequencies that depend on the relative magnitude of the transmission line L and C elements, but have frequencies that are below the system fundamental frequency.

A general equivalent circuit seen looking into a large network is shown in Fig. 3.1. The network seen from the generator includes transmission lines that have series compensation to reduce the total line reactance. This accounts for the presence of the capacitor in the series equivalent.

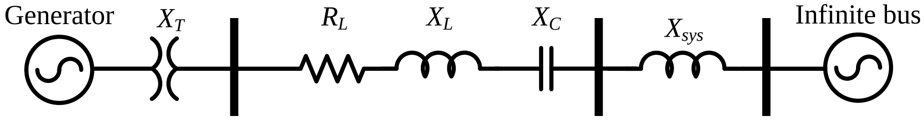

Figure 3.1: The system equivalent seen from a generator.

A general expression for the current in a simple radial $R-L-C$ network can be written as:

$$i(t) = K\left[A\sin(\omega_0 t + \Psi_1) + Be^{-\zeta\omega_2 t}\sin(\omega_2 t + \Psi_2)\right] \tag{3.1}$$

where all of the parameters in the equation are functions of the network parameters except ω_0, which is the system frequency (frequency of the driving voltages of all the generators). The frequency of the second component in Eq. (3.1), ω_2, is a function of the network elements.

Currents similar to Eq. (3.1) flow in the stator windings of the generators and are mathematically reflected in the generator rotor according to Park's transformation. This transformation makes the 60 Hz (ω_0) component appear to the rotor as a dc current, in the steady state, but the currents of frequency ω_2 are modulated into currents of frequencies containing the sum $\omega_0 + \omega_2$ and difference $\omega_0 - \omega_2$ of the two network frequencies. The difference frequencies are called *subsynchronous* frequencies. The subsynchronous currents may induce high shaft torques on the turbine-generator rotor. The forced frequencies of oscillation of the shaft are seen to be the fundamental complement of the network subsynchronous resonant frequency.

The presence of subsynchronous torques on the generator is of interest because the turbine-generator shaft itself has natural modes of oscillation. A typical lumped spring-mass model of a steam turbine-generator shaft is shown in Fig. 3.2, which represents a shaft of a typical steam generating unit with a high pressure (HP), intermediate pressure (IP), two low pressure (LPA & LPB) turbines, a generator rotor and a shaft connected exciter. Like any spring-mass system, this shaft system will oscillate with different "modes" of oscillation. For an N mass system, there exist $N-1$ distinct modal frequencies of oscillation (ω_m) and most of these frequencies for a turbine generator shaft are subsynchronous. In practical turbine-generator shafts, these natural frequencies are usually between 10 and 50 Hz for a 60 Hz generating unit.

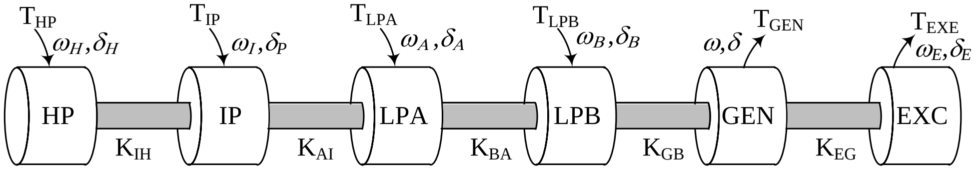

Figure 3.2: Spring-mass model of a steam turbine-generator shaft.

In a series capacitor compensated transmission system, if the mechanical shaft system has natural torsional oscillation frequencies close to the compliment of electrical resonance frequency, a self-excited resonance condition exists. This condition lead to energy exchange between mechanical and electrical system (at that frequency) in increasing manner, leading to the torque amplification in mechanical shaft system. This condition is called *subsynchronous resonance*, which can cause shaft fatigue and possible shaft damage or even failure.

3.3 SSR Supplementary Controller

The phase unbalanced hybrid TCSC and SSSC compensation schemes have inherent capability for limiting the build up of SSR oscillations. Further enhancement in SSR damping can be achieved if the TCSC and SSSC are equipped with supplementary controllers. Figure 3.3 shows a typical lead-lag type, N-channel, supplementary controller that utilizes the modal speeds as control signals. The modal speeds are derived from the turbine-generator rotating mass speeds as [69, 70]:

$$[\Delta\omega_m] = [Q]^{-1}[\Delta\omega] \tag{3.2}$$

where, $\Delta\omega_m$ is the modal speed deviation matrix, Q is the eigenvector matrix and $\Delta\omega$ is the speed deviation matrix of the turbine-generator rotating masses. The rotating mass speeds can be obtained using a torsional monitor. Each modal speed, as presented in Eq. (3.2), is phase (ϕ_i) and gain (K_i) adjusted separately to provide damping for its corresponding oscillations mode. The phase compensations are provided as:

$$\phi_i = \frac{1 + sT_{a,i}}{1 + sT_{b,i}}, \text{ for } i = 0, 1, ..., N - 1. \tag{3.3}$$

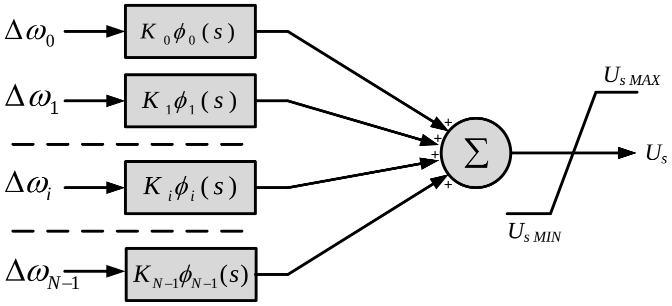

Figure 3.3: The SSR supplemental controller.

Controller Parameters Tuning

An optimal set of controller parameters is required for the best damping effect. A trial-and-error approach followed by fine tuning is pursued to obtain a set of proper parameter values. The initial values of the controller parameters are selected using trial-and-error such that they provide good damping for the corresponding mode of oscillations. The fine tuning of the parameters is then performed using repeated time domain simulation runs with the objective of minimizing a cost function given in Eq. (3.4), where T_C is the fault clearing time and T_F is the simulation end time. Minimizing the cost function expressed in Eq. (3.4) minimizes the sum of deviation of modal speeds following the disturbances, which will eventually lead to SSR suppression. During steady-state operation, there is no SSR feedback signal, and hence the damping signal becomes zero.

$$F_{obj}(K_i, T_{ai}, T_{bi}) = \int_{T_C}^{T_F} \sum_{i=0}^{N-1} (\Delta\omega_{m,i})^2 dt \tag{3.4}$$

The values of the matrices $[Q]$ for **Systems I** and **II** are given in Appendix A.4, and gain and phase compensation parameters K_i, $T_{a,i}$ and $T_{b,i}$ (for $i = 0, 1, .., N-1$) for the respective systems are given in Appendix C.3.

3.4 Test Systems Used for Simulation Studies

SSR studies are carried out on the IEEE first and second benchmark models for computer simulation of SSR [71,72], shown in Fig. 3.4 and designated as **Systems I** and **II** respectively. The shaft system of the turbine-generator of **System-I** consists of a high-pressure turbine (HP), an intermediate-pressure turbine (IP), two low-pressure turbines (LPA and LPB), the generator rotor and a rotating exciter (EXC). The shaft system of turbine-generator 1 (G_1) of **System-II** consists of a high-pressure turbine (HP), a low-pressure turbine (LP),

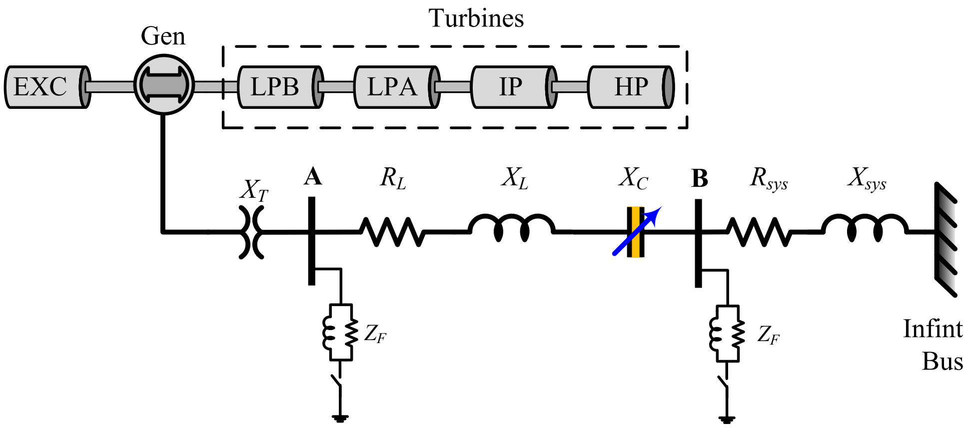

(a) First benchmark model (**System-I**)

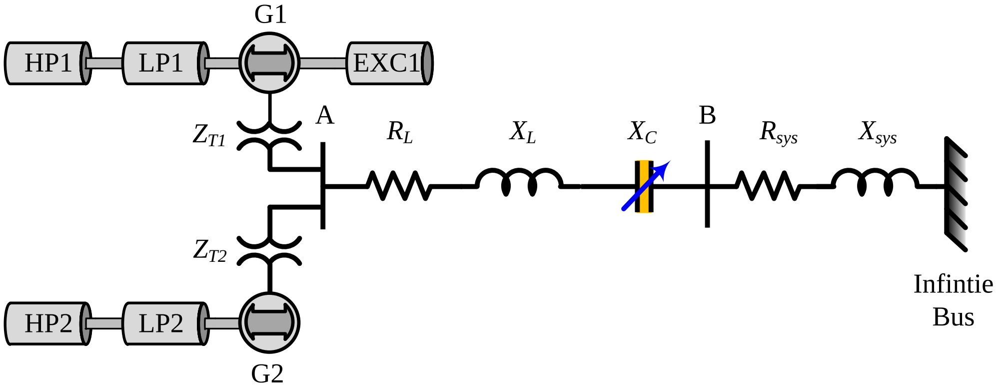

(b) Second benchmark model (**System-II**)

Figure 3.4: IEEE working group standard schematic diagram for subsynchronous resonance studies.

the generator rotor and a rotating exciter (EXC). On the other hand, turbine-generator 2 (G_2) of **System-II** comprises three masses (HP), (LP) and the generator rotor. The torsional natural frequencies of oscillations of the three turbine generator shaft systems are given in Table 3.1. For the SSR studies, series compensation degrees are chosen such that they excite one of the torsional oscillation modes of the systems. The compensation degree is defined as:

$$\text{Compensation degree} = \begin{cases} \dfrac{X_C}{X_L} * 100\%, & \text{for phases } a \ \& \ b \\ \dfrac{X_{Cc} + X_{S0}}{X_L} * 100\%, & \text{for hybrid phase - } c \end{cases} \tag{3.5}$$

where X_C is capacitive reactance, X_L is inductive reactance, X_{Cc} is capacitive reactance of phase c and X_{S0} is either the fundamental frequency TCSC impedance (for the hybrid TCSC scheme) or the SSSC impedance (for the hybrid SSSC scheme).

Table 3.1: Torsional natural frequencies of oscillations of the turbine-generator shafts systems.

System - I	
Modes	Torsional frequency (Hz)
1	15.71
2	20.21
3	25.55
4	32.28
5	47.47

System - II		
Generator	Modes	Torsional frequency (Hz)
G_1	1	24.65
	2	32.39
	3	51.10
G_2	1	24.65
	2	44.99

3.5 Time Domain Simulation Results

For time-domain simulation studies, the synchronous generators are represented in the $d-q-0$ reference frame. The transmission lines are modelled as a transposed lines using series impedance representations. The turbine-generator mechanical systems are modelled as linear multimass-spring dashpot systems where each major rotating element is modelled as a lumped mass and each shaft segment is modelled as a massless rotational spring with its stiffness given by the spring constant. Moreover, viscous damping of each mass is represented. The infinite bus is represented by a constant amplitude sinusoidal voltage at the synchronous frequency. Circuit-breakers are represented as ideal switches which can open at current zero crossings. Dynamics of the generator excitation and governor systems are included in the simulation model. The electromagnetic transient simulation software EMTP-RV$^{\text{TM}}$is used to simulate the test systems.

The series compensation degree for **Systems I** and **II** are selected as 57.4% and 65.0% respectively for SSR studies. These compensation levels excite 'Mode 3' in **System-I** (25.55 Hz) and 'Mode 1' of G_1 & G_2 on **System-II** (24.65 Hz).

Figures 3.5 and 3.6 show the time responses of **Systems I** and **II** turbine-generator electrical powers and shaft torsional torques expressed in per unit machine rating during and after clearing a 4.5 *cycle* three-phase fault at bus B. **System-I** operating condition corresponds to $0.89 + j0.06$ $p.u.$ (on the 892.4 MVA generator base) power delivered to the infinite bus system at 1.0 $p.u.$ bus voltage. **System-II** operating condition corresponds to $1.8 + j0.04$ $p.u.$ power (on 600 MVA generator 1 base) delivered to the infinite bus system at 1 $p.u.$ bus voltage. As it can be seen from these figures, the turbine-generator shaft torsional torques exhibit severe amplifications. The torsional oscillations are reaching as high as 20 $p.u.$ in **System-I** and 170 $p.u.$ in **System-II**, which are very severe and should be limited. These two cases are adopted as the reference cases for comparisons with the considered hybrid series compensation schemes.

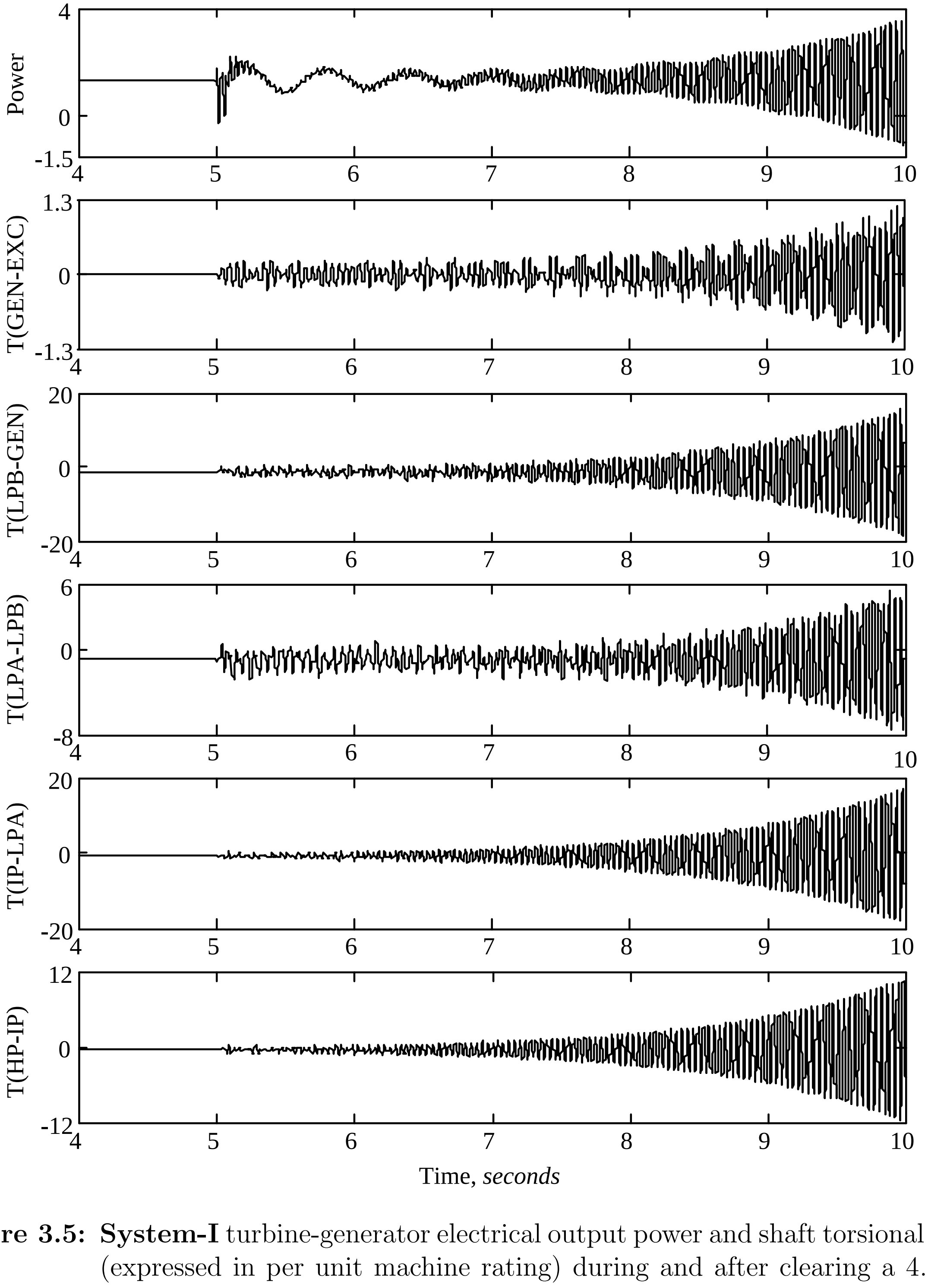

Figure 3.5: System-I turbine-generator electrical output power and shaft torsional torques (expressed in per unit machine rating) during and after clearing a 4.5 *cycle*, three-phase fault at bus B (compensation degree = 57.4%).

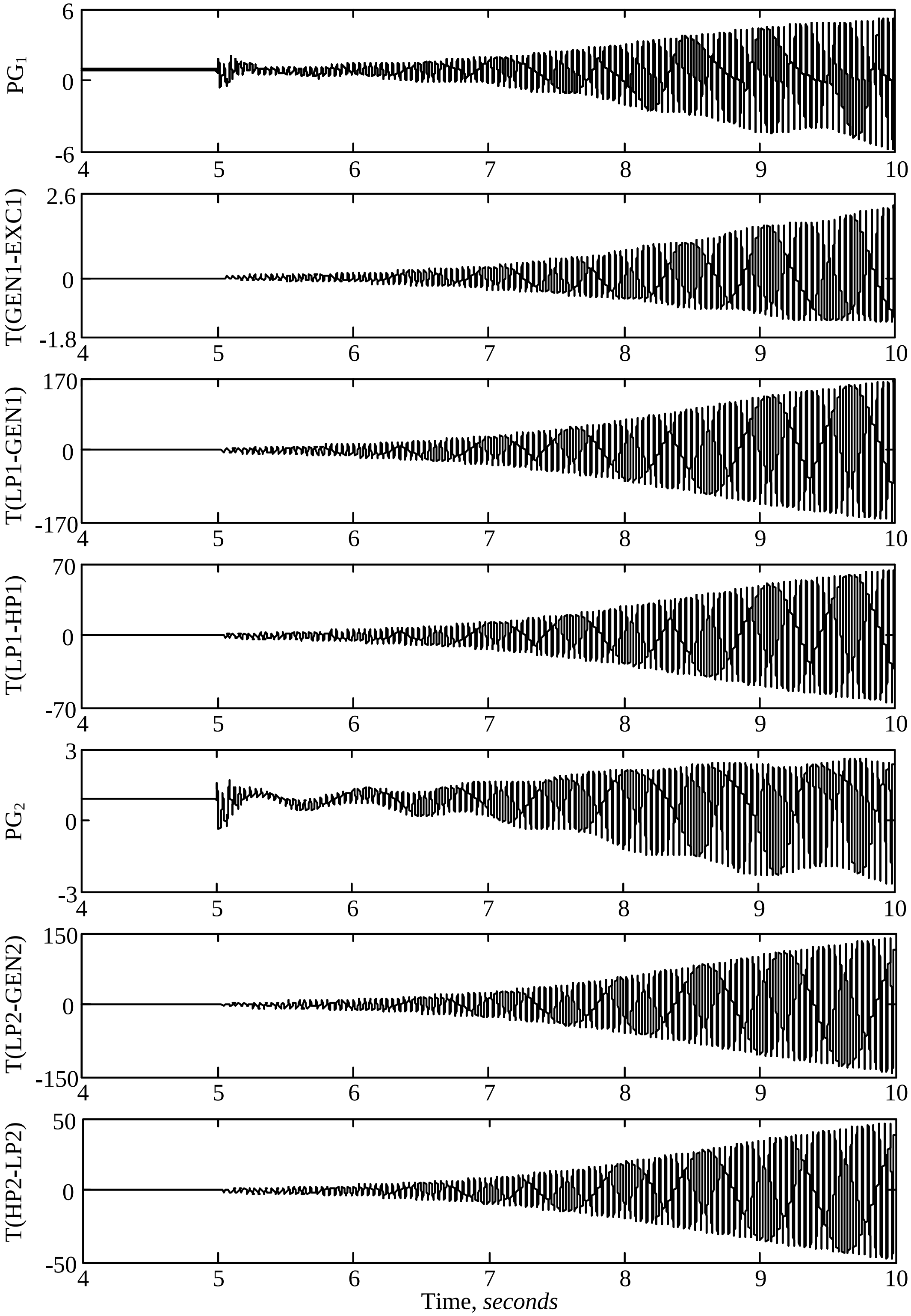

Figure 3.6: **System-II** turbine-generator electrical output powers and shaft torsional torques (expressed in per unit machine rating) during and after clearing a 4.5 *cycle*, three-phase fault at bus B (compensation degree = 65%).

3.5.1 The Hybrid TCSC Compensation Scheme

This section evaluates the capability of the proposed hybrid TCSC compensation scheme in mitigating SSR on **Systems I** and **II**. For this purpose, the scheme is assumed to be implemented in **Systems I** and **II** of Fig. 3.4 between buses **A** and **B** replacing the fixed capacitor banks. Moreover, the TCSC boost factor is assumed to be 1.75.

The turbine-generator electrical powers and shaft torsional torques expressed in per unit machine rating during and after clearing the same faults of Figs. 3.5 and 3.6 are shown respectively in Fig. 3.7 (with $X_{C_c} = 28.7\%$ and $X_{TCSC} = 28.7\%$ of the total line inductive reactance $X_L = j0.5\ p.u.$) and Fig. 3.8 (with $X_{C_c} = 32.5\%$ and $X_{TCSC} = 32.5\%$ of the total line inductive reactance $X_L = j0.054\ p.u.$). Figures 3.9(a) and (b) show respectively, the corresponding time responses of the TCSC boost factor. Moreover, the modal speed deviation corresponding to 'Mode 3' (i.e. $\Delta\omega_3$) of the turbine-generator of **System I** is shown in Figs. 3.10(a) and (b) respectively for the two study cases of Figs. 3.5 and 3.7. As it can be seen from Figs. 3.7 and 3.8, the single-phase TCSC along with its supplementary controller is able to damp effectively all the shaft torsional torques.

A. Minimum TCSC Size for Damping SSR

The minimum sizes of TCSC required for damping all SSR modes in **Systems I** and **II** are obtained using repeated time domain simulations. In each simulation run, TCSC contribution is decreased and fixed capacitor contribution is increased by certain percentage. This procedure is repeated to find out minimum size of TCSC that can damp SSR within 5 *sec* time window. The minimum size of TCSC required for **System I** and **II** are listed in Table 3.2. The turbine-generator electrical power and shaft torsional torques during and after clearing the same fault of Fig. 3.5 (4.5 *cycle*, three-phase fault at bus B, compensation degree = 57.4%) is shown in Fig. 3.11 for such a minimum TCSC size. It can be observed from these responses that the minimum size TCSC (11.48%) is able to damp all the shaft torsional torque oscillations in 5 *sec.*

Table 3.2: Minimum TCSC size for damping SSR.

System	Compensation Degree	X_{C_c}	$X_{TCSC,min}$
I	57.4%	45.92%	11.48%
II	65%	45.5%	19.5%

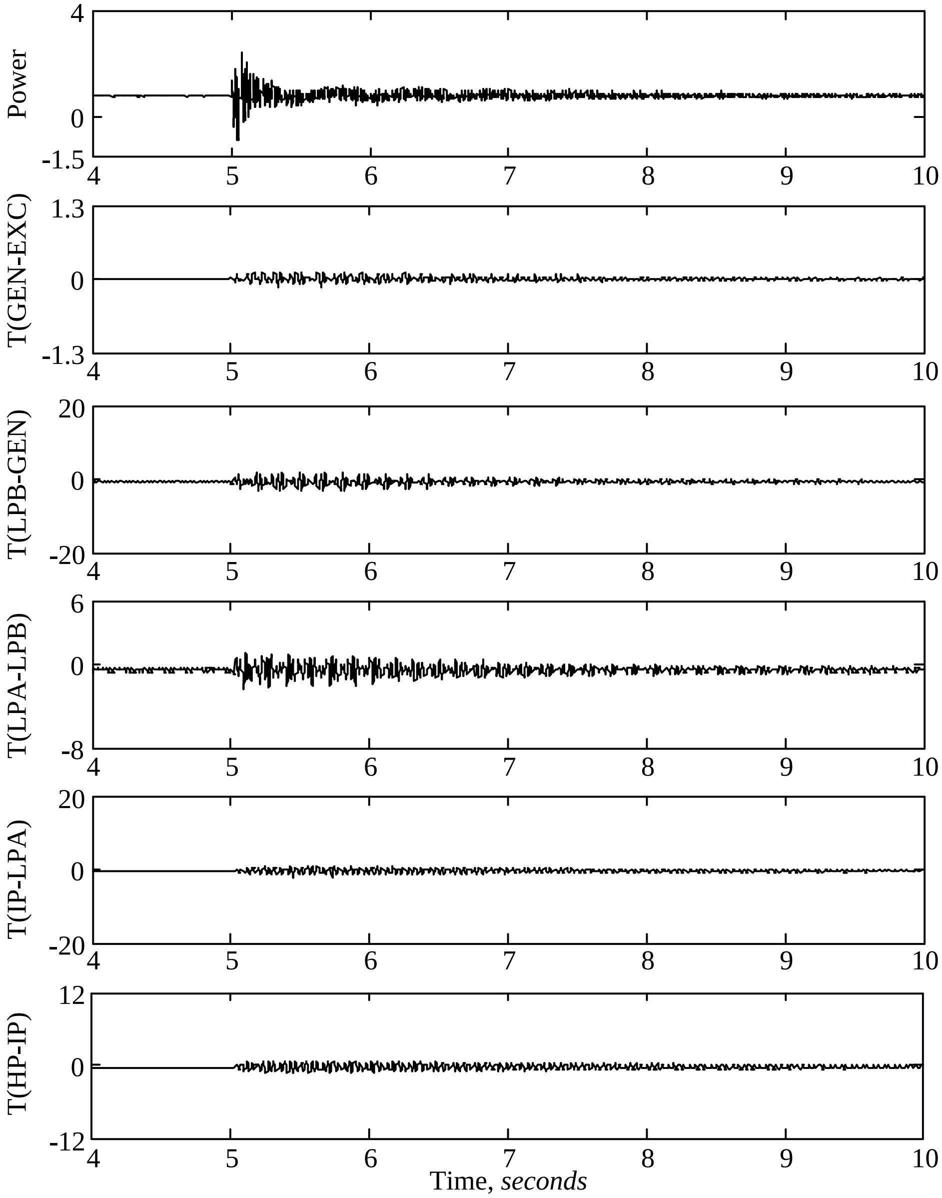

Figure 3.7: Hybrid TCSC: System-I turbine-generator electrical power and shaft torsional torques (expressed in per unit machine rating) during and after clearing a 4.5 *cycle*, three-phase fault at bus **B** (compensation degree = 57.4%, $X_{TCSC} = X_{C_c} = 28.7\%$).

B. Impact of Fault Location

The effect of the fault location on the effectiveness of the proposed scheme in damping SSR oscillations is examined by changing the location of the three-phase fault from bus **B** to bus **A** in **System-I**. This is a more severe disturbance since the fault is virtually at the generator terminal. The time responses of the turbine-generator electrical power and

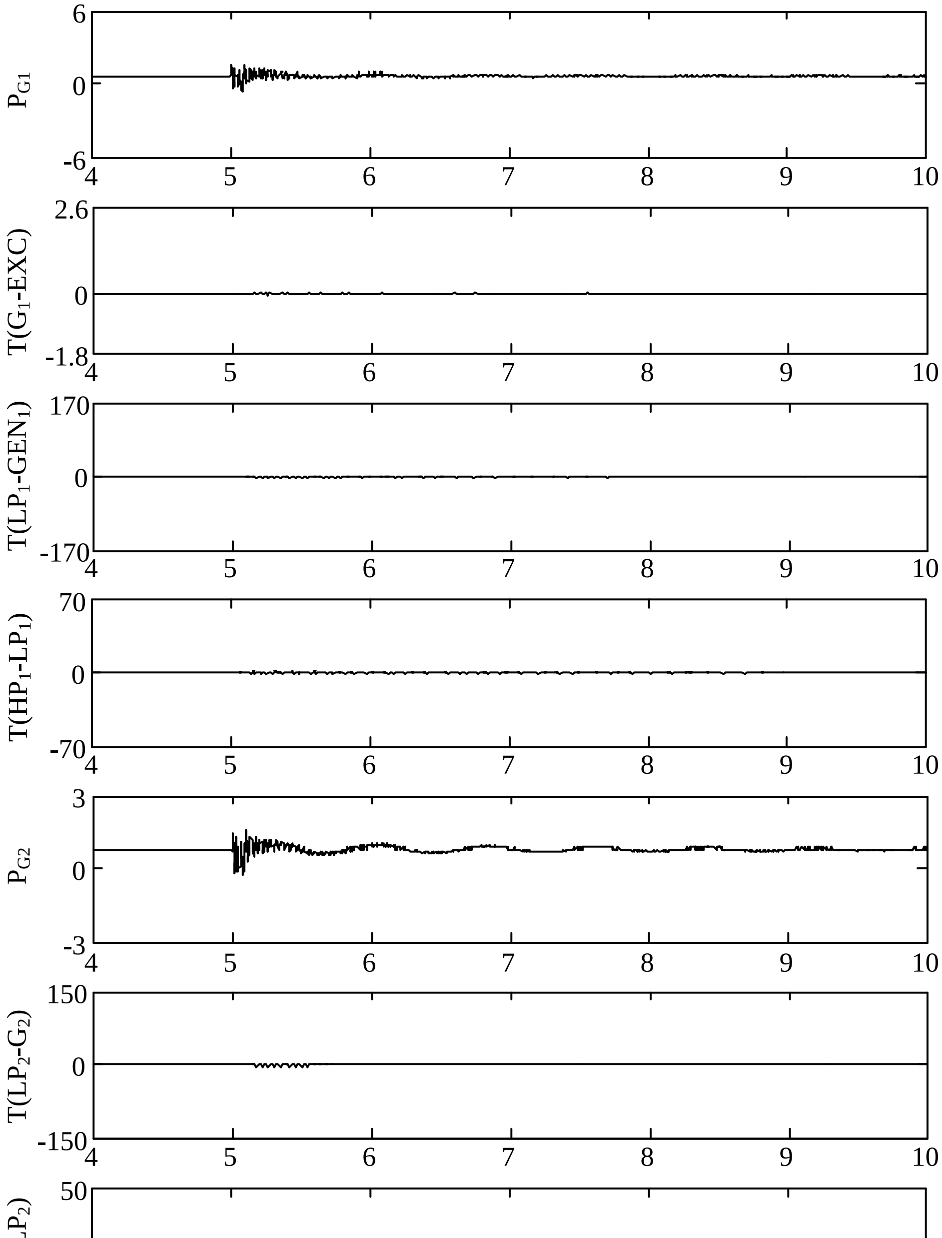

Figure 3.8: Hybrid TCSC: System-II turbine-generator electrical power and shaft torsional torques (expressed in per unit machine rating) during and after clearing a 4.5 *cycle*, three-phase fault at bus **B** (compensation degree = 65.0%, $X_{TCSC} = X_{C_c} = 32.5\%$).

shaft torques for the cases without and with the TCSC are shown in Figs. 3.12 and 3.13

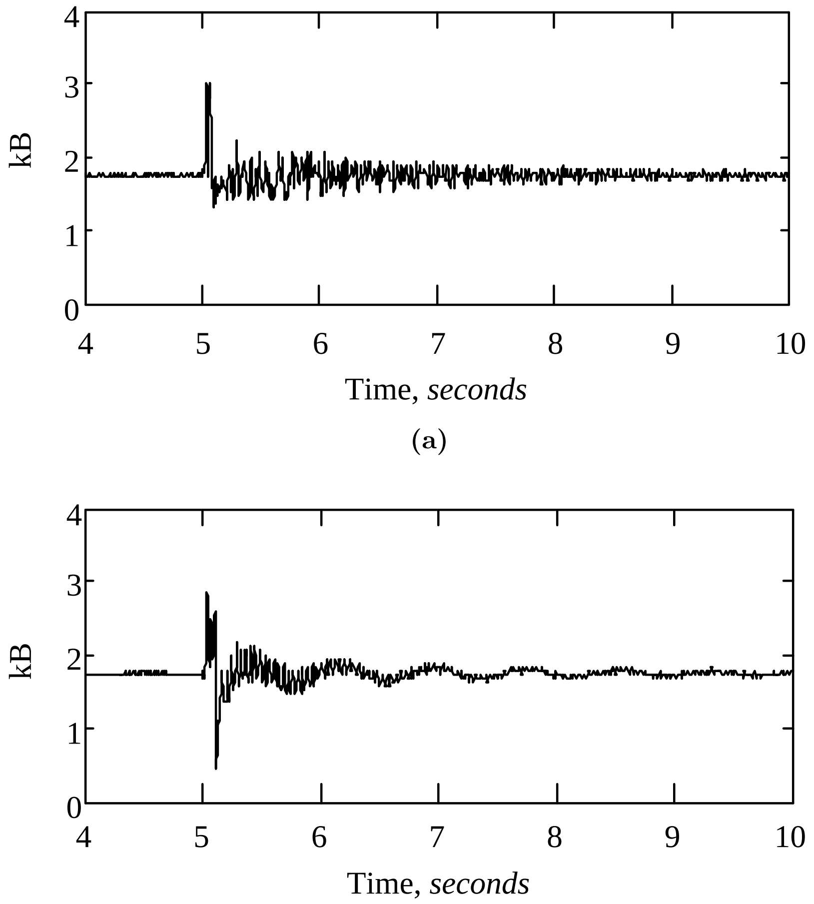

(a)

(b)

Figure 3.9: Hybrid TCSC: TCSC boost factor after clearing a 4.5-cycle, three-phase fault at bus B (a) **System-I** compensation degree = 57.4%, $X_{C_c} = 28.7\%$, $X_{TCSC} = 28.7\%$, $kB = 1.75$ and (b) **System-II**, compensation degree, = 65%, $X_{C_c} = 32.5\%$, $X_{TCSC} = 32.5\%$, $kB = 1.75$.

respectively. It can be seen from Fig. 3.12 that the magnitudes of the shaft torsional torques are higher than those in Fig. 3.5. It can also be seen from Fig. 3.13 that the proposed scheme is capable of damping the SSR oscillations resulting from such a severe disturbance.

Comparing the hybrid TCSC compensated power system torsional oscillation responses in Figs. 3.7 though 3.13 to the fixed capacitor compensation cases in Figs. 3.5, 3.6 and 3.12, it can be concluded that the proposed hybrid TCSC compensation scheme is very effective in damping SSR oscillations.

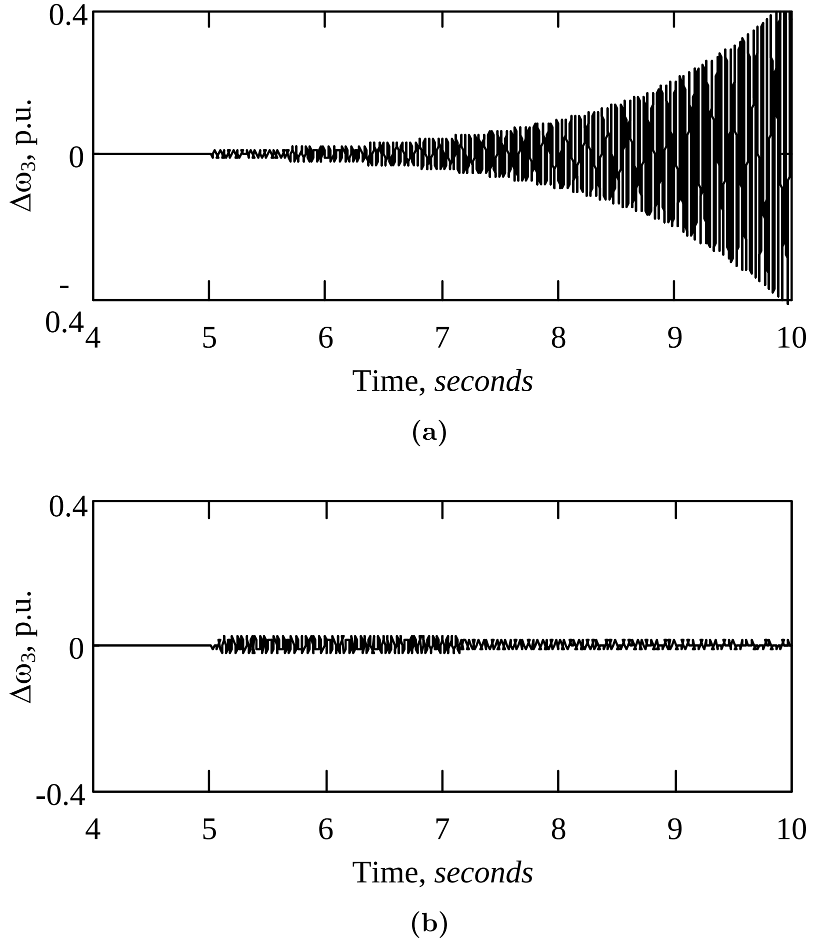

(a)

(b)

Figure 3.10: **Hybrid TCSC:** Modal speed of the turbine-generator of **System-I** during and after clearing a 4.5-cycle, three-phase fault at bus **B** (a) fixed capacitor compensation (compensation degree = 57.4%), (b) hybrid TCSC compensation (comp. deg, = 65%, $X_{C_c} = 32.5\%$, $X_{TCSC} = 32.5\%$, $kB = 1.75$).

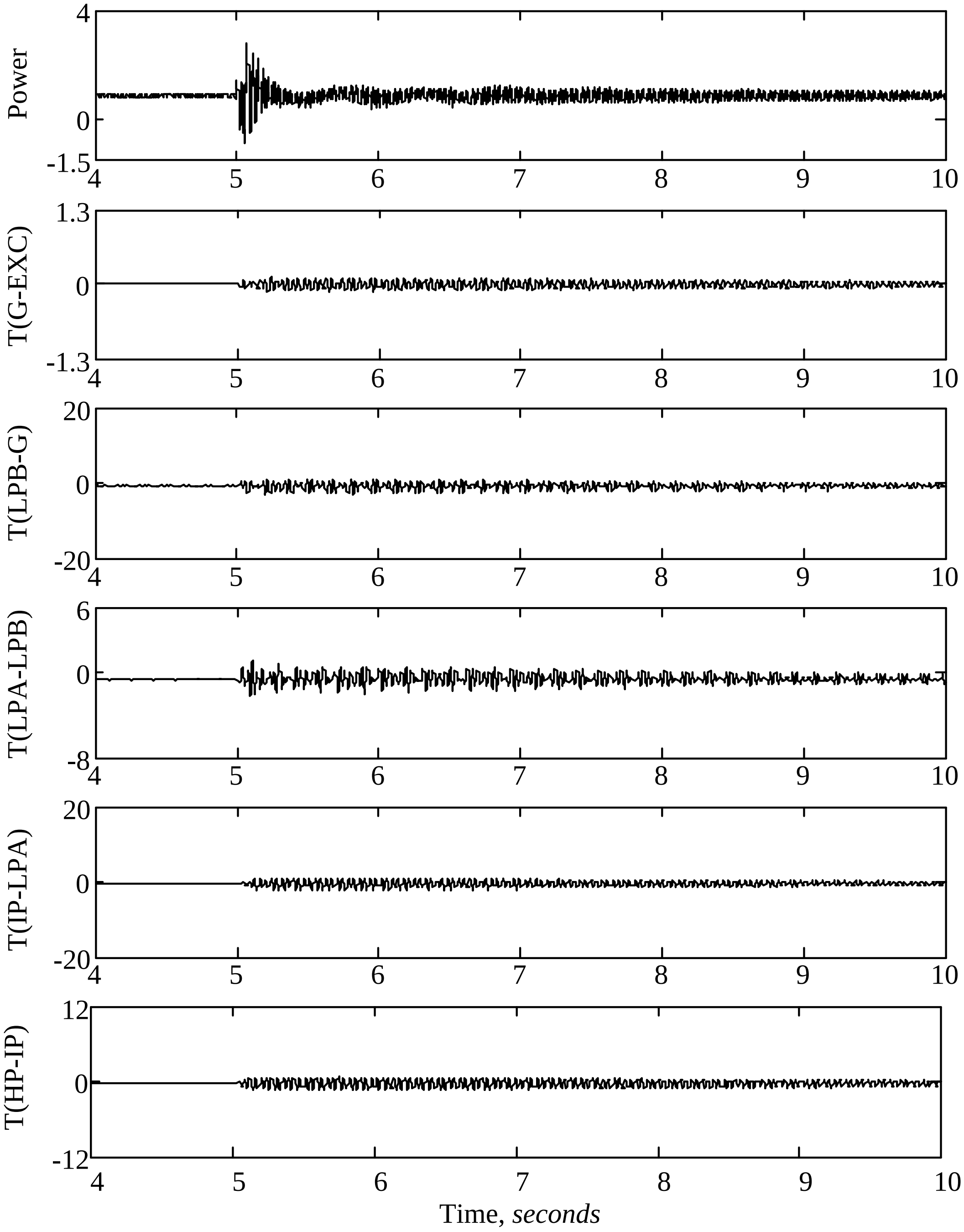

Figure 3.11: Hybrid TCSC: System-I turbine-generator electrical power and shaft torsional torques (expressed in per unit machine rating) during and after clearing a 4.5 *cycle*, three-phase fault at bus **B** (compensation degree = 57.4%, $X_{TCSC,min} = 11.48\%$, $X_{C_c} = 45.92\%$).

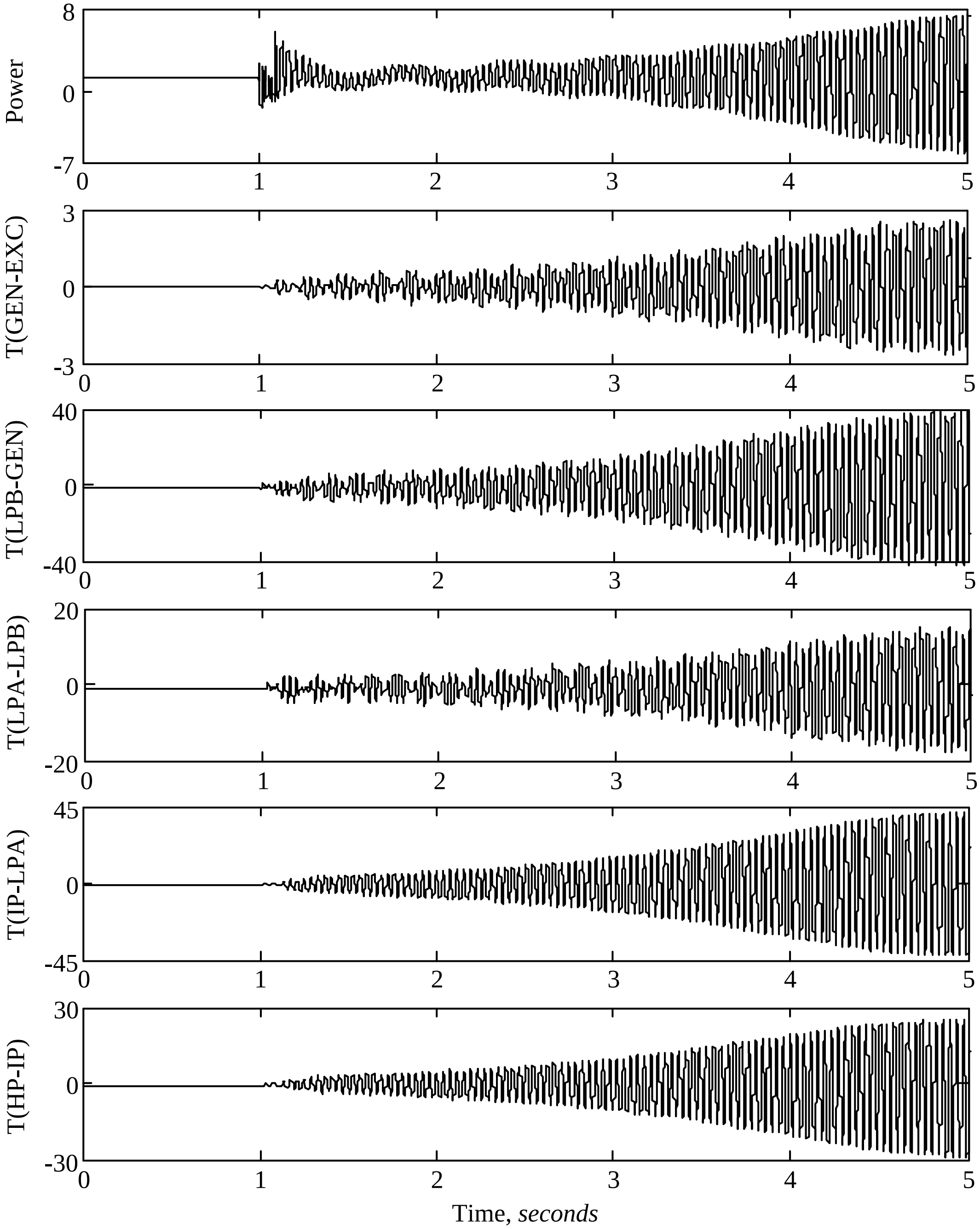

Figure 3.12: System-I turbine-generator electrical power and shaft torsional torques (expressed in per unit machine rating) during and after clearing a 4.5 *cycle*, three-phase fault at bus **A** (fixed capacitor compensation, compensation degree = 57.4%).

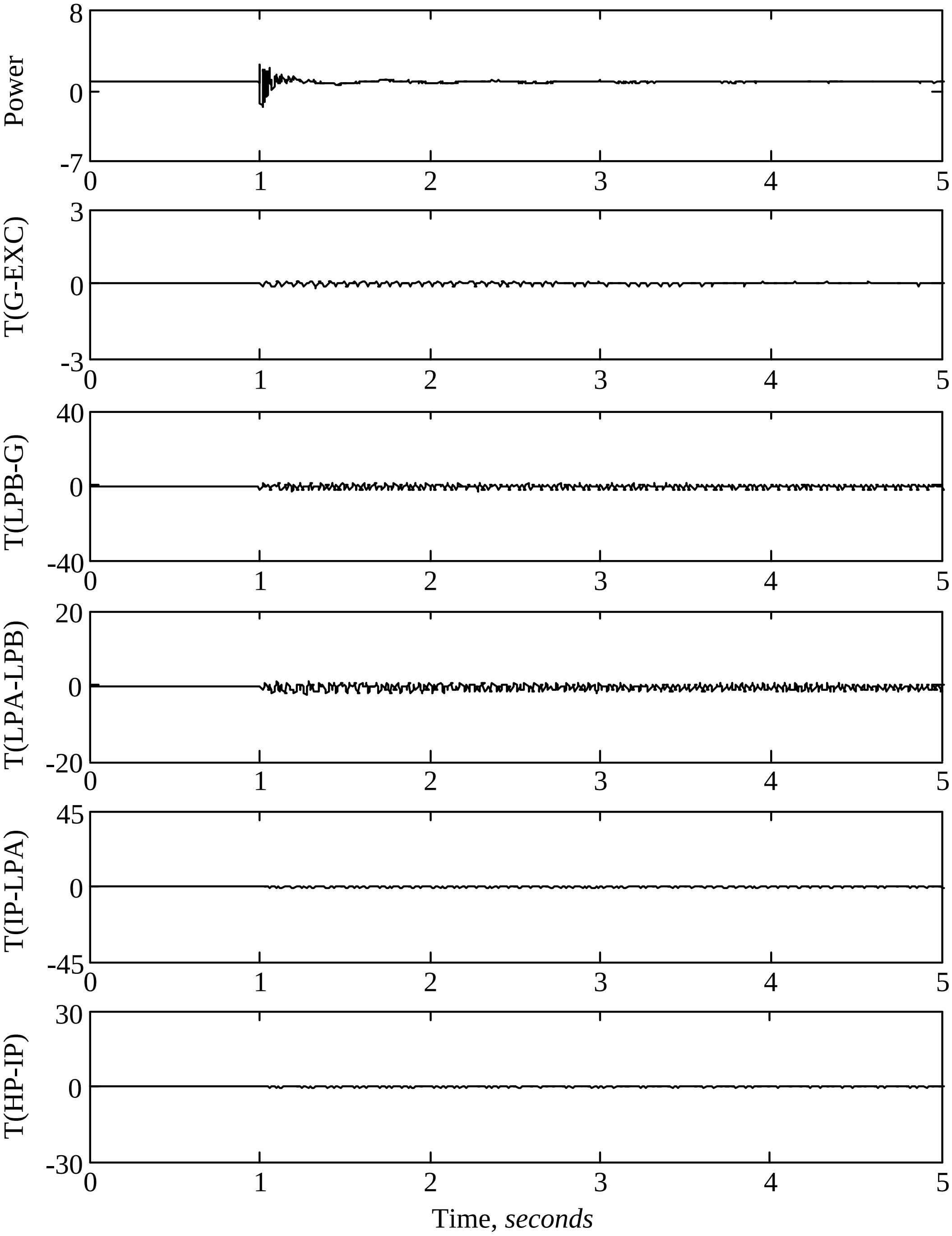

Figure 3.13: Hybrid TCSC: System-I turbine-generator electrical power and shaft torsional torques (expressed in per unit machine rating) during and after clearing a 4.5 *cycle*, three-phase fault at bus **A** (compensation degree = 57.4%, $X_{TCSC} = X_{C_c} = 28.7\%$)

3.5.2 The Hybrid SSSC Compensation Scheme

This section evaluates the effectiveness of the proposed hybrid SSSC compensation scheme in mitigating the SSR. For this purpose, the scheme is assumed to be installed in **Systems I** and **II** of Fig. 3.4 between buses **A** and **B**. The turbine-generator electrical output powers and shaft torsional torques during and after clearing the same faults of Figs. 3.5 and 3.6 are shown respectively in Fig. 3.14 (with $X_{C_c} = 47.06\%$ and $X_{SSSC,min} = 10.34\%$ of the total line inductive reactance $X_L = j0.50$ *p.u.*, i.e. SSSC provides 18% of the total compensation) and in Fig. 3.15 (with $X_{C_c} = 55.25\%$ and $X_{SSSC,min} = 9.75\%$ of the total line inductive reactance $X_L = j0.054$ *p.u.*, i.e. SSSC provides 15.10% of the total compensation). **System-II** torsional torque responses (Fig. 3.15) are '*magnified in the y-axis*' to demonstrate the damping effect in more detail. Figures 3.16 and 3.17 show respectively the corresponding time responses of the SSSC injected and DC capacitor voltages. As it can be seen from Figs. 3.14 and 3.15, the single-phase SSSC along with its supplementary controller is able to damp effectively all the shaft torsional torques in nearly two seconds.

The SSSC reactances ($X_{SSSC,min}$) used in the studies of the Figs. 3.14 and 3.15 are the minimum size of SSSC compensation required to obtain torsional damping in all the shaft sections of the turbine-generator. The minimum SSSC contribution values required for **System I** and **II** are found out using the similar technique adopted for finding out the minimum TCSC contribution required to damp SSR.

A. SSR Oscillations Damping During Unsymmetrical Faults

Figure 3.18 shows the time responses of **System-I** turbine-generator electrical output power and shaft torsional torques during and after clearing a 4.5 cycle double line-to-ground fault at bus **B** (fixed capacitor compensation, 57.4% compensation degree and b and c are the faulted phases). Figure 3.19 shows the same responses for the case when the hybrid SSSC is in service ($X_{C_c} = 47.06\%$ and $X_{SSSC,min} = 10.34\%$ of the total line inductive reactance). As it can be seen again from Figs. 3.18 and 3.19, the hybrid SSSC scheme is also effective in suppressing the SSR oscillations resulting from unsymmetrical faults.

When the responses in Figs. 3.14, 3.15 and 3.19 are compared with fixed capacitor compensation torsional torque oscillation responses shown in Figs. 3.5, 3.6 and 3.18 respectively, it is very clear that the proposed 'hybrid SSSC compensation scheme' is very effective in damping SSR oscillations.

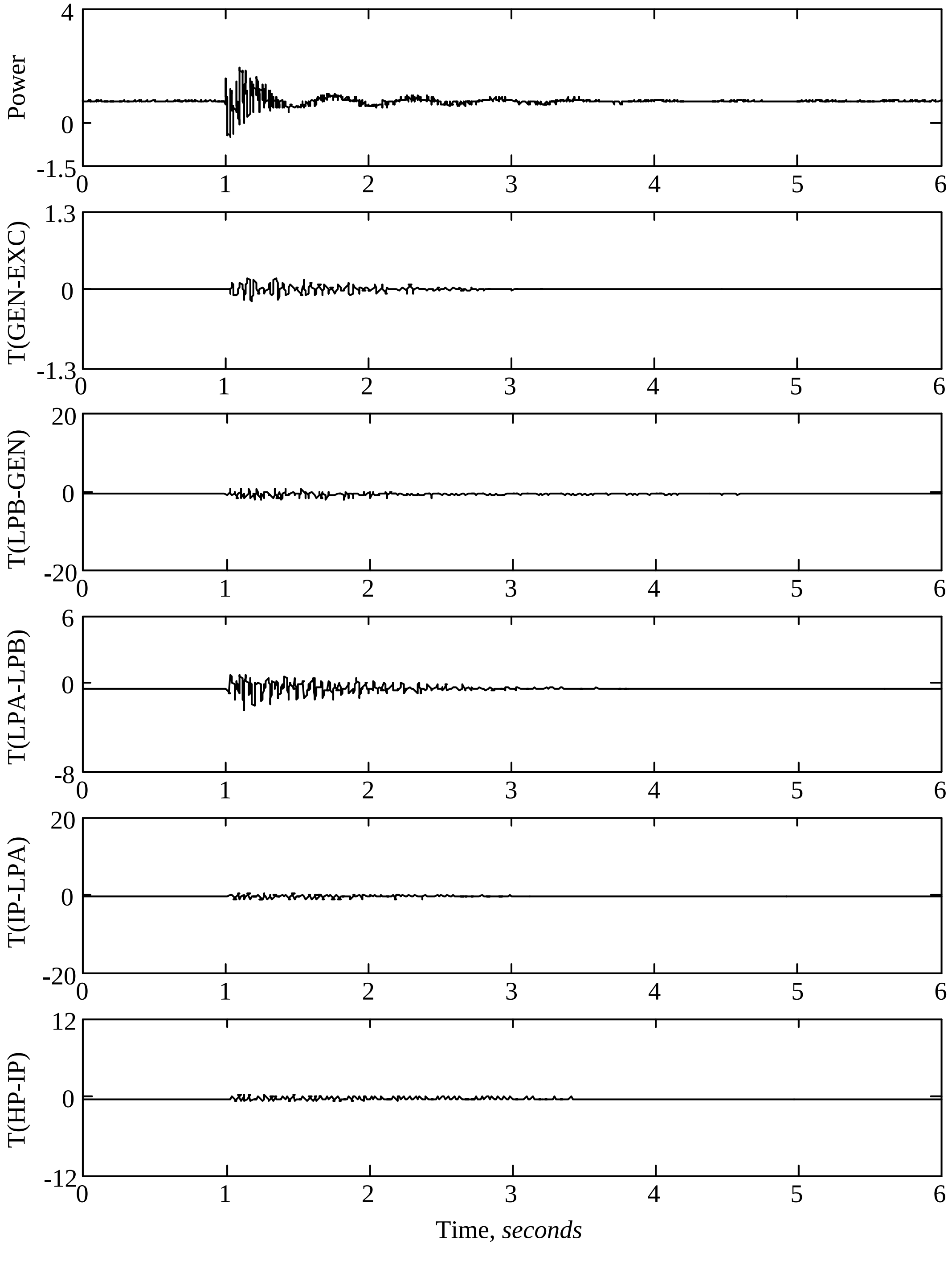

Figure 3.14: Hybrid SSSC: System-I turbine-generator electrical output power and shaft torsional torques (expressed in per unit machine rating) during and after clearing a 4.5 *cycle*, three-phase fault at bus B (compensation degree = 57.4%, $X_{C_c} = 47.06\%$, $X_{SSSC,min} = 10.34\%$).

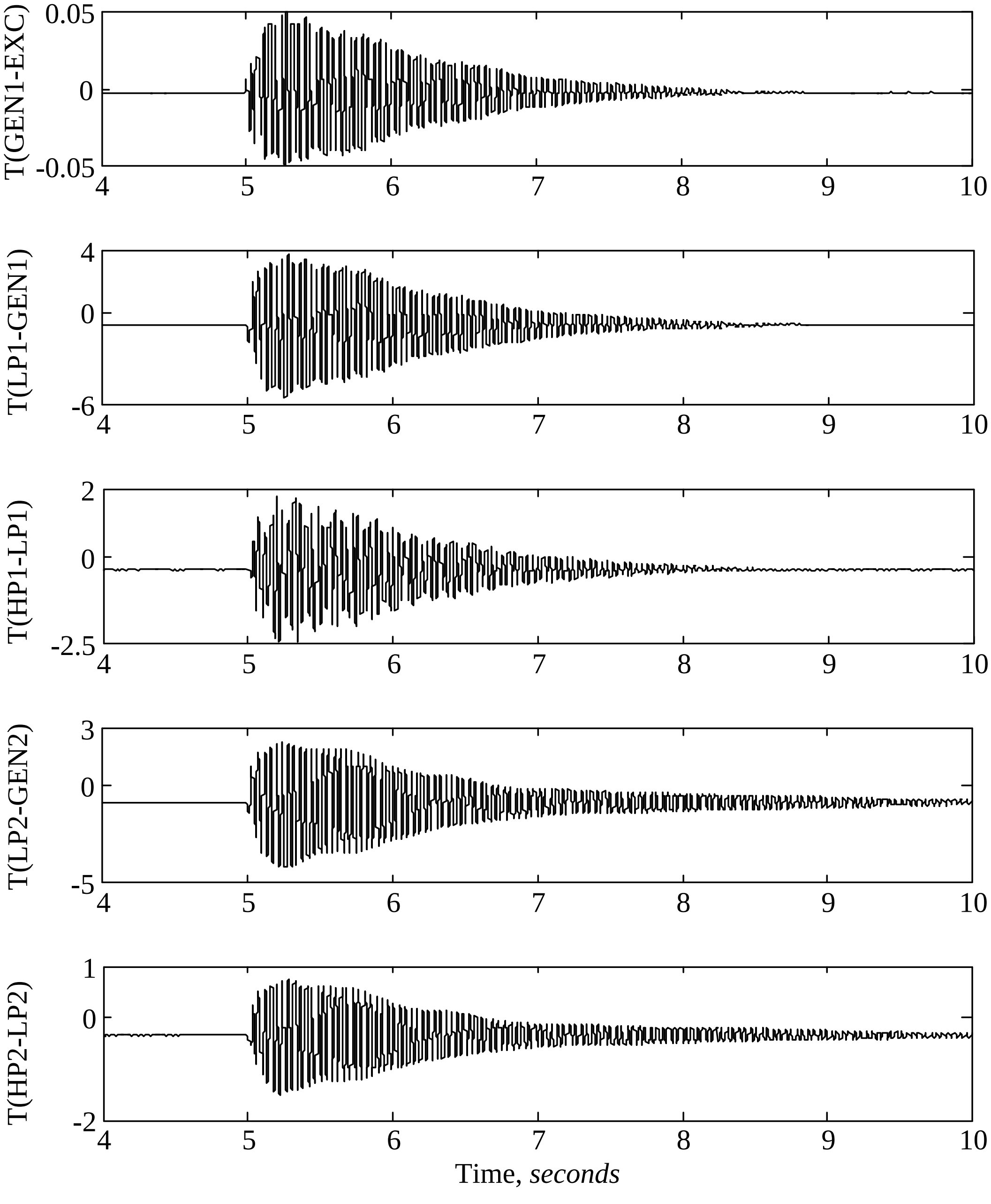

Figure 3.15: Hybrid SSSC: System-II turbine-generator electrical output power and shaft torsional torques (expressed in per unit machine rating) during and after clearing a 4.5 *cycle*, three-phase fault at bus B (compensation degree = 65.0%, $X_{C_c} = 55.25\%$, $X_{SSSC,min} = 9.75\%$), (*magnified in the y-axis*).

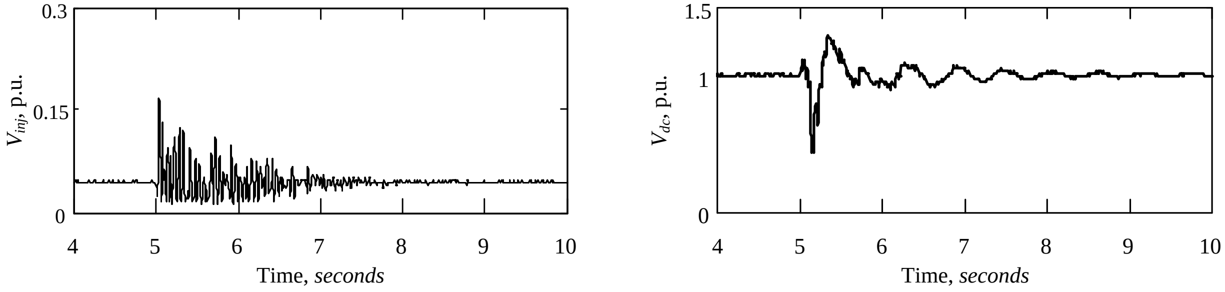

(a) **(b)**

Figure 3.16: **System-I** (a) SSSC injected and (b) dc capacitor voltages after clearing a 4.5 *cycle*, three-phase fault at bus **B** (compensation degree = 57.4%, $X_{C_c} =$ 47.06%, $X_{SSSC,min} = 10.34\%$)

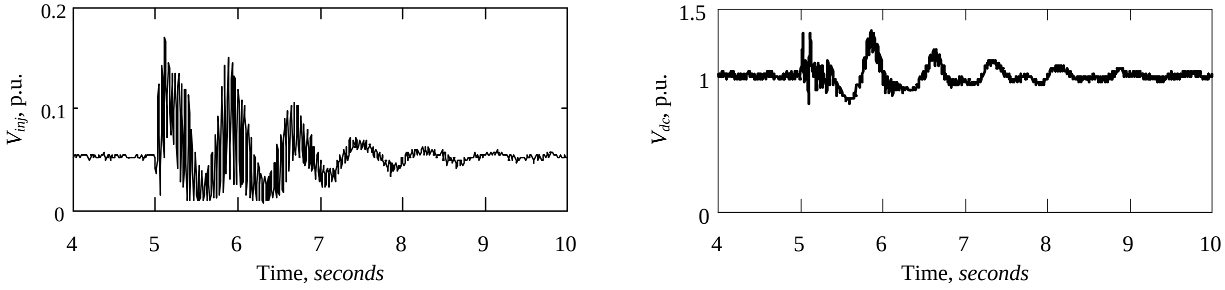

(a) **(b)**

Figure 3.17: **System-II** (a) SSSC injected and (b) dc capacitor voltages after clearing a 4.5 *cycle*, three-phase fault at bus **B** (compensation degree = 65.0%, $X_{C_c} =$ 55.25%, $X_{SSSC,min} = 9.75\%$)

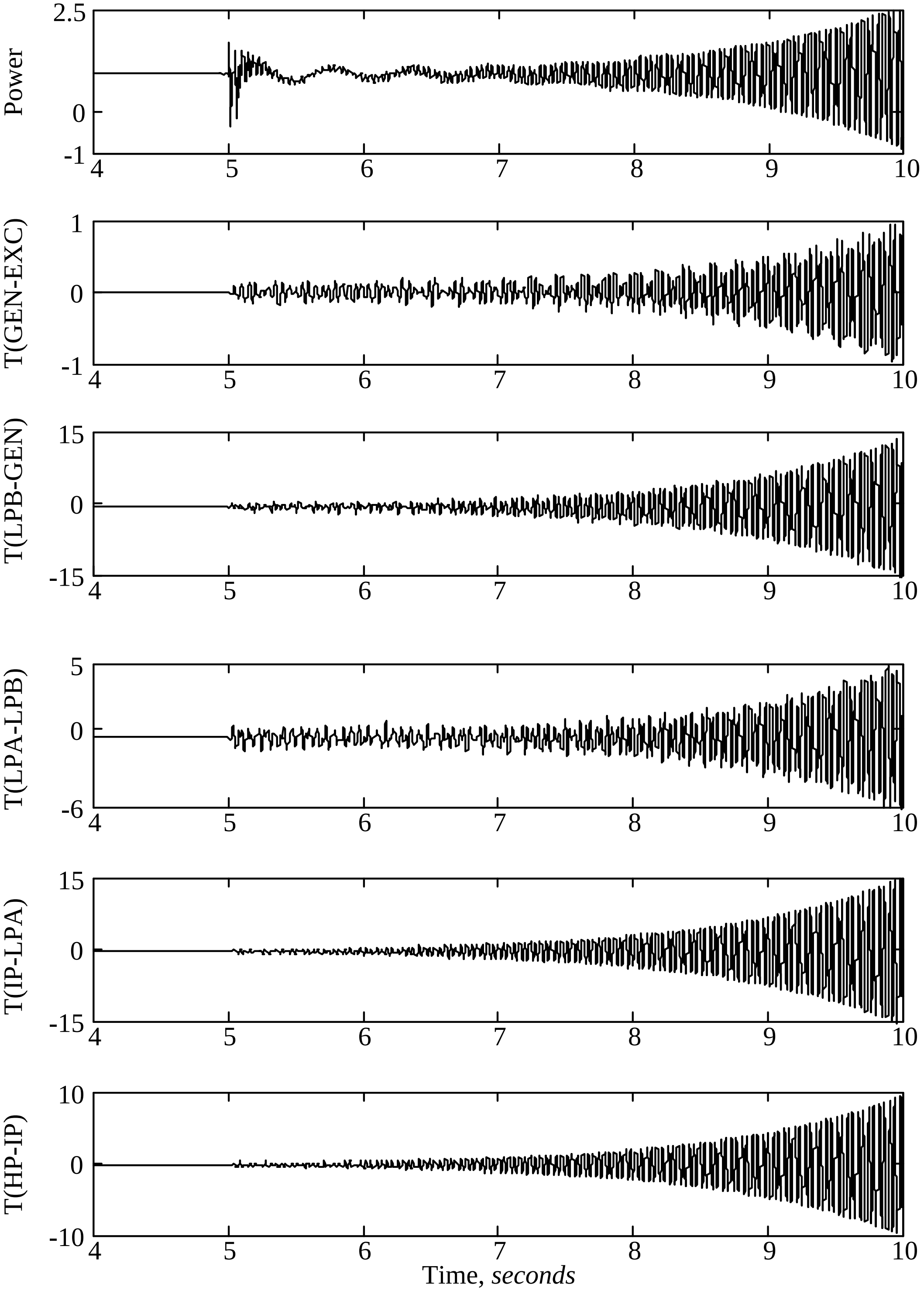

Figure 3.18: System-I turbine-generator electrical output power and shaft torsional torques (expressed in per unit machine rating) during and after clearing a 4.5 *cycle*, double line-to-ground fault at bus B (compensation degree = 57.4%, faulted phase: *b, c* to ground).

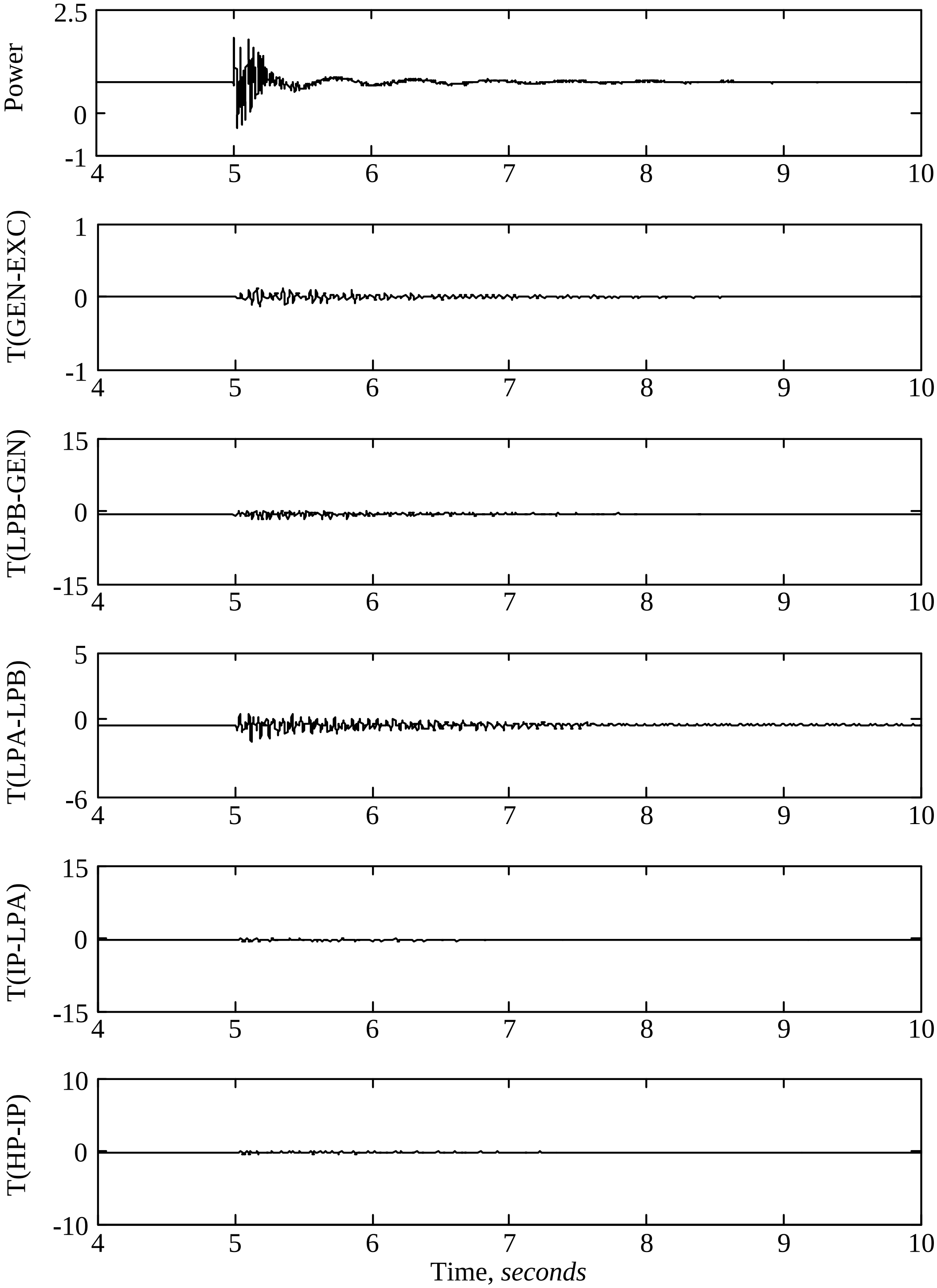

Figure 3.19: Hybrid SSSC: System-I turbine-generator electrical output power and shaft torsional torques (expressed in per unit machine rating) during and after clearing a 4.5 *cycle*, double line-to-ground fault at bus B (compensation degree = 57.4%, faulted phases: *b*, *c* to ground, $X_{C_c} = 47.06\%$, $X_{SSSC,min} = 10.34\%$).

3.5.3 Higher Compensation Degrees - System I

The effectiveness of the proposed schemes in damping SSR at higher compensation degrees in **System-I** is investigated. For this purpose, a 72.0% compensation degree is selected in order to trigger 'Mode 2' SSR oscillation (Table 3.1) in **System-I**.

Fixed Capacitor Compensation: Figure 3.20 shows the time response of the turbine-generator electrical power and shaft torsional torques for fixed capacitor series compensation. The disturbance is considered as a 4.5 *cycle*, three-phase fault applied at $t = 5$ *sec* on bus **B**. The system electrical power generation and torsional torque time-responses are presented in per unit scale on machine rating. It is very clear that the shaft torsional torques are amplified by the presence of SSR.

Hybrid TCSC Scheme: Figure 3.21 shows the time response of **System-I** for the same disturbance of Fig. 3.20 when the hybrid TCSC scheme is in service. The TCSC contribution on phase c is 21.60% and the fixed capacitor contribution is 50.40% of the line impedance.

Hybrid SSSC Scheme: Figure 3.22 shows the same responses for the case when the hybrid SSSC scheme is in service. The disturbance considered in this case is same as Fig. 3.20. The SSSC contribution in phase c is 21.60% and the fixed capacitor contribution is 50.40% of the total line inductive reactance.

The compensation contributions by TCSC and SSSC in both cases are minimum value required for damping SSR effectively. These minimum compensation values required to damp SSR are found out using multiple time-domain simulation runs. The comparison between fixed capacitor compensation (Fig. 3.20) and the hybrid compensation responses in Figs. 3.21 and 3.22 demonstrates the effectiveness of the hybrid schemes in damping SSR oscillations at higher compensation degrees.

Figure 3.23 illustrates the three-phase voltages, V_{X-Y}, across the hybrid TCSC in **System-I** for the case study of Fig. 3.21. The system phase unbalance during the disturbance is noticeable especially in phase c where the TCSC is installed. The instantaneous voltage across the TCSC is also shown in Fig. 3.23.

Similarly, Fig. 3.24(a) illustrates the three-phase voltages, V_{X-Y}, across the hybrid SSSC in **System-I** for the case study of Fig. 3.22. The system phase unbalance during the disturbance is clearly noticeable, especially in phase c where the SSSC is installed. The instantaneous and root-mean-square SSSC injected voltages are shown in Fig. 3.24(b) and (c) respectively. It is worth noting here that the peak value of the SSSC injected voltage is a design issue which is normally specified in the technical specifications of the voltage-sourced

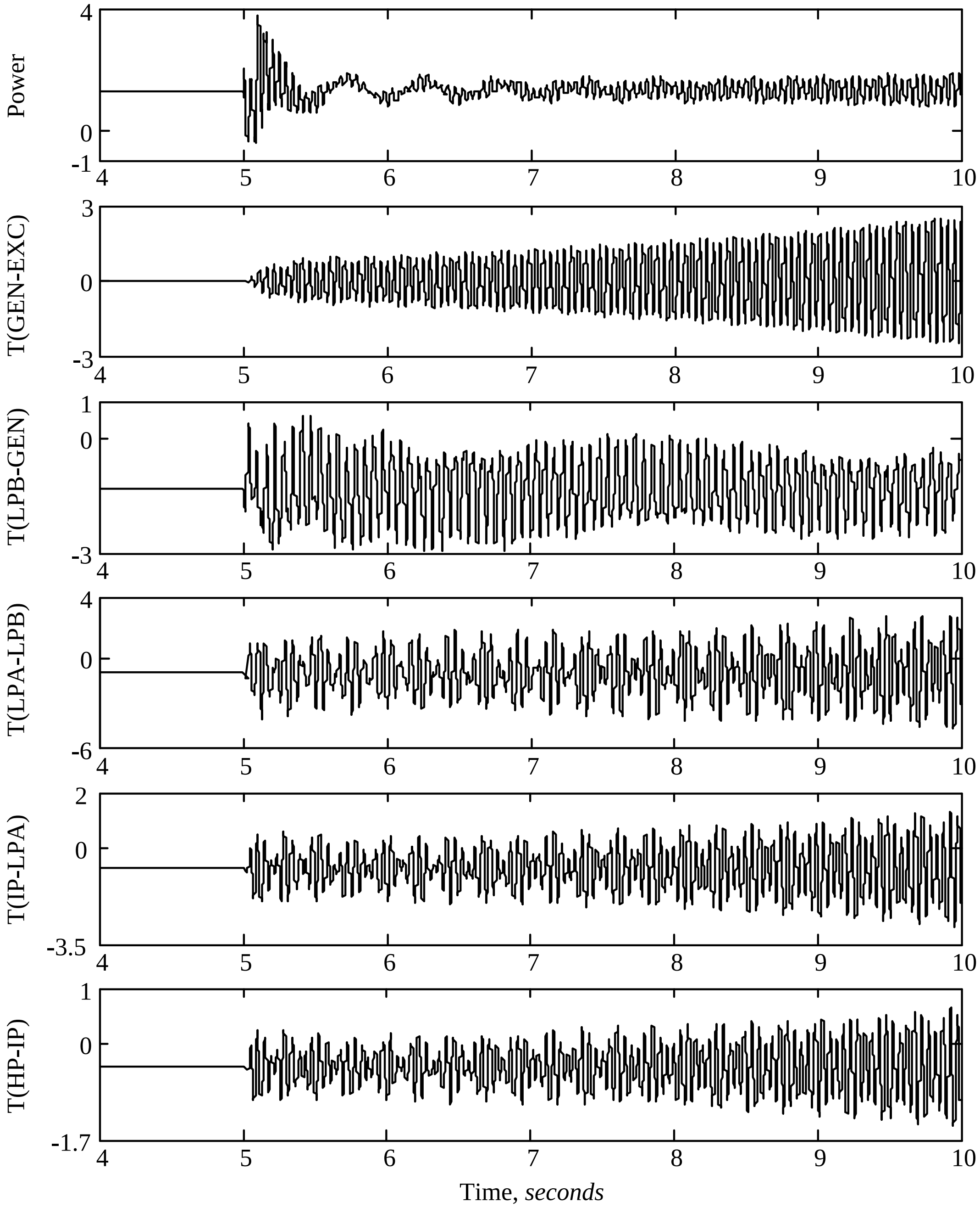

Figure 3.20: Fixed Capacitor: System-I turbine-generator electrical output power and shaft torsional torques (expressed in per unit machine rating) during and after clearing a 4.5 *cycle*, three-phase fault at bus B (compensation degree = 72.0%).

converter. It is quite common to specify 100% overload capability for a very short time, e.g. 1 to 2 *sec*. The result shown Fig. 3.24(c) is within what could be specified in a technical specification of an SSSC.

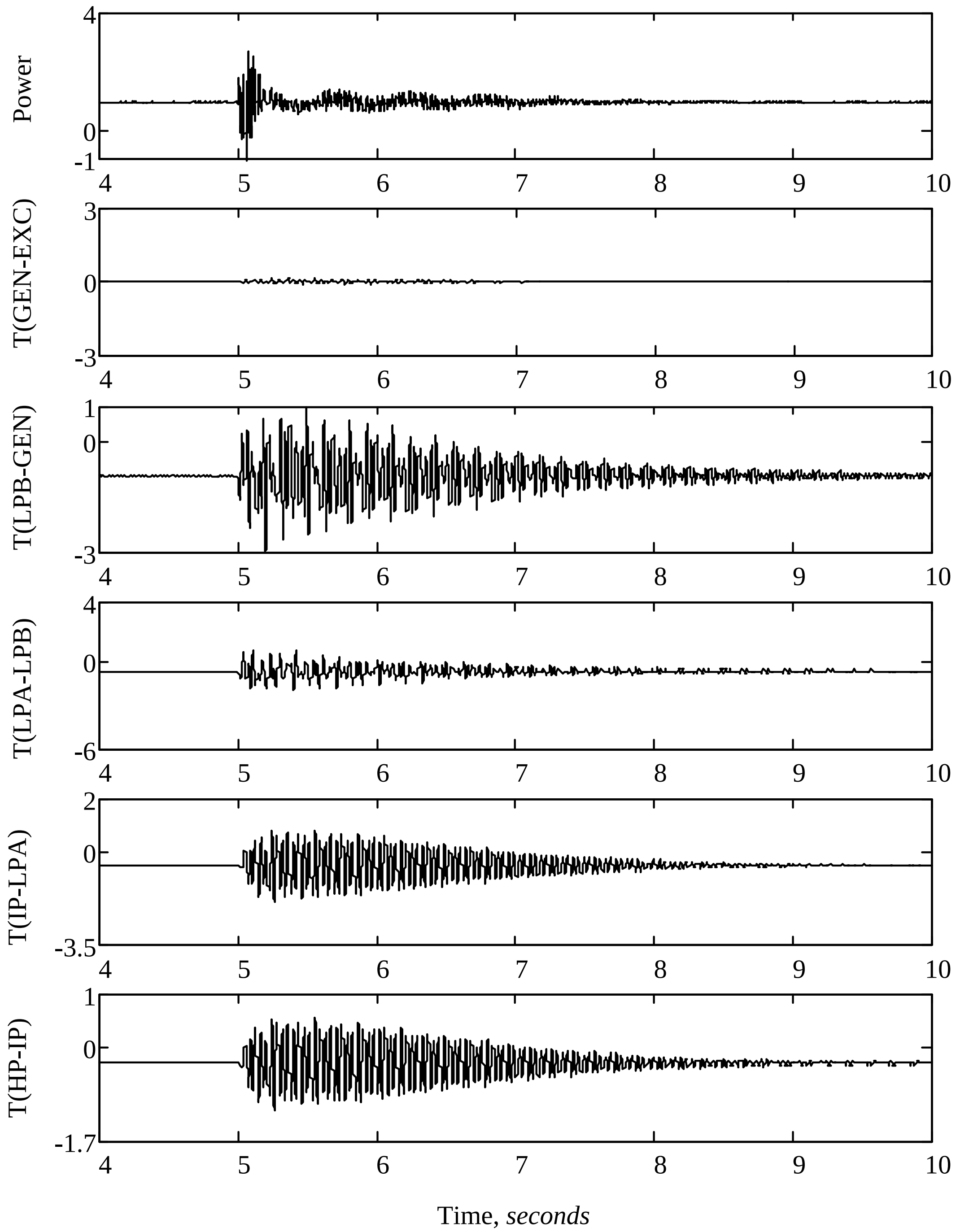

Figure 3.21: Hybrid TCSC: System-I turbine-generator electrical output powers and shaft torsional torques (expressed in per unit machine rating) during and after clearing a 4.5 *cycle*, three-phase fault at bus B (compensation degree = 72%, $X_{C_c} = 50.40\%$, $X_{TCSC,min} = 21.60\%$)

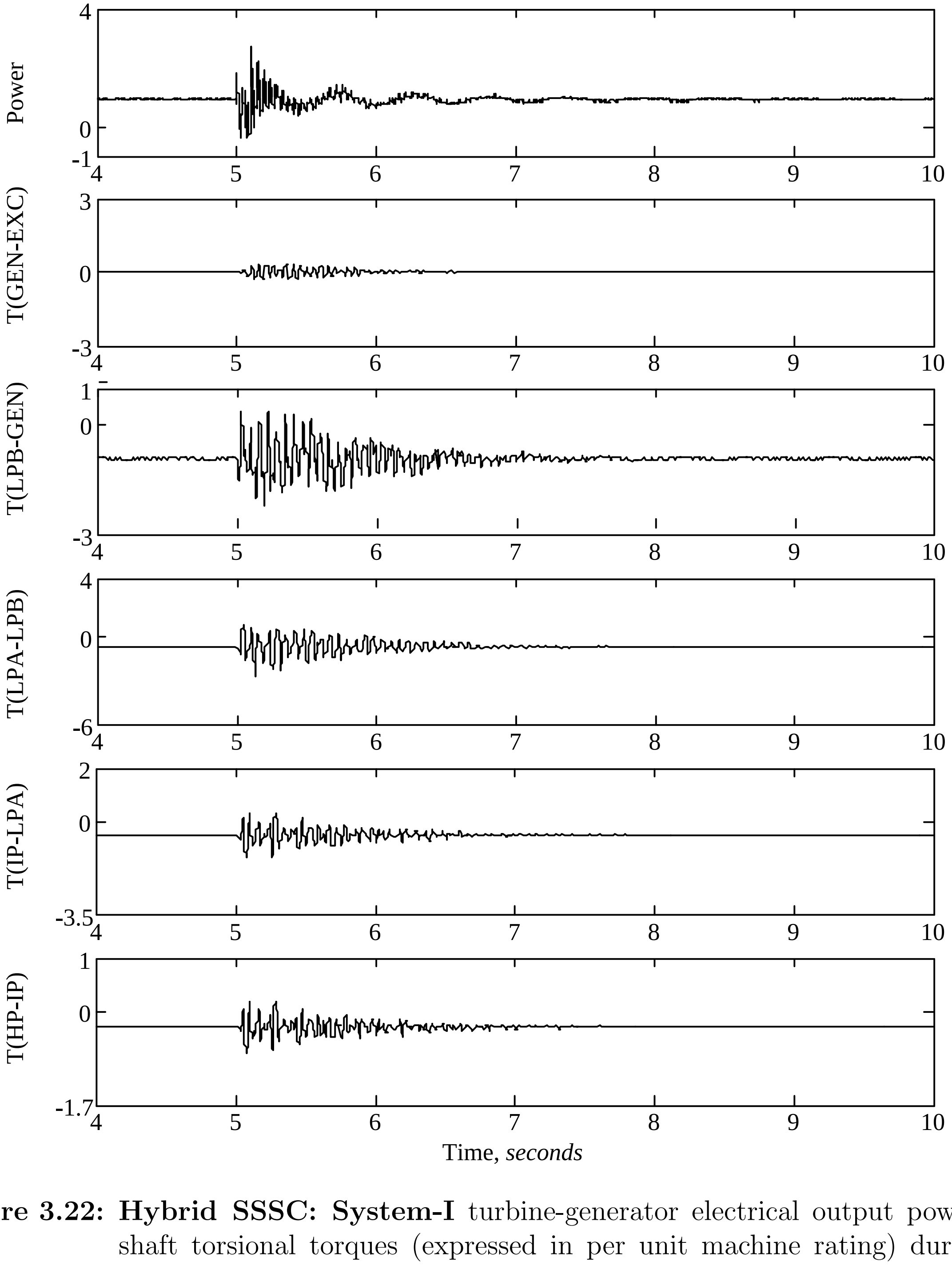

Figure 3.22: Hybrid SSSC: System-I turbine-generator electrical output powers and shaft torsional torques (expressed in per unit machine rating) during and after clearing a 4.5 *cycle*, three-phase fault at bus B (compensation degree = 72%, $X_{C_c} = 50.40\%$, $X_{SSSC,min} = 21.60\%$).

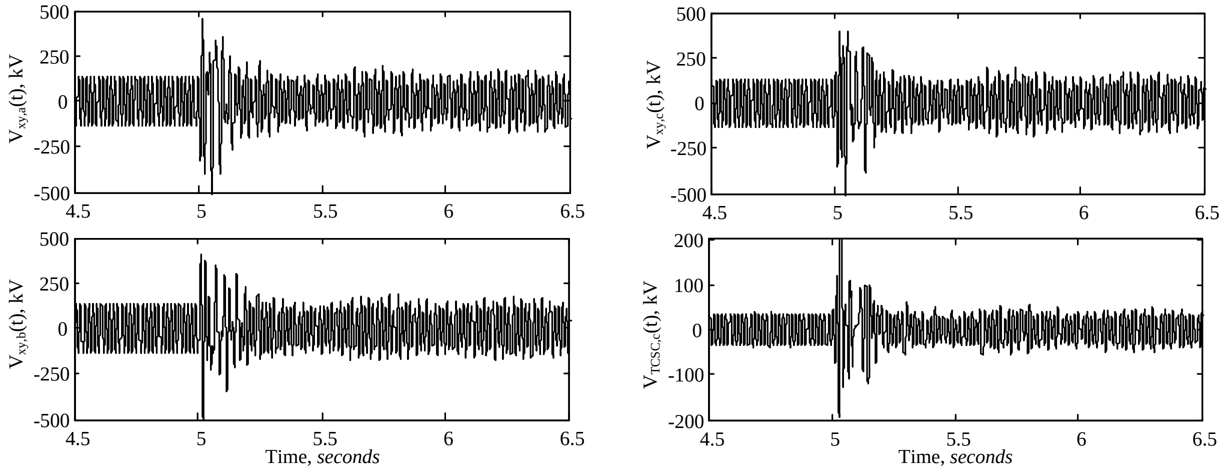

Figure 3.23: Hybrid TCSC: Instantaneous phase voltages V_{X-Y} and voltage across TCSC in **System-I** during and after the three-phase fault of Fig. 3.21 (V_{X-Y} = (121.10 kV, peak value) = 85.60 $kV\ rms$, V_{C_c} = 56.05 $kV\ rms$, V_{inj} = 29.55 $kV\ rms$).

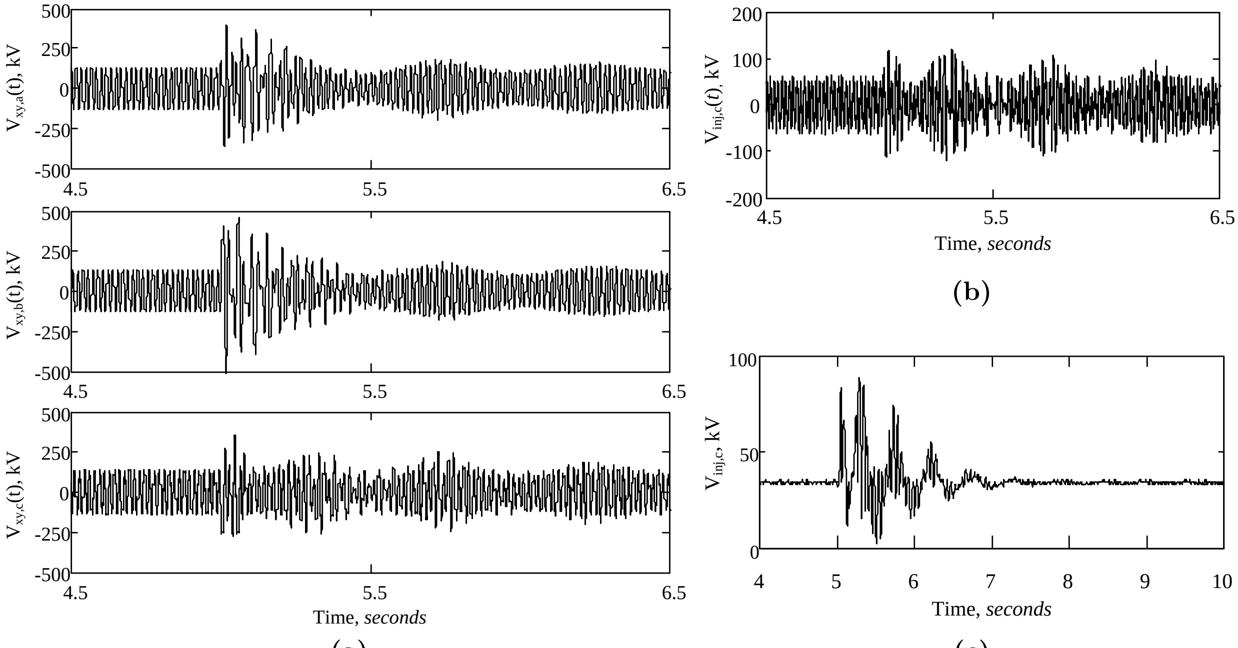

(a) **(b)** **(c)**

Figure 3.24: Phase voltages in **System-I** during and after the three-phase fault of Fig. 3.22: (a) V_{X-Y} across hybrid SSSC compensation, (b) the SSSC injected voltage in instantaneous and (c) SSSC injected voltage in rms, (V_{X-Y} = (120.77 kV, peak value) = 85.4 $kV\ rms$, V_{C_c} = 55.5 $kV\ rms$, V_{inj} = 29.9 $kV\ rms$).

3.5.4 Line Voltage Unbalance Rate (LVUR)

The Line Voltage Unbalance Rate (LVUR) measures the voltage unbalance present on the system and indicates the power quality. It is defined by the National Electrical Manufacturers Association (NEMA) in Standards Publication no. MG 1-1993 as [73], [74]:

$$\begin{aligned}(LVUR), \% &= \frac{\text{Maximum deviation from average}}{\text{Average of three line-to-line voltages}} \times 100 \qquad (3.6)\\ &= \frac{Max\left[(v_{ab} - v_{av}), (v_{bc} - v_{av}), (v_{ca} - v_{av})\right]}{v_{av}}\end{aligned}$$

where $v_{av} = (v_{ab} + v_{bc} + v_{ca})/3$.

The American National Standards Institute (ANSI) standard C84.1-1995 for Electric Power Systems and Equipment-Voltage Ratings (60 Hz), recommends that electrical supply systems should be designed and operated to limit the maximum voltage unbalance to 3% when measured at the electric-utility revenue meter under no-load conditions [75]. The International Electrotechnical Commission (IEC) recommends that the maximum voltage unbalance of electrical supply systems be limited to 2% [76].

As the proposed schemes introduce unbalanced voltage in the system during transients, it is very important to investigate the effect of these schemes on the voltage quality of the system. For this purpose, the LVUR are calculated for the **System-II** on generator terminals of G_1 and G_2 and presented in this thesis. Similar results are obtained for **System-I** studies as well.

Fixed Capacitor Compensation: The LVUR calculated at the generator terminals for the cases with no SSR mitigation in **System-II** (see Fig. 3.6) is shown in Fig. 3.25. As it can be seen from this figure, although the LVUR decreases toward zero after fault clearing, it starts to increase again because of the presence of the SSR.

Hybrid TCSC Scheme: Figure 3.26 shows the calculated LVUR with the hybrid TCSC compensation scheme is in service. The LVUR measured after clearing disturbance is found to be less than 1%.

Hybrid SSSC Scheme: Figure 3.27 shows the corresponding calculated LVUR with the hybrid SSSC compensation scheme in service. In this case as well, the LVUR measured after clearing disturbance is found to be less than 1%.

Comparing LVUR measured at the generator terminals G_1 and G_2 in the case of Figs. 3.25, 3.26, and, 3.27, it can be concluded that the proposed schemes do not deteriorate the voltage

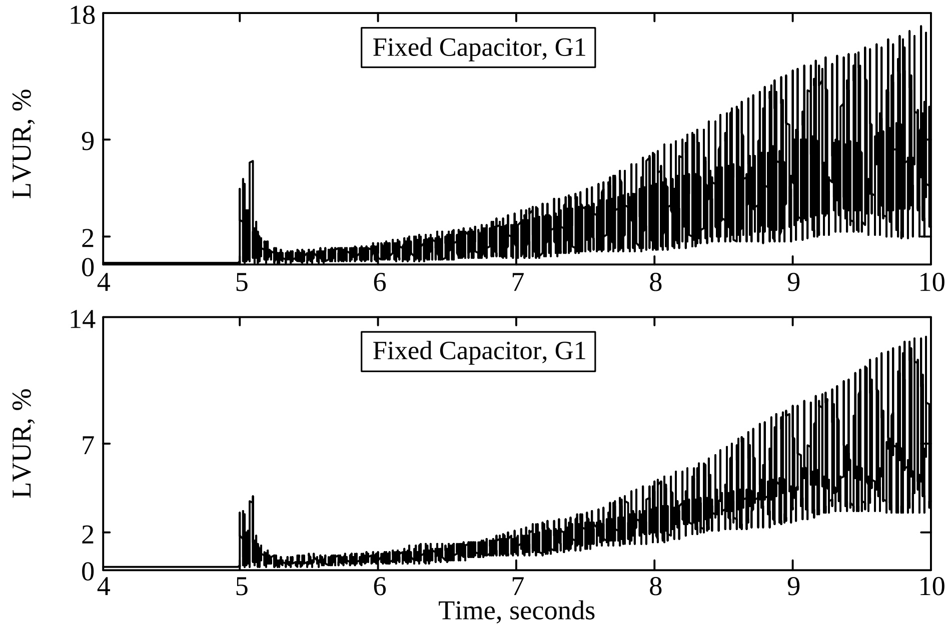

Figure 3.25: Fixed Capacitor: LVUR calculated at the generator terminals G_1 and G_2.

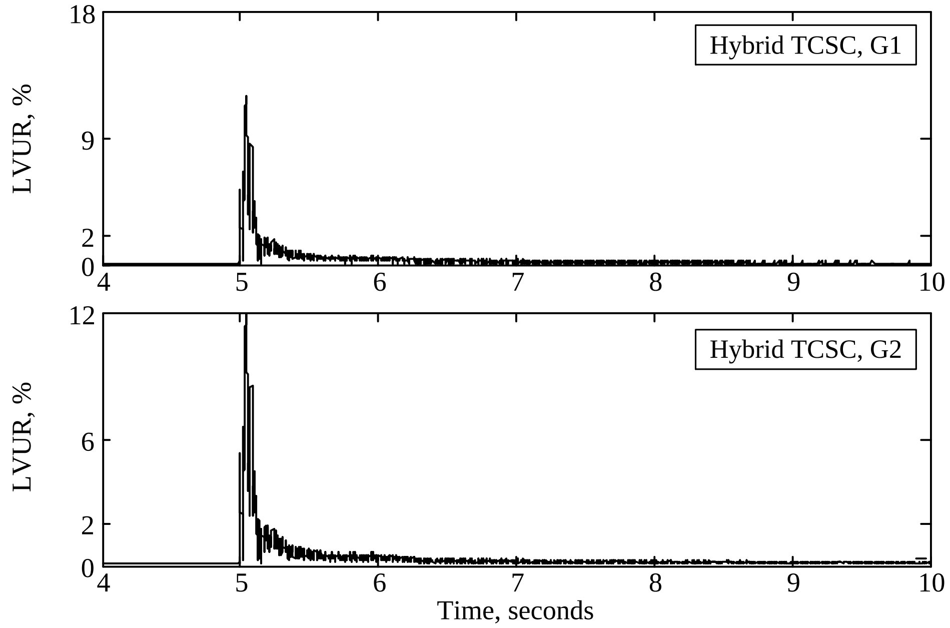

Figure 3.26: Hybrid TCSC: LVUR calculated at the generator terminals G_1 and G_2.

quality of the power system.

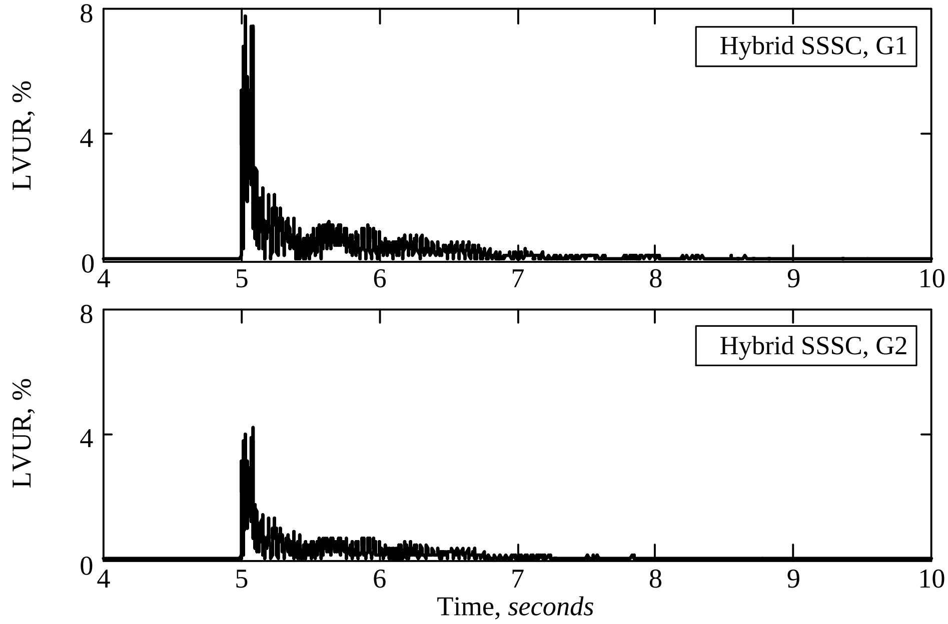

Figure 3.27: Hybrid SSSC: LVUR calculated at the generator terminals G_1 and G_2.

3.6 Summary

This chapter presented single-phase TCSC and SSSC based hybrid series compensation schemes, which have the inherent capability to damp subsynchronous resonance. The effectiveness of the presented schemes in damping SSR is demonstrated through detailed digital computer simulations on the IEEE first and second benchmark models for computer simulation of SSR. Furthermore, the Line Voltage Unbalance Rate (LVUR), which is a measure of the voltage unbalance induced in the system as the result of using the proposed schemes is found to be below the recommended limits of international standards.

The presented hybrid series capacitive compensation schemes are feasible, technically sound, and could be applied in industrial applications. The choice between using the thyristor or voltage sourced converter technologies should be based on economic and feasibility studies as well as on the expected dynamic performance from the hybrid compensation scheme. Based on the studies conducted in this chapter, it can be concluded that, for the same benchmark system, the minimum size of SSSC compensation required to obtain torsional damping in all the shaft sections of a turbine-generator ($X_{SSSC,min}$ in the hybrid SSSC scheme) is generally less than the corresponding $X_{TCSC,min}$ in the hybrid TCSC scheme.

Chapter 4

Damping of Power System Oscillations

4.1 Introduction

In an interconnected power system, electro-mechanical oscillations between synchronous generators are inherent physical phenomenon [30]. Some poorly damped or unstable low frequency oscillation modes may present between large generating systems connected via weak tie-lines. These low frequency modes have been found to involve groups of generators, or generating plants, on one side of the tie oscillating against groups of generators on the other side of the tie [77]. Such oscillations are referred to as inter-area oscillations. The lightly damped or unstable inter-area modes of rotor oscillations may get excited during disturbances leading to system instability [77, 78]. Inter-area oscillation frequency generally lies in the range of 0.1 to 0.8 Hz.

Another type of low frequency oscillation may be present between a generator connected to large system or between closely connected groups of generators. In such a scenario, oscillation frequency will be in the range of 0.5 $Hz - 2.0$ Hz. This type of oscillation is referred to as a local oscillation.

In this chapter, investigations are carried out to explore the capability of the proposed phase unbalanced hybrid compensation schemes in damping power system local and inter-area oscillations. In this context, studies are conducted on typical single and multi-area test systems.

4.2 Power Oscillations Damping - Local Modes

4.2.1 Test System Used for Simulation Studies

To demonstrate the effectiveness of the proposed scheme in low-frequency oscillation damping, the system shown in Fig. 4.1 is adopted as a test system. It consists of two nearby generating stations designated as $G1$ and $G2$, connected via transformers and short transmission lines to an infinite bus system through a series capacitor compensated transmission line. The system parameters are given in Appendix D.1.

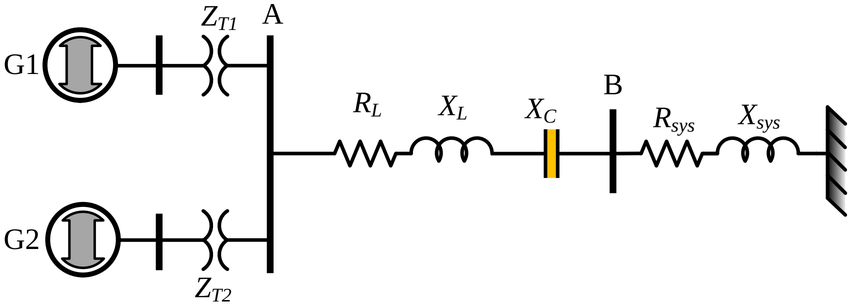

Figure 4.1: A schematic diagram of the test benchmark with fixed series capacitor compensation.

4.2.2 Time Domain Simulation Results

For time-domain simulation studies, the synchronous generators are represented in the $d-q-0$ reference frame. The generator rotor is represented by an equivalent lumped mass model. The transmission lines are modelled as a transposed line using series impedance representation. The infinite bus is represented by a constant amplitude sinusoidal voltage at the synchronous frequency. Circuit-breakers are represented as ideal switches which can open at current zero crossings. Dynamics of the generator excitation and governor systems are included in the simulation model.

The hybrid TCSC compensation scheme is used to validate its effectiveness in damping local oscillations. For this purpose, the scheme is assumed to be placed in the test benchmark between buses **A** and **B**, replacing the fixed series capacitive compensation. For the electromagnetic transient simulation initialization, the TCSC is inserted in the system at $t = 0.5$ *sec* and the disturbances are applied at $t = 5$ *sec*. The compensation degree is assumed to be 65%. In the case of hybrid compensation, $X_{C_c} = 32.5\%$ and $X_{TCSC} = 32.5\%$ of the total line inductive reactance X_L and a reference boost factor $kB = 1.75$ are assumed. The simulation studies are performed for two disturbances: 4.5 *cycles* (i) three-phase and (ii) double line-to-ground faults at bus A.

A. Three-phase Fault

Figure 4.2 shows the generator electrical power and rotor angle time responses following a 4.5 *cycles*, three-phase fault at bus **A**. Figure 4.3 shows the TCSC boost factor and thyristor firing angle time responses of the test system for same disturbance. From the responses in Fig. 4.2, it can be seen that the fixed capacitor compensated system depicts poorly damped local oscillations, whereas the hybrid TCSC scheme effectively damps the oscillations within 2 *seconds*.

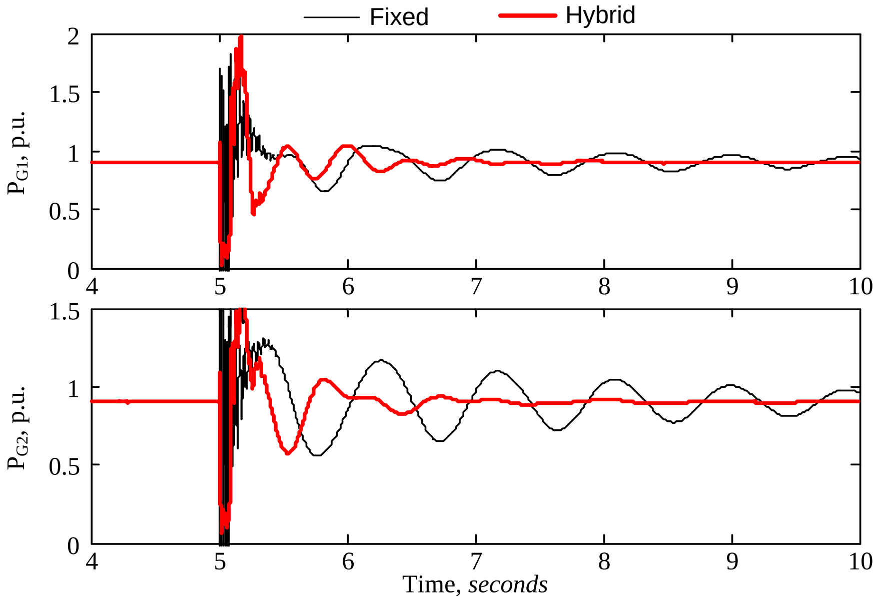

(a) Generator electrical powers

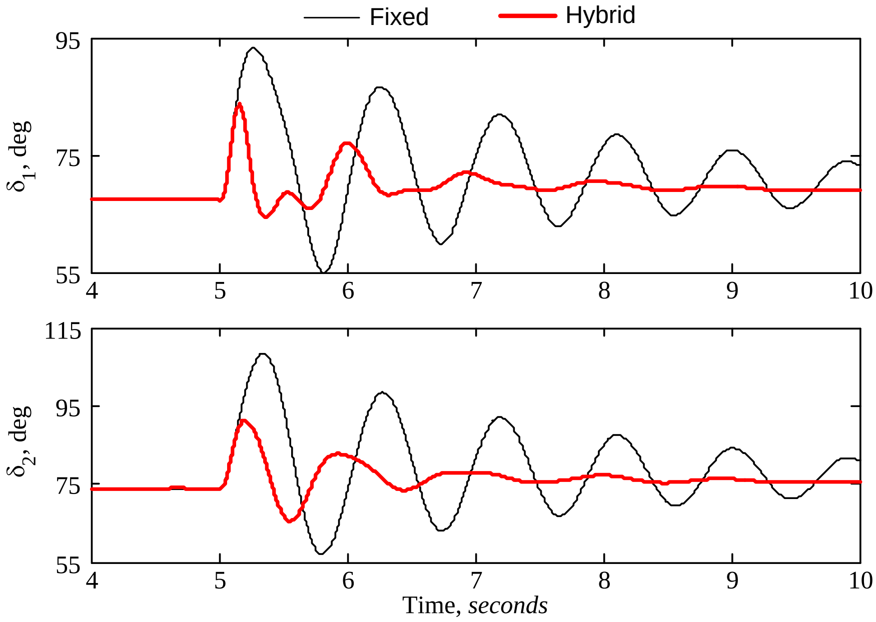

(b) Generator rotor-angles

Figure 4.2: Generator power and rotor-angle time responses for a 4.5 *cycle* three-phase fault at bus A.

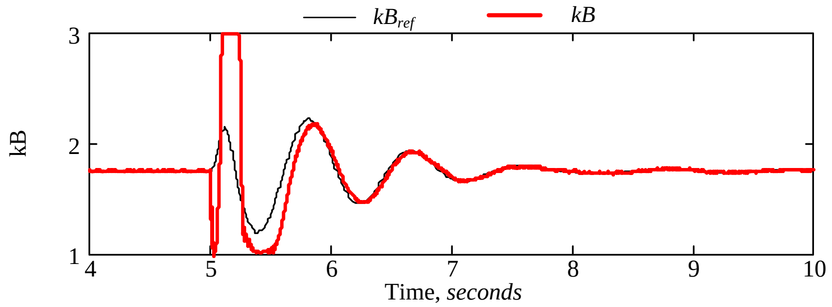

(a) TCSC boost factor

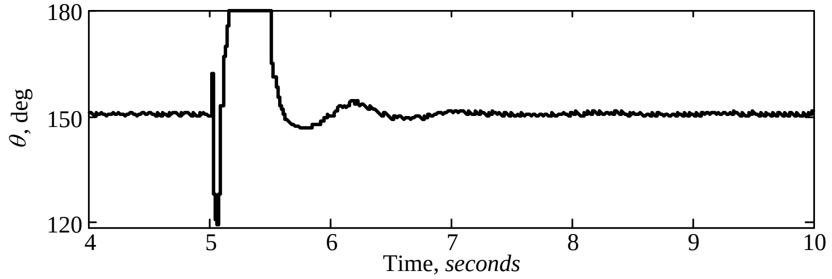

(b) Thyristor firing angle (degree)

Figure 4.3: TCSC boost factor and thyristor firing angle for three-phase fault at bus A.

B. Double Line-to-Ground Fault

Figure 4.4 shows the generator rotor angle time responses of the test system following a 4.5 *cycles* double line-to-ground (faulted phases: b and c) fault at bus **A**. The results shown

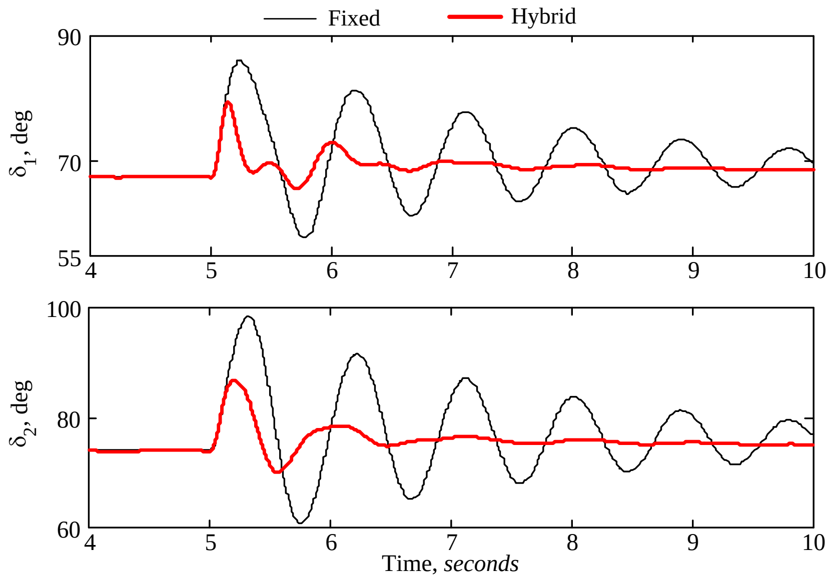

Figure 4.4: Generator electrical power and load angle time responses during and after clearing a 4.5 *cycle*, double line-to-ground fault at bus **A** (faulted phases b and c).

in this figure demonstrate the capability of the hybrid TCSC scheme in providing very good damping to the system oscillations during unsymmetrical faults.

The comparison between the responses of the fixed series compensation and the hybrid TCSC compensation scheme in Figs. 4.2 and 4.4 shows the positive contribution of the proposed hybrid scheme to the damping of the local power oscillations. As can be seen from these figures, the power swing damping controller reduces the first swing and damps the subsequent swings.

4.3 Inter-Area Oscillations Damping

As explained before, inter-area oscillations are associated with group of generators (or plants) oscillating against another group of generators (or plants) in an interconnected systems. These types of oscillations are far more complex to study and to damp. Generally, a detailed representation of the entire interconnected system is required to study inter-area modes [79]. For this reason, a complete power system model that consists of three generating areas interconnected to each other is used for inter-area oscillation damping studies.

4.3.1 Multi-Area Test System Used for Simulation Studies

The three-area, six-machine test system, shown in Fig. 4.5, is used for the inter-area oscillation damping studies. It consists of two machines in each area: G_1 and G_2 in area 1, G_3 and G_4 in area 2, and, G_5 and G_6 in area 3 respectively. Although this is a test system, it serves well to illustrate the concept, which remains the same for large systems. Area 2 is connected to Areas 1 and 3 through a 400 *km* long double-circuit transmission line. This tie-line is 50% series capacitor compensated for the purpose of increasing the power exchange through it. Shunt capacitors are installed at buses 7, 9 and 14 to support the voltage between 1 ± 0.03 *p.u.* of rated value. The electromagnetic transient simulation software EMTP-RV$^{\text{TM}}$is used to simulate the test systems.

A. Small Signal Analysis

A linearized model of a power system (around a certain operating point) is used for the small signal stability analysis. It gives in-depth information on the present modes of oscillations and corresponding damping in the system [30]. In this thesis, the rotor angle oscillation modes for the test system are obtained using small signal analysis tool available on the DSAtools$^{\text{TM},1}$ software package. The eigenvalue analysis results are given in Table

---

[1] DSATools is the registered trademark of Powertech Labs Inc, Surrey, BC, Canada

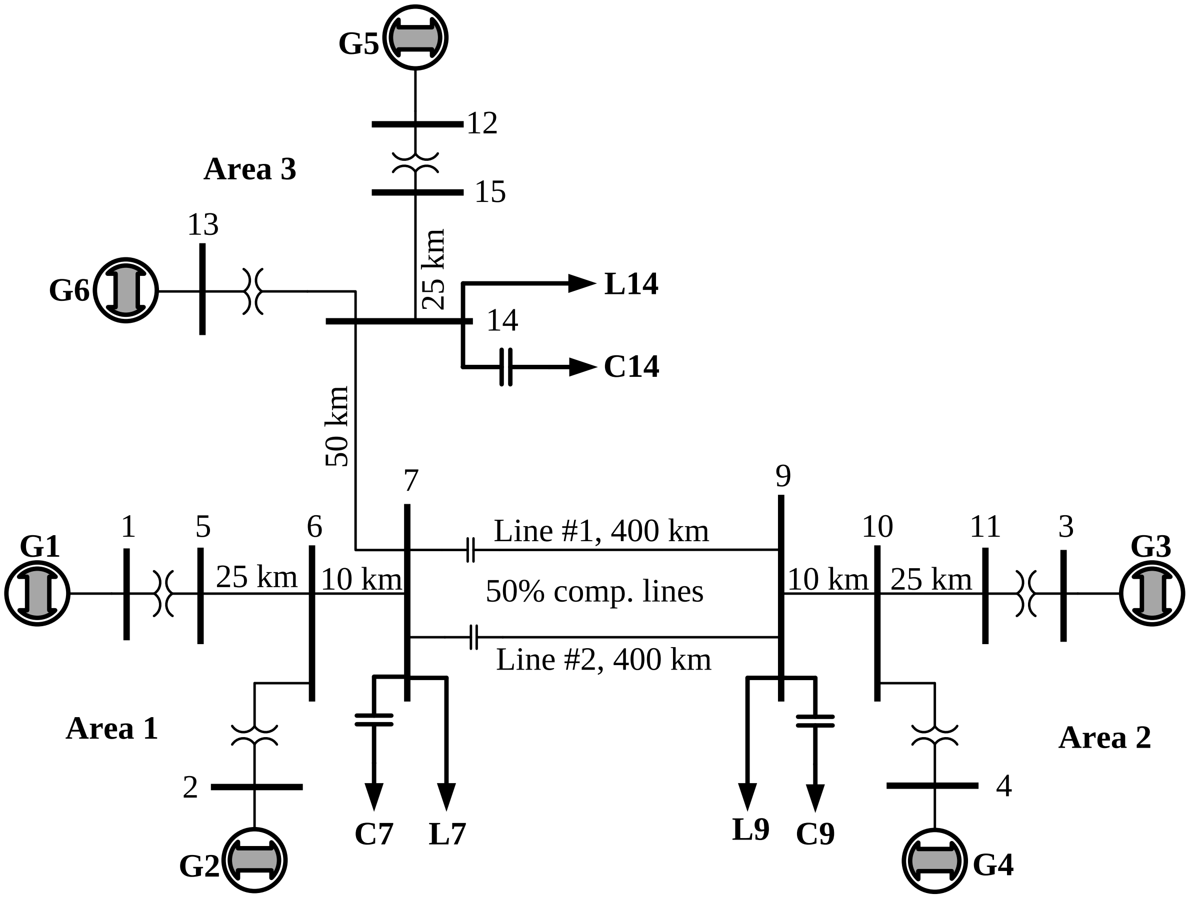

Figure 4.5: A schematic diagram of the 3-area test benchmark with fixed series capacitor compensations.

4.1. There are five different oscillations modes: three local modes, one in each area, and two inter-area modes. The inter-area Mode 1 is characterized by having a slightly higher frequency (0.78 Hz) than Mode 2 (0.46 Hz).

The inter-area oscillations mode shapes and participation factors are shown in Fig. 4.6. The mode shape reveals the relative participation of the state variables when a particular mode is excited. In this case, Mode 1 consists of generators of area 1 (G_1 and G_2) swinging against those of Area 3 (G_5 and G_6), while the Mode 2 consists of generators of Area 2 (G_3 and G_4) swinging against those of Areas 1 and 3 (G_1, G_2, G_5, and G_6). Similarly, the relative participation of the particular generator on particular oscillatory modes can be obtained using the participation factor. It can be observed from the Fig. 4.6(b) that the generator that participates highest on ‘Mode 1’ is G_5 and on ‘Mode 2’ is G_3 respectively. All modes are stable, with the eigenvalues lying on the left hand-side of the s-plane. The inter-area oscillation Mode 1 has a poor damping ratio, and the oscillations will take long time to settle if excited.

Table 4.1: Rotor angle modes of the three-area test system.

Mode type	Real part (σ)	Imaginary part (ω_d)	Frequency (Hz)	Damping ratio ($\zeta, \%$)
Local	-0.5840	7.6616	1.2194	7.60
	-0.5767	6.8333	1.0876	8.41
	-0.7099	6.6681	1.0613	10.59
Inter-area	-0.1730	4.9093	**0.7813**	3.52
	-0.8353	2.9503	**0.4696**	27.24

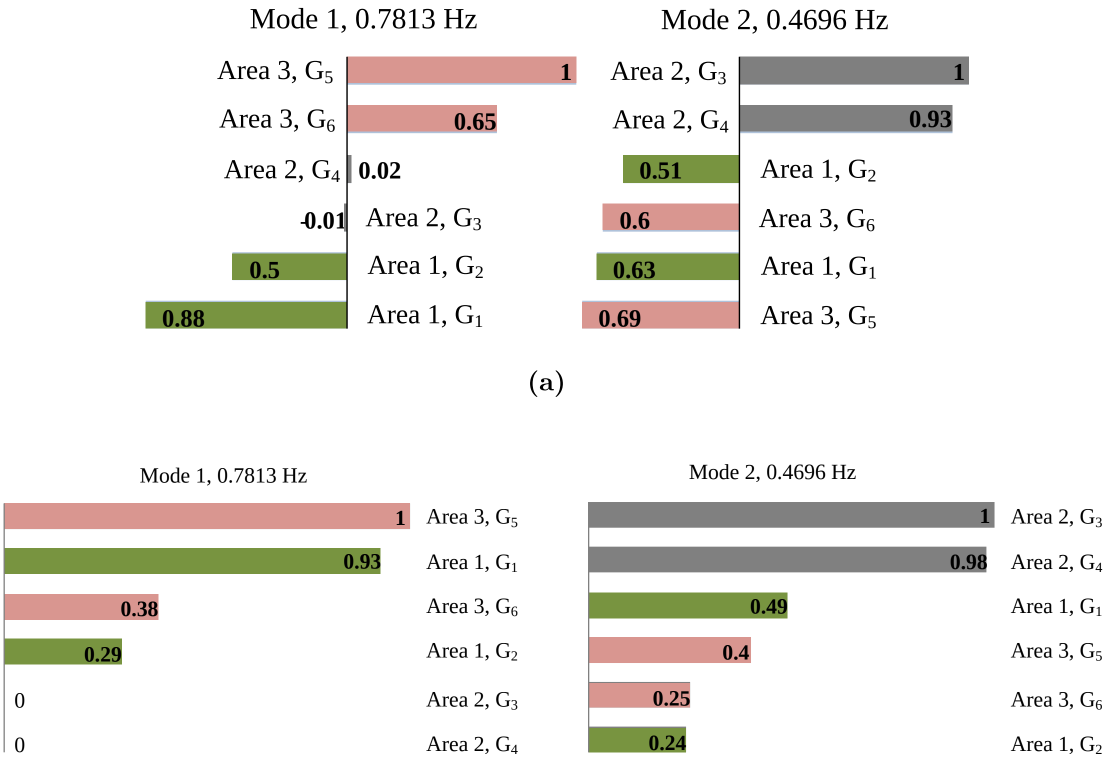

(a)

(b)

Figure 4.6: Small signal analysis of the three-area test system; (a) Mode shapes and (b) Participation factors.

B. Case Studies

Five different contingency cases have been studied to validate the effectiveness of the hybrid compensation schemes on damping of inter-area oscillations. These contingency cases, listed in Table 4.2, cover a wide range of power system operating condition and various disturbance scenarios.

Table 4.2: Inter-area oscillation damping case studies.

Approximate power flow on line 7-9	Disturbance description	Disturbance type
415 MW	3 cycle, three-phase fault at bus 7	***A***
415 MW	3 cycle, 2-phase-to-ground (a,b - ground) fault at bus 7	***B***
220 MW	3 cycle, three-phase fault at bus 7	***C***
-180 MW	3 cycle, three-phase fault at bus 7	***D***
415 MW	Line-2 is out of service at $t = 5.0sec$	***E***

C. The Supplementary Damping Controller

As the real power flow in the transmission line is proportional to the inverse of the total line reactance, inter-area oscillation damping can be achieved by properly modulating the TCSC/SSSC impedance [80]. For this purpose, supplementary controllers are used to modulate the TCSC and SSSC impedances. The operation of the TCSC and SSSC are controlled using the controller structure shown in Fig. 4.7. The detailed descriptions of the TCSC and the SSSC controllers are discussed in Sections 2.3.2 and 2.4.2 respectively. The supplementary control, U_s, for damping inter-area oscillations is shown in Fig. 4.7. The proportional-integral controllers are used to control the steady-state TCSC and SSSC impedances at the desired levels.

An m stage lead-lag compensation-based supplementary controller, as shown in Fig. 4.8, is adopted for modulating the apparent TCSC/SSSC reactance. The supplementary controller input (stabilizing) signals could be local (e.g. real power flows) or remote (e.g. load angles or speed deviations of remote generators). Local signals are generally preferred over remote signals, as they are more reliable since they do not depend on communications. The available local signals are studied using Prony analysis to select proper inputs to the supplementary controller. Prony analysis decomposes a signal into series of damped complex exponentials or sinusoids and is very helpful to identify the most dominant modes of oscillations present in the signal [81]. Prony analysis of the rotor angle oscillations of area 2 generators reveals that the generators participate in both Mode 1 and Mode 2 oscillations. It is obvious that to damp-out multi-mode oscillations, appropriate supplementary signal containing both modes of oscillation is necessary. For this reason, the local input to the damping controller is chosen as a combination of tie-line power flows of bus 7-9 and bus 15-7 measured near bus 7. The

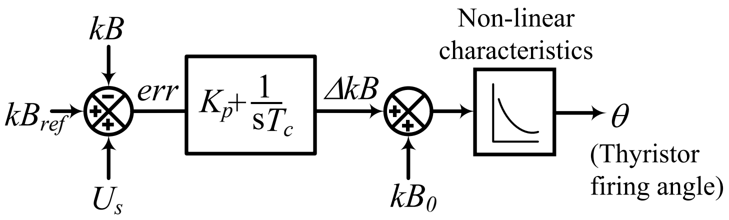

(a) TCSC control

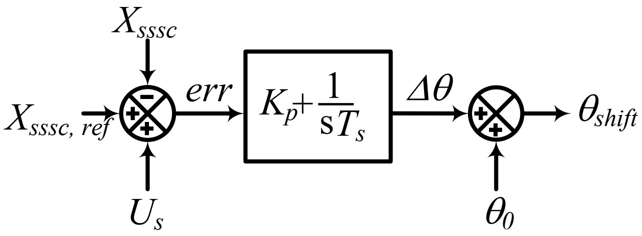

(b) SSSC control

Figure 4.7: TCSC and SSSC steady-state control.

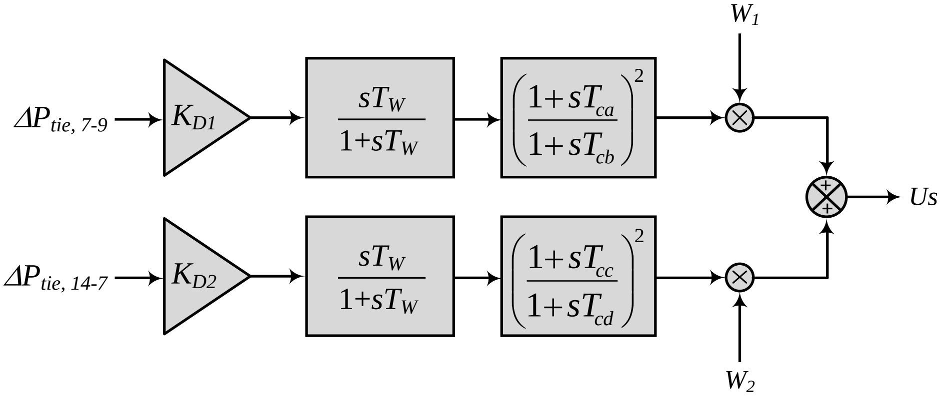

Figure 4.8: Lead-lag supplementary controller used for the studies.

aggregate damping signal is obtained as:.

$$U_s = W_1 \cdot U_{s,1} \cdot \Delta P_{tie,7-9} + W_2 \cdot U_{s,2} \Delta P_{tie,14-7}. \tag{4.1}$$

The weighting values W_1 and W_2 are chosen as inversely proportional to their normalized dominant mode damping ratio obtained from Prony analysis ($W_1 = 1.15, W_2 = 1$). The damping signal thus obtained from the controller is then added to the reference boost factor value (kB_{ref0}) or reference SSSC reactance ($X_{SSSC,ref}$) and new modulated impedance reference is generated.

D. Controller Parameters Tuning

It is worth noting here that due to the inherently unbalanced nature of the hybrid compensation schemes during transients, the design of their supplemental controllers using classical linear control techniques would be very difficult, if not virtually impossible, to achieve. Moreover, these techniques are not valid for investigating large disturbances. Hence a multiple run approach is adopted for finding appropriate gain K_D and time constants T_{ca}, T_{cb}, T_{cc} and T_{cd}. The initial values of the parameters that give satisfactory response are obtained using trial-and-error approach. The fine-tuning of the parameters were performed by carrying out strategic incremental search of variables to minimize a cost function defined as:

$$F_{obj}(T_{ca,cb,cc,cd}) = \int_{T_C}^{T_F} \left\{ \left(\frac{\Delta P_{tie,7-9}}{P_{tie0,7-9}} \right)^2 + \left(\frac{\Delta P_{tie,14-7}}{P_{tie0,14-7}} \right)^2 \right\} dt. \tag{4.2}$$

where T_C is the time of fault clearing, T_F is the final simulation time and $P_{tie0,7-9}$ and $P_{tie0,15-7}$ are the tie line power flow during steady state from bus $7-9$ and bus $14-7$ respectively. The controller parameters obtained after the several transient simulation runs which gave satisfactory response to wide range of operation of the system are given in Appendix D.2.2.

4.3.2 Time Domain Simulation Results

For time-domain simulation studies, the synchronous generators are represented in the $d-q-0$ reference frame. The transmission lines are modelled as a constant parameter, continuously transposed line model available in EMTP-RV$^{\text{TM}}$library. Circuit-breakers are represented as ideal switches which can open at current zero crossings. Dynamics of the generator excitation are included in the simulation. The machine and excitation parameters, operating condition of the test system, and loads used for the studies are presented in Appendix D.2.

A. The Hybrid TCSC Scheme

This section demonstrates the capability of the proposed TCSC based hybrid series compensation scheme in damping inter-area oscillations. For this purpose, the scheme is assumed to be installed in the test system of Fig. 4.5 near bus 7 between buses 7 and 9, replacing the fixed series capacitive compensation of both lines. The TCSC contribution in the hybrid compensated phase is 0.25 *p.u.* of the total capacitive compensation ($X_{TCSC} = 0.25X_C$, $X_{C_c} = 0.75X_C$). For the EMTP-RV initialization, the hybrid TCSC scheme is inserted in the system at $t = 0.5$ *sec* and the disturbances are applied at $t = 5$ *sec*. Moreover, in the following figures illustrating the system time responses, "*Fixed*" refers to the system performance with fixed capacitor compensation (base case of Fig. 4.5).

A.1. Case Study A

The operating condition in **Case A** corresponds to 415 *MW* tie-line power flow from bus 7 to bus 9. This case is considered as a base operating case for rest of the contingency case studies. The lead-lag supplementary controller parameters are tuned for this operating condition using multiple time-domain simulation runs with the objective of minimizing the deviation in tie-line power flows (Eq. 4.2), and, the parameter values are given in Appendix D.2.2.

The time responses of the TCSC boost factor and the firing angle θ are shown in Fig. 4.9 for disturbance **Case A**. The time responses of G_3, G_4 (area 2) and G_5 (area 3) load angles, measured with respect to G_1 load angle (area 1) for the same disturbance are shown in Fig. 4.10. Figure 4.11 shows the tie-line (7-9, line 1) power flow time responses of the

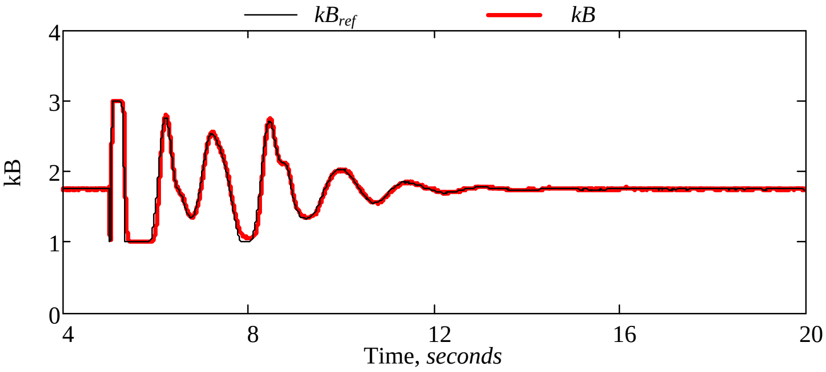

(a) Boost factor

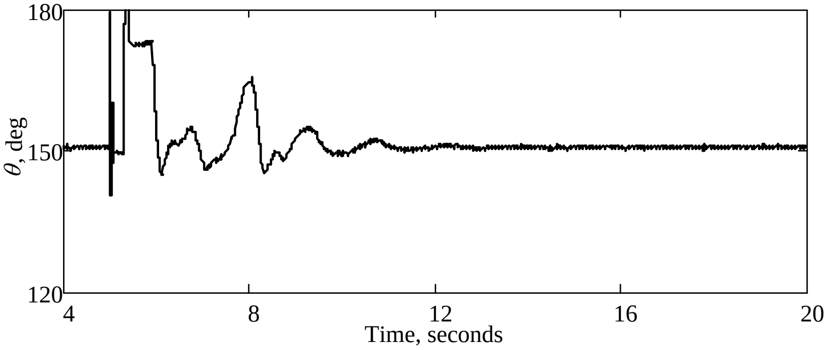

(b) Thyristor firing angle

Figure 4.9: Hybrid TCSC: TCSC boost factor and thyristor firing angle time responses for disturbance **Case A**.

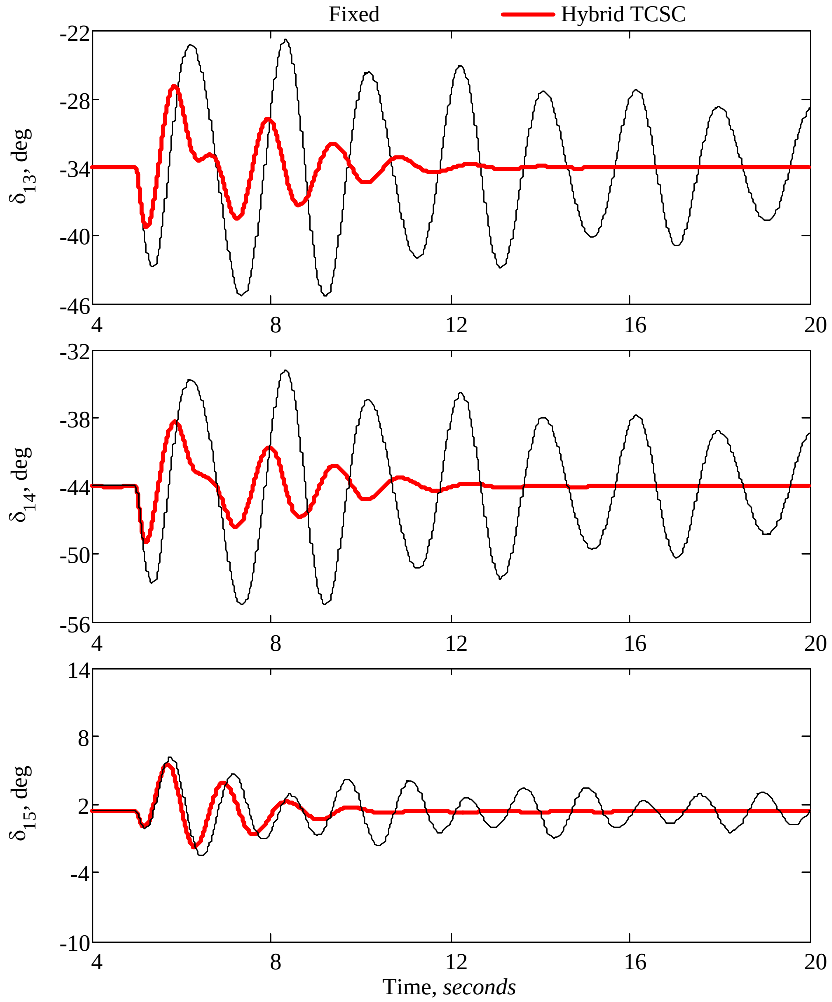

Figure 4.10: Hybrid TCSC: relative generator rotor angle time responses for disturbance case **A**.

test system for same disturbance. From the response plots in Fig. 4.10, it is evident that the system with fixed capacitor compensation exhibits poor damping and takes longer than 20 *sec* to settle down the oscillations, whereas in the case of the hybrid TCSC scheme, it can be observed that the amplitude of the oscillations has been reduced, and also the oscillations settle down within $8-10$ *sec* after the disturbance. The line compensating reactance increase just after clearing the fault increases the tie-line transfer capacity between the two areas that results in reducing the generator first swings.

Figure 4.12 illustrates the three-phase voltages, V_{X-Y}, and voltage across TCSC in the hybrid TCSC scheme of Fig. 4.5 during and after disturbance **Case A**. The system phase unbalance during the disturbance is clearly noticeable here again, especially in phase *c* where the TCSC is installed.

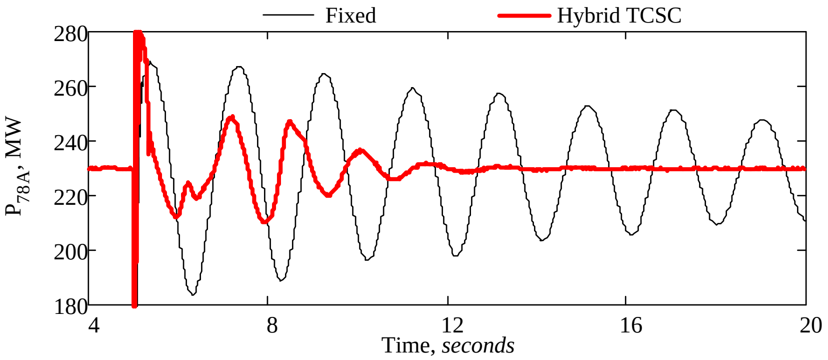

Figure 4.11: Hybrid TCSC: Tie line (line 1) power flow time responses for disturbance **Case A**.

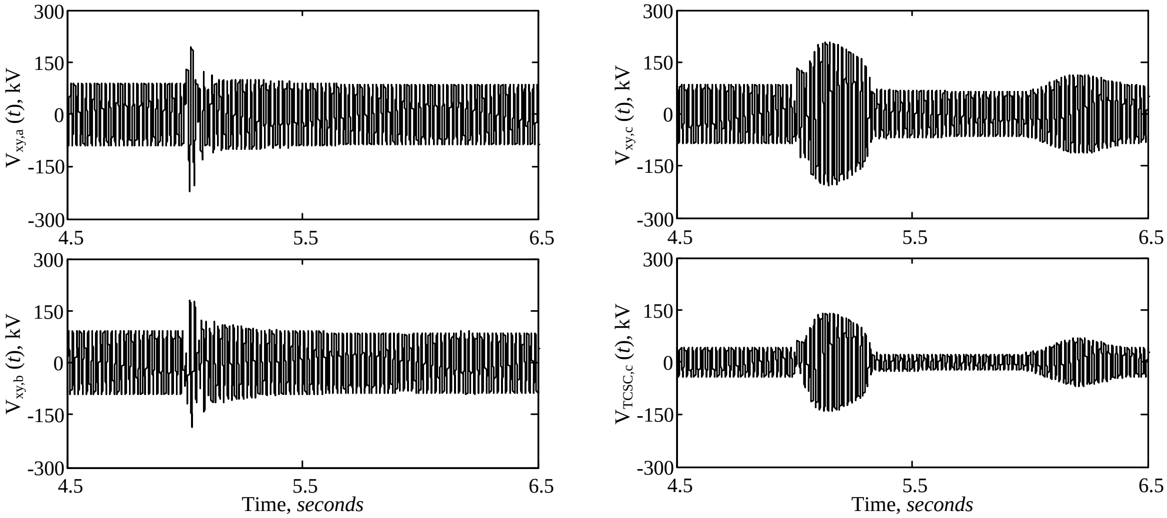

Figure 4.12: Phase voltages, V_{X-Y}, and voltage across TCSC in the hybrid TCSC scheme of Fig. 4.5 during and after disturbance **Case A**.

A.2. Case Study B

Case study **B** is very similar to test **Case A**, except that the disturbance is a double line-to-ground fault at bus 7. This case is used to study the performance of the proposed schemes during unsymmetrical faults.

Figure 4.13 shows the tie-line (7-9, line 1) power flow time responses of the test benchmark for disturbance case A. The time responses of G_3, G_4 (area 2) and G_5 (area 3) load angles, measured with respect to G_1 load angle (area 1) for the same disturbance, are shown respectively in Fig. 4.14. From the response plots in Fig. 4.14, it is evident that the proposed compensation scheme is able to suppress first swing and settles the subsequent swings within $8 - 10$ *sec* after the clearance of the disturbance.

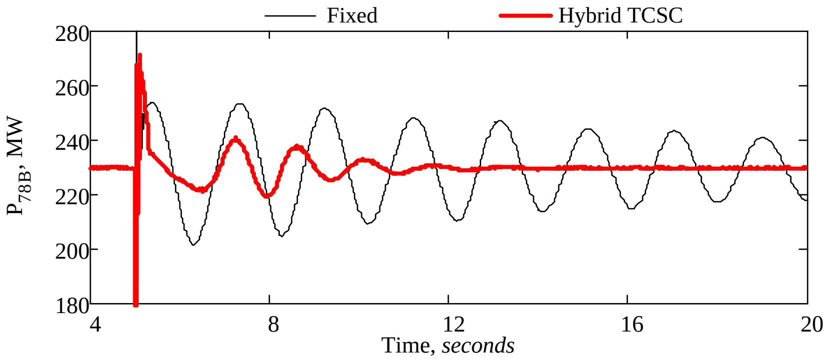

Figure 4.13: Hybrid TCSC: Tie line (line 1) power flow time responses for disturbance **Case B**.

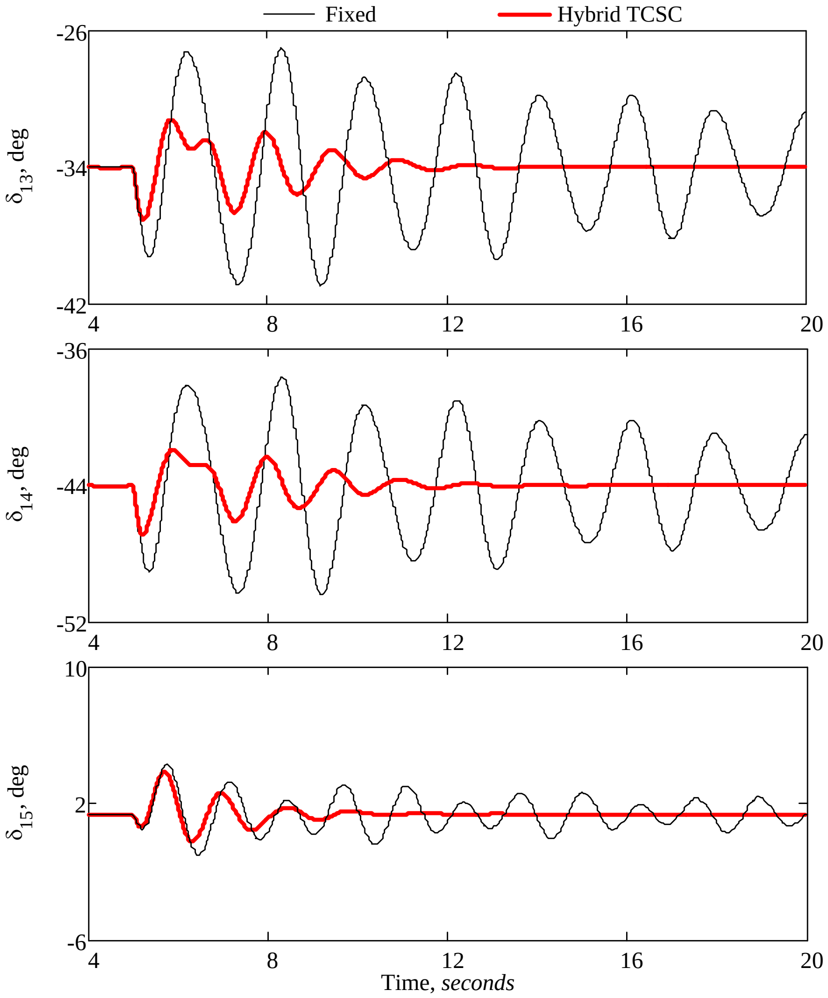

Figure 4.14: Hybrid TCSC: relative generator rotor angle time responses for disturbance **Case B**.

A.3. Case Study C

Case study **C** represents 220 MW tie-line power flow from bus 7 to bus 9. This operating condition is achieved by decreasing the load at bus 9 and increasing the load at bus 7. This case is used to study performance of proposed schemes at lower tie-line power flow conditions.

Figure 4.15 shows the time responses of the relative generator rotor angles $G_1 - G_3$, $G_1 - G_4$ and $G_1 - G_5$ for the disturbance **Case C**. It is evident from the responses that the hybrid TCSC compensation scheme is very effective in damping inter-area oscillation at light loading conditions.

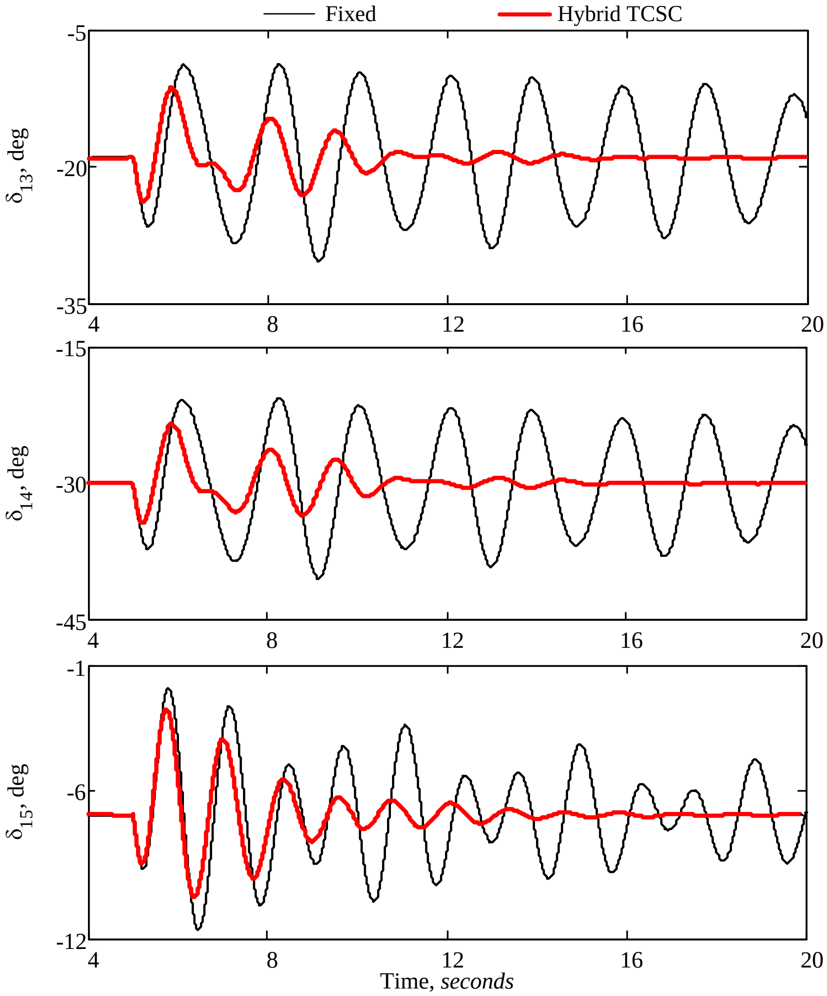

Figure 4.15: Hybrid TCSC: relative generator rotor angle time responses for **Case C**.

A.4. Case Study D

Case study **D** represents a 180 MW reverse tie-line power flow (i.e. from bus 9 to bus 7). This operating condition is achieved by decreasing the load at bus 9 and increasing the load at bus 7. This case is used to study the performance of proposed schemes for a drastic change in operating condition.

Figure 4.16 shows the time responses of the relative generator rotor angles $G_1 - G_3$, $G_1 - G_4$ and $G_1 - G_5$ for the disturbance **Case D**. It is evident from the responses that the proposed hybrid compensation method is very effective in damping inter-area oscillation, even at reverse power flow situations.

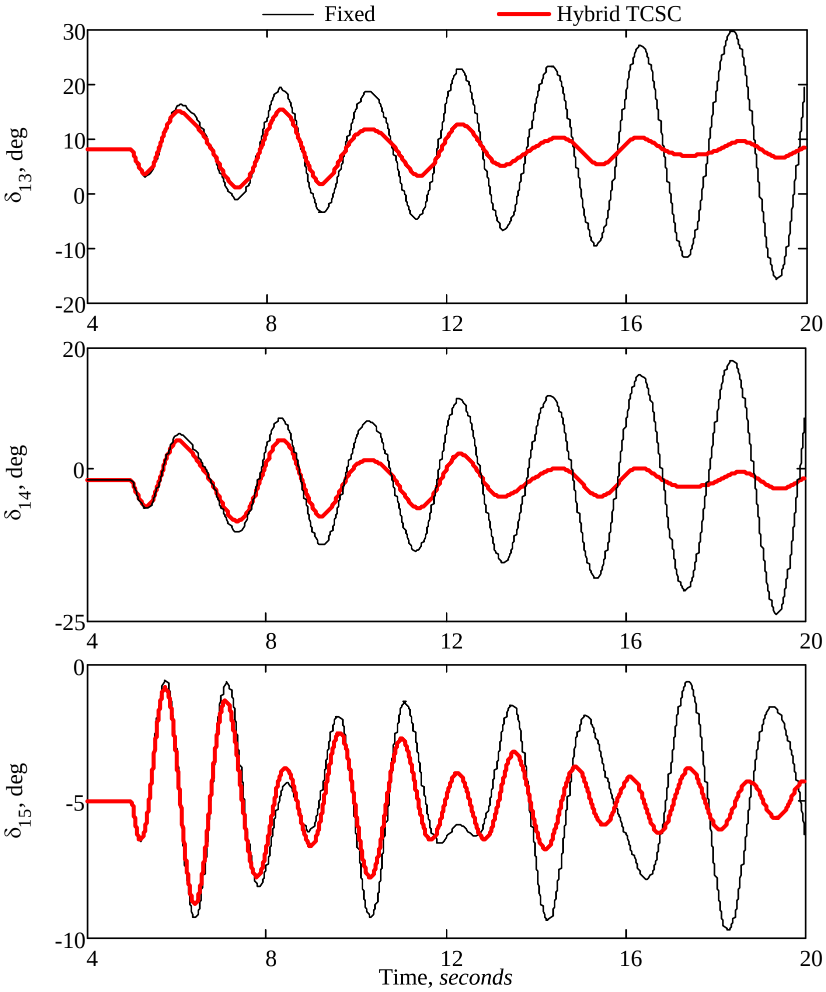

Figure 4.16: Hybrid TCSC: relative generator rotor angle time responses for disturbance **Case D**.

A.5. Case Study E

Case study **E** is similar to **Case A** in terms of operating condition. The disturbance in this case is considered as the tie-line 2 between buses 7 and 9 is opened at $t = 5$ *sec*. The disruption of the tie-line 2 causes severe disturbance in the system and also changes the power flow though line 1. This case is used to study the performance of hybrid TCSC scheme for very severe disturbance followed by increase in the tie-line power flow.

Figure 4.17 shows the time responses of the relative generator rotor angles $G_1 - G_3$, $G_1 - G_4$ and $G_1 - G_5$ for the disturbance **Case D**. It can be observed from the response in Fig. 4.17 that the fixed capacitor compensated system exhibits poorly damped inter-area oscillation. In the case of the hybrid TCSC compensation scheme, the first swings have less magnitude and the oscillations settle down within $8-10$ *sec* following the disturbance. This study demonstrates the capability of hybrid compensation schemes in damping inter-area oscillation, even during severe disturbances.

A comparison of the responses of the fixed series capacitor compensation to the hybrid TCSC compensation scheme in Figs. 4.10 through 4.17, shows very clearly the positive contribution of the proposed hybrid TCSC scheme to the damping of the inter-area oscillations.

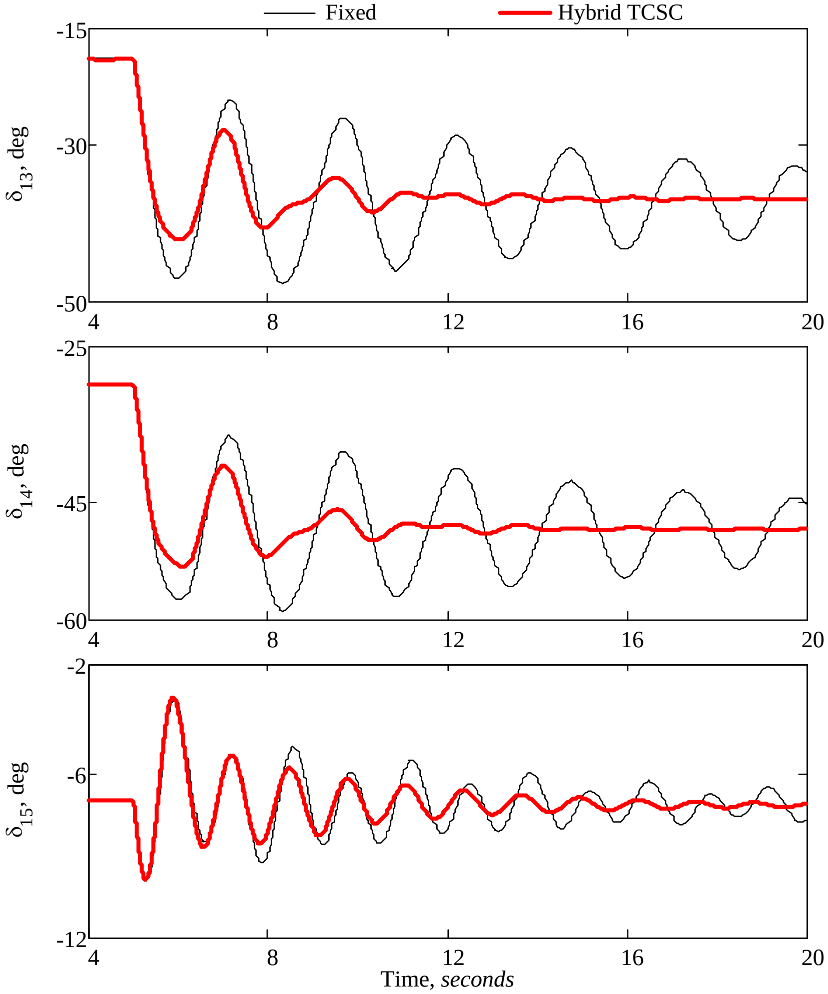

Figure 4.17: Hybrid TCSC: relative generator rotor angle time responses for disturbance **Case E**.

As can be seen from the relative rotor angle responses in Figs. 4.10 - 4.17, the inter-area oscillation damping controller reduces the first swing and effectively damps the subsequent swings.

B. The Hybrid SSSC Scheme

This section evaluates the capability of the single-phase SSSC-based hybrid series compensation scheme in damping inter-area oscillations. Similar to the case of hybrid TCSC scheme, the hybrid SSSC scheme is assumed to be installed in the test system near bus 7 between buses 7 and 9 replacing the fixed series capacitive compensation of both lines. The SSSC contribution in the hybrid compensated phase is 0.25 $p.u.$ of the total capacitive compensation ($X_{SSSC} = 0.25X_C$, $X_{C_c} = 0.75X_C$). For the electromagnetic transient software initialization, the SSSC is inserted in the system at $t = 1$ sec and the disturbances are applied at $t = 5$ sec.

B.1. Case Study A

The operating condition in **Case A** corresponds to a 415 MW tie-line power flow from bus 7 to bus 9. This test case is considered as a base operating case for rest of the contingency cases. The lead-lag supplementary controller parameters are tuned for this operating condition and given in Appendix D.2.2.

Figure 4.18 shows the tie-line (7-9, line 1) power flow time responses of the test system for disturbance **Case A**. The time responses of G_3, G_4 (area 2) and G_5 (area 3) load angles, measured with respect to G_1 load angle (area 1) for the same disturbance, are shown in Fig. 4.19. The SSSC injected reactance and DC side capacitor voltage for the case of Fig. 4.18 are shown in Figure 4.20. The sudden jump in SSSC reactance demand causes

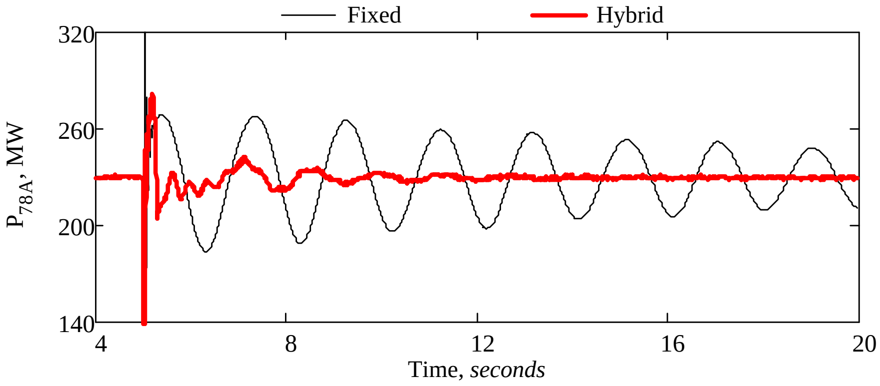

Figure 4.18: Hybrid SSSC: Tie line (line 1) power flow time responses for disturbance **Case A**.

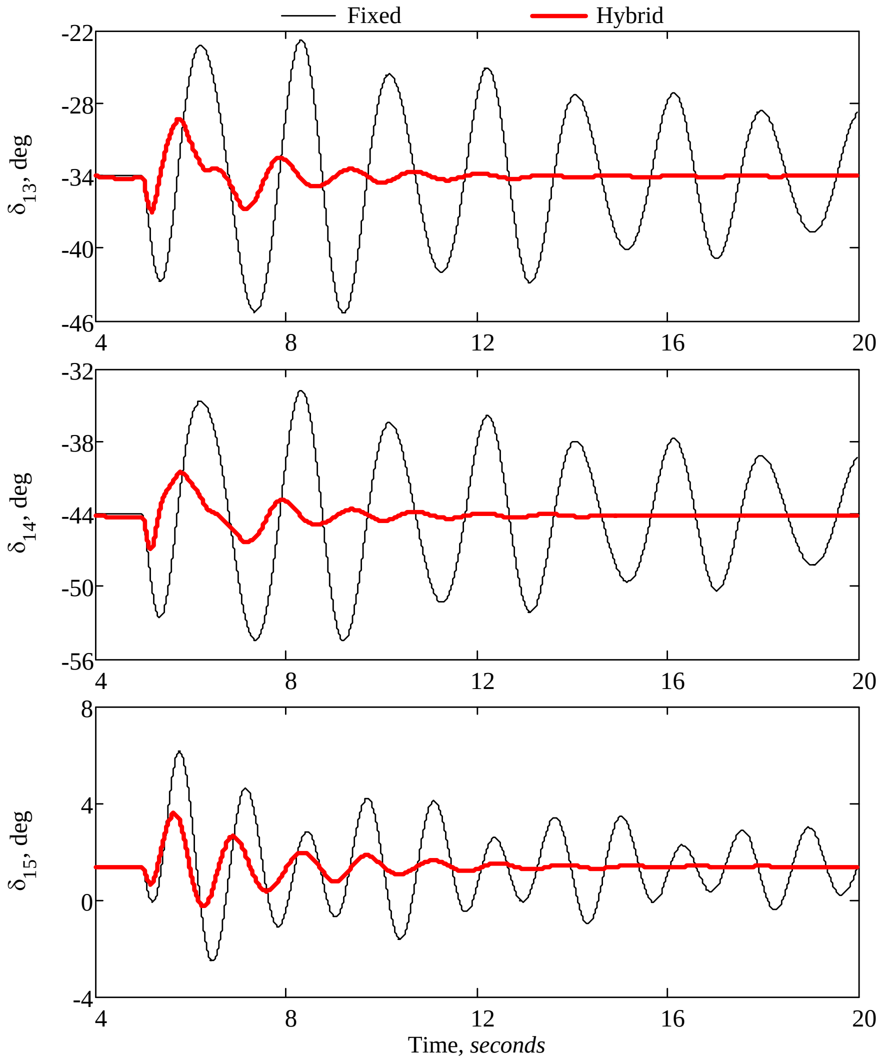

Figure 4.19: Hybrid SSSC: relative generator rotor angle time responses for disturbance **Case A**.

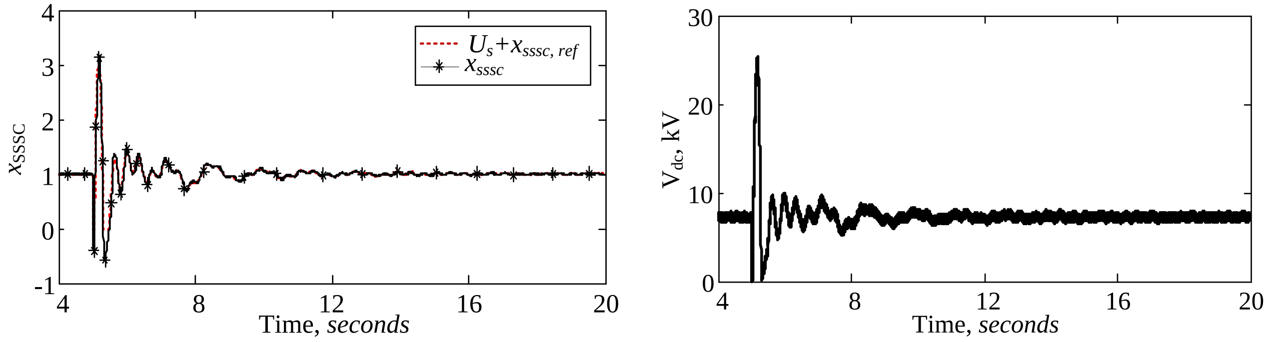

(a) SSSC injected reactance

(b) DC capacitor voltage

Figure 4.20: SSSC series injected reactance and DC capacitor voltage plots for disturbance **Case A**.

rapid charging of the DC side capacitor. Charging of capacitor increases the DC side voltage and consequently the injected series voltage to the system increases. This sudden increase in capacitive reactance causes increase in tie-line coupling, which helps in reducing the first swing of generator load angles as it can be seen from Fig. 4.19.

Figure 4.21 illustrates the three-phase voltages, V_{X-Y} and injected SSSC voltage across the hybrid SSSC scheme of Fig. 4.5 for disturbance **Case A**. The system phase unbalance during the disturbance is clearly noticeable here again, especially in phase c where the SSSC is installed.

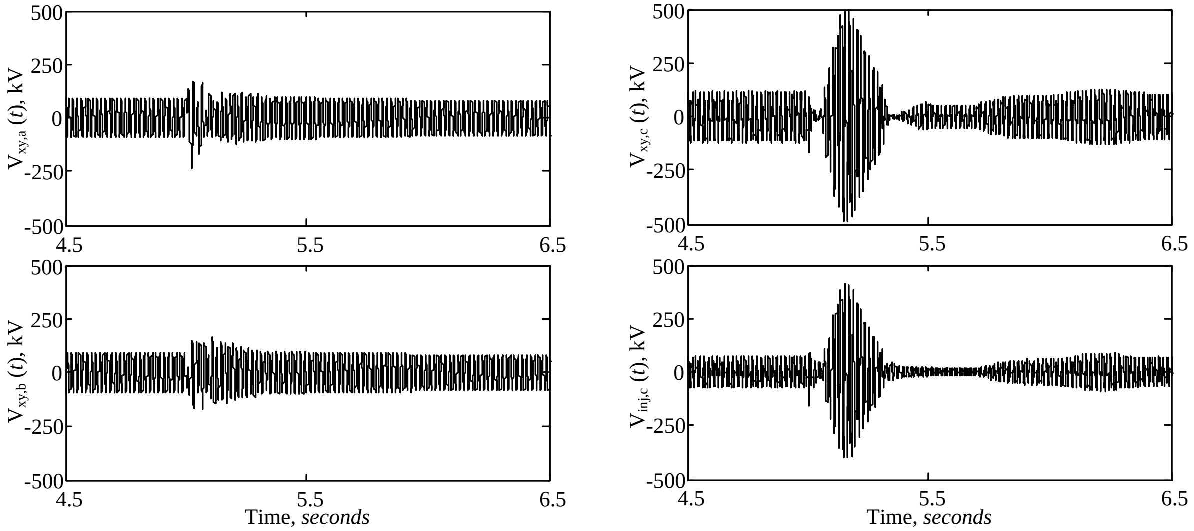

Figure 4.21: Phase voltages, V_{X-Y}, and injected series voltage by SSSC across hybrid SSSC scheme of Fig. 4.5 during and after disturbance **Case A**.

From the response plots in Fig. 4.19, it is evident that the hybrid SSSC compensation scheme is very effective in limiting first swing and damps the subsequent oscillations within $8-10$ *sec* following the disturbance. These results clearly demonstrate the effectiveness of the proposed hybrid SSSC compensation scheme in damping inter-area oscillations.

B.2. Case Study B

This test case is used to evaluate the performance of the hybrid SSSC compensation scheme in damping inter-area oscillations during unsymmetrical faults. Figure 4.22 shows the tie-line (7-9, line 1) power flow and Fig. 4.23 shows the relative generator rotor angle time responses of the test system for disturbance **Case B**. These results clearly demonstrate the effectiveness of the proposed hybrid SSSC compensation scheme in damping inter-area oscillation for unsymmetrical faults.

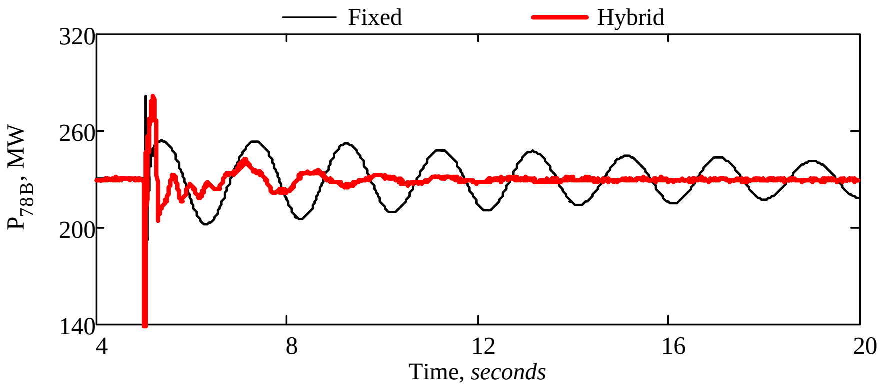

Figure 4.22: Hybrid SSSC: Tie line (line 1) power flow time responses for disturbance **Case B**.

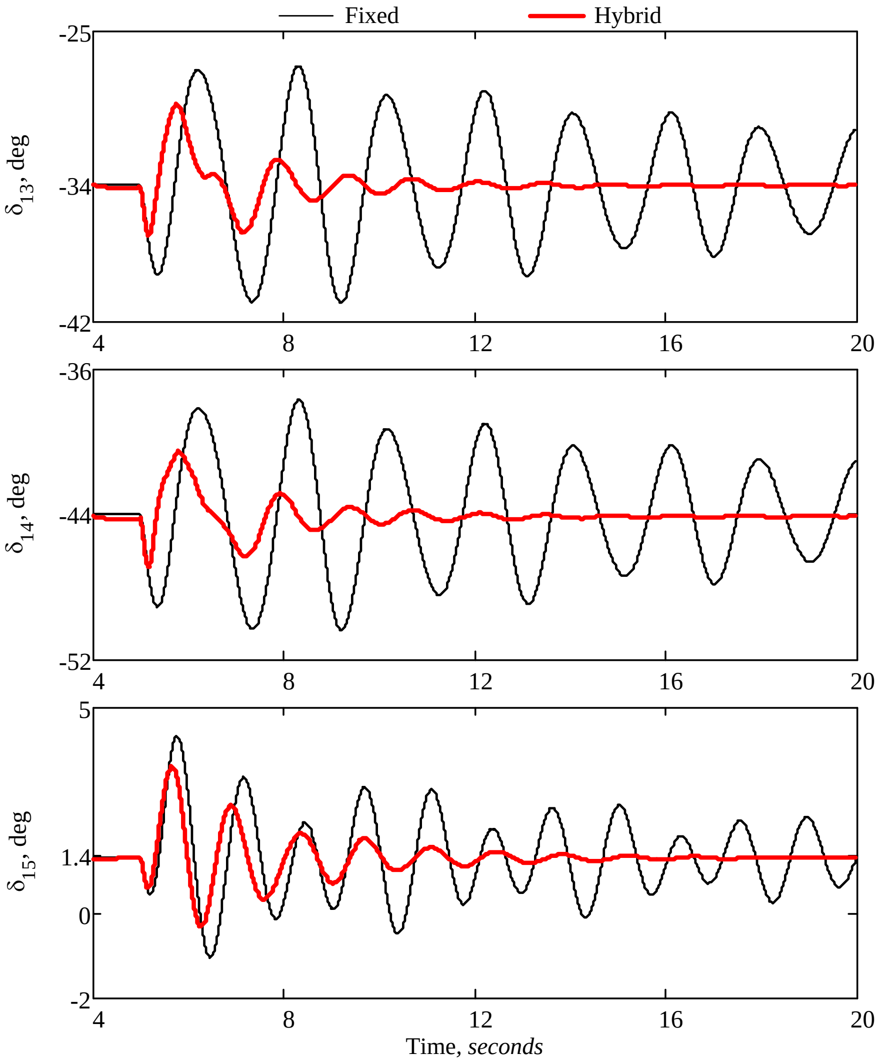

Figure 4.23: Hybrid SSSC: relative generator rotor angle time responses for disturbance **Case B**.

B.3. Case Study C

This test case is used to evaluate the performance of the hybrid SSSC compensation scheme in damping inter-area oscillations during lower values of tie-line power flows. Figure 4.24 shows the relative generator rotor angle time responses of the test system for disturbance **Case B**. These results clearly demonstrate the effectiveness of the proposed hybrid SSSC compensation scheme in damping inter-area oscillations for lower tie-line power flow cases.

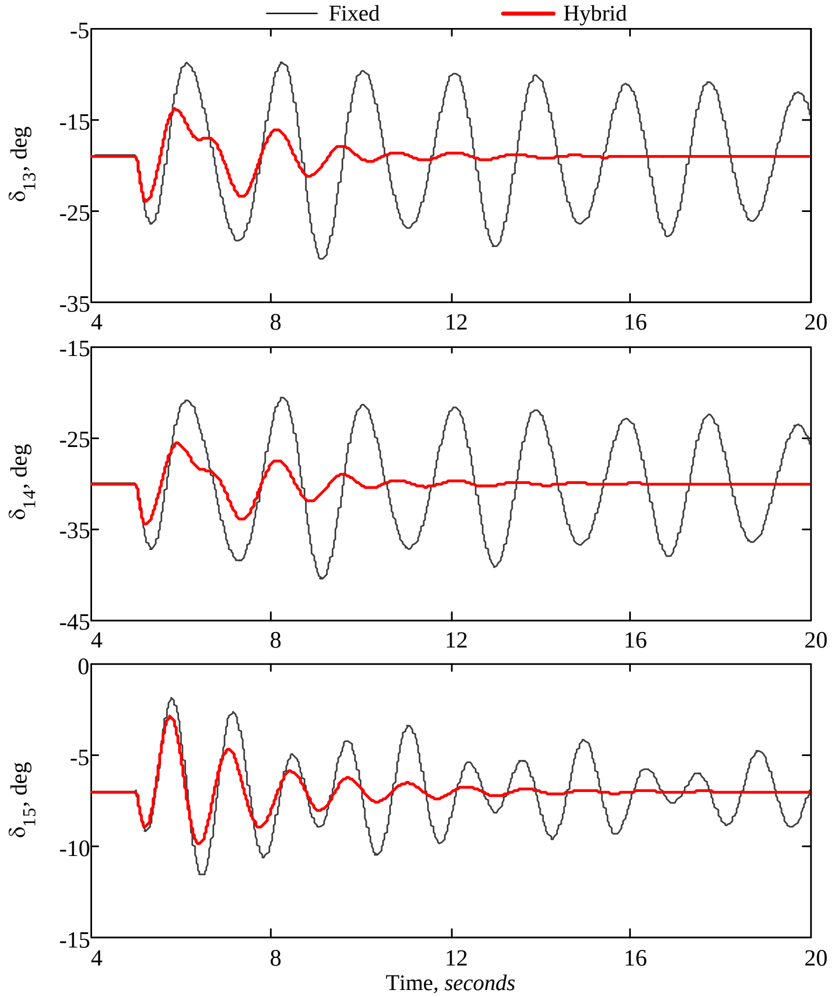

Figure 4.24: Hybrid SSSC: relative generator rotor angle time responses for disturbance **Case C**.

B.4. Case Study D

This test case is used to evaluate the performance of the hybrid SSSC compensation scheme in damping inter-area oscillations during tie-line power flow reversal, i.e. drastic change in power system operating conditions. Figure 4.25 shows the relative generator rotor angle time responses of the test system for disturbance **Case D**. The time responses shown in Fig. 4.25 clearly demonstrate the effectiveness of the proposed hybrid SSSC compensation scheme in damping inter-area oscillations during power reversal cases.

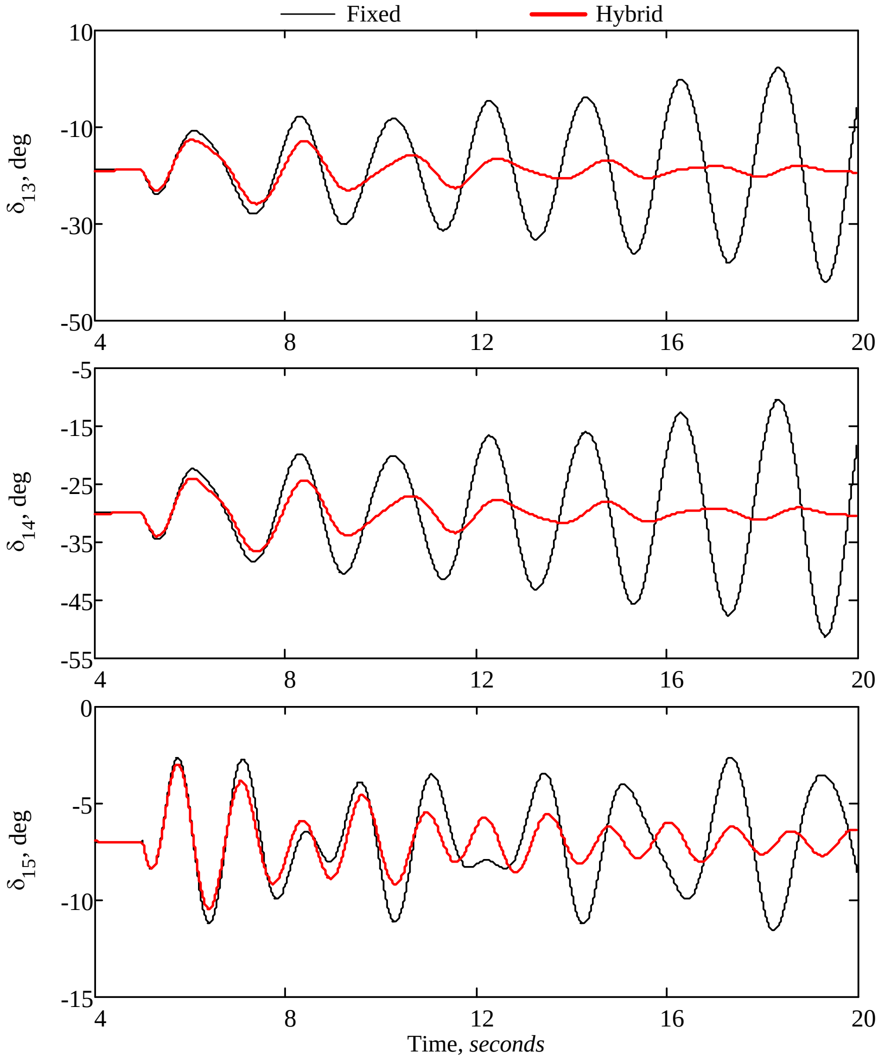

Figure 4.25: Hybrid SSSC: relative generator rotor angle time responses for disturbance **Case D**.

B.5. Case Study E

This test case is used to evaluate the performance of the hybrid SSSC compensation scheme in damping inter-area oscillations during severe disturbance e.g. loss of one tie-line transmission line. Figure 4.26 shows the relative generator rotor angle time responses of the test system for disturbance **Case E**. These results clearly demonstrate the effectiveness of

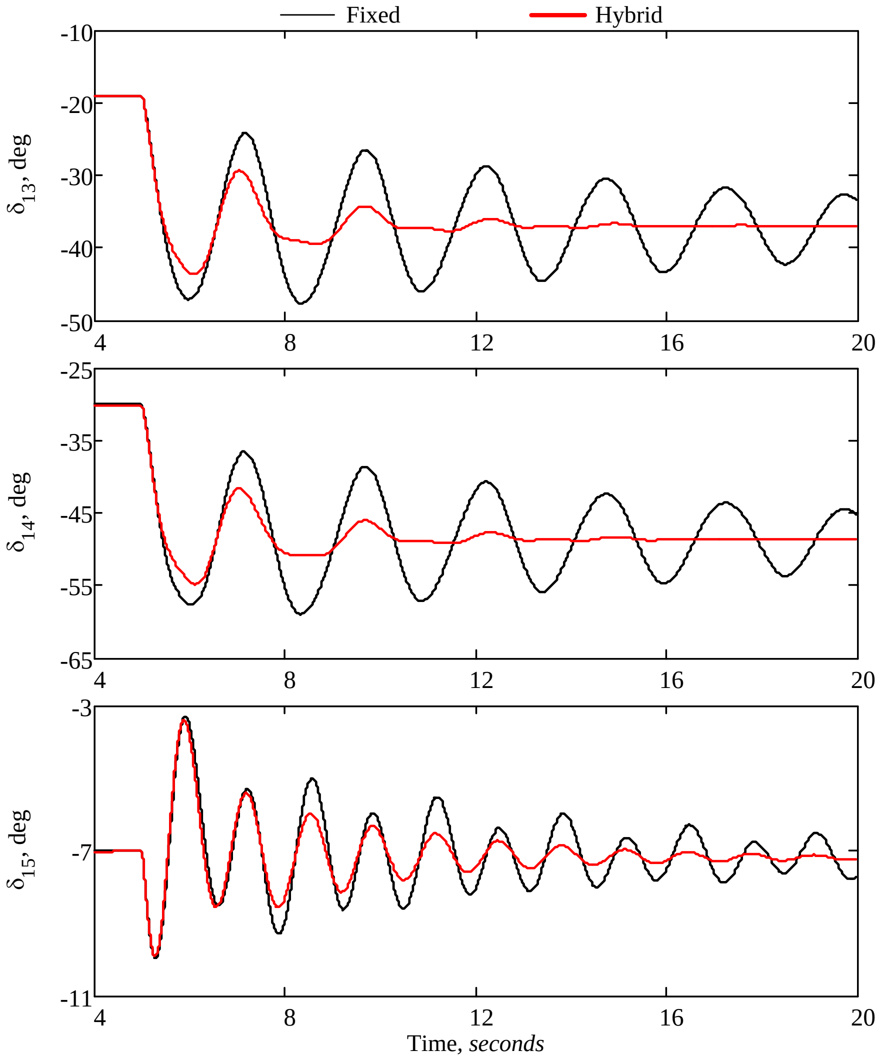

Figure 4.26: Hybrid SSSC: relative generator rotor angle time responses for disturbance **Case E**.

the proposed hybrid SSSC compensation scheme in damping inter-area oscillations for very severe disturbance followed by increase in the tie-line power flow.

A comparison of the responses of the fixed series capacitor compensation to the hybrid SSSC compensation scheme in Figs. 4.19 through 4.26 shows clearly the positive contribution of the hybrid SSSC scheme in damping inter-area oscillations. As can be observed from the relative rotor angle responses in Figs. 4.19 - 4.26, the inter-area oscillation damping controller reduces the first swing and effectively damps the subsequent swings.

4.4 Comparison Between Inter-Area Oscillations Damping Using Schemes I and II

The calculation of the damping coefficients of the power flow on $Line-1$ gives an approximate representation of the degree of damping of the inter-area oscillation modes. For this purpose, the approximate damping factors of the dominant modes in the power flow on $Line-1$ are calculated using Prony analysis. The Prony analysis is a curve fitting algorithm which decomposes a signal into number of damped sinusoids [82, 83]. More details of Prony analysis is given in Appendix A.3. The analyzed data of the power signals lie between a time-window of 5.5 *sec* and 20 *sec*, which represents power oscillations after fault clearing.

Figure 4.27 shows the results of the original and reconstructed signals using Prony analysis. The Fig. 4.27(a) represents the base case (fixed capacitor) response, Fig. 4.27(b) represents the hybrid TCSC compensation case (**Scheme I**) and Fig. 4.27(c) represents the hybrid SSSC compensation case (**Scheme II**) respectively. The disturbance case for this studies is **Case C**. For signal reconstruction, the two most dominant components obtained from Prony analysis are used.

It can be seen from Fig. 4.27 that all the three reconstructed signals closely match the original signals. It can also be seen from the tables in Fig. 4.27(a) that the dominant frequencies obtained from the Prony analysis also closely match the frequencies obtained from the small signal analysis given in Table 4.1.

The approximate damping factors obtained from Prony analysis are presented in Table 4.3 for all the contingency cases of Table 4.2. The introduction of the hybrid compensation scheme in the system slightly modifies the dominant frequencies as depicted by the Prony analysis results.

It can be seen from Table 4.3 that the use of hybrid TCSC and SSSC compensation schemes significantly improves the inter-area damping coefficient in all case studies compared to the fixed series capacitor compensation. It can also be seen from Table 4.3 that, in general, the hybrid SSSC compensation scheme (Scheme II) provides better inter-area oscillations damping than the hybrid TCSC compensation scheme (Scheme I).

4.5 Summary

This chapter presented the application of the hybrid series capacitive compensation schemes in damping low frequency local and inter-area oscillations. The effectiveness of the schemes in damping these oscillations has been demonstrated through several digital

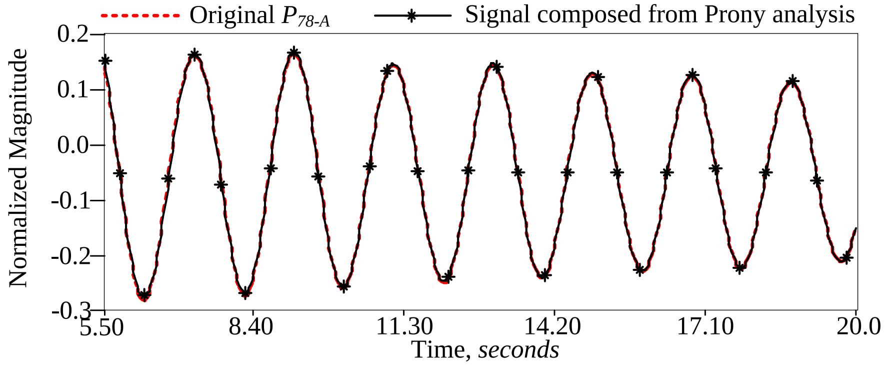

No.	Magnitude	Phase(deg)	Freq(Hz)	Damp(%)	Real(1/s)	Imag(rad/s)
1	0.4642	30.641	0.522	0.758	-0.0248	3.277
2	0.0197	67.384	0.769	1.911	-0.0923	4.830

(a) Fixed capacitor compensation

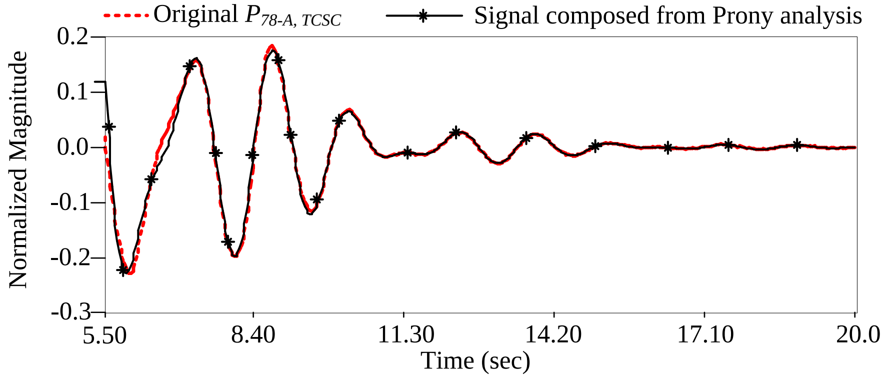

No.	Magnitude	Phase(deg)	Freq(Hz)	Damp(%)	Real(1/s)	Imag(rad/s)
1	0.4085	33.268	0.586	11.119	-0.4120	3.682
3	0.2332	136.092	0.795	7.418	-0.3713	4.992

(b) Hybrid TCSC - Scheme I

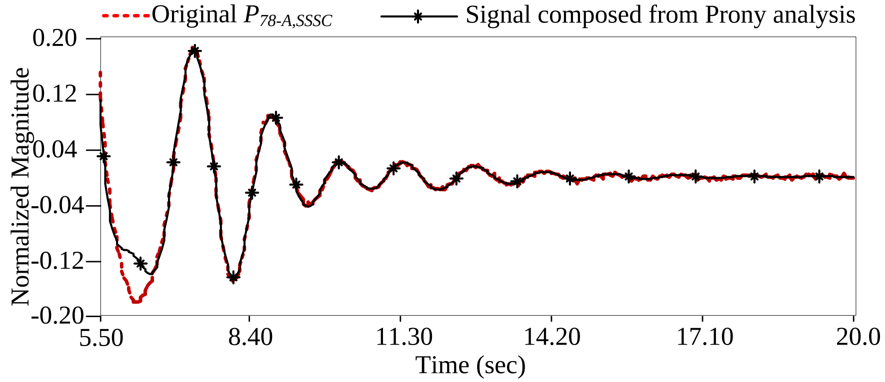

No.	Magnitude	Phase(deg)	Freq.(Hz)	Damp(%)	Real(1/s)	Imag(rad/s)
1	0.4480	44.063	0.533	20.901	-0.7160	3.350
2	0.2132	-176.170	0.758	8.259	-0.3948	4.764

(c) Hybrid SSSC - Scheme II

Figure 4.27: Signal composition of power flowing through line 1 from bus 7 to bus 9 using Prony analysis for disturbance **Case C**.

Table 4.3: Approximate damping for the most dominant modes

Cases	Fixed capacitor		Scheme I (Hybrid TCSC)		Scheme II (Hybrid SSSC)	
	Damp. (%)	Freq. (Hz)	Damp. (%)	Freq. (Hz)	Damp. (%)	Freq. (Hz)
A	1.966	0.513	18.794	0.775	69.995	0.434
	1.534	0.763	14.552	0.641	8.385	0.719
B	1.970	0.513	18.322	0.755	35.574	0.471
	1.497	0.763	14.775	0.635	7.682	0.723
C	0.758	0.522	11.119	0.586	20.901	0.533
	1.911	0.769	7.418	0.795	8.259	0.758
D	2.996	0.395	17.368	0.441	18.931	0.378
	3.569	0.799	5.366	0.774	5.802	0.759
E	-2.215	0.498	4.774	0.490	5.935	0.476
	3.259	0.772	1.193	0.778	2.323	0.777

computer simulations for case studies on test benchmarks.

An approximate computation of damping contributed by hybrid TCSC and hybrid SSSC are performed using Prony analysis. The results of the studies conducted in this chapter demonstrate the effectiveness in damping low frequency power system oscillations. Moreover, the hybrid SSSC scheme was found to be providing relatively better damping in most of the case studies, compared to the hybrid TCSC scheme.

PART - II

Adaptive Control

CHAPTER 5

Proposed Adaptive Controller

5.1 Introduction

During the process of inter-area oscillation damping studies carried out in the previous chapter, it was found out that the performance of the fixed parameter lead-lag controller (Fig. 4.8) degraded as the operating conditions change (Table 4.3). One issue with the earlier supplementary controller is that it has been tuned using a multiple-run time domain optimization approach for disturbance **Case A** (Table 4.2). This tuning technique is very time consuming, and the parameters tuned for one operating condition may not provide effective control over a wide operating range, especially for systems that are nonlinear and time-varying in nature, such as power systems. For the nonlinear power system applications, an adaptive controller having the ability to adjust its own parameters to yield satisfactory control performance is more desirable [46–49]. A general discussion of adaptive controller application in power system area has been given in Section 1.7.

An adaptive controller is formed by combining an on-line parameter estimator, which provides estimates of unknown parameters at each sampling instant, with a control law that is formulated to meet certain operating criterion [54, 84]. The controller can be realized using the parameter estimator and the control law in two different approaches. In the first approach, referred to as *indirect adaptive control*, the plant parameters are estimated on-line and used to calculate the controller parameters. This approach has also been referred to as explicit adaptive control, because the design is based on an explicit plant model. In the second approach, referred to as *direct adaptive control*, the plant model is parameterized in terms of the controller parameters that are estimated directly without intermediate calculations involving plant parameter estimates. This approach has also been referred to as implicit adaptive control because the design is based on the estimation of an implicit plant model.

In this thesis, plant dynamics is expressed by an explicit mathematical model using Autoregressive Moving-Average (ARMA) model, and an indirect adaptive pole-shift control strategy is used to control plant. Figure 5.1 shows a typical structure of an indirect adaptive control method [54]. In such a control, identifier module tracks the system dynamics using an input and output relation. The identified parameters are then used to generate control action using a pole-shift control algorithm. In the pole-shift control algorithm, the control signal is generated by moving the open-loop poles radially toward the origin of the unit circle in z plane by a shifting factor α using a miimum variance based optimization criterion. The control procedure is simple; i.e. there is only one parameter α that needs to be determined for the controller.

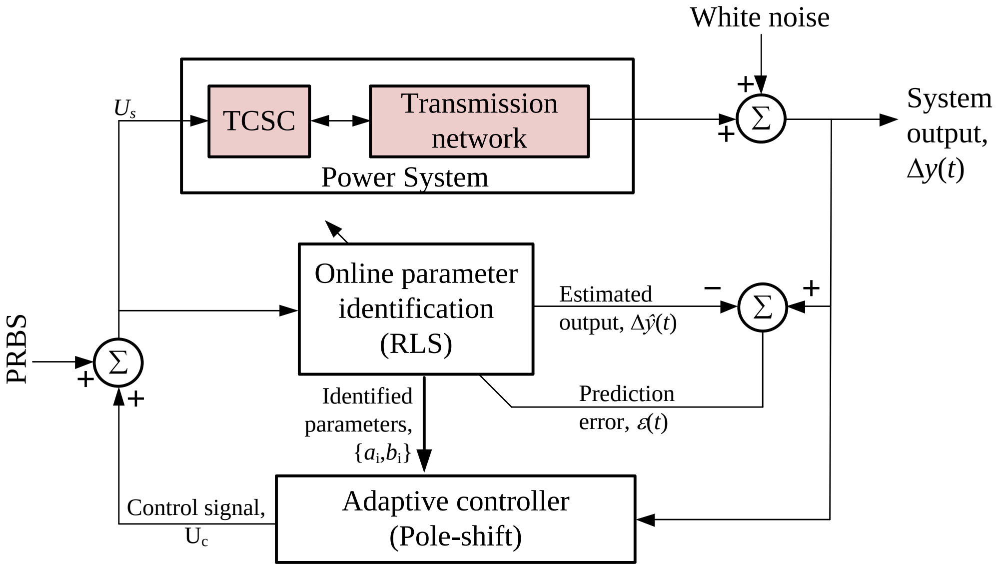

Figure 5.1: An schematic diagram of an indirect adaptive control.

The advantage of adaptive pole-shift controller for damping low frequency oscillations using Power System Stabilizers (PSS) have been studied in various literatures [46, 47, 49]. However, very limited studies have been reported for transmission line controls. One of the practical reason for such limited applications is because of the fact that the least-square based estimation becomes inaccurate for large disturbance conditions in power systems, such as system faults. The recent literatures [55–58] reported such identification issues during large disturbance conditions, which led to improper controller action. Authors in [55–58] used computationally extensive and sophisticated methods such as higher order plant models, constant trace based Kalman filter, random walk based RLS estimation, controller dead-zone and parameter freeze during disturbances to improve the accuracy of identification.

This chapter presents a computationally efficient solution to address the problem associated with RLS technique in a power system (during large disturbances) by proposing the use of a simple *Sigmoid* like nonlinear function in parameter update equation. Using this non-linear function, a large error will have less effect on parameter update, whereas the parameters will be updated in a linear fashion when the error magnitude is small. This method helps in smoothing out the parameter variations effectively during major disturbances, and thus produces a stable control response without the need for parameter freezing or controller dead-zone.

In this chapter, detailed studies are conducted to evaluate the effectiveness of pole-shift adaptive control algorithm in damping inter-area oscillations. The self-tuning damping capability of the controller is investigated on a three-area, six-machine test system using balanced three-phase TCSC/SSSC compensation as well as the hybrid TCSC/SSSC compensation schemes. Further investigations are carried out on an IEEE 12-bus test system using a balanced three-phase TCSC device.

5.2 Indirect Adaptive Control

An indirect adaptive control schematics shown in Fig. 5.1 consists of a plant model with time-varying coefficients. In this thesis, the response of the non-linear power system, including the FACTS device, is modelled by an ARMA model. This type of model is basically a reduced-order model. The coefficients of the model of the plant are then estimated in real time, using a recursive algorithm. The estimated parameters are then used to design a controller to meet the specific control requirements. A Pseudo Random Binary Sequence (PRBS) signal is used to excite the system.

5.2.1 System Identification

The power system dynamics is approximated by a discrete ARMA model of the form [48, 49] given in Eq. (5.1). Recursive Least Square (RLS) algorithm is used for the plant parameter identification. The RLS algorithm is selected because of its simplicity and robustness.

$$A(z^{-1})y(t) = z^{-n_d}B(z^{-1})u(t) + C(z^{-1})e(t) \tag{5.1}$$

where $y(t)$, $u(t)$ and $e(t)$ are system output, system input and noise terms, respectively. $A(z^{-1})$, $B(z^{-1})$ and $C(z^{-1})$ are the polynomials expressed in terms of the backward shift operator z^{-1} and are defined as:

$$\begin{aligned} A(z^{-1}) = &\quad 1 + a_1 z^{-1} + a_2 z^{-2} + ... + a_{n_a} z^{-n_a} \\ B(z^{-1}) = &\quad b_1 z^{-1} + b_2 z^{-2} + ... + b_{n_b} z^{-n_b} \\ C(z^{-1}) = &\quad 1 + c_1 z^{-1} + c_2 z^{-2} + ... + c_{n_c} z^{-n_c}. \end{aligned}$$

n_a, n_b and n_c are the order of the polynomials $A(z^{-1})$, $B(z^{-1})$, and $C(z^{-1})$, respectively. The variable n_d represents the delay term.

As the noise term $e(t)$ cannot be directly measured, the regression model of Eq. (5.1) can be obtained by a suitable approximation as [85]:

$$y(t) = \Psi^T(t)\theta + e(t) \tag{5.2}$$

where, $\Psi(t)$ is the measurement variable vector given as:

$$\begin{aligned} \Psi(t) = [-y(t-1) \;\; .. \;\; -y(t-n_a) \;\; u(t-n_d) \;\; .. \\ u(t-n_d-n_a) \;\; \epsilon(t-1) \;\; .. \;\; \epsilon(t-n_c)]^T \end{aligned} \tag{5.3}$$

θ is the parameter weight vector given as:

$$\theta = \begin{bmatrix} a_1 & .. & a_{n_a} & b_1 & .. & b_{n_b} & c_1 & .. & c_{n_c} \end{bmatrix}^T \tag{5.4}$$

and,

$$\epsilon(t) = y(t) - \Psi(t)\hat{\theta}(t-1) \tag{5.5}$$

is the estimation error. Here, the variable $e(t)$ in Eq. (5.5) is approximated by the estimation error $\epsilon(t)$.

The system parameter weight vector, $\theta(t)$ can be estimated using the following extended recursive least square (RLS) equations algorithm [85]:

$$\hat{\theta}(t) = \hat{\theta}(t-1) + K(t)\left[y(t) - \Psi(t)^T\hat{\theta}(t-1)\right] \tag{5.6a}$$

$$K(t) = \frac{P(t-1)\Psi(t)}{\lambda(t) - \Psi(t)^T P(t-1)\Psi(t)} \tag{5.6b}$$

$$P(t) = \frac{1}{\lambda(t)}\left[P(t-1) - K(t)\Psi^T(t)P(t-1)\right] \tag{5.6c}$$

where $\lambda(t)$ is the time varying forgetting factor, $P(t)$ is the covariance matrix, and $K(t)$ is the gain vector. The forgetting factor $\lambda(t)$ is calculated as:

$$\lambda(t) = \lambda_0\lambda(t-1) + (1-\lambda_0) \tag{5.7}$$

where λ_0 is a positive value between 0 and 1.

Proposed Robust RLS Identification

During the power system transients, the power system may shift from one operating state to another, and the error between actual plant output and estimated plant output may vary significantly. In actual studies, errors are not purely Gaussian, and a single large error will have a drastic influence on the result. To limit the effect of such large deviations in the estimation errors, the update algorithm Eq. (5.6a) is modified as given in Eq. (5.8) [54].

$$\hat{\theta}(t) = \hat{\theta}(t-1) + K(t)f(\epsilon(t)) \tag{5.8}$$

A constant multiplier with a value of less than unity can be used to penalize the gain term in Eq. (5.8). However, doing so decreases the sensitivity of the algorithm to smaller errors. The objective is to have an algorithm very sensitive to smaller errors, but to make it less sensitive for larger errors. So a functional value of $f(\epsilon)$ is selected such that it is linear for small error (ϵ) but increases more slowly than linear for large ones. This type of estimation is robust toward the large errors. The following *Sigmoid* like nonlinear expression for $f(\epsilon)$ is used in the thesis:

$$f(\epsilon(t)) = \frac{\epsilon}{1 + a|\epsilon|} \tag{5.9}$$

where a is the design constant that determines the parameter update rate. For $a = 0$, the algorithm will become normal RLS. However, for $a > 0$, penalty on the error increases with increase in absolute error magnitude as shown in Fig. 5.2.

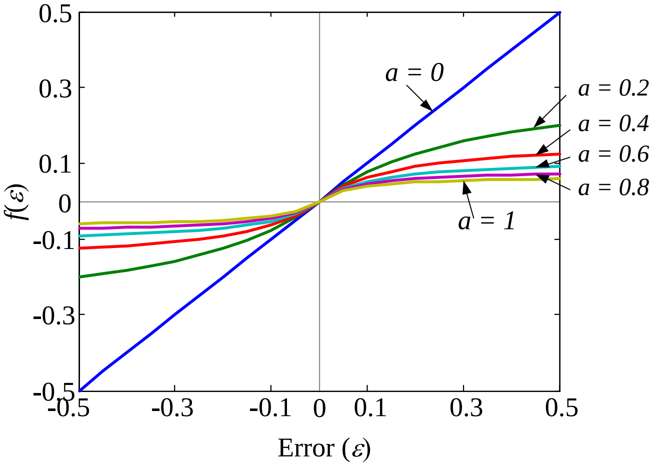

Figure 5.2: Update value as a function of error ϵ for various values of a.

During the course of research, several identification techniques proposed in the literatures which are suitable for large disturbances conditions in the power systems are studied.

Chen et al. [86] discusses a tracking constrained identification procedure for power stabilizer applications to limit the parameter variations during model transition due to the change in operating conditions or disturbances. A tracking constrained coefficient was introduced in the covariance matrix update expression. The issue with the method proposed in [86] is that it needed careful selection of parameter update rate constant and also need to calculate norms of the weight vectors and update vectors in each iteration, which increases computational burden. The details of the algorithm are presented in Appendix A.2.

Rai et al. [87] used the H_∞ equations discussed in the signal processing literature [88] to handle the large disturbance conditions in the earlier part of the thesis work. The algorithm resembles the RLS algorithm in its structure and is robust with respect to persistent bounded perturbations in the data. It is termed as approximate robust recursive least square and the equations are given in Eq. (5.10).

$$\begin{aligned}
\eta(t) &= y_r(t) - \psi^T(t)\theta(t-1) \\
P(t) &= P(t-1) + \frac{P(t-1)P(t-1)}{\gamma^2} - \frac{P(t-1)\psi(t)\psi^T(t)P(t-1)}{1+\psi^T(t)P(t-1)\psi(t)} \\
\theta(t) &= \left[I + \frac{P(t-1)}{\gamma^2}\right]\theta(t-1) + P(t)\psi(t)\eta(t)
\end{aligned} \tag{5.10}$$

where, $y_r(t)$ is the reference plant output, $\eta(t)$ is the prediction error and $P(t)$ is the covariance matrix. The initial conditions are $P(0) = cI$, and $\theta(0) = 0$. The tuning parameters are $c > 1$ and γ. The initial value of c should satisfy the conditions $c/\gamma^2 < 1$ and P(1) $\leq P(0)$. Furthermore, selection of γ should satisfy the condition $||\delta\phi(t)|| < 2/\gamma^2$, where δ is a small positive number and $\phi(t) = 1/n \sum \psi\psi^T$.

The method presented in Eq. (5.10) is computationally extensive and algorithm initialization is very sensitive to the initial values of the tuning parameters. The computation complexity is due to the presence of the term $[P(t-1)P(t-1)]/\gamma^2$ in the update equation for $P(t)$ (Eq. 5.10).

The identification techniques discussed in Chen et al. [86], Rai et al. (Eq. 5.10) and the proposed method (Eq. 5.9) are implemented in a simple single machine infinite bus system to evaluate the performance. The parameter tracking ability of these three methods during large disturbances are found to be almost identical. The final goal of the research is to implement the algorithm on a stand-alone DSP, and, for this purpose, the proposed method (Eq. 5.9) is found to be attractive, as it provides a very good result with minimum computing resources.

5.2.2 Pole-Shift Control Technique

Once the parameters of the model are properly estimated, an optimized pole placement control algorithm know as pole-shift control is implemented to generate optimal control signal [47,49,86]. The pole-shift feedback controller has the transfer function given in Eq. (5.11).

$$\frac{u(t)}{y(t)} = -\frac{G(z^{-1})}{F(z^{-1})} \tag{5.11}$$

where,

$$F(z^{-1}) = 1 + f_1 z^{-1} + f_2 z^{-2} + ... + f_{n_f} z^{-n_f}.$$
$$G(z^{-1}) = g_0 + g_1 z^{-1} + g_2 z^{-2} + ... + g_{n_g} z^{-n_g}.$$

and $n_f = n_b - 1$, $n_g = n_a - 1$. From Eq. (5.1) and (5.11), characteristics equation of the closed loop control can be derived as:

$$T(z^{-1}) = A(z^{-1})F(z^{-1}) + B(z^{-1})G(z^{-1}) \tag{5.12}$$

If the characteristic polynomial $T(z^{-1})$ is predefined as in pole-assignment control, the controller polynomials $F(z^{-1})$ and $G(z^{-1})$ can be calculated from Eq. (5.12). However, in pole-shift control, the characteristics equation of Eq. (5.12) takes the form of $A(z^{-1})$ with the pole shifted by factor of 'α'. The new characteristics equation can be obtained by replacing 'z^{-1}' in $A(z^{-1})$ by 'αz^{-1}' as follows:

$$A(\alpha z^{-1}) = T(z^{-1}) = A(z^{-1})F(z^{-1}) + B(z^{-1})G(z^{-1}) \tag{5.13}$$

Rearranging and expressing the Eq. (5.13) in matrix form as:

$$\begin{bmatrix} 1 & 0 & . & 0 & b_1 & 0 & . & 0 \\ a_1 & 1 & . & 0 & b_2 & b_1 & . & 0 \\ . & a_1 & . & . & . & b_2 & . & . \\ a_{n_a} & . & . & 1 & b_{n_b} & . & . & b_1 \\ 0 & a_{n_a} & . & a_1 & 0 & b_{n_b} & . & b_2 \\ . & 0 & . & . & . & 0 & . & . \\ . & . & . & . & . & . & . & . \\ 0 & 0 & . & a_{n_a} & 0 & 0 & . & b_{n_b} \end{bmatrix} \begin{bmatrix} f_1 \\ f_2 \\ . \\ f_{n_f} \\ g_0 \\ g_1 \\ . \\ g_{n_g} \end{bmatrix} = \begin{bmatrix} a_1(\alpha_t - 1) \\ a_2(\alpha_t^2 - 1) \\ . \\ a_{n_a}(\alpha_t^{n_a} - 1) \\ 0 \\ . \\ 0 \\ 0 \end{bmatrix} \tag{5.14}$$

or,

$$Mw(\alpha_t) = L(\alpha_t)$$

where

$$M = \begin{bmatrix} 1 & 0 & . & 0 & b_1 & 0 & . & 0 \\ a_1 & 1 & . & 0 & b_2 & b_1 & . & 0 \\ . & a_1 & . & . & . & b_2 & . & . \\ a_{n_a} & . & . & 1 & b_{n_b} & . & . & b_1 \\ 0 & a_{n_a} & . & a_1 & 0 & b_{n_b} & . & b_2 \\ . & 0 & . & . & . & 0 & . & . \\ . & . & . & . & . & . & . & . \\ 0 & 0 & . & a_{n_a} & 0 & 0 & . & b_{n_b} \end{bmatrix}, \ w(\alpha_t) = \begin{bmatrix} f_1 \\ f_2 \\ . \\ f_{n_f} \\ g_0 \\ g_1 \\ . \\ g_{n_g} \end{bmatrix}, \ L(\alpha_t) = \begin{bmatrix} a_1(\alpha_t - 1) \\ a_2(\alpha_t^2 - 1) \\ . \\ a_{n_a}(\alpha_t^{n_a} - 1) \\ 0 \\ . \\ 0 \\ 0 \end{bmatrix},$$

and α_t is the pole-shift factor at time t.

The Eq. (5.14) can be solved for f_i and g_i for a known value of α_t. Once the values of f_i and g_i are obtained, the control signal can be computed using Eq. (5.11). It can be observed that the control signal is a function of α_t at any time t. The control signal, $u(t, \alpha_t)$, can be expressed in a Taylor series in terms of factor α_t at any operating point α_0.

$$u(t, \alpha_t) = u(t, \alpha_0) + \sum_{i=1}^{\infty} \frac{1}{i!} \left[\frac{\partial^{(i)} u(t, \alpha_t)}{\partial \alpha_t^{(i)}} \right] \tag{5.15}$$

From Eq. (5.11) and (5.14), the control signal can be calculated as:

$$u(t, \alpha_t) = X^T(t) w(\alpha_t) = X^T(t) M^{-1} L(\alpha_t) \tag{5.16}$$

where $X(t) = [-u(t-1) \ ... \ -u(t-n_f) \ \ -y(t) \ \ -y(t-1) \ ... \ y(t-n_g)]^T$ is the measurement variable vector. The ith order differential of $u(t, \alpha_t)$ with respect to α_t becomes:

$$\left[\frac{\partial^{(i)} u(t, \alpha_t)}{\partial \alpha_t^{(i)}} \right]_{\alpha_t = \alpha_0} = X^T(t) M^{-1} L^{(i)}(\alpha_0) \tag{5.17}$$

Equation (5.15) can be written in simple form as

$$u(t, \alpha_t) = u(t, \alpha_0) + \sum_{i=1}^{n_a} s_i \alpha_t^i \tag{5.18}$$

where

$$s_i = \frac{1}{i!} X^T(t) M^{-1} L^{(i)}(\alpha_0)$$

Once the input is computed at time t, the system output $\hat{y}(t+1)$ at time $t+1$ can be predicted as follows:

$$\hat{y}(t+1) = X^T(t)\beta + b_1 u(t, \alpha_t) \tag{5.19}$$

where

$$\beta = \begin{bmatrix} -b_2 & -b_3 & \dots & -b_{n_b} & a_1 & a_2 & \dots & a_{n_a} \end{bmatrix}$$

is an identified parameter vector.

For fixed value of α_t, the control algorithm becomes a special case of the pole-assignment control. However, in pole-shift control algorithm, the value of α_t can be selected to satisfy some optimized performance indices. One such performance index is the minimization of the one time-step ahead system output prediction error, i.e.

$$\min_{\alpha_t} J(t+1, \alpha_t) = E\left[\hat{y}(t+1) - y_r(t+1)\right]^2 \tag{5.20}$$

where $y_r(t+1)$ is the reference output for next time step. By minimizing the performance index of Eq. (5.20), the controlled system output $y(t)$ follows the pre-specified reference $y_r(t)$ as closely as possible.

Minimization of the objective function defined in Eq. (5.20) yields the optimal value of α_t. The value of α_t should be kept in the range of:

$$-\frac{1}{\lambda_t}(1-\Lambda) < \alpha_t < \frac{1}{\lambda_t}(1-\Lambda)$$

to satisfy the stability constraints, where λ_t represents the largest absolute value of the roots of characteristics equation $T(z^{-1})$ and Λ is the security coefficient [89]. The value of the security coefficient can be chosen between 0% to 100%. Furthermore, the control signal also should lie within the control constraint:

$$u_{min} \le u(t, \alpha_t) \le u_{max}$$

where u_{min} and u_{max} are minimum and maximum control signal boundaries.

Since α_t reflects the stability of the closed-loop system, it is desirable to assign the pole-shifting factor α_t to a specified value under steady state, such as 'α_{ss}'. To accommodate this ability, the cost function given in Eq. (5.20) can be modified as:

$$\min_{\alpha_t} J(t+1, \alpha_t) = E\left[\hat{y}(t+1) - y_r(t+1)\right]^2 + \mu(\alpha_t - \alpha_{ss})^2 \tag{5.21}$$

where μ is a weighting coefficient. Equation (5.21) is second order in nature and modern optimization routines can easily find the exact roots in few iterations provided the starting point as previous sampling time root. Minimization of the objective function (Eq. 5.21) gives optimal pole-shift factor α_{opt}. This information is used in Eq. (5.16) to generate optimal control signal so that the next time-step system output $\hat{y}(t+1)$ follows reference signal $y_r(t+1)$ with minimum variance.

5.2.3 Example: Servo-motor Position Control Using Pole-Shift Control

A servo motor system, as shown in Fig. 5.3, is used to demonstrate the performance of the adaptive pole-shift algorithm. The plant dynamics is modelled using sets of differential equations as follows:

$$\frac{di}{dt} = \frac{v_i}{L} - \frac{R}{L}i - \frac{K_m}{L}\omega \tag{5.22a}$$

$$\frac{d\omega}{dt} = \frac{K_m}{J}i - \frac{b}{J}\omega \tag{5.22b}$$

$$\frac{d\theta}{dt} = \omega \tag{5.22c}$$

where v_i is input voltage, R and L are armature resistance and inductance, K_m is armature emf constant, e_b is back emf, J is rotor inertia, b is viscous friction constant, ω is rotor speed in *rad/sec*, and, θ is rotor position in *radian*. The DC servomotor differential equation model and discrete pole-shift control are developed in MATLAB Simulink environment. The sampling time of 0.1 *sec* is used. Zero order hold facilitates the interaction between discrete controller and continuous time model. The plant discretized at the sampling time of 0.1 *sec* has roots at 1.0, 0.9453, and 0.1417, indicating an oscillatory system.

The $e(t)$ term represents white noise of 0.5% magnitude. The system coefficients are identified using the robust recursive least square algorithm presented in Eq. (5.6)-(5.9). The control signal is calculated using Eq. (5.14), such that the cost function given in Eq. (5.21) is minimized. Steady state value of pole-shift factor is chosen as 0.76. The identification is enabled at $t = 0$ *sec* and pole-shift controller is enabled at $t = 0.5$ *sec*. The control signal is limited between ± 1.5 *units*.

The system time response to the square wave reference position of magnitude ± 1 *rad* is

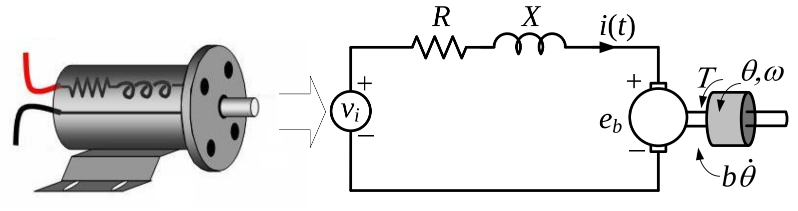

$L = 0.1H$
$K_m = 0.30$
$J = 0.10\ kgm^2$
$b = 0.01$
$R = 2.0\Omega$

(a) DC motor equivalent circuit

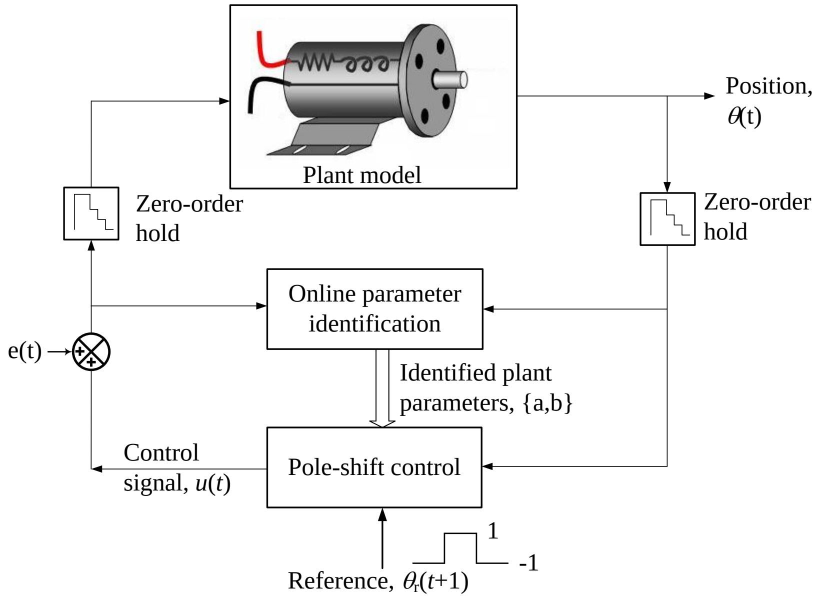

(b) Indirect adaptive position control

Figure 5.3: DC motor indirect adaptive position control.

plotted in Fig. 5.4. As seen in Fig. 5.4(a), the controlled plant is able to track the reference signal effectively. The plant response at $t = 20$ *sec* has a small overshoot compared to the first overshoot, indicating that the identification has reached an optimal sets of parameters. Furthermore, the robust RLS identification algorithm is able to identify plant coefficients effectively, as shown in Figs. 5.4(b) and (d). The identified coefficient variations are smooth even for large step changes in the reference waveform: -1 to $+1$ or $+1$ to -1. The control signal is plotted in Fig. 5.4(c).

The dynamic locations of open and closed loop poles of the system captured at $t = 0.7sec$ are plotted in Fig. 5.5. Open loop poles are shown in *black-marks* and closed loop poles are shown in *red-marks*. The identified open loop poles are at $\{-0.3008, 1.1752 \pm \jmath 0.5402\}$, closed loop poles are at $\{-0.1503, 0.5870 \pm \jmath 0.2699\}$, and the pole-shift factor is $\alpha = 0.4995$. It is very evident from the figure that the pole-shift controller improves the stability of the system during transient, by moving the poles outside the unit circle to inside the unit circle. The identified steady state open loop poles for this system are at $[1,\ 0.9446,\ 0.1446]$, which are al-

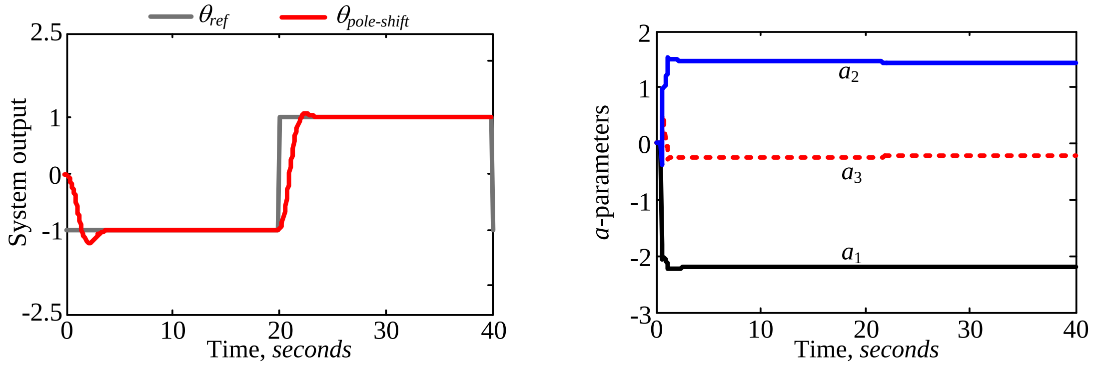

(a) Reference and output

(b) Numerator coefficients

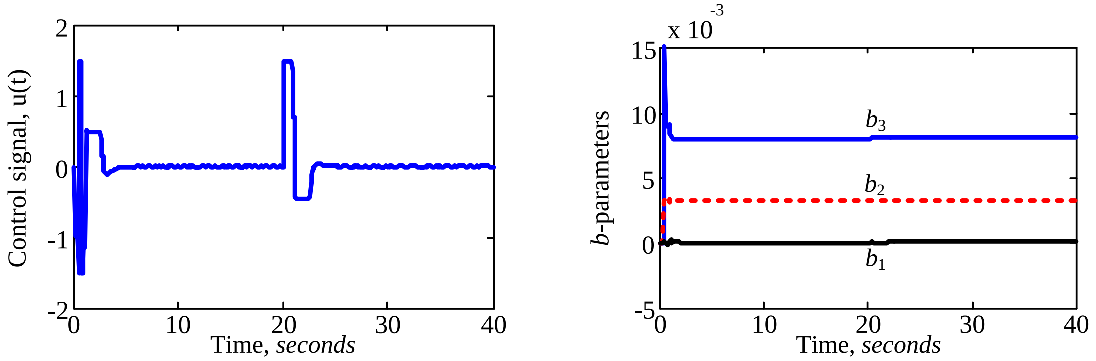

(c) Control signal

(d) Denominator coefficients

Figure 5.4: Servo-motor system position response to step change in reference signal.

most identical to roots of the linearized model obtained from MATLAB - $[1,\ 0.9453,\ 0.1417]$, and closed loop poles are at $[0.76,\ 0.7179,\ 0.1859]$ respectively.

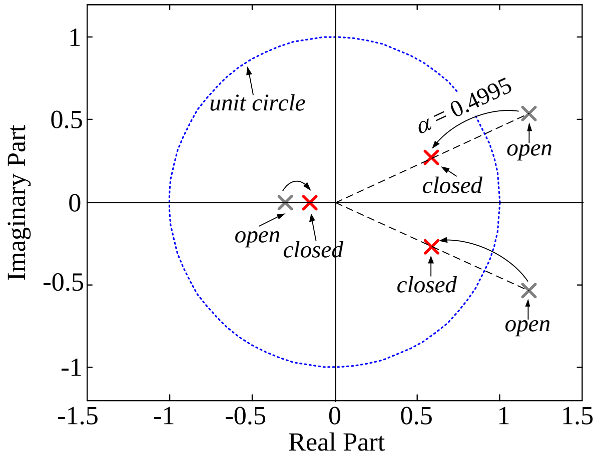

Figure 5.5: Dynamic pole-movement with respect to the pole-shift factor α captured at $t = 0.7$ *sec*.

5.3 Test Systems Used for Simulation Studies

To demonstrate the effectiveness of the proposed adaptive controller in damping inter-area oscillations, two multi-area test benchmark systems are adopted. The first test system considered is a three-area, six-machine system described in Chapter 4 (Fig. 4.5). The second test system considered for the study is an IEEE 12-bus power system suitable for inter-area oscillation studies using FACTS devices [59].

5.3.1 Three-Area, Six-Machine System

The three-area, six-machine test system is redrawn in Fig. 5.6 for reference. To simplify the adaptive controller design, two transmission lines between bus 7 and 9 are replaced by an equivalent single transmission line. The deviation in power flow through line 7-9 is used as input to the supplementary controllers. The output of the supplementary controller is added to the steady-state TCSC and SSSC controllers (Fig. 4.7).

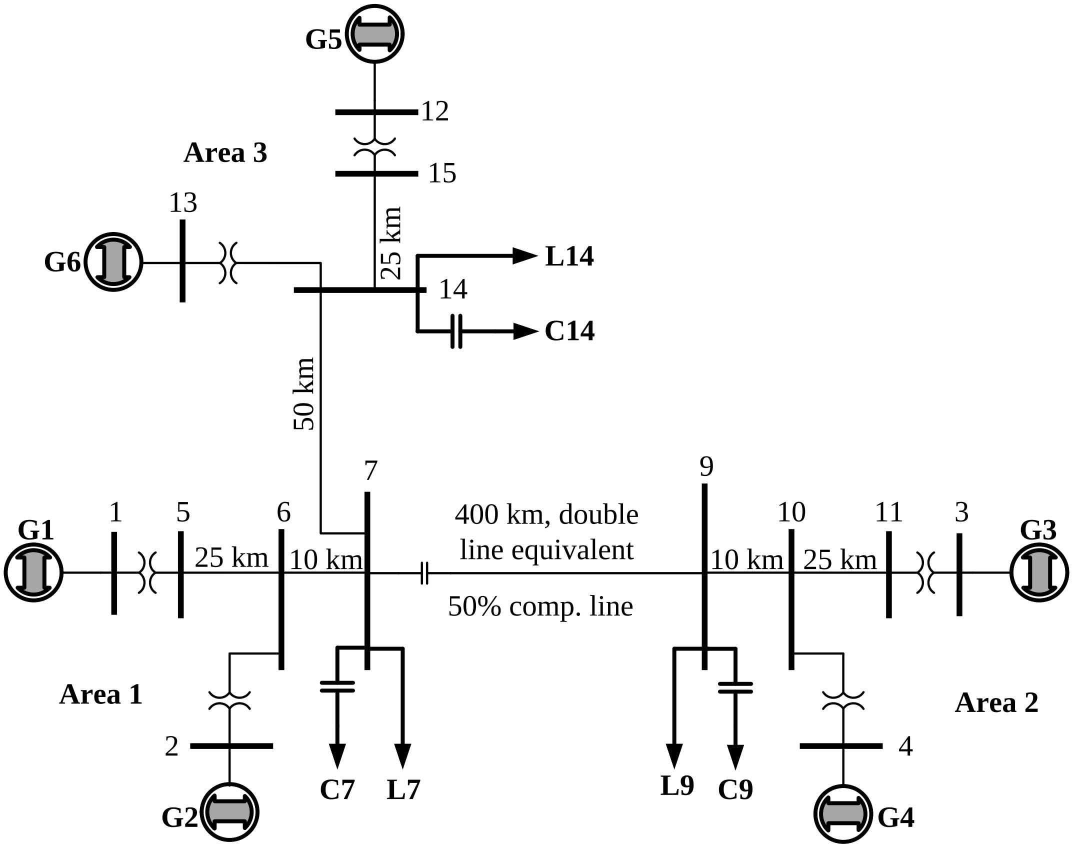

Figure 5.6: A schematic diagram of the 3-area test benchmark with fixed series capacitor compensation.

For the time domain simulation studies, the electromagnetic transient simulation software PSCAD/EMTDC^{TM} is used. The synchronous generators are represented in the $d-q-0$ reference frame using 7^{th} order differential equations [90]. The complete TCSC and SSSC models described in [5] are used in the simulation studies. The transmission lines are modelled as lumped impedances. Dynamics of the generator excitations and governors are included in the simulation to mimic the real power system operation. The inclusion of governor dynamics stabilized the plant for simulation initialization and improves stability during large disturbances. Machine electrical parameters are taken from [77] and given in the Appendix D.2.1.

Case studies: *Three-Area, Six-Machine System*

Five different contingency cases listed in Table 5.1 are considered for the verification of the proposed control algorithm. These cases cover a wide range of power system operating condition and various disturbance scenarios.

Table 5.1: Three-area system: inter-area oscillation damping case studies.

Approximate power flow on line 7-9	Disturbance description	Disturbance type
415 MW	3 cycle, three-phase fault at bus 7	**5A**
415 MW	3 cycle, 2-phase-to-ground (a,b-ground) fault at bus 7	**5B**
220 MW	3 cycle, three-phase fault at bus 7	**5C**
-180 MW	3 cycle, three-phase fault at bus 7	**5D**
415 MW	300 MW load rejection at bus 9, at $t = 1sec.$	**5E**

5.3.2 IEEE 12-Bus System

To further verify the effectiveness of the proposed adaptive controller, an IEEE 12-bus test power system shown in Fig. 5.7 is used [59]. This test system exhibits three lightly damped inter-area modes of oscillation frequencies: 1.12 Hz, 0.85 Hz, and 0.75 Hz, respectively as shown in Table 5.2. The oscillation modes have damping factors of 3.30%, 1.07%, and 7.17%, respectively, which are very close to each other. The size of the system is such that it is large enough to exhibit phenomena such as congestion in power corridors and inter-area oscillations; and yet is small enough to be modelled in detail on electromagnetic transients simulation program. The system is suitable for various FACTS device related studies.

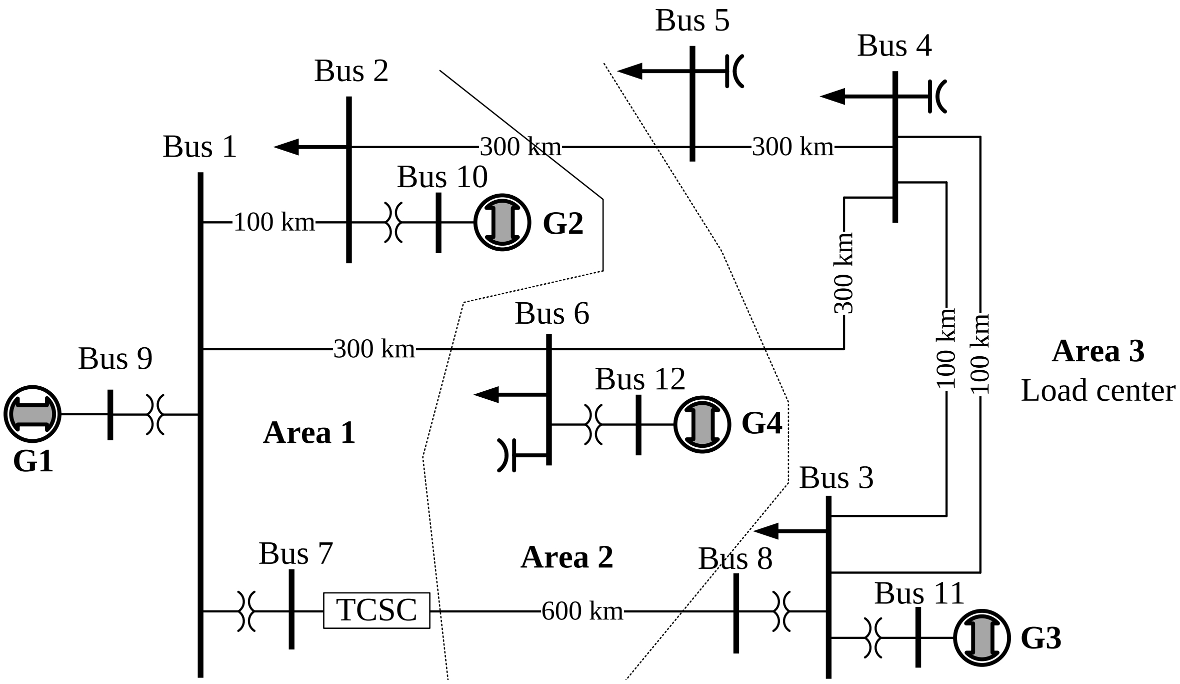

Figure 5.7: IEEE 12-bus test system.

The details of the test system, machine parameters, line data, and system loading conditions are given in the Appendix D.2.3.

Case studies: *IEEE 12-Bus System*

Three contingency cases are studied as shown in Table 5.3 for the validation of the proposed controller.

5.3.3 Lead-lag Supplementary Controller

An optimally tuned fixed parameter lead-lag supplementary controller, as shown in Fig. 5.8, is used to compare the performance of the proposed adaptive controller. It consists of a washout filter, two lead-lag phase compensation blocks, and a gain compensation block.

Table 5.2: Inter-area modes of the IEEE 12-bus test system.

Modes	Real part (σ)	Imaginary part (ω_d)	Frequency (Hz)	Damping ratio ($\zeta, \%$)
1	-0.232	7.027	**1.12**	3.30
2	-0.058	5.332	**0.85**	1.07
3	-0.339	4.710	**0.75**	7.17

Table 5.3: Type of studies on the IEEE 12-bus test system.

Disturbance description	Disturbance type
1-phase-to-ground (a-ground) 200 *ms* fault (bus 3)	**5F**
Three-phase, 200 *ms* fault (bus 3 and 6)	**5G**
Three-phase fault at 100 *km* from bus 4 on line 4-5, fault cleared by disconnecting line 4-5 after 9 *cycles*	**5H**

The time constants and gain of the controller are optimized using multiple time-domain simulation based Simplex algorithm. The multiple time-domain simulation based Simplex optimization technique is discussed in [91], which exploits the advantage of multiple run enabled electromagnetic transient computer simulation tool to optimize the non-linear controller parameters. This tuning procedure is currently being used by the industry for tuning of the controller parameters. More details on the simplex algorithm can be found in [91].

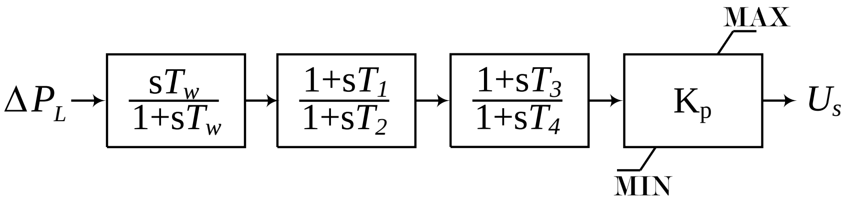

Figure 5.8: Conventional lead-lag supplementary controller.

The objective function used for tuning the conventional lead-lag supplementary controller is given in Eq. (5.23). The symbols T_c and T_s represent fault clearing time and simulation end time, respectively. Similarly, P_L is the tie-line power flow, and P_{L_0} is the steady state pre-disturbance tie-line power flow from line 7-9. Controller tuned to satisfy the objective function expressed in Eq. (5.23) will damp the tie-line power flow deviation effectively.

$$F_{obj}(T_{1,..,4}, K_P) = \int_{T_c}^{T_s} \left[\frac{P_L - P_{L_0}}{P_{L_0}} \right]^2 dt \tag{5.23}$$

5.3.4 Adaptive Pole-shift Controller Development and Integration

A user defined component is created in PSCAD/EMTDC to implement the robust RLS identifier and the pole-shift controller algorithm. The identification and control algorithms are written in FORTRAN programming language using Intel Visual Fortran and Microsoft Visual Studio Integrated Development Environment. This component receives deviation in power flow as input and generates an optimal supplementary control signal for the TCSC or SSSC devices.

A third-order ARMA model is used to approximate the power system dynamics. An Intel Visual Fortran code is developed for implementing identification, control and optimization algorithms and interfaced to the PSCAD/EMTDC simulation environment via the user defined component. A single variable Nelder-Mead simplex optimization algorithm is used to find the optimum pole-shift factor α_{opt} by minimizing the cost function expressed in Eq. (5.21) [92, 93]. This minimizes the deviation between predicted next time-step plant output $\Delta P_L(t+1)$ to the reference plant output $\Delta P_{L,ref}(t+1)$.

Sampling time for the controller is set to 10 Hz (i.e. identifier and controller subroutine are allowed to run at 100 ms interval). The systems under investigation have maximum inter-area oscillation frequencies of 0.78 Hz (for three-area, six-machine system) and 1.12 Hz (for IEEE 12-bus system), and the sampling time of 100 ms is found to be sufficient for both cases.

5.4 Time Domain Simulation Results

In time domain simulation studies, disturbances are applied at 1 *sec* for 3 *cycles*. The performance of the adaptive controller in each case studies listed in Table 5.1 is compared to the:

i. Corresponding case without supplementary controller, and,

ii. Corresponding case with optimally tuned lead-lag supplementary controller.

Moreover, in the following figures illustrating the system time responses, no supplementary controller, traditional lead-lag supplementary controller, and adaptive pole-shift controller are denoted as "*No suppl.*" in red-*dotted*, "*Lead-lag*" in blue-*thin with triangle*, and "*Pole-shift*" in black-*thick* color respectively.

5.4.1 Three-area, Six-Machine System

A. Three-phase Balanced TCSC compensation

This section evaluates the performance of adaptive pole-shift controller in a TCSC compensated three-area, six-machine system. The TCSC is assumed to be installed in the test system near bus 9 between buses 7 and 9 replacing portion of fixed series capacitive compensation of tie-line. The total series compensation is 0.5 *p.u.* of the total line reactance and the TCSC contribution in the total compensation is 0.25 $p.u.$. The deviation in power flow through line 7-9 is considered as plant output. The supplementary control signal ΔkB is considered as plant input.

A.1. Identification - TCSC Compensated System

The estimated system parameters using two RLS estimation algorithms are shown in Fig. 5.9 for disturbance **Case 5A**. Fig. 5.9(a) shows the identified plant parameters using robust RLS algorithm while (b) shows that of commonly used RLS procedure. It is evident that the proposed identification method helps to identify system parameters smoothly even during the large disturbance. In the case of RLS, drastic change in parameter values occurs during and after clearing the disturbance. This sudden change causes the undesirable controller output which leads to poorer damping performance.

Dynamic pole-shifting process that takes place during and after the disturbance for the case study of Fig. 5.9(a) is shown in Fig. 5.10. The closed-loop poles and open-loop poles are captured for the duration of 1 sec to 4.4 sec and plotted as a function of pole-shift factor α. The closed-loop and open-loop poles of the system at time $t = 1.18$ sec are indicated in *triangle*, and, at this time, the pole-shift factor is found to be $\alpha = 0.149$. It can be observed

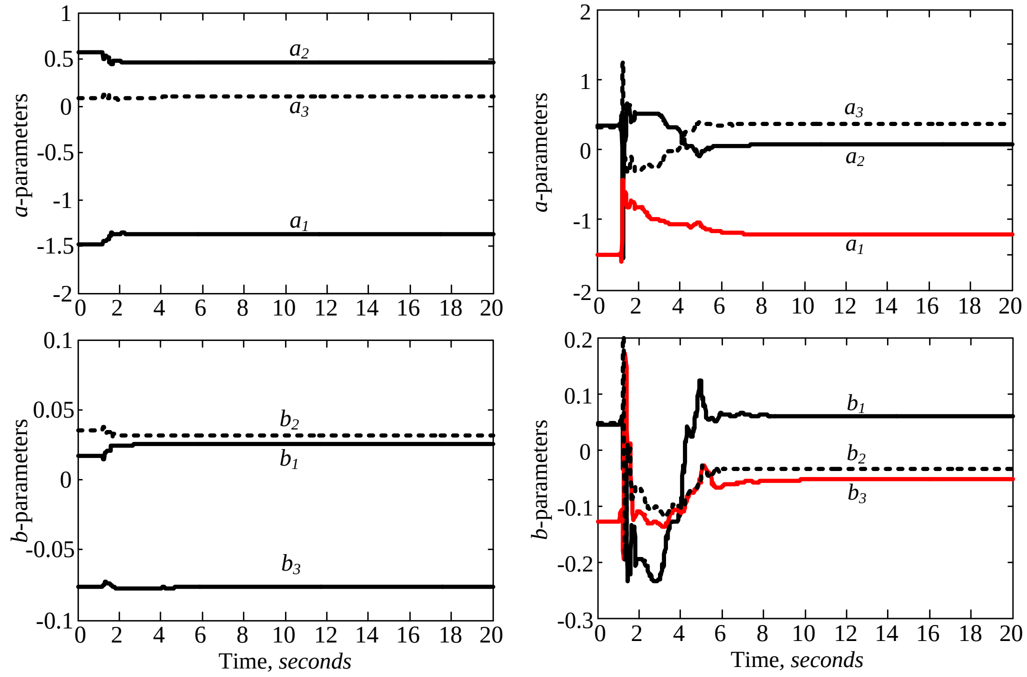

(a) Proposed robust RLS

(b) RLS

Figure 5.9: System parameter identification using RLS techniques in three-area test system, during and after disturbance **Case 5A**.

that, during the transient, there is significant pole-shifting. The controller is generating an optimal control signal by moving poles toward origin. Moreover, it can be noted from the projected plot that the open-loop poles are almost stationary, while the closed-loop poles are being shifted dynamically.

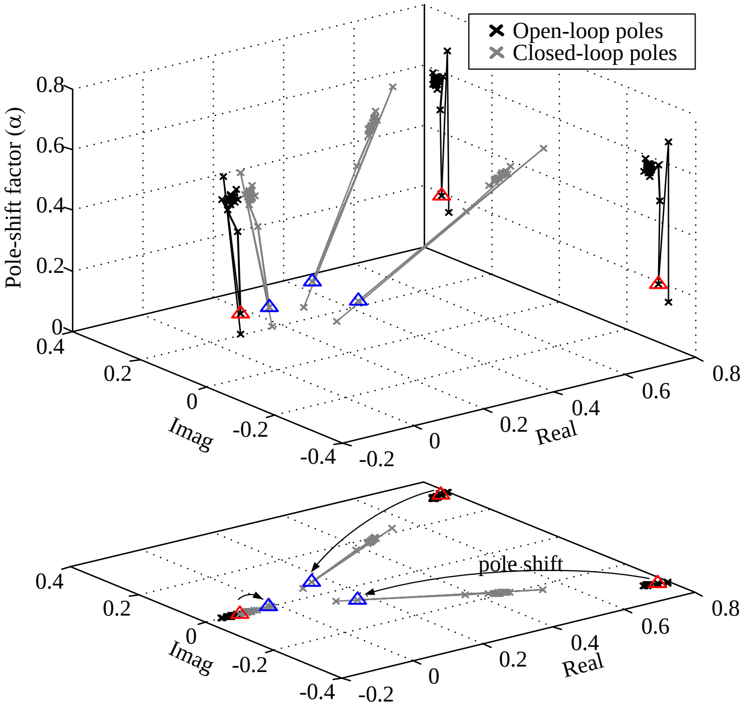

Figure 5.10: Open-loop (*blue*) and closed-loop (*red*) dynamic pole movements as a function of pole-shift factor α, and projection of pole-shifting process in *Real-Imag* axis for the disturbance **Case 5A**.

*A.2. TCSC Case Study **5A***

Case study **5A** corresponds to a 415 MW tie-line power flow through bus 7 to bus 9 and is considered as a base operating case for the rest of the study cases. The fixed parameter lead-lag controller is tuned for this operating condition and the parameters are given in Appendix D.2.2.

Figure 5.11 shows the time response of tie-line power flow (line 7-9) for disturbance **Case 5A**. The identified plant parameters and dynamic pole movement with respect to pole-shift factor for the case of Fig. 5.11a are shown in Fig. 5.9a and 5.10 respectively.

It is evident from the responses that the system is exhibiting poorly damped oscillations and both supplementary controllers helped to damp out the inter-area oscillations significantly faster than without a supplementary controller. The performance of the pole-shift

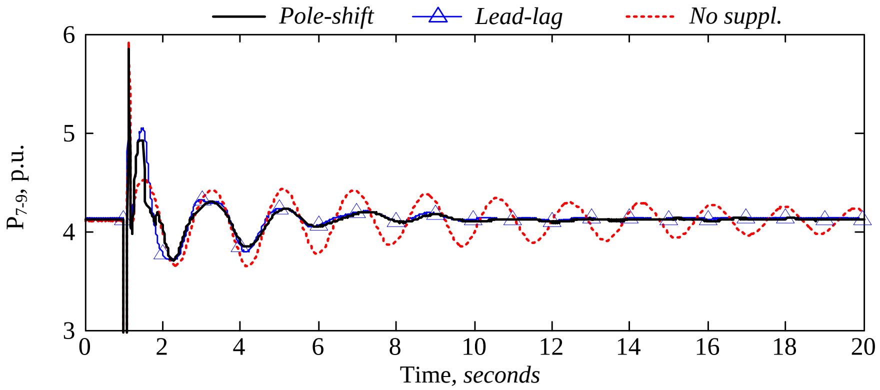

(a) Tie-line power flow (P_{79})

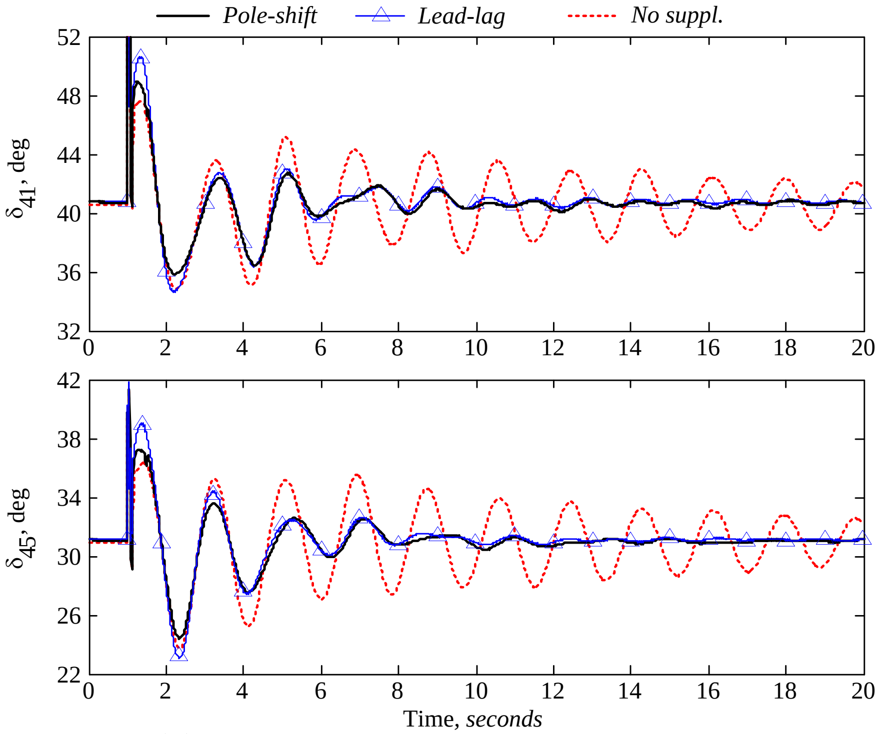

(b) Generator load-angles $G_1 - G_4$ and $G_5 - G_4$

Figure 5.11: Time responses of the (a) tie-line power flow and (b) generators load angle for disturbance **Case 5A**.

controller in this operating condition is slightly better than the Simplex tuned lead-lag controller. The real advantage of the pole-shift controller is that the algorithm needs very little information of the plant, and the control response will be consistent for wide range of operating condition, whereas in the case of lead-lag controller, a detailed model of the system is required to properly tune the parameters.

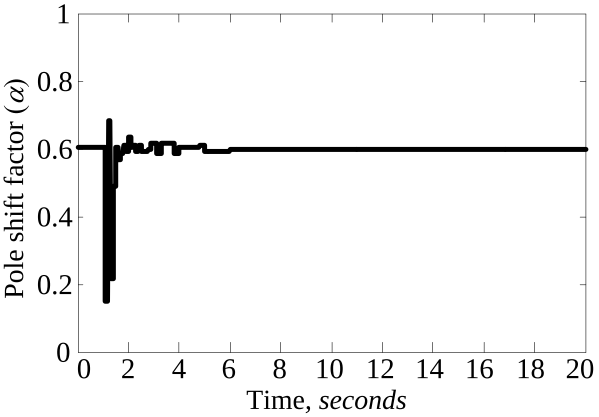

(a) Pole-shift factor α

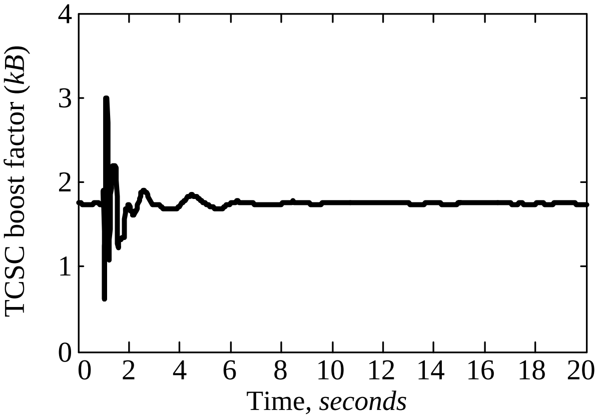

(b) TCSC boost factor kB

Figure 5.12: Time response of the (a) pole-shift factor and (b) TCSC boost factor for disturbance **Case 5A**.

*A.3. TCSC Case Study **5B***

The case study **5B** is a two phase-to-ground (a,b-ground) unsymmetrical fault at bus 7, and the power flow is similar to the study **Case 5A**. Figure 5.13 shows the time response of tie-line power flow (line 7-9) and generator rotor angle deviations of G_1 and G_5 with respect to G_4. From the response plots in Fig. 5.13, it is evident that the proposed controller is able to suppress the first swing and settles the subsequent swings within $8 - 10$ *sec* after the clearance of the disturbance. Furthermore, the performance of the pole-shift controller is relatively better than the lead-lag controller.

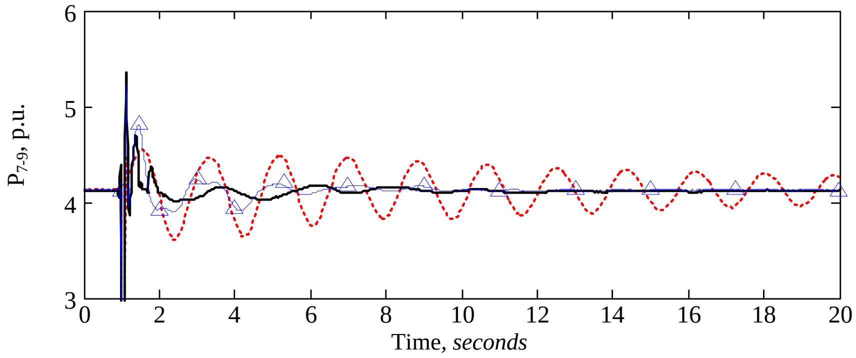

(a) Tie-line power flow (P7-9)

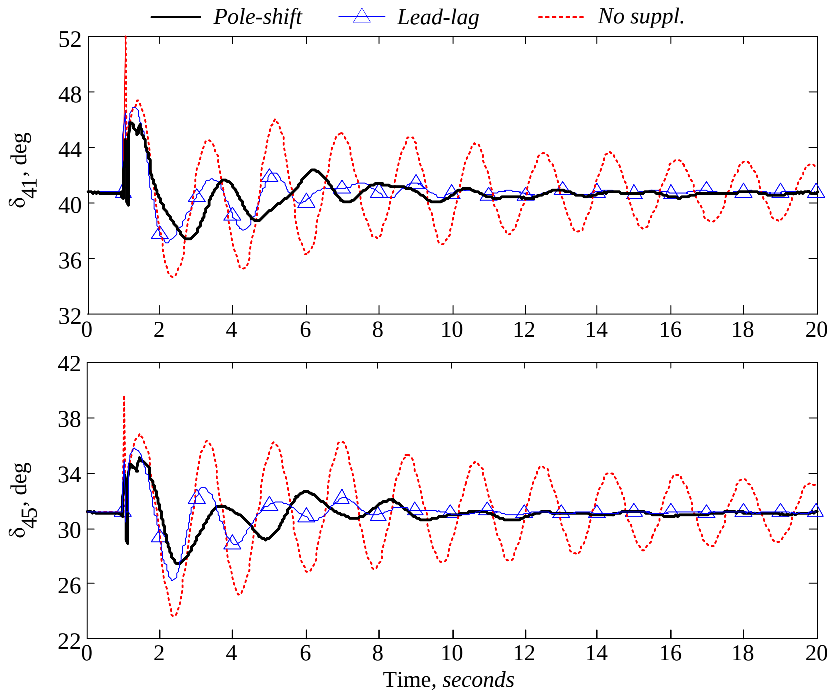

(b) Generator rotor angles $G_1 - G_4$ and $G_5 - G_4$

Figure 5.13: Tie-line power flow and relative generator load angle time responses for disturbance **Case 5B**.

A.4. TCSC Case Study ***5C***

The case study **5C** corresponds to the lower tie-line power flow scenario. The operating condition is achieved by reducing load on bus 9. This type of operation is very common in the complex power system. In this operating condition, the generator oscillation will have less amplitude. The conventional controller may give small damping effort leading to longer settling time, whereas the adaptive controller adapts to new operating conditions automatically and yields optimal performance. Fig. 5.14 shows the time response of the generator rotor angle deviations of G_1 and G_5 with respect to G_4. Note that the generator

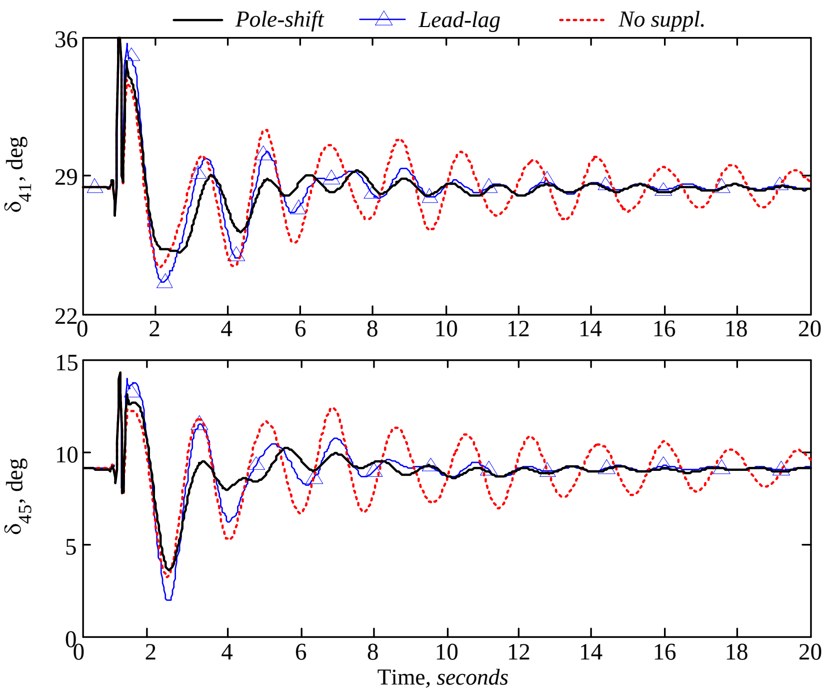

Figure 5.14: Relative generator load angle time responses for disturbance **Case 5C**.

angle deviation has smaller magnitude than study **Case 5A** (Fig. 5.11b). The pole-shift controller is providing lower oscillation amplitude and faster settling time compared to the lead-lag controller, as expected.

*A.5. TCSC Case Study **5D***

The case study **5D** is used to test performance of adaptive controller to the tie-line power flow reversal. The tie-line power flow on line 7-9 (from bus 9 to bus 7) is set to 180 MW by increasing loads on bus 7 and decreasing loads on bus 9. This type of operation is very likely to occur in a highly inter-connected power system.

Figure 5.15 shows the time response of the generator rotor angle deviations of G_1 and G_5 with respect to G_4. Note that in the case of lead-lag supplementary controller, a negative gain is used, because of the reversal in power flow through tie-line 7-9. The lead-lag controller would need a logical element, such as a power reversal function (for example, power reversal relay (32) [94]), or in the context of modern power systems, a Phasor Measurement Unit (PMU) to detect the power reversal and adjust the sign of the gain for the controller. However, the adaptive controller without any additional logical element very effectively damps the inter-area oscillations, for the reversed power flow condition.

Similarly, Fig. 5.16 shows the same time responses of Fig. 5.15 for a positive gain. In this case, system becomes unstable after the clearing of the disturbance. The reason behind

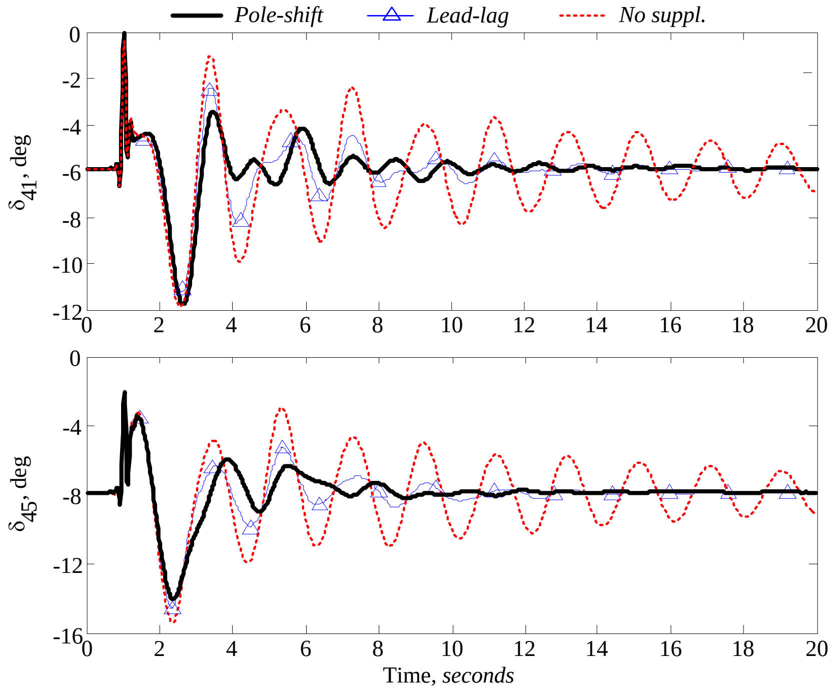

Figure 5.15: Generators G_1 and G_5 load angle time responses, measured with respect to G_4 load angle for disturbance **Case 5D** (negative lead-lag controller gain).

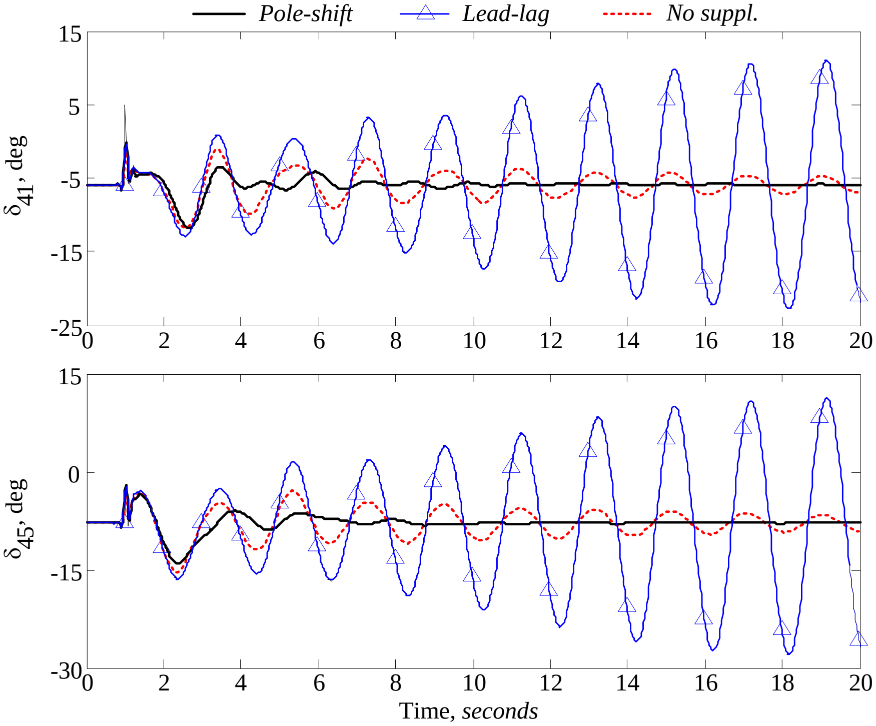

Figure 5.16: Generators G_1 and G_5 load angle time responses, measured with respect to G_4 load angle for disturbance **Case 5D** (positive lead-lag controller gain).

this is that the actual lead-lag controller is tuned for study **Case 5A**, and stabilizing signal reverses its polarity in this operating condition. The conventional controller should be re-tuned at this new operating condition for the proper operation. It is to be noted that, however, in case of pole-shift controller, the identifier properly identifies parameters for new operating conditions and the controller generates a stable supplementary control signal.

*A.6. TCSC Case Study **5E***

In this case study, a 300 MW load is disconnected from bus 9 at $t = 1$ sec keeping the operating condition of **Case 5A**. This causes huge disturbance on the network. The tie-line power flow and the load angle of generator G_1 measured with respect to G_4 at these operating conditions are shown in Figs. 5.17.

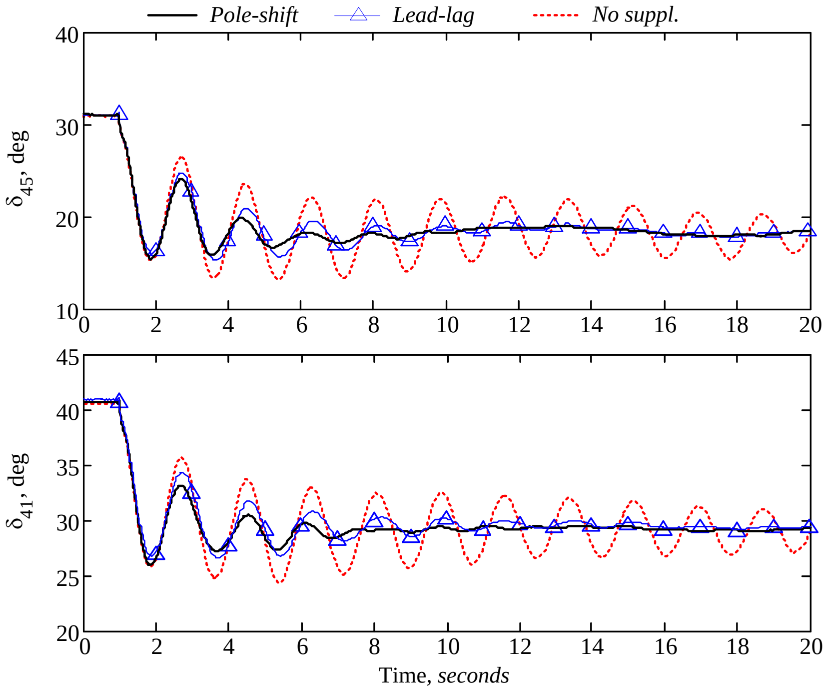

Figure 5.17: Tie-line power flow and relative generator load angle time responses for disturbance **Case 5E**.

Comparing the responses of the Figs. 5.11 to 5.17, the positive contribution of the proposed adaptive pole-shift controller to the damping of the inter-area oscillations is very clear. As it can be observed from Figs. 5.11(b), 5.13(b), 5.14, 5.15 and 5.17, the adaptive pole-shift controller reduces the first swing and effectively damps the subsequent swings during different operating conditions.

To verify the effectiveness of the adaptive pole-shift based damping controller in presence of PSSs in the system, three PSSs are then connected to generators G_1, G_3, and G_5 of area 1, 2 and 3, respectively. The operating condition of the system is the same as **Case 5A**. A set of optimal PSSs parameters used in this case study are obtained using a multiple time-domain simulation based Simplex optimization procedure and those values are given in Appendix D.2.2.

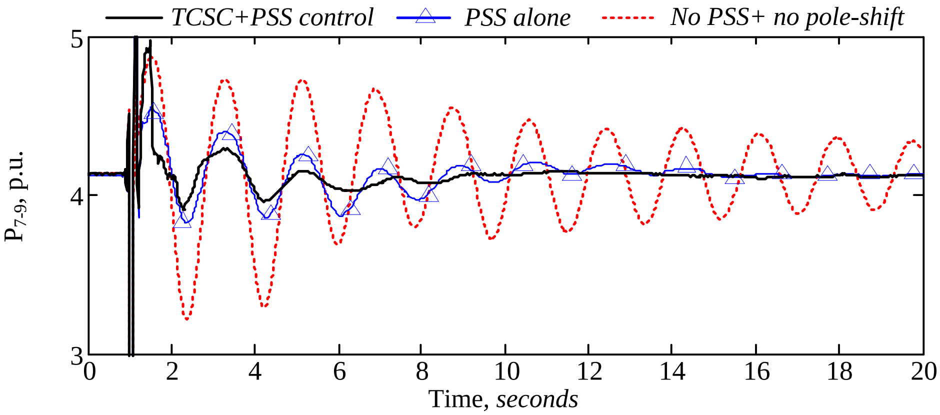

Figure 5.18: Tie-line power flow time responses in presence of PSS units for disturbance **Case 5A**.

Figure 5.18 shows the time response for the tie-line (line 7-9) power flow during and after disturbance **Case 5A**. The Prony analysis reveals the approximate damping factors as 1.96, 7.31 and 15.23% for (*i*) in absence of PSSs and supplementary pole-shift controller for TCSC, (*ii*) only PSSs, and (*iii*) in presence of PSS and supplementary pole-shift controller for TCSC, respectively. The result shows that even with PSSs in the system, TCSC, aided by adaptive pole-shift damping controller, provides better damping and reduces the settling time of the system oscillatory modes.

B. Three-Phase Balanced SSSC Compensation Studies

This sub-section evaluates the effectiveness of the proposed adaptive pole-shift controller for damping inter-area oscillation on the three-area, six-machine test system (Fig. 5.6) consisting of an SSSC compensated transmission line. The SSSC is installed on the test system near bus 9 between buses 7 and 9, replacing the portion of fixed series capacitive compensation of the tie-line. The total series compensation is 0.5 *p.u.* of the total line reactance and the SSSC contribution in the total compensation is 0.25 *p.u.* The deviation in power flow through line 7-9 is also considered as plant output. The supplementary control signal

U_s is considered as plant input. The studies are carried out for contingency cases presented in Table 5.1.

B.1. System Identification - SSSC Compensated System

The parameter tracking capability of the two RLS estimation algorithms is shown in Fig. 5.19 for the disturbance **Case 5A**. Figure 5.19(a) shows the identified plant parameters using the robust RLS algorithm. Similarly, Fig. 5.19(b) shows the estimated plant parameters for the same case study of Figure 5.19(a), using the RLS algorithm. It is evident from these tracking responses that the proposed identification method helps to identify the system parameters smoothly, even during a large disturbance. The normal RLS algorithm exhibited large deviation in parameter estimation during the disturbance and after clearing it. This large deviation in parameters value cause an undesirable controller output, which leads to a poorly damped performance, as shown in Fig. 5.20.

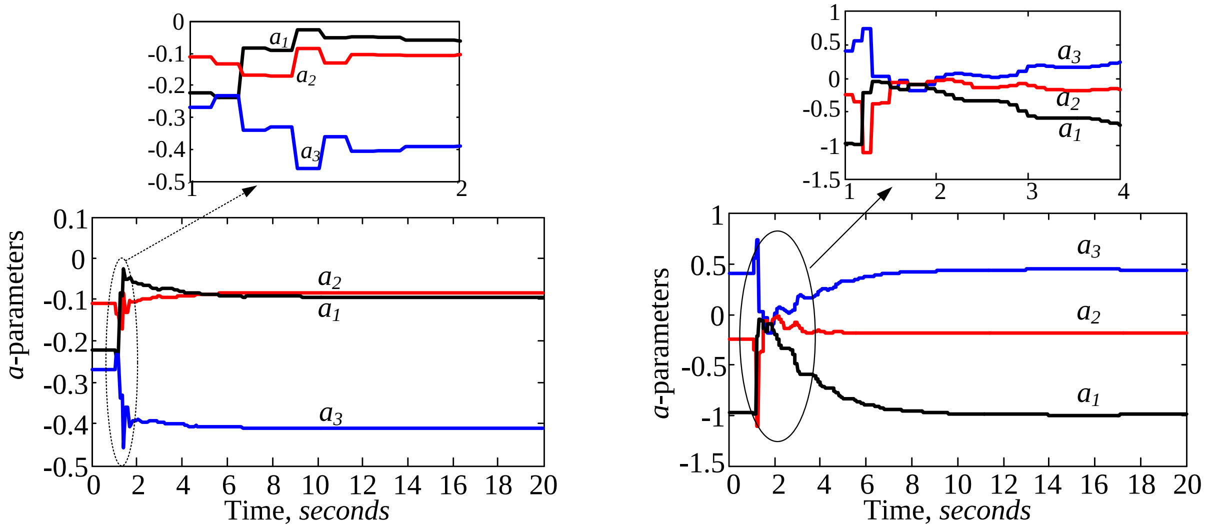

(a) Proposed robust RLS

(b) Normal RLS

Figure 5.19: Parameter identification using RLS technique for the disturbance **Case 5A**.

Figure 5.21 shows the dynamic pole-shifting process for the case study of Fig. 5.19(a). The closed-loop poles and open-loop poles are captured for the time stamp of $t = 1.18$ *sec* and corresponding pole-shift factor is $\alpha = 0.59$. It can be observed from the result that there is a significant pole-shifting taking place during transients. The controller generates optimal control signal by moving poles closer to the origin.

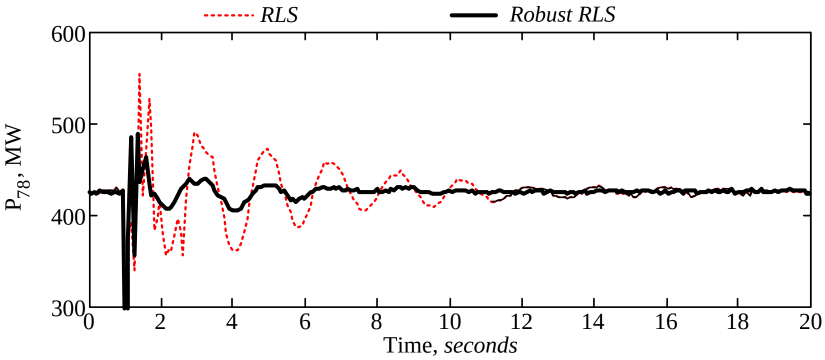

Figure 5.20: Damping comparison for two RLS algorithms for the disturbance **Case 5A**

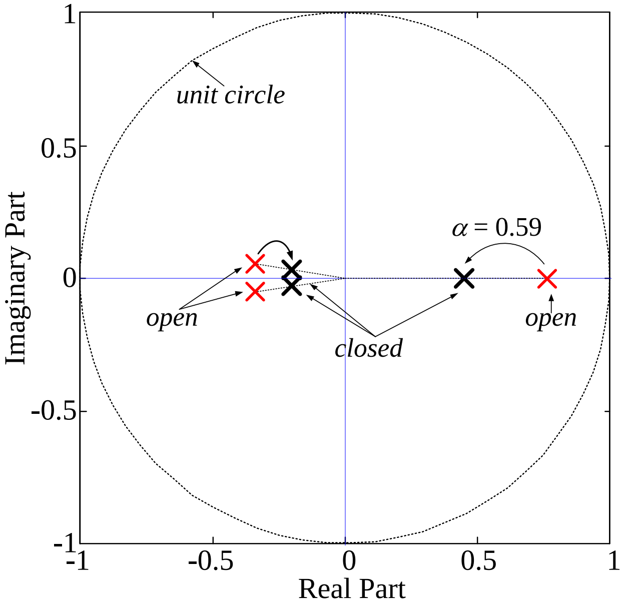

Figure 5.21: Dynamic poles movement as a function of pole-shift factor α for the disturbance **Case 5A**, captured at $t = 1.18$ *sec.*

*B.2. SSSC Case Study **5A***

Case study **5A** is considered as a base operating case for the rest of the contingency cases. The fixed parameter lead-lag controller is tuned for this operating condition, and the parameters are given in Appendix D.2.2.

Figure 5.22 shows the time response of tie-line power flow (line 7-9) and relative generator rotor angle plot for disturbance **Case 5A**. The effectiveness of the proposed adaptive pole-shift supplementary controller in damping inter-area oscillations is demonstrated through relative generator rotor angle time response shown Fig. 5.22(a). The response shows that the adaptive controller damps the tie-line power oscillations relatively faster than the lead-

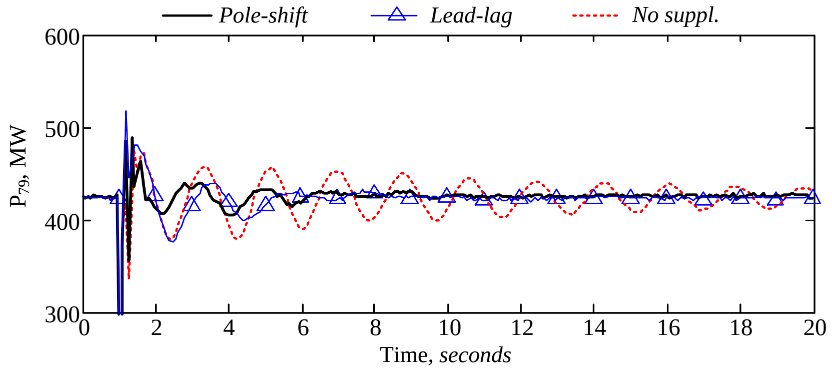

(a) Tie-line power flows (P7-9)

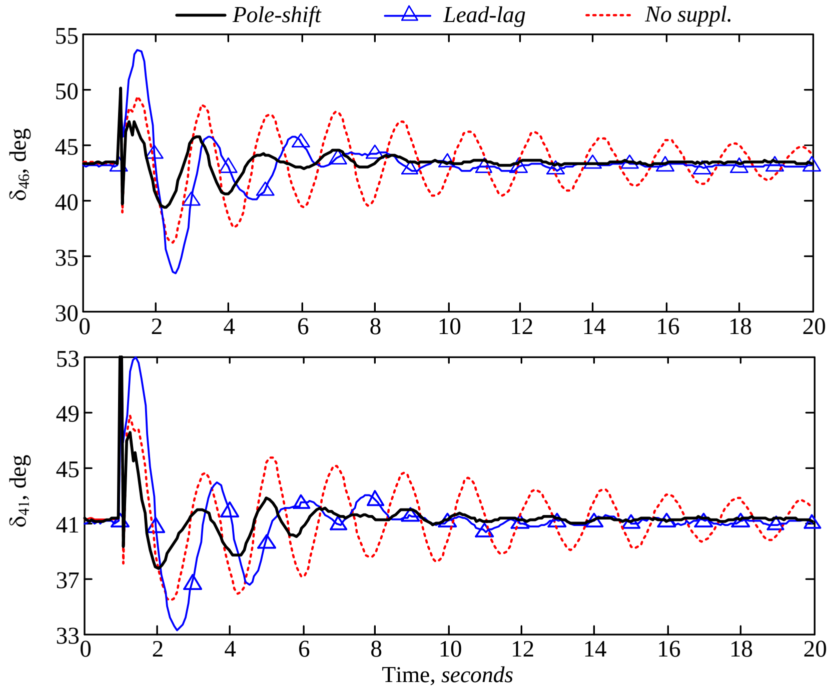

(b) Generator rotor angle $G_4 - G_1$ and $G_4 - G_5$

Figure 5.22: Tie-line power flow and relative generator rotor angle time responses for disturbance **Case 5A**.

lag controller. The identified plant parameters and dynamic pole movement with respect to pole-shift factor for the case of Fig. 5.22 are shown in Figs. 5.19(a) and 5.21 respectively. Furthermore, Fig. 5.23 shows the control signal generated and DC capacitor voltage of SSSC.

*B.3. SSSC Case Study **5B***

The case study **5B** is a two phase-to-ground (a,b-ground) unsymmetrical fault at bus 7, and the power flow is similar to the **Case 5A**. Fig. 5.24 shows the time response of tie-line

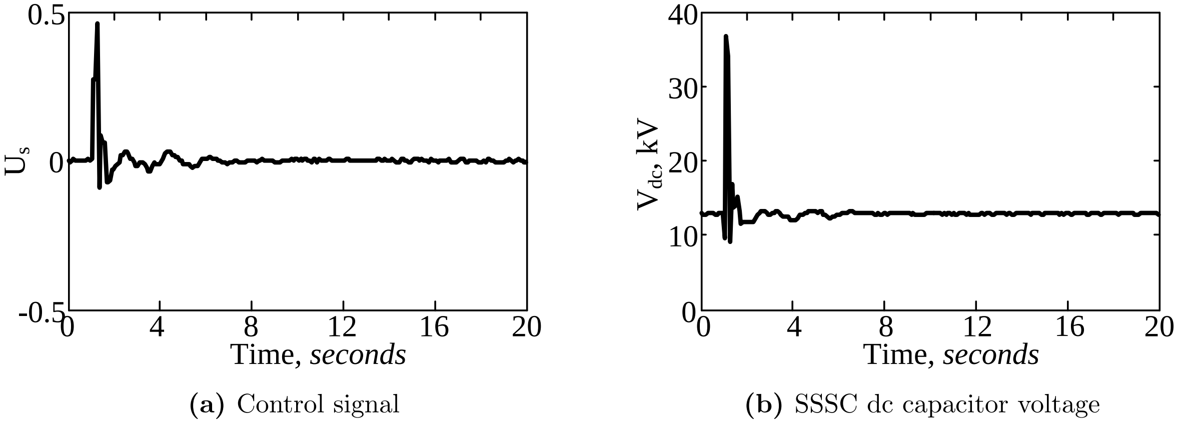

(a) Control signal

(b) SSSC dc capacitor voltage

Figure 5.23: Control signal and SSSC dc capacitor voltage variations for the disturbance **Case 5A**.

power flow (line 7-9) and generator rotor angle deviations of G_1 and G_5 with respect to G_4. The time response plots in Fig. 5.24 clearly demonstrate the effectiveness of the proposed controller in power oscillations. The adaptive controller is able to suppress first swing and damps the subsequent swings within $8 - 10$ *sec* after the clearance of the disturbance. The performance of the pole-shift controller is relatively better than the lead-lag controller.

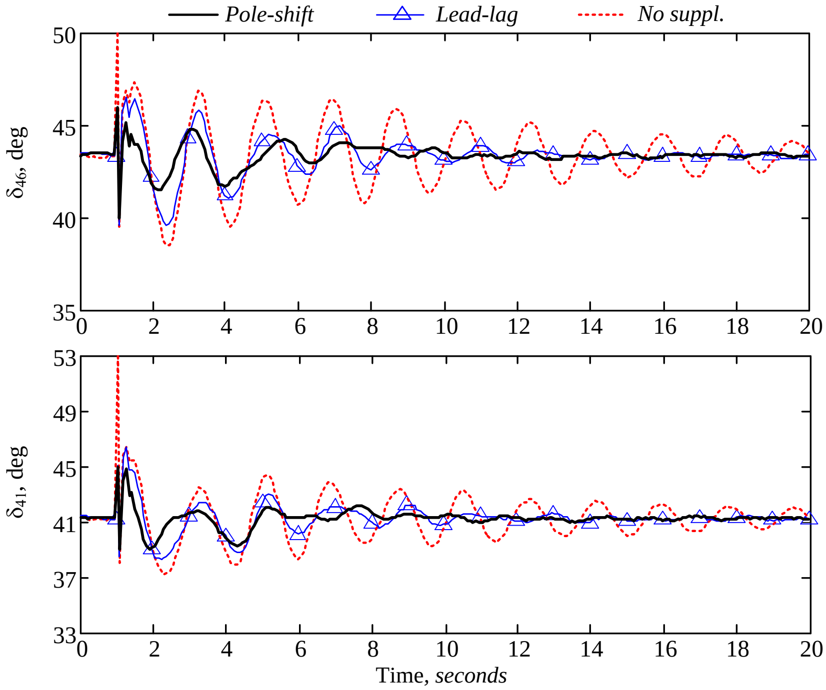

Figure 5.24: Relative generator load angles time response for disturbance **Case 5B**.

B.4. SSSC Case Study ***5C***

This case study **5C** is used to study performance of the adaptive pole-shift controller during lower tie-line power flow scenarios. Figure 5.25 shows the time response of the relative generator rotor angle deviations $G_4 - G_1$ and $G_4 - G_5$. Note that the generator angle deviation has smaller magnitude than **Case 5A** (Fig. 5.22b). The pole-shift controller results in lesser oscillation amplitude and faster settling time compared to the lead-lag controller, as expected.

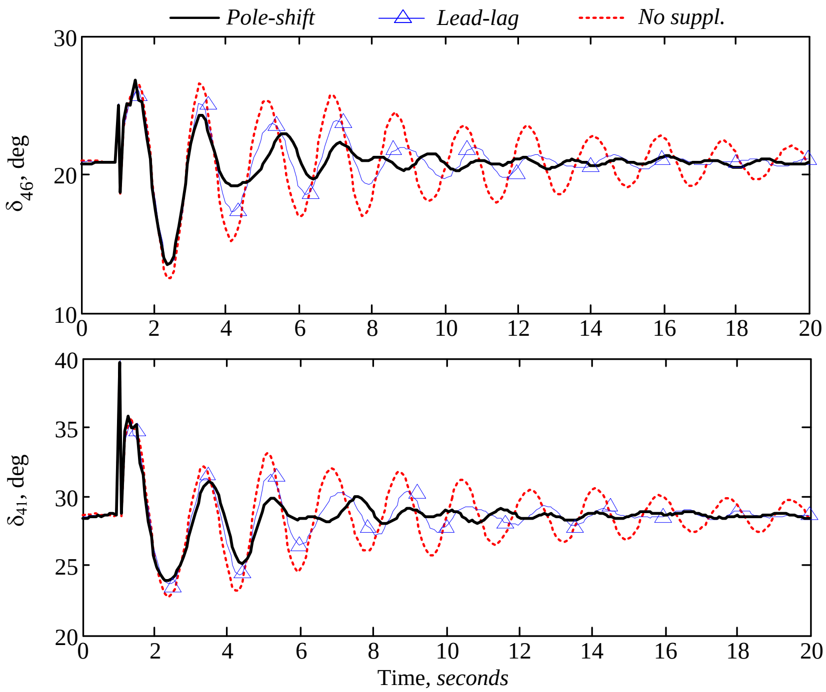

Figure 5.25: Relative generator load angles time response for disturbance **Case 5C**.

B.5. SSSC Case Study ***5D***

The case study **5D** is used to test performance of adaptive controller to the tie-line power flow reversal. The tie-line power flow on line 7-9 (from bus 9 to bus 7) is set to 180 MW by increasing loads on bus 7 and decreasing loads on bus 9. This type of operation is very likely to occur in a highly inter-connected power system. Although the power flow changed direction, the input to the supplementary controllers (lead-lag and pole-shift) are kept the same as previous cases.

Figure 5.26 shows the G_1 and G_6 load angles, measured with respect to G_4 load angle for the disturbance **Case 5D**. Note that again in the case of lead-lag supplementary controller, a negative gain is used, because of the reversal in power flow through tie-line 7-9. It can be

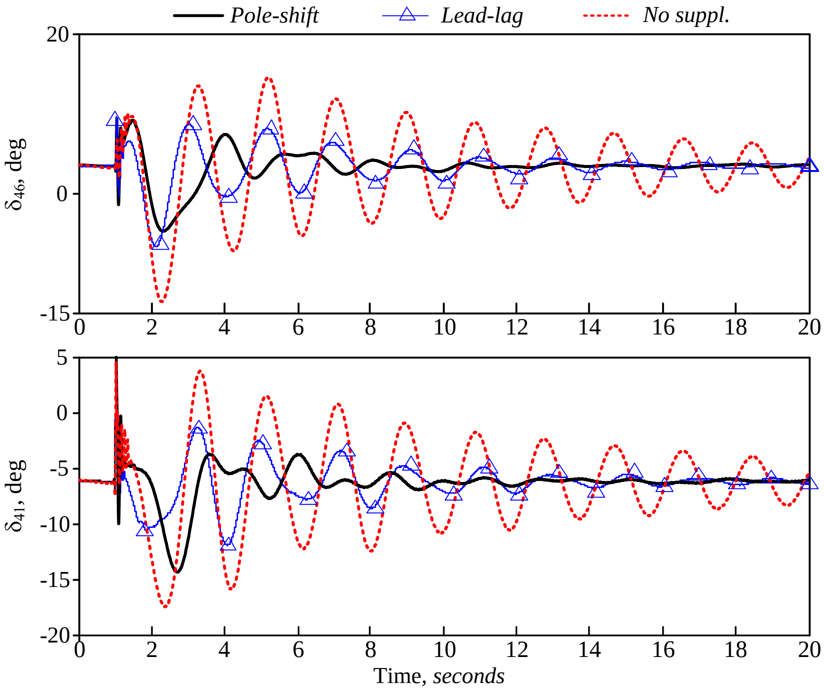

Figure 5.26: Tie-line power flow and relative generator rotor angle time responses for disturbance **Case 5D** (negative lead-lag gain).

seen from the responses again that the adaptive controller self-adjusts without any external logical element to effectively damp the inter-area oscillations, when the power flow reverses.

Figure 5.27 shows the same time responses of Fig. 5.26 for a positive gain. The time response of the conventional lead-lag controller case shows sustained oscillation, when the feedback signal is as it is. The conventional controller would need a separate triggering signal to detect the reversal of power flow so that the gain can be adjusted to a negative value in order to achieve the proper operation for the controller. On the other hand, the proposed adaptive controller, without any external interference, adjusts to a correct set of identified parameters, and generates a stable control behaviour.

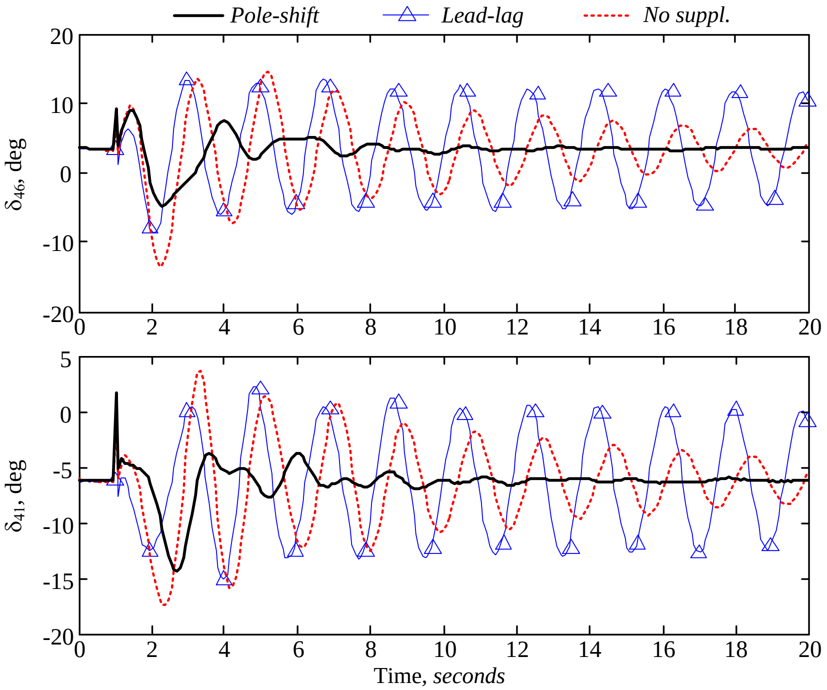

Figure 5.27: Tie-line power flow and relative generator rotor angle time responses for disturbance **Case 5D** (positive lead-lag gain).

B.6. SSSC Case Study ***5E***

This case is used to study the performance of proposed adaptive controller during significant change in operating condition. A significant change in operating point is achieved by disconnecting a 300 MW load at bus 9 at $t = 0$ sec, connecting at $t = 10$ sec and again disconnecting at $t = 35$ sec . The time response of relative generator rotor angles $G_4 - G_1$ and $G_4 - G_6$ are shown in Fig. 5.28. The simulation results shown in Fig. 5.28 demonstrates that the pole-shift control provides better damping and faster settling time than the lead-lag controller. It should be noted here that the lead-lag controller has been optimized for **Case 5A**, and its performance deteriorated as the operating point changed to a new value.

From the responses shown in Figs. 5.22 to 5.28, it can be easily seen that the pole-shift controller is very effective in damping the inter-area oscillations. As seen from Figs. 5.22(b), 5.24, 5.25, 5.27, and 5.28, the proposed controller reduces the first swing and also effectively damps the subsequent swings for various operating conditions.

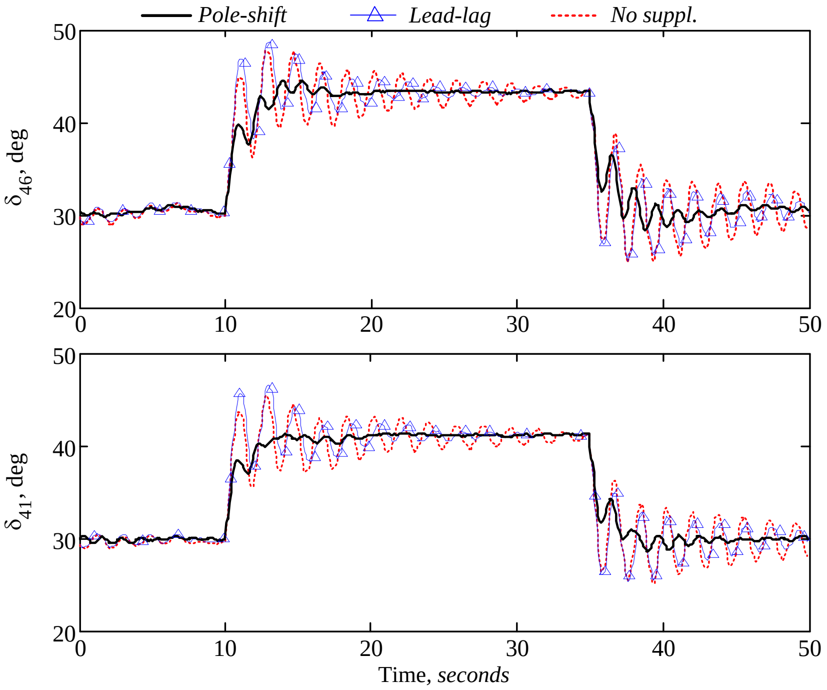

Figure 5.28: Generators G_1 and G_6 load angle, measured with respect to G_4 load angle, for the disturbance **Case 5E**.

C. Approximate Damping Factor Calculation for Three-Area, Six-Machine Test System

The approximate damping factor is calculated using Prony analysis tool provided in the commercial power system analysis software tool DSATools$^{\text{TM}}$. For this purpose, tie-line power flow between buses 7-9 is taken under consideration.

C.1. Three-phase TCSC Compensation Studies

The damping factors are calculated for the most dominant mode and are given in Table 5.4. The damping provided in the presence of the pole-shift supplementary controller is relatively higher than that of no supplementary case and lead-lag supplementary case. Furthermore, the table shows that the pole-shift controller in the presence of the power system stabilizers is very effective in damping the oscillations.

Table 5.4: Approximate damping factor (in %) - Balanced TCSC.

Simulation cases	Controllers		
	No suppl.	Lead-lag	Pole-shift
5A	1.963	12.676	13.715
5B	1.71	12.861	10.171
5C	2.093	11.544	24.91
5D	2.44	-2.291	13.957
5E	1.586	6.436	13.404
In presence of PSS, **Case 5A**	No PSSs	PSSs	PSSs+ Pole-shift
	1.96	7.31	15.23

C.2. Three-phase SSSC Compensation Studies

For this purpose, tie-line power flow through SSSC, between buses 7-8, is taken under consideration. The damping factors are presented in Table 5.5.

Table 5.5: Approximate damping factor (in %) - Balanced SSSC.

Simulation cases	Controllers		
	No suppl.	Lead-lag	Pole-shift
5A	2.316	7.24	11.23
5B	2.622	7.302	12.346
5C	2.66	6.288	17.73
5D	2.52	0.327	15.32
5E	2.431	3.958	5.351

It can be observed that the damping provided in presence of the pole-shift supplementary controller is significantly higher than that of no supplementary case and lead-lag supplementary case, indicating effectiveness of the proposed method.

D. Hybrid TCSC and SSSC Compensated System

The hybrid TCSC and SSSC compensation schemes are used to replace the fixed capacitors of the test system in Fig. 5.6. The simulation results for the disturbance **Case 5A** (Table 5.1) are presented in Figs. 5.29 and 5.30, respectively.

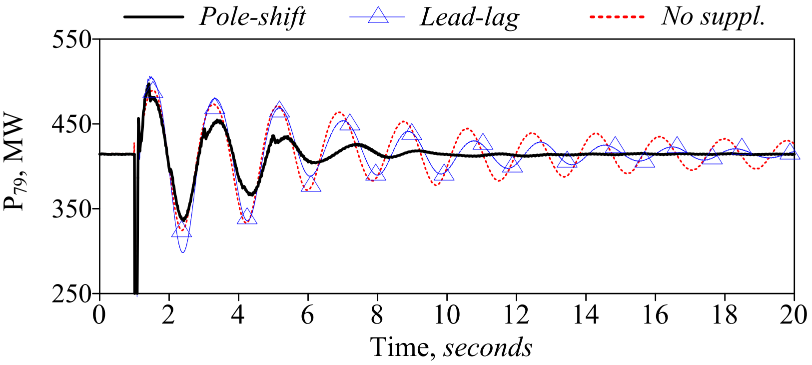

(a) Tie-line power flow (P_{79})

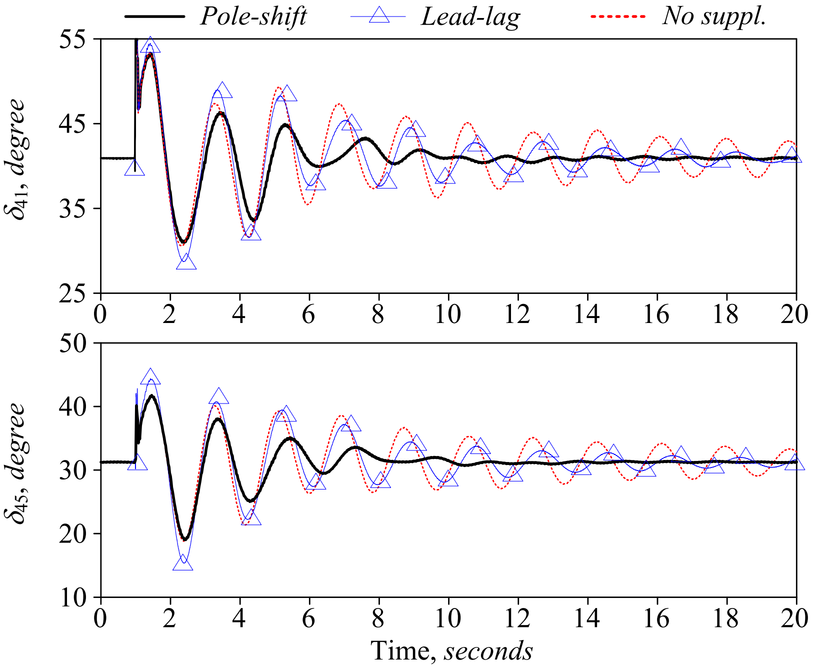

(b) Generator load-angles ($G_1 - G_4$ and $G_5 - G_4$)

Figure 5.29: Hybrid TCSC case: Tie-line power flow and generators load angle responses for disturbance **Case 5A**.

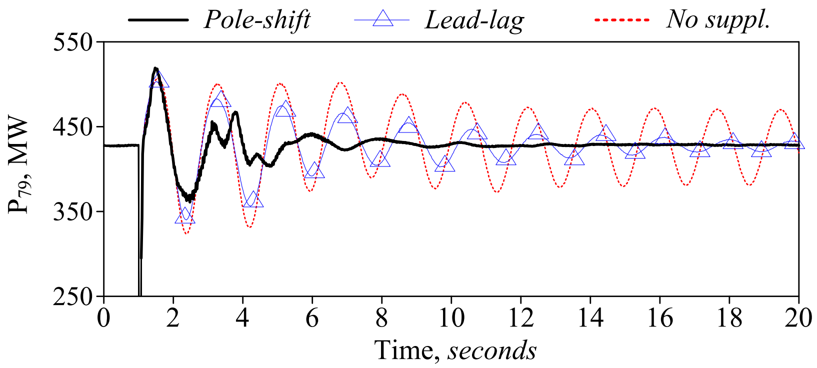

(a) Tie-line power flow (P_{79})

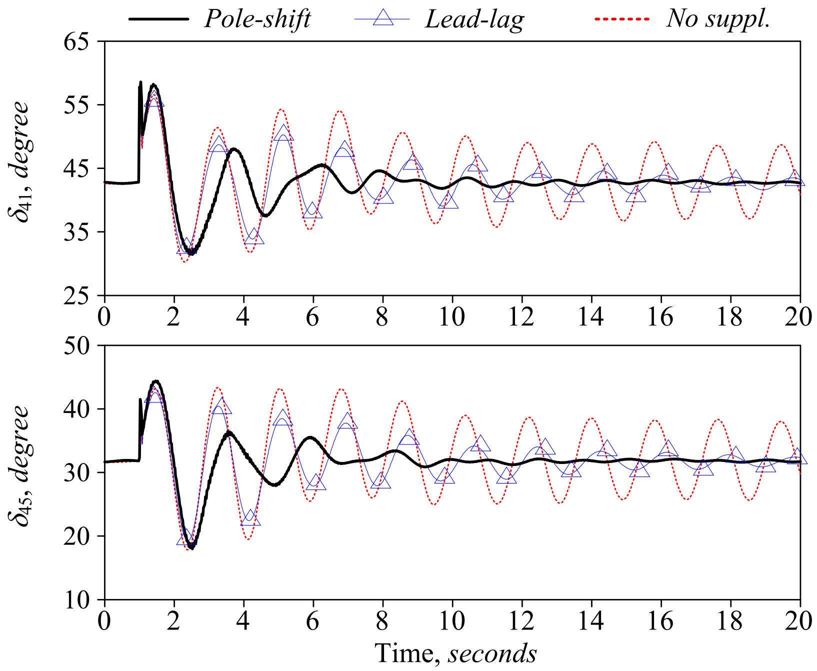

(b) Generator load angles ($G_4 - G_1$ and $G_4 - G_6$)

Figure 5.30: Hybrid SSSC case: Tie-line power flow and generators load angle responses for disturbance **Case 5A**.

5.4.2 IEEE 12-Bus System

For the time domain simulation studies, a TCSC unit is placed near bus 7 between line 7-8 of the test system shown in Fig. 5.7. The steady-state series capacitive compensation provided by the TCSC is 0.15 *p.u.* of the total line impedance. The power flowing through line 7-8 is taken as input to the supplementary controller [59]. Three test cases (Table 5.3) are studied to validate the performance of the proposed adaptive controller. The disturbances are applied at $t = 1$ *sec* and responses are plotted for a 0 to 10 *sec* time window. Moreover, in the following figures illustrating the system time responses, no supplementary controller, traditional lead-lag supplementary controller and adaptive pole-shift controller are denoted as "*No suppl.*" in red-*dotted*, "*Lead-lag*" in blue-*with triangles*, and "*Pole-shift*" in black-*thick* color, respectively.

A. Case Study 5F

This test case represents a single line-to-ground fault at bus 3. This type of disturbance is most common in power systems. Figure 5.31 shows the time responses of the tie-line power flow (line 7-8) and relative rotor angle deviation of G_3 with respect to G_1 for the disturbance **Case 5F**. The simulation results shown in Fig. 5.31 demonstrate that the pole-shift control provides better damping and faster settling time compared to the lead-lag controller.

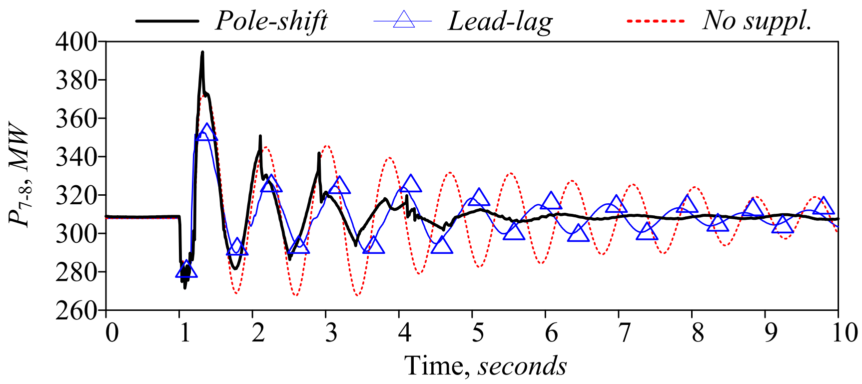

(a) Power flow on line 7-8

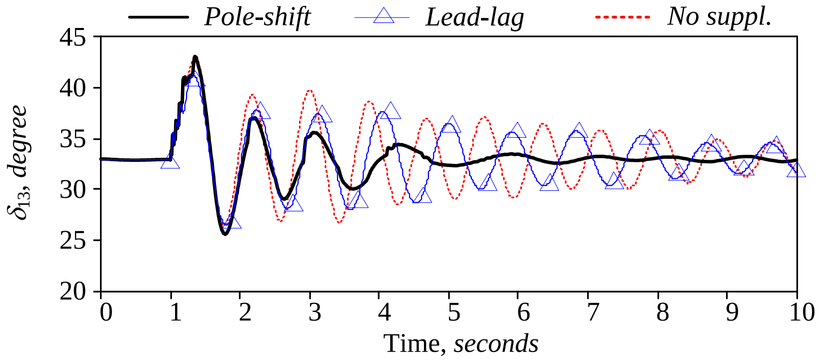

(b) Generator rotor angle δ_{13}

Figure 5.31: Line power flow and relative rotor angle variations for the disturbance **Case 5F** (IEEE 12-bus test system, balanced TCSC).

The identified system parameters, control signal generated using pole-shift algorithm and pole-shift factor for the case studies of **Case 5F** (Fig. 5.31) are shown in Fig. 5.32.

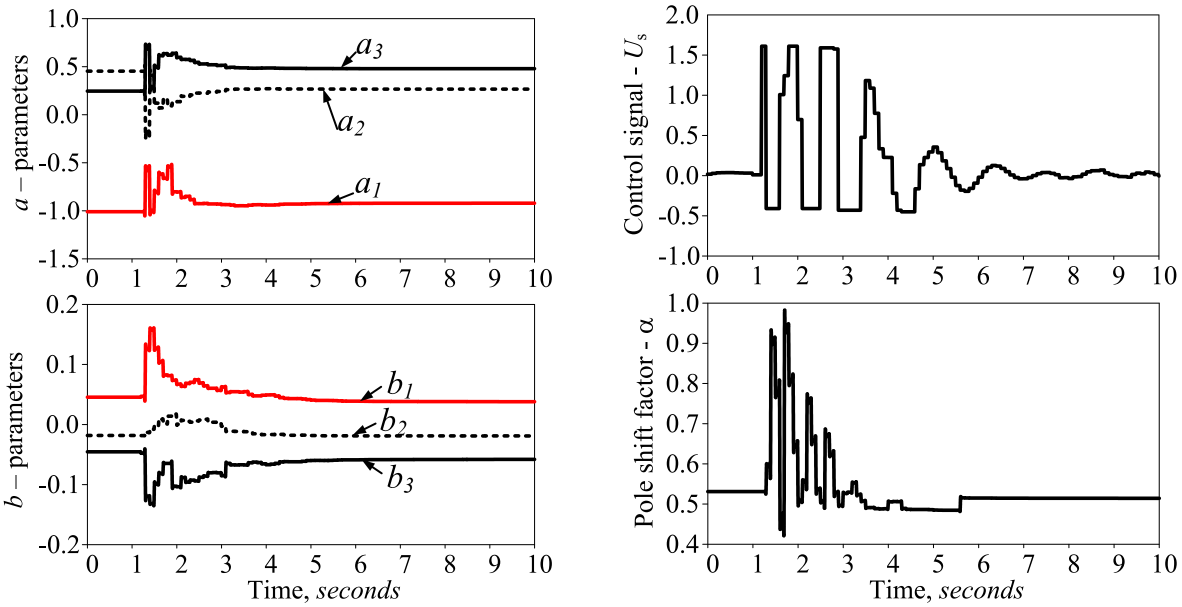

(a) System parameters: a and b **(b)** Control signal and pole-shift factor

Figure 5.32: Identified system parameters, control signal and pole-shift factor plots for disturbance of Fig. 5.31.

The response plot of Fig. 5.32(a) shows the smooth parameter variation during and after disturbance.

B. Case Study 5G

This case study is used to study the performance of the proposed controller during severe system disturbance. The disturbance is created by applying simultaneous three-phase fault at buses 3 and 6. Two simultaneous faults are applied to excite the multi-mode oscillations in the system. The lead-lag supplementary controller is tuned for this operating condition and parameters are given in Appendix D.2.3.

Figure 5.33 shows time response of the tie-line power flow (line 7-8) and relative generator rotor angle deviation of generator G_3 with respect to G_1. It is evident from the responses that the system exhibits poorly damped oscillations and both supplementary controllers help to damp out the inter-area oscillations significantly faster than without supplementary controller. The performance of pole-shift controller in this operating condition is relatively better than Simplex tuned lead-lag controller.

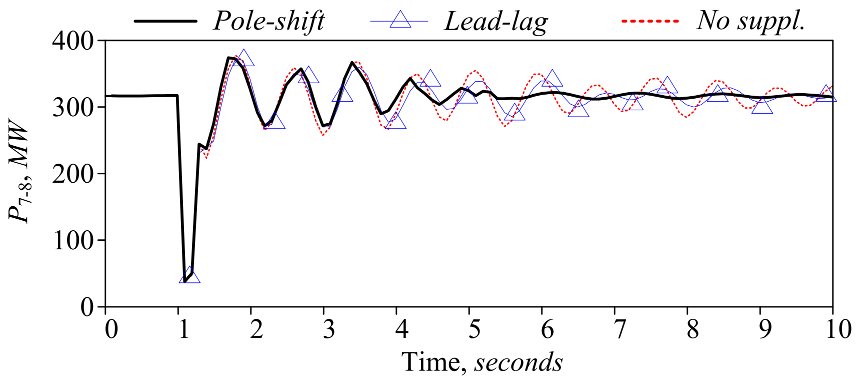

(a) Power flow on line 7-8

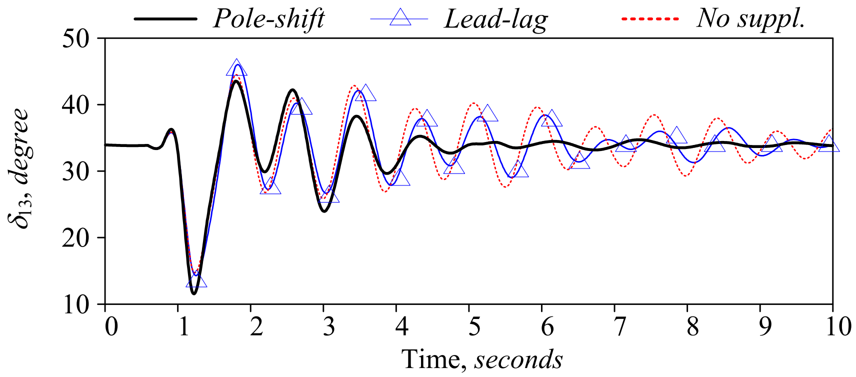

(b) Generator rotor angle δ_{13}

Figure 5.33: Line power flow and relative rotor angle variations for the disturbance **Case 5G** (IEEE 12-bus test system, balanced TCSC).

C. Test Case 5H

This case study corresponds to a three-phase system fault followed by a line (4-5) trip after 9 *cycles*. The case is used to test adaptive controller performance on delayed breaker operation (9 *cycles*) for clearing the faulted line. Figure 5.34(a) shows the tie-line power flow through line 7-8 for disturbance **Case 5H**. Similarly, Fig. 5.34(b) shows the relative generator rotor angle deviation of generator G_3 with respect to G_1 for same disturbance. The responses plotted in Fig. 5.34 demonstrate that even under such a severe situation, the proposed algorithm is able to damp the oscillations very effectively.

It is evident from the response plots in Figs. 5.31, 5.33 and 5.34 that the proposed controller provides better damping and faster settling time compared to the conventional controller. The lead-lag supplementary controller is tuned for disturbance **Case 5G**, and hence its performance is better for this case and deteriorates on other disturbances, whereas

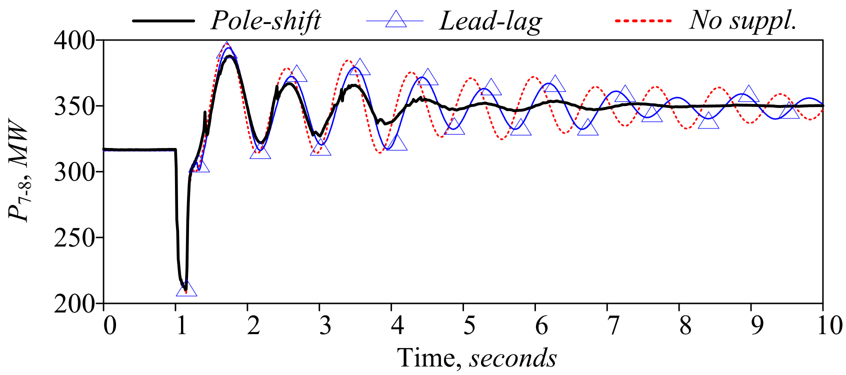

(a) Power flow on line 7-8

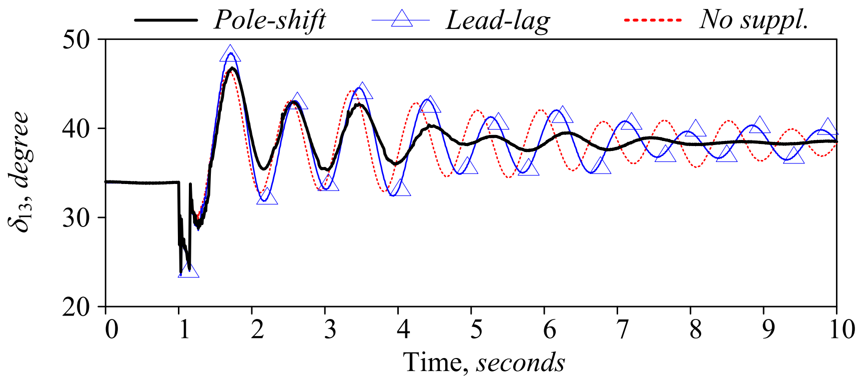

(b) Generator rotor angle δ_{13}

Figure 5.34: Line power flow and load angle variations for the disturbance **Case 5H** (IEEE 12-bus test system, balanced TCSC).

the operating condition does not affect the performance of the proposed controller.

D. Approximate Damping Factor Calculation for IEEE 12-Bus Test System

The severe disturbances on **Cases 5G** and **5H** excite multi-mode oscillations. The Prony analysis on the power flow on line 7-8 for **Case 5G** reveals the presence of three modes, as shown in Table 5.6. The approximate damping factors from Table 5.6 show that the pole-shift controller improves the multi-mode oscillation damping. The response shows that the proposed third-order identifier and pole-shift controller provide better damping compared to a lead-lag supplementary controller, even when the inter-area modes are closely spaced.

Table 5.6: Prony analysis of power flow on line L7-8 (disturbance **Case 5F**).

Modes	Controllers		
	No suppl.	Lead-lag	Pole-shift
Mode 1 - f(Hz), Damping (%)	1.209 Hz, 2.18%	1.185 Hz, 4.10%	1.221 Hz, 9.38%
Mode 2 - f(Hz), Damping (%)	0.891 Hz, 1.32%	0.901 Hz, 1.81%	0.870 Hz, 11.69%
Mode 3 - f(Hz), Damping (%)	0.762 Hz, 4.14%	0.764 Hz, 5.01%	0.660 Hz, 32.74%

5.5 Summary

This chapter presented the application of the adaptive pole-shift control algorithm in a TCSC or SSSC compensated power system to improve inter-area oscillation damping for wide range of operating conditions. The effectiveness of the algorithm in damping inter-area oscillations has been demonstrated through several digital computer simulations of case studies on three-area, six-machine test system as well as on the IEEE 12-bus test system.

The use of a robust recursive least square identification technique is also proposed to minimize parameter deviation during large disturbances in power systems (faults, line switching etc). The proposed estimation procedure helped in achieving effective control actions using the pole-shift type control technique, and also overcame the problems discussed in recent literature with regard to applying this technique during the faulted conditions.

An approximate computation of damping contributed by proposed adaptive controller and lead-lag controller are calculated using Prony analysis. The results of the studies conducted in this chapter demonstrates the effectiveness of the proposed controller over fixed parameter lead-lag controller in damping inter-area oscillations for a wide range of operating conditions.

Chapter 6

Hardware-in-the-Loop Testing of the Adaptive Controller

6.1 Introduction

The theoretical model development and computer simulation studies using the proposed adaptive controller are presented in Chapter 5. The simulation results showed that the proposed robust RLS technique is able to smooth out parameter variations during large disturbances. Furthermore, results showed that the pole-shift controller performance is consistent for wide range of operating conditions on both three-area, six-machine and IEEE 12-bus test systems.

The advantage of computer simulation studies is that the control algorithm can be easily studied and tested for various operating scenarios. However, in actual system, the controller would have to be implemented on a hardware. So it is necessary to conduct hardware-in-the-loop tests of the proposed controller to further assess the performance obtained from the computer simulation before implementing it on an actual system. This type of study is very important for the power system studies because the resulting damage from improper control action could be very extensive. The HIL study helps to observe the effect of the controller action on the overall performance of the power system.

Furthermore, the embedded controller may face real-time implementation issues which would have to be addressed. The unmodelled noise present in the system, proper communication protocols, communication delays between the controller and the system, and fitting the algorithm within the computational capacity of the processor are some of the issues that need to be properly addressed for a real-time implementation and testing.

This chapter presents details of the experimental verification of the proposed adaptive controller; i.e. design, implementation and testing of the controller in real-time. The proposed adaptive controller prototype is developed on a Texas Instruments DSP board (TMS320C6713 DSP Starter Kit DSK 6713) and performance of the controller is throughly tested in real-time HIL using a Real-Time Digital Simulator (RTDS) platform. The RTDS provides very accurate models of the power system and simulates the power system in real-time basis. The work reported in this chapter demonstrates that the adaptive controller can be realized in real-time, and, results of the work highlight the advantage of such controller for wide range of power systems operation.

6.2 Real-Time Digital Simulator (RTDS)

Real-Time Digital Simulator from RTDS Technologies® is a fully digital, real-time power system simulator widely used in the industries. The system is capable of providing continuous real-time electromagnetic transient simulations at time steps of 50 μs [95]. The simulator can be used for development and dynamic performance testing of various control and protection devices. This type of platform helps to study the impact of the controllers on the network without endangering real power system operation. It also helps to conserve resources since prime-mover energy is not required for testing devices.

The RTDS facility available in the Power System Laboratory consists of two 3PC cards, two GPC cards, a Gigabit Transceiver Analog Input (GTAI) card, a Gigabit Transceiver Front Panel Digital input/output interface card (GTFPI), and a Workstation Interface Card (WIF). The WIF card facilitates communication between RTDS unit and host Computer via Ethernet link. Each 3PC cards and GPS cards are equipped with 24 numbers of 12-bits Digital to Analog (D/A) output ports.

The GTAI Card is used to input signals to the RTDS unit. The GTAI analog input interface has 12 differential channels. The individual input channels are equipped with a first order anti-aliasing filter. The anti-aliasing filter has two manually selective cut-off frequencies of either 10.1 kHz or 84.2 kHz. The analogue output channels available in each 3PC processors are used to get signals from the RTDS.

6.3 DSP Strater Kit (DSK 6713)

The DSK 6713 has a 225 MHz TMS320C6713 Floating Point DSP from Texas Instruments. The DSP is capable of fetching eight 32-bit instruction per cycle or 4.44 ns and very well suited for numerically intensive algorithms [96]. It has built-in stereo audio codec $AIC23$. The codec is capable of handling a stereo audio signal (two inputs: left and right channels) and a stereo audio output (two outputs: left and right channels). The codec uses 16-bit ADCs and DACs to convert analog signal to digital and vice versa, and has selective sampling frequency of 8, 16, 24 or 48 kHz. To avoid the possible DC bias, the audio codec is

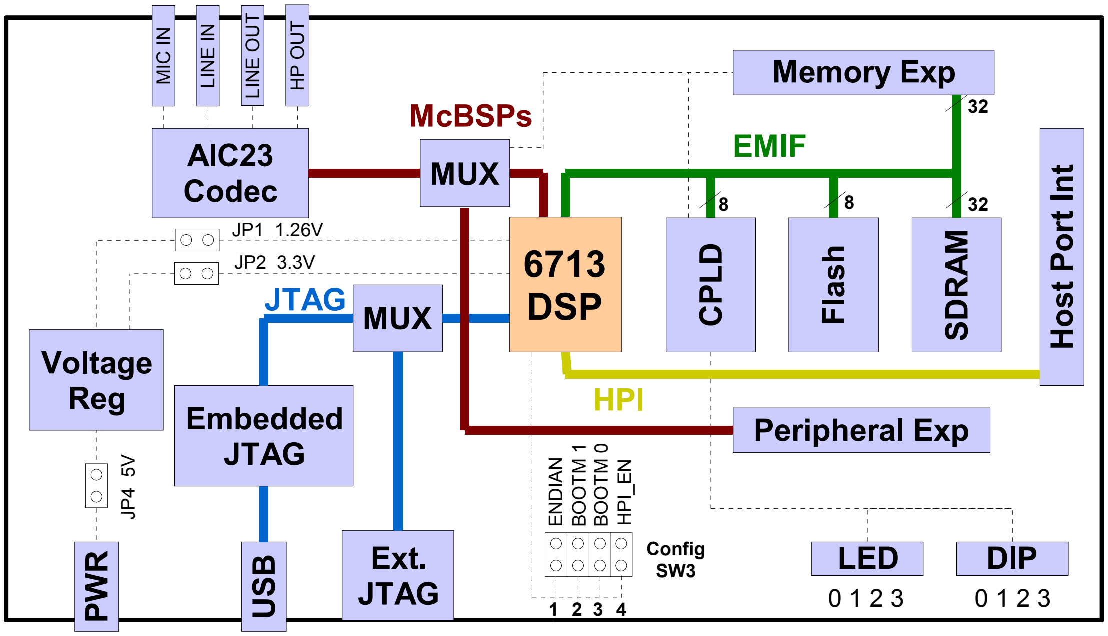

Figure 6.1: DSK 6713 block diagram[1].

---

[1] Source: Digital Spectrum Incorporated, "TMS320C6713 DSK Technical Reference", 2003.

equipped with a DC blocking capacitor of 470 nF [97]. Figure 6.1 shows the block diagram of the DSK 6713 DSP board.

The DSK 6713 can be operated in the hardware interrupt mode for real-time applications. In this mode, the DSP responds to the hardware interrupts generated by audio codec. Audio codec generates interrupts for every received samples. The higher the sampling frequency selected, lesser is the time available between two consecutive interrupts for the signal processing. In order to maximize the time available between two consecutive samples, the lowest sampling rate (8 kHz) is selected. At this sampling rate, the time available for the computation is 0.125 ms. If the algorithm takes more than 0.125 ms to run, the next sample data will be lost. So, to limit the time consumed by a piece of software code within 0.125 ms, some longer pieces of codes are divided into smaller parts.

6.4 Communication between RTDS and DSK 6713

The DSK 6713 board analog input/output interface is designed for the audio processing applications. It has only one stereo analog input and one stereo analog output channels. The number of available input/output channels imposes restriction on number of electrical signals that can be exchanged between the RTDS and the DSP board. To overcome this limitation, the supplementary signal (i.e. power deviation) is passed to the DSP from RTDS instead of calculating power deviation inside the DSP controller. This simplified the signal exchange between the RTDS and the DSP (passing only a signal necessary for the supplementary controller, i.e. power deviation, and receiving only the controller output). The supplementary control signal is then added to the main TCSC controller inside the RTDS.

Furthermore, the DSP codec I/O signal bandwidth is between 20 Hz to $F_s/2$, where F_s is the sampling frequency of the codec [97]. This bandwidth imposes another restriction on how the communication between DSP and RTDS should be done. The inter-area frequency is in the range of $0.1 - 0.8$ Hz, and as the DSP audio codec attenuates signals below 20 Hz; therefore, the communication between RTDS and the DSP board at the frequency of interest is not directly possible. This problem is resolved using an amplitude modulation technique known as Double Sideband-Suppressed Carrier (DSB-SC) modulation [98]. The DSB-SC modulation scheme is selected because of its simplicity in hardware implementation. The low frequency oscillation signal is modulated with a carrier frequency of 0.5 kHz and sent to the DSP. Similarly, the output of the controller in DSP is modulated by the same carrier and sent back to the RTDS.

6.4.1 Double Sideband-Suppressed Carrier Modulation (DSB-SC)

In this modulation technique, the signal of interest (baseband frequency) is multiplied with a carrier signal and sent through the channel. At the receiving end, the carrier signal and modulated signals are multiplied and passed through a low-pass filter to retrieve the original baseband signal. The modulation process translates the spectrum of the baseband signal by $\pm f_c$, where f_c is the carrier frequency. The demodulated baseband signal will have a scale of 0.5 *units*. The frequency spectrum of the supplementary signal and DSB-SC modulated signal are shown in Fig. 6.2. Mathematically, the process is described as follows:

A. Modulation:

$$\text{Carrier signal:} \qquad v_{carrier} = A_c \ \cos(\omega_c t) \tag{6.1}$$

$$\text{Modulated signal:} \qquad y_{mod} = \underbrace{A_p \cos(\omega_p t)}_{\Delta P} \times v_{carrier} \tag{6.2}$$

$$= \frac{1}{2} A_c A_p \left[\cos((\omega_c + \omega_p)t) + \cos((\omega_c - \omega_p)t)\right] \tag{6.3}$$

where ω_c is carrier frequency, A_c is amplitude of the carrier signal which is unity, and ΔP is a baseband (supplementary power deviation) signal. A_p is the magnitude and ω_p is the frequency of the supplementary signal.

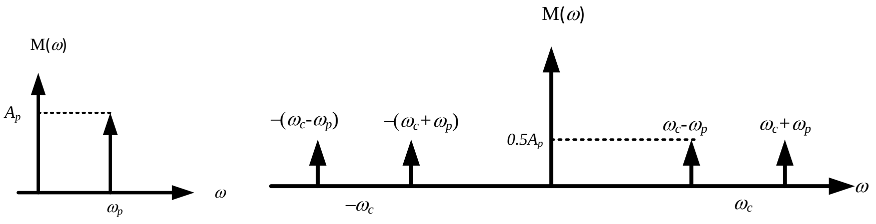

(a) **(b)**

Figure 6.2: DSB-SC modulation: (a) baseband and (b) modulated spectrum.

B. Demodulation:

The received modulated and carrier signal are multiplied and passed through low pass filter to extract the original supplementary signal. Figure 6.3 shows the demodulation process.

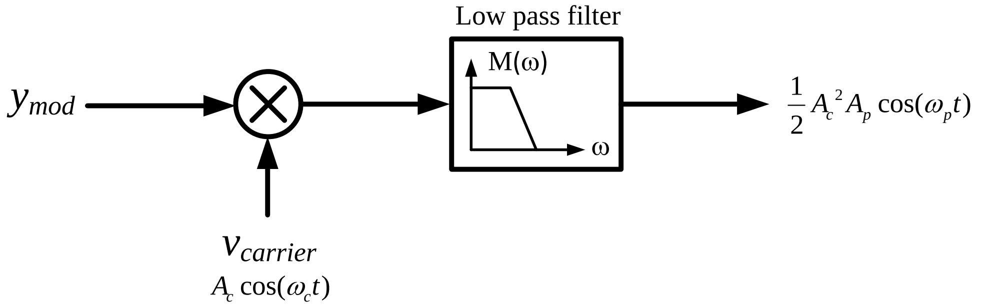

Figure 6.3: DSB-SC demodulation process.

C. Example: DSB-SC modulation and demodulation process

A supplementary signal of 0.8 Hz is modulated using DSB-SC modulation technique. To mimic the oscillation in the power system, the magnitude of the signal is selected as an exponential decaying signal. The carrier signal is chosen to be a 0.5 kHz sinusodial signal. The supplementary signal and the carrier signal are expressed in Eq. 6.4 and 6.5 respectively.

$$y(t) = e^{-0.8t}\cos(2\times\pi\times0.8\times t) \tag{6.4}$$

$$v_c(t) = \cos(2\times\pi\times500\times t) \tag{6.5}$$

The signals in different stages of the modulation and demodulation process are shown in Fig. 6.4. For the demodulation process, a second-order Butterworth filter of cut-off frequency 5 Hz is used. The original supplementary signal has maximum amplitude of 1.0 *unit* and the demodulated signal has maximum amplitude of 0.5 *unit*.

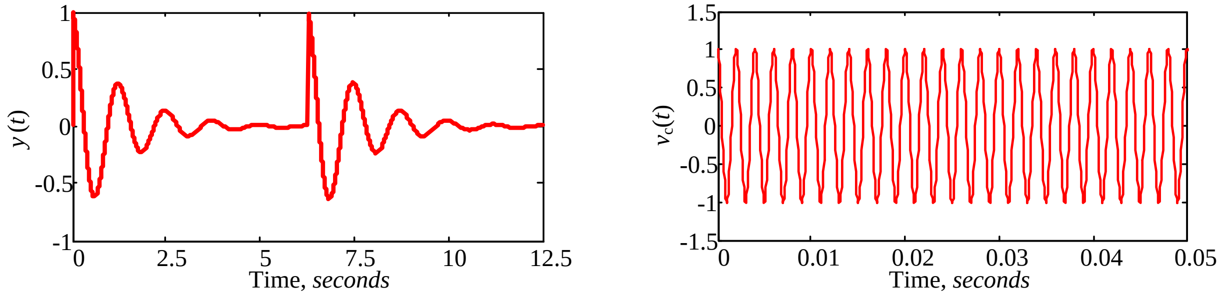

(a) Supplementary signal

(b) Carrier signal (0.5 kHz)

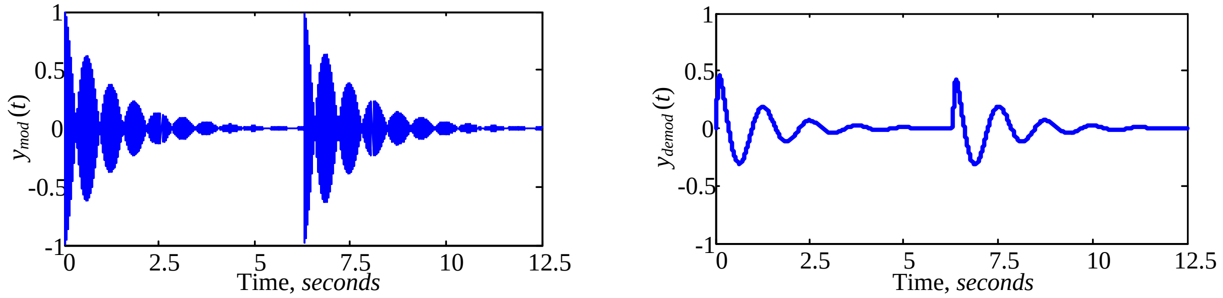

(c) Modulated signal

(d) Demodulated signal

Figure 6.4: DSB-SC modulation and demodulation process.

6.5 Test System Used for Experimental Studies

The simulation facility processing capability allowed for modelling a two-area test system [30] with a TCSC device. The test system is shown Fig. 6.5. It includes two generating areas inter-connected through a 210 km long transmission line. Each area consists of two generators. The exciter and governor models are used to regulate terminal voltage and input mechanical power. The tie-line is partially series compensated (capacitive), using a three-phase TCSC module. The steady state series capacitive compensation of the TCSC is 0.2 $p.u.$ of the total line reactance of 111.1 Ω. The system has one inter-area mode of oscillation of 0.5 Hz. The system used is a fairly well sized system for experimental studies. Further details of the system are provided in Section 6.6.1.

6.5.1 Cases Studies

Five test scenarios listed in Table 6.1 are considered for the testing of the controller performance. These case studies cover a wide range of operating conditions and different type of disturbances.

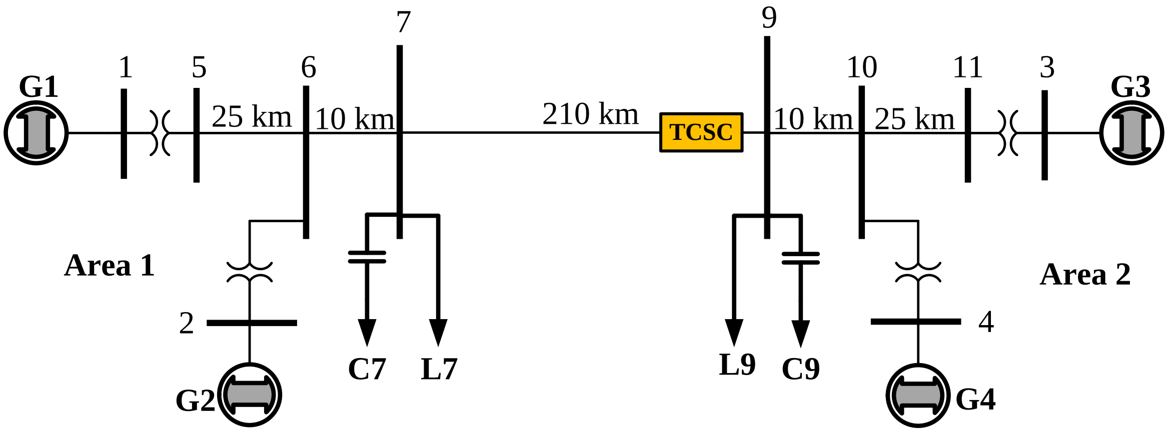

Figure 6.5: Two-area test system.

Table 6.1: Test cases for the two-area system studies in RTDS.

Approximate power flow on line 7-9	Disturbance description	Disturbance type
315 MW	3 cycle, three-phase fault at bus 7	**6A**
315 MW	6 cycle, three-phase fault at bus 7	**6B**
150 MW	3 cycle, three-phase fault at bus 7	**6C**
-230 MW	3 cycle, three-phase fault at bus 7	**6D**
167 MW	Load rejection at bus 9 (Load flow of case A), at $t = 1sec.$	**6E**

6.6 Experimental Set-up

6.6.1 Power System Model

The two area system including TCSC is developed in RSCAD software. The RSCAD provided the ability to set up simulations, control, modify system parameters during simulation, data acquisition, and analysis of the results. The DRAFT module of the RSCAD Software Suite is used for developing power system models. The developed model is then uploaded to the RTDS unit using RunTime module. The RunTime module also allows the user to run and control the simulation in real time.

The synchronous generators are modelled in a $d-q-0$ reference frame. The generators are equipped with IEEE type ST1 exciters [99] and IEEE type 1 turbine-governors [100] to mimic real power system operation. The transmission line are represented as lumped impedance model.

Three units of single-phase TCSC model are used on each phase for series compensation. The closed loop impedance control method is implemented for the steady state TCSC impedance control [6]. The Discrete Fourier Transform (DFT) technique is used to estimate line current and voltage across the TCSC. The estimated components are used to calculate the TCSC impedance. A proportional-integral controller is used to regulate firing angle of the TCSC to achieve desired TCSC impedance.

For the inter-area oscillation damping control, the power deviation through line $7-9$ is used as a supplementary signal. This supplementary signal is modulated using a sinusoidal carrier signal of frequency 0.5 kHz. The machine and line parameters used for the study are given in Appendix E.

The experimental set-up is depicted in Fig. 6.6.

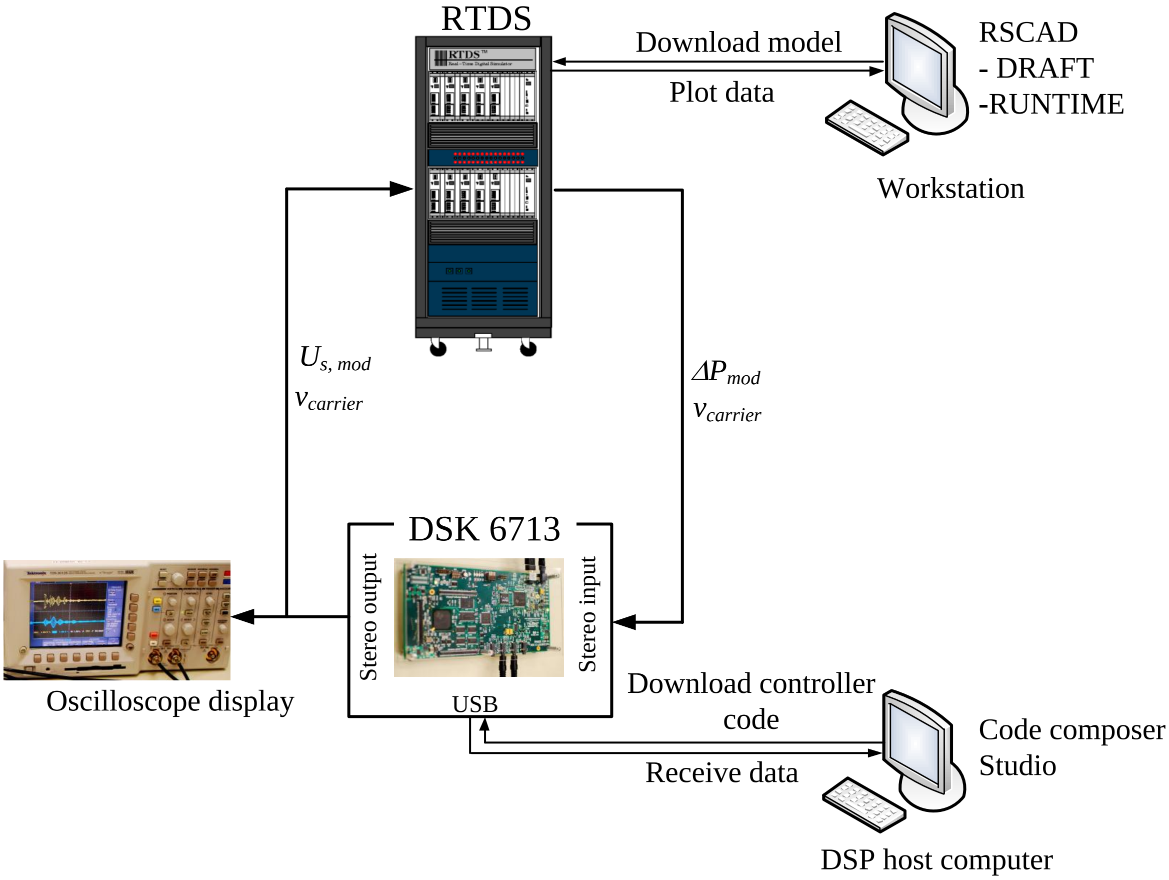

Figure 6.6: Real-Time Digital Simulator hardware in the loop test schematic.

6.6.2 Controller Implementation in DSP

The Code Composer Studio (CCStudio[1]) version 3.1 is used to develop the controller algorithm. The CCStudio provides facility to write source codes in machine assembly language and/or C/C++ language. C programming language is used to write codes in this work.

A. Signal Conditioning

The $AIC23$ audio codec uses $16-bit$ signed integer I/O channels. The maximum allowable input signal level is 1 V rms. However, DSK C6713 contain a potential divider with a gain of 0.5 between *Line IN* sockets which increases maximum allowable input signal level to 2 V rms. A safe input voltage level of ±1 V peak-to-peak is used for input/output from the DSP board. The input level gain is set-up such that that the peak-to-peak input of ±1 V to the DSP corresponds to 0.5 $p.u.$ of the power deviation, whereas output level of ±1 V peak-to-peak corresponds to ±1 $p.u.$ TCSC impedance change. The input samples received from codec has 16-bit signed integer format and is converted to voltage values using ADC conversion constant for the processing inside the DSP.

Two analog input signals (modulated power deviation and carrier signals) from RTDS are received via audio codec at sampling frequency of 8 kHz. The signals are passed to demodulation algorithm, and low frequency power oscillation is extracted. Since the frequency of inter-area oscillation is around 0.5 Hz, the input samples received from the codec are further downsampled to 10 Hz. It means only one input data sample out of 800 (8 $kHz/10\ Hz = 800$) received from input codec is processed. To minimize the effect of aliasing, a second order anti-aliasing Butterworth filter of 10 Hz cut-off frequency is used.

The output of the control algorithm is modulated using a carrier signal and converted back to integer count using DAC conversion constant. The controller output is demodulated inside RTDS and used as a supplementary control signal for the TCSC.

The basic flow chart of the DSP implementation is shown in Fig. 6.7. The pole-shift control code is executed before identification code. This minimizes the delay introduced by adaptation process because the parameter update and controller design are done after sending the control signal to the plant [54]. The code execution time is maintained within 0.125 ms limit by executing only a certain portion of code in each interrupt. It is a valid approach, since the next set of data will arrive only after 799 interrupts for sampling rate of 8 kHz and 10 Hz downsampling considered in the study.

---

[1] Code Composer Studio is an integrated development environment for developing DSP code for the Texas Instruments TMS320 DSP processor family.

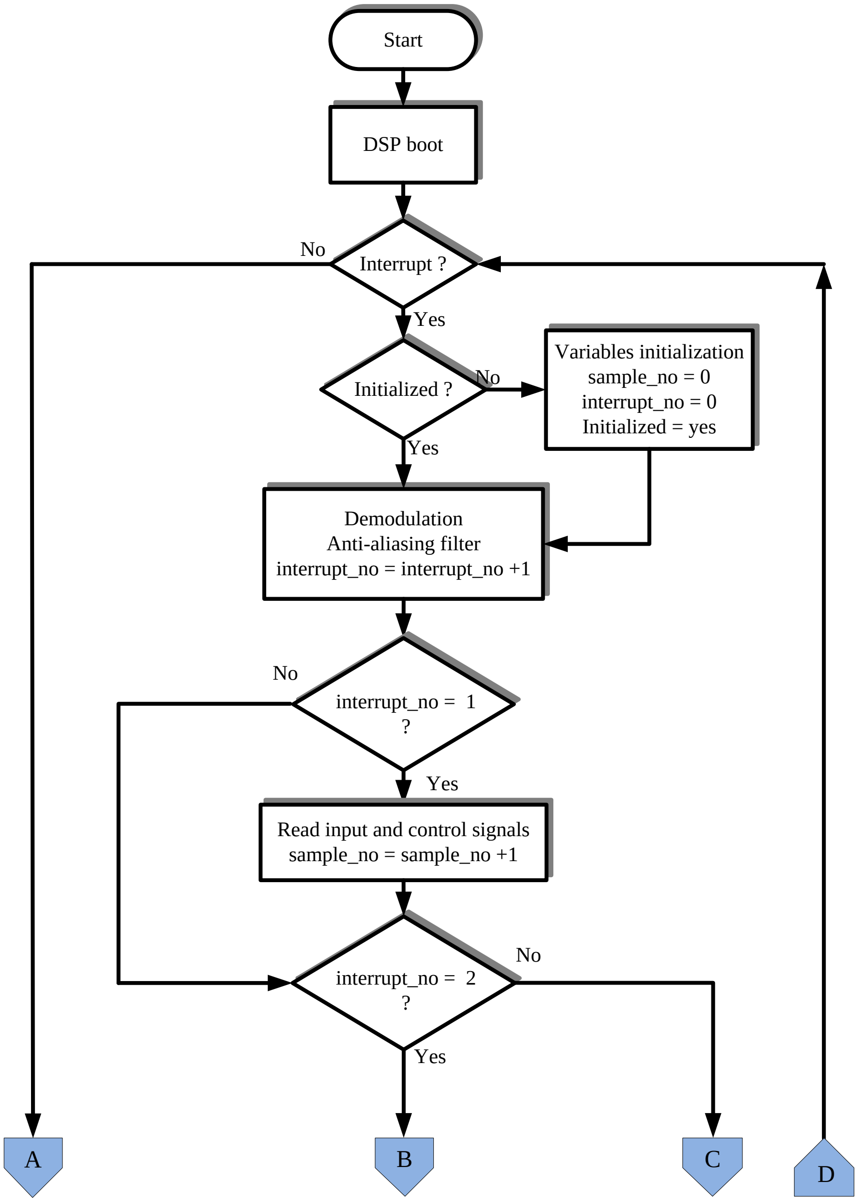

Figure 6.7: Program flow chart of the adaptive pole-shift controller implementation on DSP (contd. on next page).

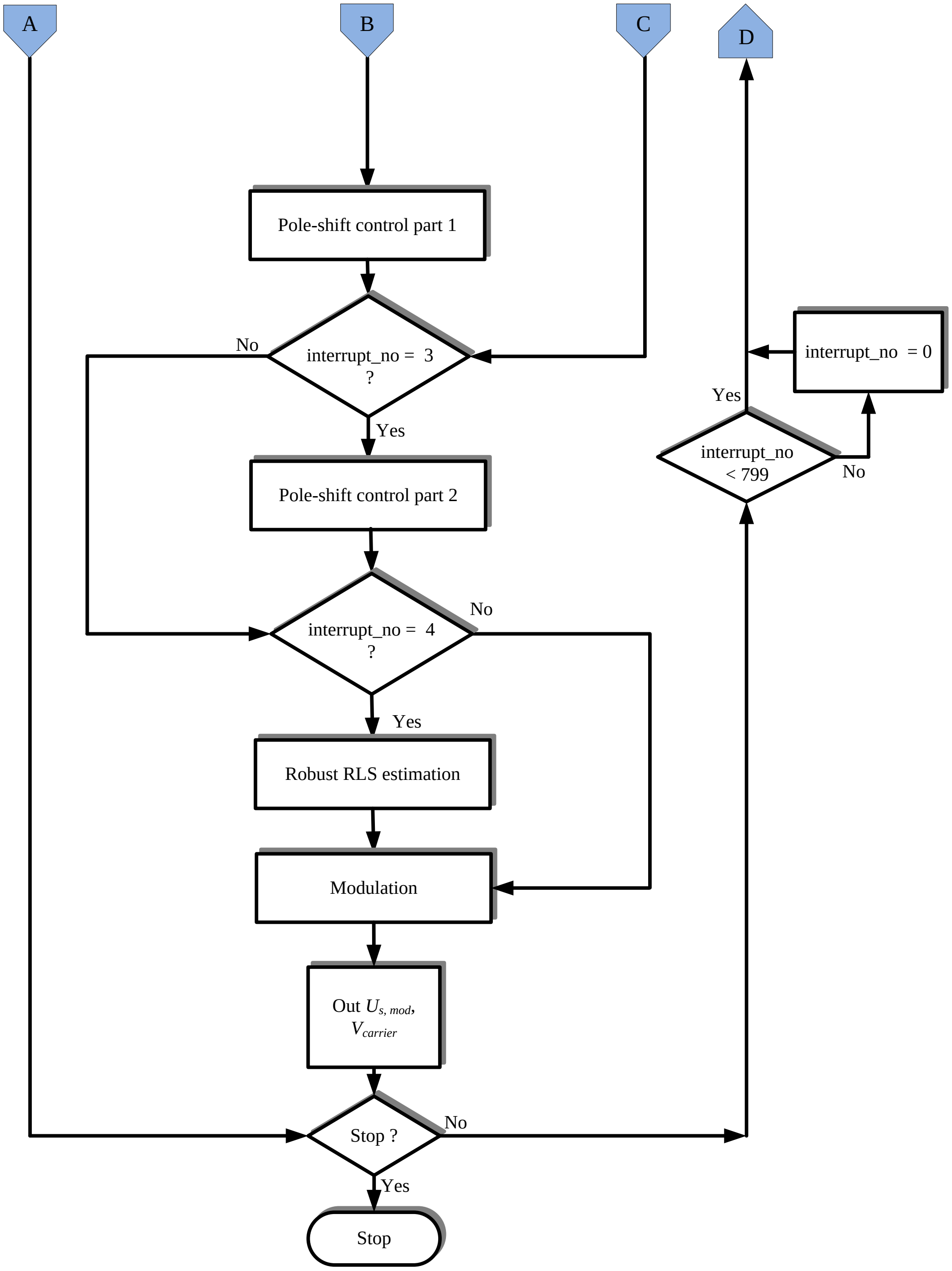

Figure 6.7: Program flow chart of the adaptive pole-shift controller implementation on DSP (contd. from previous page).

B. Robust RLS Identification

The identification subroutine consists of the robust RLS algorithm which can be easily switched to normal RLS algorithm by setting parameter update rate $a = 0$ (Eq. 5.9). The identification routine takes 0.10 *ms* to execute in the DSP. The theoretical details of the algorithms are explained in the Section 5.2.1.

The identifier coefficient values are frozen if the difference between maximum and minimum input values in the last 25 *samples* is below a threshold value. The threshold is selected as 1% of the peak-to-peak input signal. The number of samples used for calculating power deviation (25 *samples*) is selected such that it includes slightly more than 1 *cycle* of data for 0.5 *Hz* signal. The frozen coefficients are used as initial value for the next disturbance. This process helps parameter estimation to converge faster. If there is disturbance in the system, the supplementary signal deviation will be higher than the threshold value, which activates the identification subroutine.

C. Pole-Shift Controller

The adaptive pole-shift control algorithm explained in Section 5.2.2 is developed in C programming language. Optimization of the cost function expressed in Eq. (5.21) is carried out using a Brent's optimization method [101]. Minimization of the cost function in Eq. (5.21) yields optimal pole-shift factor α_{opt}. This information is used to compute optimal control signal required to minimizes the deviation between predicted next time-step plant output $\Delta P_L(t+1)$ to the reference plant output $\Delta P_{L,ref}(t+1)$.

Brent's optimization is selected because of its simplicity in implementation. It is very good for predefined boundaries of the roots, which in this case is the stability constraints $[\frac{1}{\lambda}(1-\Lambda), \frac{1}{\lambda}(1-\Lambda)]$, where Λ is the safety factor. The safety factor $\Lambda = 0.05$ is considered for the studies. Also, the weighting coefficient (μ) and steady-state pole-shift factor (α_{ss}) (refer to Eq. 5.21) are selected for the studies as 0.5 and 0.7, respectively.

The complete pole-shift controller algorithm took 0.18 *ms* to execute, which is larger than the sampling interval of input codec. So the controller code is broken down into two parts. The first section of code performs basic calculations such as preparing input matrices and inverting M matrix. The second section of code performs root calculation of the characteristics equation, optimization and control signal calculation. The two section of codes are allowed to run in two consecutive interrupts. This process reduces code execution time well below the sampling time interval, i.e. 0.092 *ms* for the first section and, 0.088 *ms* for the second section.

6.7 Real-Time HIL Test Results

The effectiveness of the proposed adaptive controller for damping inter-area oscillation is demonstrated on a two-area test system consisting of a TCSC compensated transmission line as shown in Fig. 6.5. The deviation in power flow through line 7-9 is considered as plant output. The supplementary control signal U_s is considered as plant input. The performance of the robust RLS estimation and adaptive pole-shift control algorithms are evaluated for various disturbance scenarios listed on Table 6.1.

6.7.1 System Identification

The identified system parameters for disturbance **Case 6A** are shown in Fig. 6.8. Figure 6.8(a) shows the identified plant parameters using robust RLS algorithm; whereas Fig. 6.8(b) shows the estimated plant parameters for the same disturbance using RLS algorithm. The estimated error for these two algorithms are plotted in Fig. 6.8(c). It is evident that the proposed identification method helps to identify system parameters smoothly even during the large disturbance (large errors). In the case of the normal RLS, the large deviation in estimation error causes significant deviation in the estimated parameters. This rapid change in parameter values causes undesirable controller output, which leads to poor damping performance as shown in Fig. 6.9.

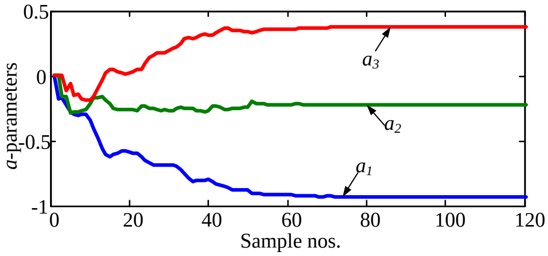

(a) Proposed robust RLS

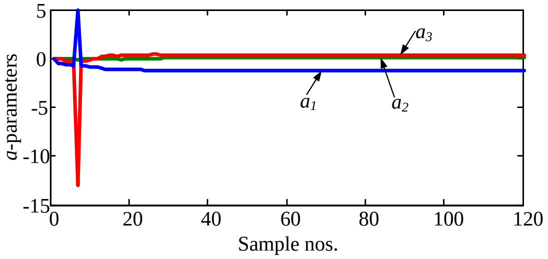

(b) Normal RLS

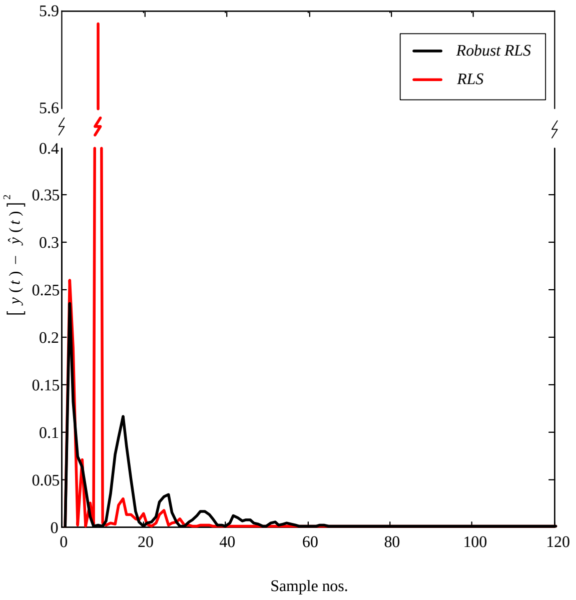

(c) Estimation error $[y - \hat{y}]^2$

Figure 6.8: System parameter identification using RLS techniques and error comparison.

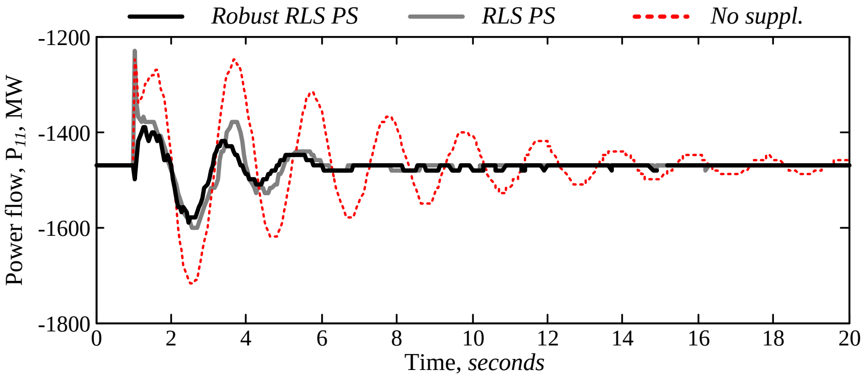

Figure 6.9: The tie-line power time response of line 9-10 for disturbance **Case 6A**.

6.7.2 Inter-Area Oscillation Damping

This section evaluates the effectiveness of the proposed pole-shift control algorithm for damping inter-area oscillations. For each case listed in Table 6.1, two sets of studies are carried out. The first sets of studies are for when the pole-shift controller is disabled, denoted by "*No suppl.*" and second sets of studies are for the pole-shift controller in service, denoted by "*Pole-shift*". The time-domain results for each disturbance cases are reported in the following sub-sections.

A. Case Study 6A

This **Case 6A** represents a 400 MW tie-line power flow through line 7-9 and considered as a base operating condition for rest of the cases. Figure 6.10 shows the time response of tie-line power flow (line 7-9) and relative generator rotor angles for disturbance **Case 6A**. The rotor angle deviation between G_1-G_2 and G_4-G_3 represents the local oscillations at area 1 and area 2, and angle deviation between G_4-G_1 represents the inter-area oscillation between area 1 and area 2, respectively. The responses without and with the pole-shift supplementary controller are presented in red-*dotted* and black-*thick* color respectively. Note that the inter-area oscillation takes more than 20 *sec* to settle the oscillations when the controller is disabled. The introduction of adaptive controller significantly reduces the settling time - oscillations settled within 8 *sec* of fault clearing.

The time responses of the control signal generated by the pole-shift controller and TCSC reactance for the case of Fig. 6.10 are shown in Figs. 6.11(a) and (b), respectively. The corresponding open and closed-loop poles of the identified system are plotted in Fig. 6.11(c). The open loop and closed loop poles are located at $[0.8 \pm j0.2966, -0.3058]$ and $[0.56 \pm j0.2076, -0.2140]$ respectively. The steady-state pole-shift factor is found to be $\alpha = 0.69$. It

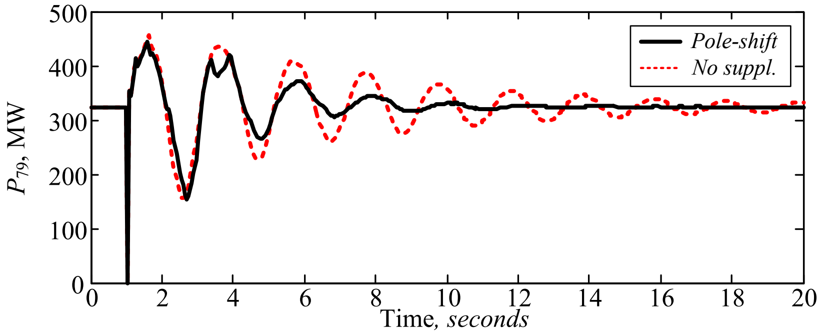

(a) Tie-line power flow, P_{79}

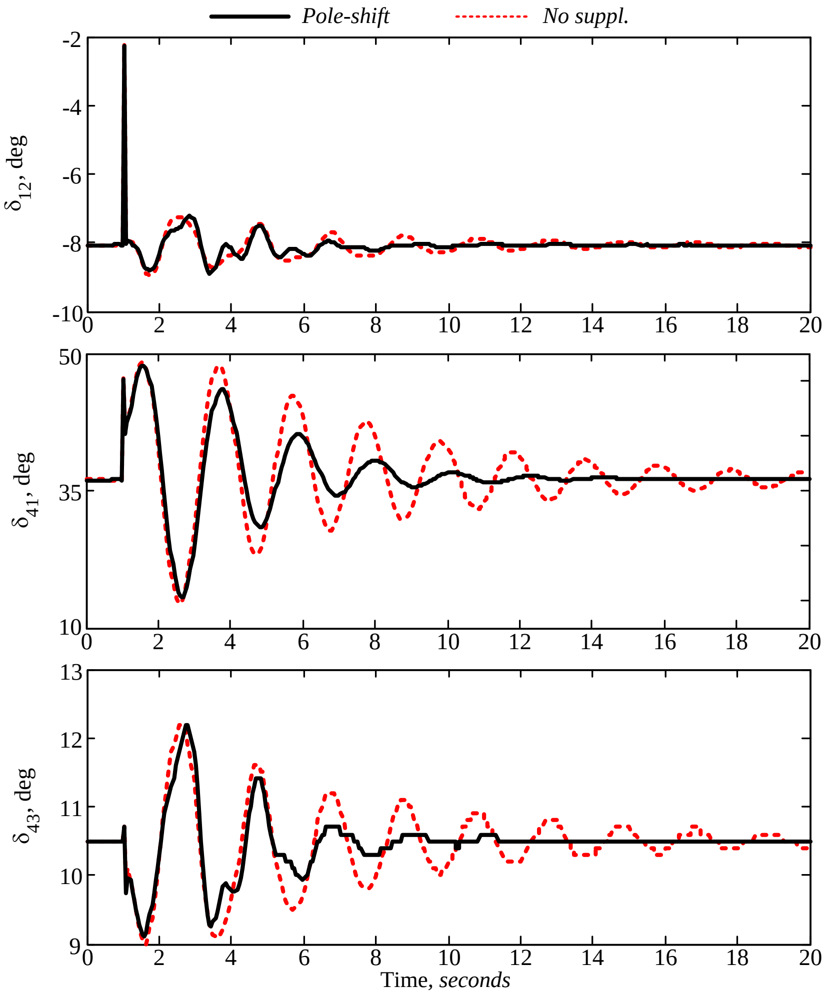

(b) Relative generator rotor angles: $G_1 - G_2$, $G_4 - G_1$, $G_4 - G_3$

Figure 6.10: Tie-line power flow and relative generator rotor angle time responses for disturbance **Case 6A**.

is evident from Fig. 6.11(c) that the pole-shift controller moves open loop poles closer to the origin and improves the system damping.

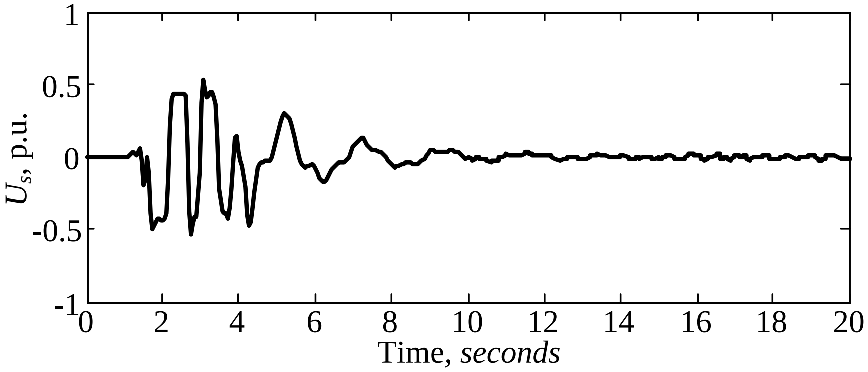

(a) Control signal

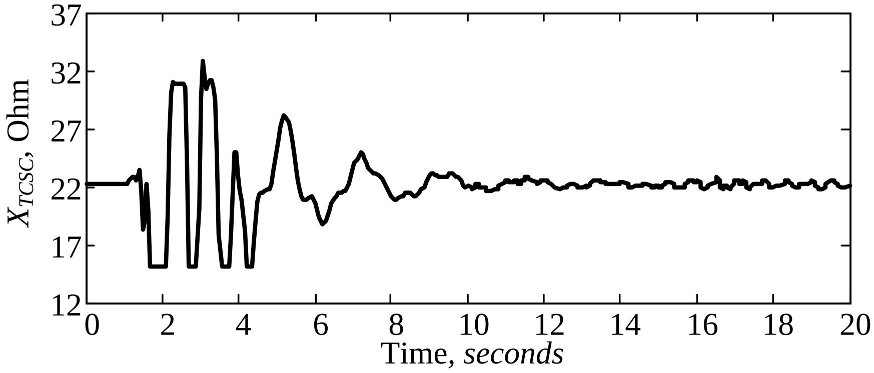

(b) TCSC reactance

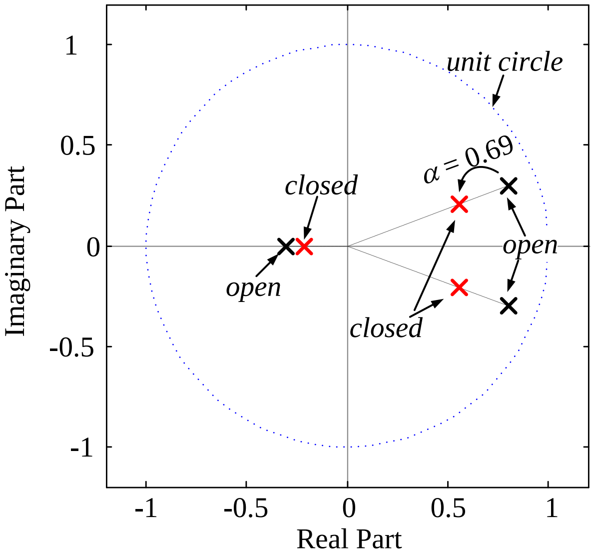

(c) Dynamic open and closed-loop poles

Figure 6.11: Time response of the (a) controller output and (b) TCSC reactance and (c) dynamic pole-zero plot for disturbance **Case 6A**.

Figure 6.12 shows the modulated and carrier signals captured from Oscilloscope for the case study of Fig. 6.10. A two-channel digital phosphor oscilloscope (Tektronix TDS3012B) is used to capture the signals into Floppy Disk. The data captured in Fig. 6.12 corresponds to the plot of Fig. 6.10(a). Note that the modulated power deviation signal has decaying sinusoidal envelop.

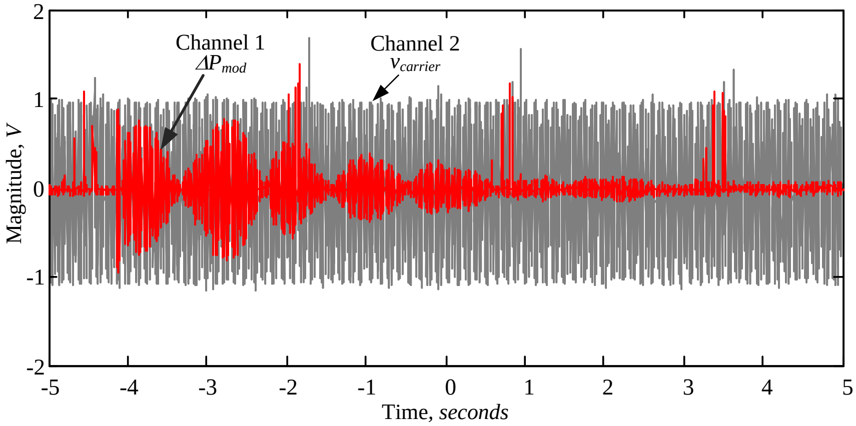

Figure 6.12: Signals from RTDS to DSP: oscilloscope data captured for the case of Fig. 6.10.

B. Case Study 6B

For the study of the controller performance under a severe disturbance, a 6 *cycle* three-phase fault is applied at bus 7 on the operating condition of **Case 6A**. The longer duration fault causes large oscillation on the network. The effectiveness of the controller for such fault is demonstrated on Fig. 6.13. Note here the magnitude of oscillation in δ_{41} reaches as high as 80^o as compared to 50^o for a 3 *cycle* fault of disturbance **Case 6A**.

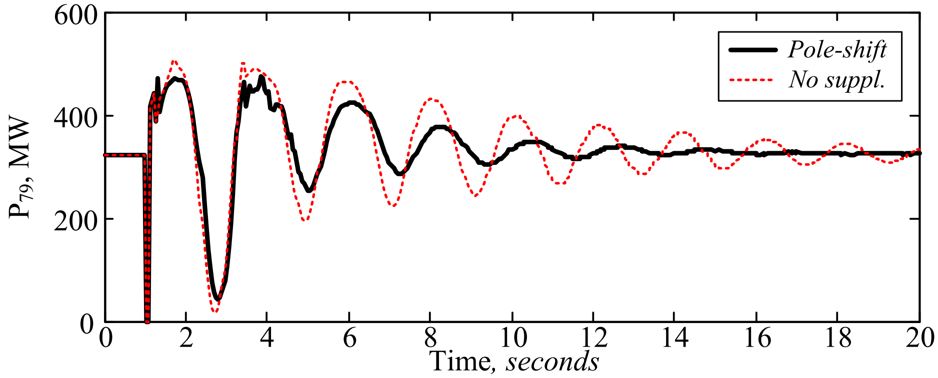

(a) Tie-line power flow - P_{79}

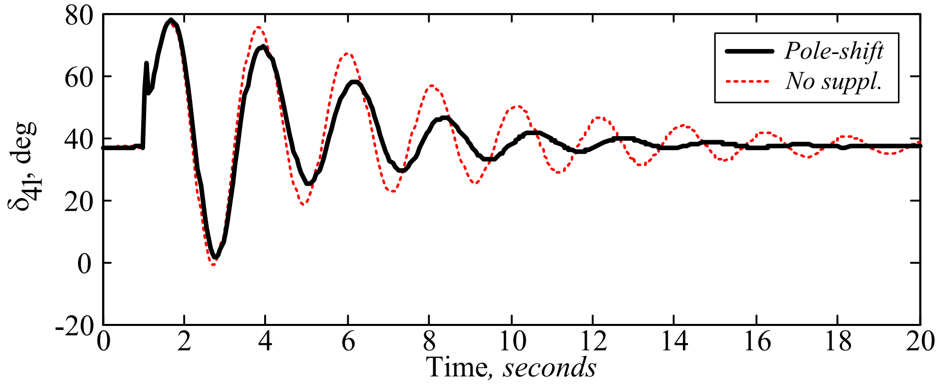

(b) Relative generator rotor angle between $G_4 - G_1$

Figure 6.13: Tie-line power flow and relative generator rotor angle time response for disturbance **Case 6B**.

C. Case Study 6C

Case 6C is used to test the controller performance for lower tie-line power flow than designed value. The tie-line power flow from bus 7 to bus 9 is set to 150 MW by decreasing load on bus 9. This kind of operating condition is very common on a power system. In this operating condition, the tie-line power oscillation (feedback signal) may have lower magnitude than that of 400 MW power flow. Even in such a condition, the adaptive controller will adjust the gain automatically yielding optimal damping.

Figure 6.14 shows the tie-line power flow and relative generator rotor angle deviation time δ_{41} responses for disturbance **Case 6C**. The adaptive controller performance is found to be similar to **Case 6A**.

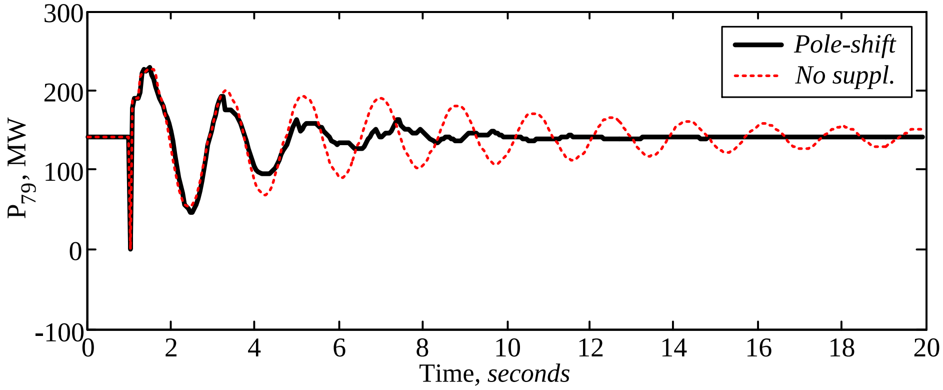

(a) Tie-line power flow - P_{79}

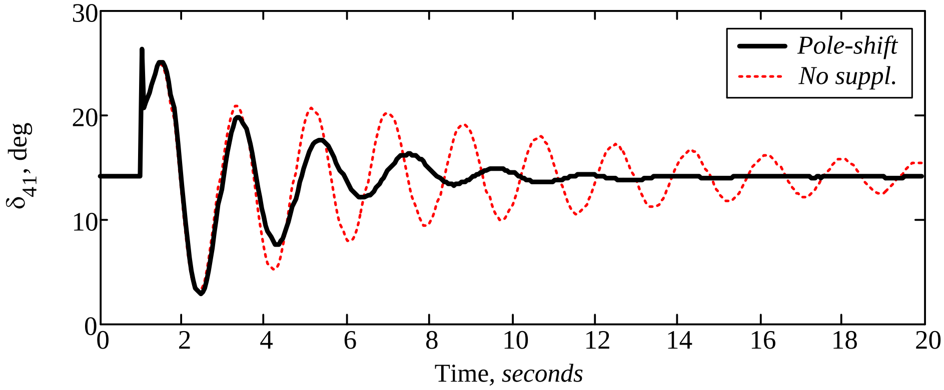

(b) rotor angle between $G_4 - G_1$

Figure 6.14: Time response for tie-line power flow reversal for disturbance **Case 6C**.

D. Case Study 6D

Case 6D is used to test the controller for the change in reverse power flow condition through tie-line. This type of operation is very likely to occur in a highly inter-connected power system. For this case, the tie-line power flow on line 7-9 (from bus 9 to bus 7) is set to 230 MW by increasing loads on bus 7 and decreasing loads on bus 9. The input to the controller, i.e. deviation of the power flow through line 7-9, is kept same as earlier cases.

Figure 6.15 shows the tie-line power flow and relative generator rotor angle δ_{41} time response for disturbance **Case 6D**. The response shows that the adaptive controller significantly improves the settling time. The controller performance is not affected by change in operating condition and reversal of the feedback signal.

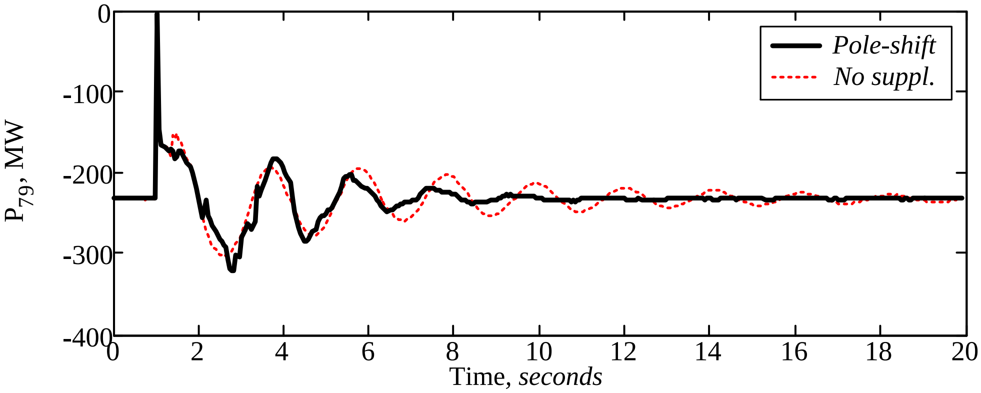

(a) Tie-line power flow - P_{79}

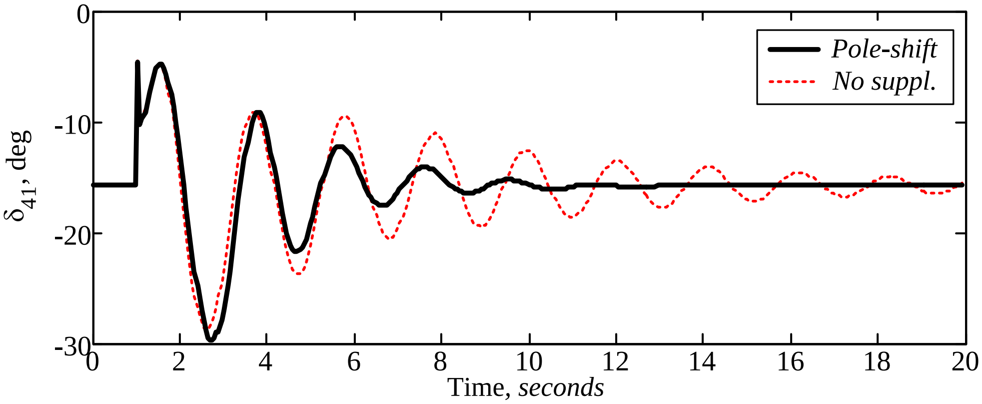

(b) rotor angle between $G_4 - G_1$

Figure 6.15: Time response for tie-line power flow reversal for disturbance **Case 6D**.

E. Case Study 6E

In this case, a 167 MW load is disconnected from bus 9 at $t = 1$ *sec.* This causes severe disturbance on the network and shifts the steady-state generator operation to new equilibrium point. The tie-line power flow and the relative generator rotor angle $(G_4 - G_1)$ time responses are shown in Fig. 6.16. It can be observed from these responses that the tie-line power flow decreases significantly and relative generator rotor angle also decreases in the same fashion. Even in such severe situations, the proposed adaptive controller is able to damp the oscillations effectively.

A comparison of the responses in Figs. 6.10 through 6.16 demonstrates the benefit of the proposed adaptive pole-shift controller for damping inter-area oscillations very clearly. The results show that the proposed adaptive controller reduces the first swing oscillation and also effectively damps the subsequent swings in all cases.

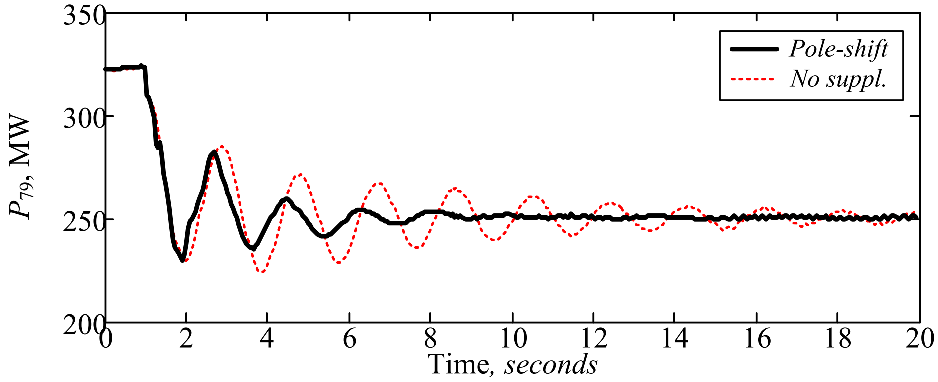

(a) Tie-line power flow - P_{79}

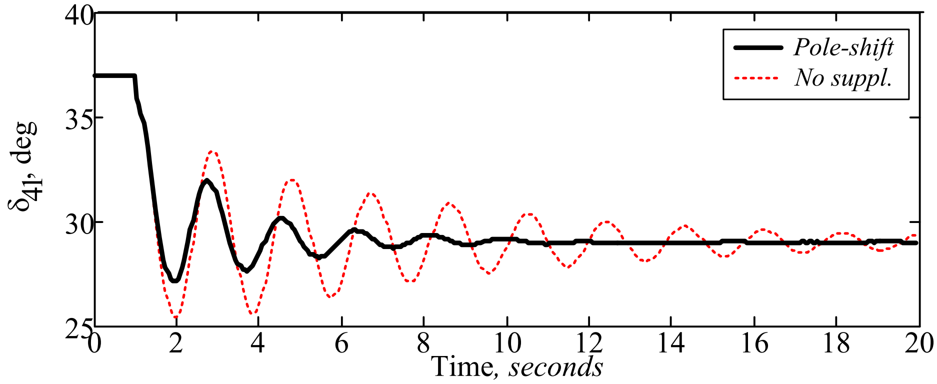

(b) rotor angle between $G_4 - G_1$

Figure 6.16: Time response for load rejection for disturbance **Case 6E**.

6.7.3 Damping Contribution by Adaptive Pole-Shift Controller

The calculation of the damping coefficients of the power flow on '*Line* $7-9$' gives an approximate representation of the degree of damping provided by adaptive pole-shift controller to the inter-area oscillation mode. For this purpose, the approximate damping factor of the dominant mode in the power flow on Line $7-9$ is calculated for all the study cases using Prony analysis. The analyzed data of the tie-line power time response lie between 1.1 *sec* to 19 *sec* time window.

The approximate damping factors obtained using Prony analysis are presented in Table 6.2 for all the contingency cases of Table 6.2. The table summarizes the results for the cases when (*i*) pole-shift controller is disabled, and (*ii*) pole-shift controller is enabled. The system exhibits poor damping of around 5% when the controller is disabled. When pole-shift controller is enabled, the system exhibits significantly improved damping, which is around 12%. Note the damping provided by adaptive controller is very consistent for all operating conditions.

Table 6.2: Approximate damping for the inter-area oscillation mode.

Cases	Pole-shift disabled		Pole-shift enabled	
	Freq. (Hz)	Damp. (%)	Freq. (Hz)	Damp. (%)
6A	0.497	5.430	0.471	13.661
6B	0.496	5.119	0.458	11.054
6C	0.545	3.180	0.465	13.249
6D	0.480	5.181	0.512	13.552
6E	0.500	5.123	0.540	12.721

6.8 Summary

This chapter presented the details of the implementation of the proposed adaptive pole-shift controller in a DSP and hardware-in-the-loop testing using RTDS platform. The various real-time implementation issues have been discussed, such as, communication between DSP and RTDS, downsampling and code execution time in DSP, and resolutions to the respective issues have been presented. The two-area test system experimental results demonstrated the effectiveness in damping the dominant mode of inter-area oscillations.

As the inter-area oscillation frequency of the system under study is 0.5 Hz, a sampling frequency of 10 Hz is found to be sufficient to represent the frequency of interest. The power signal samples acquired by DSP at 8 kHz are down-sampled to 10 Hz and used in the adaptive controller algorithm. This downsampling also gives extra room for the computation time - the code execution time will be higher than actual sample intervals. The challenge of establishing the communication between RTDS and audio DSP (DSK 6713) at low frequency is resolved using signal modulation/demodulation technique known as Double Side-Band Suppressed Carrier. A sinusoidal carrier signal of 0.5 kHz is used to modulate/demodulate the supplementary control and controller output signals.

The real-time execution of the identification and controller codes in the DSP is achieved using hardware interrupt mode. The interrupt is generated in every 0.125 ms and it imposed the maximum limit to the code execution time. To limit the code execution time, longer codes are divided into smaller sections and each sections are sequentially evaluated in consecutive interrupts. For example, the identifier algorithms took 0.1 ms to execute whereas the pole-shift control algorithm took 0.18 ms. As the controller code execution time is higher than interrupt interval, the code is further divided into two sections, each sections taking 0.092 ms and 0.088 ms.

The Prony analysis revealed that the approximate damping contribution by the adaptive controller is very consistent (at around 12%) for all the operating conditions under study. The experimental results of the studies conducted in this chapter demonstrate the effectiveness of the proposed controller in damping inter-area oscillations for a wide range of operating conditions.

The controllers have to be finally implemented on a piece of hardware and it is very important to study the hardware implementation issues. The practical issues outlined in this chapter, mainly code execution time limits and communication between RTDS and DSK 6713, would not have surfaced if the studies were conducted using only pure computer simulation softwares. The proper resolutions of the issues finally resulted in the proper functioning of the hardware prototype of the controller.

Chapter 7

Summary and Conclusions

7.1 Summary of the Thesis

The possibility of adverse interaction between the series capacitor and the mechanical shaft system in a turbine-generator is a limiting factor for the widespread use of fixed capacitors in the transmission lines. The subsynchronous resonance poses real problem for utilities as it could cause major damage to the shaft system. Another serious issue in an inter-connected system is the presence of low frequency inter-area oscillations, which may arise in corridors between generating areas as a result of poor damping of the interconnection. Such oscillations can be excited by a number of reasons, such as line faults, bulk load switching, switching of lines, or a sudden change of generator output. The presence of the poorly damped inter-area oscillations may trigger widespread disturbances, leading to partial or system wide blackouts, if cascading outages of transmission lines occur due to oscillatory power swings.

Recent developments in FACTS controllers have shown to be very effective for power system dynamics enhancements. The potential benefits of these FACTS controllers are now widely recognized by the power system engineers and the transmission and distribution communities. The TCSC and SSSC series FACTS controllers have shown to be attractive alternatives to the fixed capacitors as they possess very effective power flow control and system oscillations damping capabilities. However, the FACTS technology uses costly switching components and the three-phase TCSC and SSSC schemes for series compensation are still uneconomical compared to the traditional fixed capacitor compensation.

This thesis presented new type of hybrid series compensation schemes capable of damping both subsynchronous resonance and low frequency oscillations. The scheme combined the advantages of economic and reliable fixed capacitors and a single-phase FACTS device, either a TCSC or an SSSC. The results of the investigations that were carried out to explore the effectiveness of the hybrid single-phase TCSC and SSSC compensation schemes in damping subsynchronous resonance and low frequency oscillations in power systems were reported in the thesis.

This thesis also described a robust recursive least-square-based adaptive pole-shift controller to damp low frequency oscillations for a wide range of operating conditions. The adaptive controller damping investigations were carried out for the three-phase TCSC/SSSC and the hybrid TCSC/SSSC devices. The results of the effectiveness of the adaptive controller in damping inter-area oscillations in multi-area power systems were also reported in the thesis. Furthermore, experimental verification of the proposed controller in damping inter-area oscillations using real-time hardware-in-the-loop test were presented in the thesis. The following paragraphs provide chapter-wise summary of the dissertation.

Chapter 1 presented the advantages of a fixed series capacitor compensation in improving power transfer though a transmission line and explained the possible adverse interaction with mechanical shaft system at frequency below the system frequency, known as subsynchronous resonance. The SSR phenomenon develops torsional stress on the shaft and damages or shortens the shaft life. Another limitation is that the fixed capacitor compensation method does not provide controllable reactance, and low frequency damping is not possible.

In Chapter 2, new types of "hybrid" series capacitive compensation schemes which take advantage of modern FACTS devices (TCSC or SSSC) and low cost conventional fixed capacitors were presented. The hybrid scheme operate as unbalanced device during transients which has capability to limit build up of SSR oscillations. The devices can also be used to damp low frequency oscillations using supplementary controllers. The proposed schemes are very attractive for industrial applications, because they have technical advantages over fixed capacitor compensation, and the schemes are economical compared to three-phase FACTS counterparts.

The effectiveness of the proposed hybrid schemes in damping SSR oscillations was evaluated in Chapter 3 using detailed electromagnetic transient simulation studies on a IEEE first and second test benchmark model. The studies were carried out for various compensation levels at different fault locations. The schemes were found to be very effective in damping SSR oscillations. The line voltage unbalance rate introduced by the devices were also found to be less than 1% in all study cases, which is well below the standard values recommended by regulatory agencies -- the American National Standards Institute and the International Electrotechnical Commission.

The damping of low frequency oscillations using the proposed hybrid compensation scheme was demonstrated in Chapter 4 using detailed electromagnetic transient simulations on a two-machine infinite bus and a three-area, six-machine system. Several contingency cases were evaluated to demonstrate the effectiveness of the proposed schemes. The fixed parameter lead-lag supplementary controller was used as a supplementary damping controller. The results demonstrated that the hybrid schemes were very effective in damping inter-area oscillations. However, fixed parameter controller performance became poorer when the operating condition changed.

To improve inter-area oscillations damping for the wide range of operating conditions, an adaptive pole-shift controller was presented in Chapter 5 and the performance was evaluated on the three-area, six-machine system and IEEE 12-bus system. The robust recursive least squares algorithm was proposed to improve the tracking capability which smooths out the parameter variations during large disturbance conditions. The effectiveness of the identifier and controller was verified by testing it for a wide range of operating conditions and various disturbance cases.

Finally, the experimental verification of the proposed adaptive pole-shift controller in hardware-in-the-loop testing was presented in Chapter 6. The controller was developed on a Texas Instrument Digital Signal Processor (DSK 6713). The prototype controller was then interfaced to the Real Time Digital Simulator (RTDS). The studies were carried out on a TCSC compensated two area four machine system for wide range of operating conditions. The hardware-in-the-loop simulation results verified the usefulness of the adaptive controller in providing effective damping for wider range of power system operating conditions.

7.2 Contributions of the Thesis

Following are the main contributions of this thesis dissertation:

1. **A new hybrid series compensation using fixed capacitors and FACTS:** The proposed hybrid FACTS compensation schemes are economical compared to the full three-phase FACTS solutions. Furthermore, the scheme requires fewer switching components, and therefore the reliability of the device will be higher compared to the three-phase FACTS counterpart in terms of switching failures.

2. **Unbalanced operation of FACTS:** The unbalanced operation of the FACTS device in the hybrid compensation scheme during transient conditions have an inherent capability to damp subsynchronous resonance. The hybrid scheme also have the capability to damp low frequency power oscillations through the use of a proper supplementary controller. The effectiveness was verified through detailed electromagnetic transient simulations for various test benchmark systems.

3. **Proposed adaptive controller:** The proposed adaptive controller addressed the practical problem associated with system identification during large disturbance conditions in power system.

A simple Sigmoid like nonlinear function is proposed in RLS parameter update equation, which increases the accuracy of the identifier during large disturbances. The proposed method is simple and accurate compared to the other methods given in literatures. It smoothed out the parameter variations with a minor computation during large disturbances and does not require a large-order model (10^{th} or 12^{th} order model), controller dead-zone or parameter freezing during large disturbance conditions.

The hardware implementation of the adaptive controller (using Texas Instruments TMS320C6713 DSK) and experimental verification using the hardware-in-the-loop simulation demonstrated the practical applicability of the adaptive controller in power systems. The proposed controller is computationally efficient and simple to implement in DSP hardware.

7.3 Conclusions

The following conclusions are drawn from the work described in this thesis:

1. The hybrid single-phase TCSC and SSSC compensation schemes were very effective in damping SSR oscillations at different compensation levels (normal and very high compensation levels).

   Increasing the proportion of the single-phase TCSC and SSSC to the fixed capacitor of its phase resulted in improved damping of the SSR oscillations. Choosing a minimum value of TCSC or SSSC required to damp the SSR effectively at various operating conditions can be considered as an optimization task between the SSR damping improvements versus the economical and reliability advantages of fixed series capacitors.

   The minimum size of SSSC compensation required to obtain torsional damping in all the shaft sections of a turbine-generator ($X_{SSSC,min}$ in the hybrid SSSC scheme) was found to be generally less than the corresponding $X_{TCSC,min}$ in the hybrid TCSC scheme.

2. The hybrid single-phase TCSC and SSSC compensation schemes were very effective in damping low-frequency local and inter-area oscillations at different operating conditions.

3. In general, the hybrid SSSC compensation scheme provides better inter-area oscillation damping than the hybrid TCSC compensation scheme.

4. The fixed parameter lead-lag supplementary controller needed detailed information of the system to optimally tune the parameters, and the performance was found to degrade as the operating condition changes.
5. Adaptive pole-shift controller with robust recursive least-square estimation algorithm was very effective in providing consistent damping for a wide range of operating conditions.
6. Real-time hardware-in-the-loop testing results of the proposed adaptive controller demonstrated the practicality of the adaptive pole-shift controller in damping inter-area oscillations in various operating conditions.

7.4 Suggestions for Future Works

The following studies are recommended for future investigations based on the research carried out in this thesis work.

1. **RTDS Verification for Phase Unbalanced Hybrid Compensation Schemes:** The studies carried out in this dissertation for the phase unbalanced hybrid compensation schemes were limited to the computer simulations because of the hardware limitation of the available RTDS. The modelling of a hybrid TCSC compensation requires one unit of 3PC or 2 units of RISC processing power, and modelling of a hybrid SSSC compensation requires the use of an extra GPC processing power. These hybrid compensation studies can be conducted on an enhanced RTDS facility using either a three-area, six-machine or a complex IEEE 39 bus system.
2. **Multi-Machine System for Adaptive Controller Studies:** The studies carried out in this dissertation for the adaptive controller studies uses a three-area, six-machine and an IEEE 12-bus test system. The studies can be extended to a complex IEEE 39 bus system which demonstrates multiple inter-area oscillations.
3. **Experimental Verification of Adaptive Controller for SSSC:** The studies carried out in this dissertation for hardware-in-the-loop studies was limited to a TCSC device because of the hardware limitation of the available RTDS. The modelling of SSSC in RTDS would require more processing power. The studies can be extended to include SSSC with the proposed enhancement of the RTDS facility.
4. **RTDS Verification for Large Multi-machine Case Studies:** A two-area test system, consisting of two synchronous machines in each area, was considered for the

experimental hardware-in-the-loop testing of the proposed adaptive controller in this dissertation. The test system was of adequate size, which fitted into the current computational capability of the RTDS, but the system exhibited only a single frequency inter-area oscillation. The studies can be extended to further verify the effectiveness of the proposed controller in damping dominant mode of inter-area oscillations present in a more complex power system that exhibits more than one mode of inter-area oscillations.

References

[1] P. M. Anderson, B. L. Agrawal, and J. E. V. Ness, *Subsynchronous resonance in power systems.* New York: IEEE Press, 1990.

[2] D. Walker, C. Bowler, R. Jackson, and D. Hodges, “Results of subsynchronous resonance test at Mohave,” *IEEE Transactions on Power Apparatus and Systems*, vol. 94, no. 5, pp. 1878–1889, 1975.

[3] IEEE FACTS Working Group, IEEE Transmission and Distribution Committee, “FACTS applications,” *IEEE Publication No. 96-TP-116-0.*

[4] Y. H. Song and A. T. Johns, *Flexible AC transmission systems (FACTS).* London: The Institution of Electrical Engineers, Michael Faraday House, 1999.

[5] N. G. Hingorani, *Understanding FACTS: concepts and technology of flexible AC transmission systems*, L. Gyugyi, Ed. New York: IEEE Press, 2000.

[6] R. Mathur and R. Varma, *Thyristor-Based FACTS Controllers for Electrical Transmission Systems*, 1st ed. IEEE Press, New York, 2002.

[7] P. M. Anderson and R. G. Farmer, *Series compensation of power systems.* PBLSH! Inc, 1996.

[8] G. D. Breuer, H. M. Rustebakke, R. A. Gibley, and H. O. Simmons, “The use of series capacitors to obtain maximum EHV transmission capability,” *IEEE Transactions on Power Apparatus and Systems*, vol. 83, no. 11, pp. 1090–1102, 1964.

[9] P. M. Anderson, *Analysis of Faulted Power Systems.* IEEE Press, 1995.

[10] R. Billinton, M. Fotuhi-Firuzabad, and S. O. Faried, “Power system reliability enhancement using a thyristor controlled series capacitor,” *IEEE Transactions on Power Systems*, vol. 14, no. 1, pp. 369–374, 1999.

[11] N. Christl, P. Luelzberger, M. Pereira, K. Sadek, P. E. Krause, A. H. Montoya, D. R. Torgerson, and B. A. Vossler, “Advanced series compensation with variable impedance,” in *Proceedings of EPRI Conference on FACTS*, 1990.

[12] C. Gama, "Brazilian North-South Interconnection control-application and operating experience with a TCSC," in *Proc. IEEE Power Engineering Society Summer Meeting*, vol. 2, 1999, pp. 1103–1108.

[13] D. G. Holmes, *Pulse width modulation for power converters: principles and practice.* Hoboken, NJ: Wiley-Interscience, 2003.

[14] N. R. Raju, S. S. Venkata, and V. V. Sastry, "The use of decoupled converters to optimize the power electronics of shunt and series ac system controllers," *IEEE Transactions on Power Delivery*, vol. 12, no. 2, pp. 895–900, 1997.

[15] M. H. Rashid, Ed., *Power Electronics Handbook.* Academic Press, 2001.

[16] IEEE Subsynchronous Resonance Working Group, "Terms, definitions and symbols for subsynchronous oscillations," *IEEE Transactions on Power Apparatus and Systems*, no. 6, pp. 1326–1334, 1985.

[17] K. R. Padiyar, *Analysis of Subsynchronous Resonance in Power Systems.* Boston: Kluwer Academic Publishers, 1999.

[18] IEEE Torsional Issues Working Group, "Fourth supplement to a bibliography for the study of subsynchronous resonance between rotating machines and power systems," *IEEE Transactions on Power Systems*, vol. 12, no. 3, pp. 1276–1282, Aug. 1997.

[19] C. E. J. Bowler, D. H. Baker, N. A. Mincer, and P. R. Vandiveer, "Operation and test of the Navajo SSR protective equipment," *IEEE Transactions on Power Apparatus and Systems*, no. 4, pp. 1030–1035, 1978.

[20] K. K. Anaparthi, B. C. Pal, and H. El-Zobaidi, "Coprime factorisation approach in designing multi-input stabiliser for damping electromechanical oscillations in power systems," *IEE Proceedings-Generation, Transmission and Distribution*, vol. 152, no. 3, pp. 301–308, 2005.

[21] A. E. Hammad and M. El-Sadek, "Application of a thyristor controlled var compensator for damping subsynchronous oscillations in power systems," *IEEE Transactions on Power Apparatus and Systems*, no. 1, pp. 198–212, 1984.

[22] A. Rahim, A. Mohammad, and M. Khan, "Control of subsynchronous resonant modes in a series compensated system through superconducting magnetic energy storage units," *IEEE Transaction on Energy Conversion*, vol. 11, no. 1, pp. 175–180, March 1996.

[23] K. Patil, J. Senthil, J. Jiang, and R. Mathur, “Application of STATCOM for damping torsional oscillations in series compensated ac systems,” *IEEE Transaction on Energy Conversion*, vol. 13, no. 3, pp. 237–243, 1998.

[24] H. A. Othman and L. Angquist, “Analytical modeling of thyristor-controlled series capacitors for SSR studies,” *IEEE Transactions on Power Systems*, vol. 11, no. 1, pp. 119–127, Feb. 1996.

[25] B. Perkins, B. Perkins, and M. Iravani, “Dynamic modeling of a TCSC with application to SSR analysis,” *IEEE Transactions on Power Systems*, vol. 12, no. 4, pp. 1619–1625, 1997.

[26] R. Piwko, C. Wegner, S. Kinney, and J. Eden, “Subsynchronous resonance performance tests of the Slatt thyristor-controlled series capacitor,” *IEEE Transactions on Power Delivery*, vol. 11, no. 2, pp. 1112–1119, April 1996.

[27] W. Zhu, R. Spee, R. Mohler, G. Alexander, W. Mittelstadt, and D. Maratukulam, “An EMTP study of SSR mitigation using the thyristor controlled series capacitor,” *IEEE Transactions on Power Delivery*, vol. 10, no. 3, pp. 1479–1485, July 1995.

[28] F. Jowder and O. Boon-Teck, “Series compensation of radial power system by a combination of SSSC and dielectric capacitors,” *IEEE Transactions on Power Delivery*, vol. 20, no. 1, pp. 458–465, Jan 2005.

[29] M. Bongiorno, J. Svensson, and L. Angquist, “Single-phase VSC based SSSC for subsynchronous resonance damping,” *IEEE Transactions on Power Delivery*, vol. 23, no. 3, pp. 1544–1552, July 2008.

[30] P. Kundur, *Power system stability and control.* New York: McGraw-Hill, 1994.

[31] J. Machowski, J. W. Bialek, and J. R. Bumby, *Power System Dynamics Stability and Control*, 2nd ed. Wiley, 2008.

[32] O. I. Elgerd, *Electric Energy Systems Theory: An Introduction*, 2nd ed. McGraw-Hill College, 1982.

[33] D. N. Kosterev, C. W. Taylor, and W. A. Mittelstadt, “Model validation for the August 10, 1996 WSCC system outage,” *IEEE Transactions on Power Systems*, vol. 14, no. 3, pp. 967–979, 1999.

[34] J. Hauer, D. Trudnowski, G. Rogers, B. Mittelstadt, W. Litzenberger, and J. Johnson, "Keeping an eye on power system dynamics," *IEEE Computer Applications in Power*, vol. 10, no. 4, pp. 50–54, 1997.

[35] E. V. Larsen, J. J. Sanchez-Gasca, and J. H. Chow, "Concepts for design of FACTS controllers to damp power swings," *IEEE Transactions on Power Systems*, vol. 10, no. 2, pp. 948–956, 1995.

[36] N. Yang, Q. Liu, and J. D. McCalley, "TCSC controller design for damping interarea oscillations," *IEEE Transactions on Power Systems*, vol. 13, no. 4, pp. 1304–1310, 1998.

[37] J. J. Sanchez-Gasca, "Coordinated control of two FACTS devices for damping interarea oscillations," *IEEE Transactions on Power Systems*, vol. 13, no. 2, pp. 428–434, 1998.

[38] B. Chaudhuri, B. C. Pal, A. C. Zolotas, I. M. Jaimoukha, and T. C. Green, "Mixed-sensitivity approach to H_∞ control of power system oscillations employing multiple FACTS devices," *IEEE Transactions on Power Systems*, vol. 18, no. 3, pp. 1149–1156, 2003.

[39] B. Chaudhuri and B. C. Pal, "Robust damping of multiple swing modes employing global stabilizing signals with a TCSC," *IEEE Transactions on Power Systems*, vol. 19, no. 1, pp. 499–506, 2004.

[40] R. Majumder, B. C. Pal, C. Dufour, and P. Korba, "Design and real-time implementation of robust FACTS controller for damping inter-area oscillation," *IEEE Transactions on Power Systems*, vol. 21, no. 2, pp. 809–816, 2006.

[41] Q. Liu, V. Vittal, and N. Elia, "LPV supplementary damping controller design for a thyristor controlled series capacitor (TCSC) device," *IEEE Transactions on Power Systems*, vol. 21, no. 3, pp. 1242–1249, 2006.

[42] S. Ray and G. K. Venayagamoorthy, "Wide-area signal-based optimal neurocontroller for a UPFC," *IEEE Transactions on Power Delivery*, vol. 23, no. 3, pp. 1597–1605, 2008.

[43] A. Edris, "Series compensation schemes reducing the potential of subsynchronous resonance," *IEEE Transaction on Power System*, vol. 5, no. 1, pp. 219–226, 1990.

[44] A. A. Edris, "Subsynchronous resonance countermeasure using phase imbalance," *IEEE Transactions on Power Systems*, vol. 8, no. 4, pp. 1438–1447, 1993.

[45] M. Iravani and A. Edris, "Eigen analysis of series compensation schemes reducing the potential of subsynchronous resonance," *IEEE Transactions on Power Systems*, vol. 10, no. 2, pp. 876–883, 1995.

[46] S. J. Cheng, O. P. Malik, and G. S. Hope, "Damping of multi-modal oscillations in power systems using a dual-rate adaptive stabilizer," *IEEE Transactions on Power Systems*, vol. 3, no. 1, pp. 101–108, 1988.

[47] A. Ghosh, G. Ledwich, O. P. Malik, and G. S. Hope, "Power system stabilizer based on adaptive control techniques," *IEEE Transactions on Power Apparatus and Systems*, no. 8, pp. 1983–1989, 1984.

[48] O. P. Malik, G. P. Chen, G. S. Hope, Y. H. Qin, and G. Y. Xu, "Adaptive self-optimising pole shifting control algorithm," *IEE Proceedings D Control Theory and Applications*, vol. 139, no. 5, pp. 429–438, Sep 1992.

[49] R. Gokaraju and O. Malik, "Radial basis function identifier and pole-shifting controller for power system stabilizer application," *IEEE Transaction on Energy Conversion*, vol. 19, no. 4, pp. 663–670, Dec 2004.

[50] D. A. Pierre, "A perspective on adaptive control of power systems," *IEEE Transactions on Power Systems*, vol. 2, no. 2, pp. 387–395, 1987.

[51] R. You, H. J. Eghbali, and M. H. Nehrir, "An online adaptive neuro-fuzzy power system stabilizer for multimachine systems," *IEEE Transactions on Power Systems*, vol. 18, no. 1, pp. 128–135, 2003.

[52] S. Ray and G. K. Venayagamoorthy, "Real-time implementation of a measurement-based adaptive wide-area control system considering communication delays," *IET Generation, Transmission & Distribution*, vol. 2, no. 1, pp. 62–70, 2008.

[53] M. A. Abido, "Optimal design of power-system stabilizers using particle swarm optimization," *IEEE Transactions on Energy Conversion*, vol. 17, no. 3, pp. 406–413, 2002.

[54] K. J. Åström and B. Wittenmark, *Adaptive Control*, 2nd ed. Dover Publications Inc., 2008.

[55] R. Sadikovic, P. Korba, and G. Andersson, "Self-tuning controller for damping of power system oscillations with FACTS devices," in *Proc. IEEE Power Engineering Society General Meeting*, 2006.

[56] A. Domahidi, B. Chaudhuri, P. Korba, R. Majumder, and T. C. Green, "Self-tuning flexible ac transmission system controllers for power oscillation damping: a case study in real time," *IET Generation, Transmission & Distribution*, vol. 3, no. 12, pp. 1079–1089, 2009.

[57] A. Rahim, E. Nowicki, and O. Malik, "Enhancement of power system dynamic performance through an on-line self-tuning adaptive SVC controller," *Electric Power Systems Research*, vol. 76, no. 9-10, pp. 801 – 807, 2006.

[58] N. R. Chaudhuri, A. Domahidi, R. Majumder, B. Chaudhuri, P. Korba, S. Ray, and K. Uhlen, "Wide-area power oscillation damping control in Nordic equivalent system," *IET Generation, Transmission & Distribution*, vol. 4, no. 10, pp. 1139–1150, 2010.

[59] S. Jiang, U. Annakkage, and A. Gole, "A platform for validation of FACTS models," *Power Delivery, IEEE Transactions on*, vol. 21, no. 1, pp. 484 – 491, jan. 2006.

[60] M. Karimi-Ghartemani and M. R. Iravani, "A nonlinear adaptive filter for online signal analysis in power systems: applications," *IEEE Transactions on Power Delivery*, vol. 17, no. 2, pp. 617–622, 2002.

[61] D. Jovcic, "Phase locked loop system for FACTS," *IEEE Transactions on Power Systems*, vol. 18, no. 3, pp. 1116–1124, 2003.

[62] *PSCAD/EMTDC User Manual, V4.2.1*, Manitoba HVDC Research Centre Inc., July 13, 2006.

[63] *RTDS/RSCAD User Manual*, RTDS Technologies, 2009.

[64] H. Xie and L. Ängquist, "Synchronous voltage reversal control of TCSC impact on SSR conditions." in *Proc. of the Nordic Workshop on Power and Industrial Electronics*, Trondheim, Norway, Jun. 2004.

[65] L. Ängquist, "Synchronous voltage reversal control of thyristor controlled series capacitor," Ph.D. dissertation, Royal Institute of Technology, Department of Electrical Engineering, 2002.

[66] L. A. S. Pilotto, A. Bianco, W. F. Long, and A. A. Edris, "Impact of TCSC control methodologies on subsynchronous oscillations," *IEEE Transactions on Power Delivery*, vol. 18, no. 1, pp. 243–252, 2003.

[67] L. Ängquist, G. Ingeström, and H. Jönsson, "Dynamical performance of TCSC schemes," CIGRE Session 1996 Paper 14-302.

[68] P. M. Anderson, *Power System Protection.* Wiley-IEEE Press, 1998.

[69] A. A. Fouad and K. T. Khu, "Subsychronous Resonance Zones in the IEEE "Bench Mark" Power System," *IEEE Transactions on Power Apparatus and Systems*, vol. PAS-97, no. 3, pp. 754–762, May 1978.

[70] O. Wasynczuk, "Damping subsynchronous resonance using reactive power control," *IEEE Transactions on Power Apparatus and Systems*, no. 3, pp. 1096–1104, March 1981.

[71] IEEE Subsynchronous Resonance Task Force, "First benchmark model for computer simulation of subsynchronous resonance," *IEEE Transactions on Power Apparatus and Systems*, vol. 96, no. 5, pp. 1565–1572, 1977.

[72] IEEE Subsynchronous Resonance Working Group, "Second benchmark model for computer simulation of subsynchronous resonance," *IEEE Transactions on Power Apparatus and Systems*, vol. PAS-104, no. 5, pp. 1057–1066, 1985.

[73] *Motors and Generators*, NEMA Standards Publication no. MG 1-1993 Std.

[74] A. von Jouanne and B. Banerjee, "Assessment of voltage unbalance," *IEEE Transactions on Power Delivery*, vol. 16, no. 4, pp. 782 –790, Oct. 2001.

[75] *Electric Power Systems and Equipment - Voltage Ratings (60 Hertz)*, ANSI Standard Publication no. ANSI C84.1-1995 Std.

[76] Rotating Electrical Machines, "Effects of unbalanced voltages on the performance of three-phase cage induction motors," International Electrotechnical Commission, Tech. Rep. IEC 60034-26, 2006.

[77] M. Klein, G. Rogers, and P. Kundur, "A fundamental study of inter-area oscillations in power systems," *IEEE Transactions on Power Systems*, vol. 6, no. 3, pp. 914–921, 1991.

[78] V. Vittal, N. Bhatia, and A. A. Fouad, "Analysis of the inter-area mode phenomenon in power systems following large disturbances," *IEEE Transactions on Power Systems*, vol. 6, no. 4, pp. 1515–1521, 1991.

[79] P. Kundur, M. Klein, G. J. Rogers, and M. S. Zywno, "Application of power system stabilizers for enhancement of overall system stability," *IEEE Transactions on Power Systems*, vol. 4, no. 2, pp. 614–626, 1989.

[80] L. Angquist and C. Gama, "Damping algorithm based on phasor estimation," in *Proc. IEEE Power Engineering Society Winter Meeting*, vol. 3, 28 Jan.–1 Feb. 2001, pp. 1160–1165.

[81] D. J. Trudnowski, M. K. Donnelly, and J. F. Hauer, "Estimating damping effectiveness of BPA's thyristor controlled series capacitor by applying time and frequency domain methods to measured response," *IEEE Transactions on Power Systems*, vol. 11, no. 2, pp. 761–766, 1996.

[82] J. F. Hauer, C. J. Demeure, and L. L. Scharf, "Initial results in Prony analysis of power system response signals," *IEEE Transactions on Power Systems*, vol. 5, no. 1, pp. 80–89, 1990.

[83] J. F. Hauer, "Application of Prony analysis to the determination of modal content and equivalent models for measured power system response," *IEEE Transactions on Power Systems*, vol. 6, no. 3, pp. 1062–1068, 1991.

[84] P. Ioannou and J. Sun, *Robust Adaptive Control*. Prentice Hall, Inc, 1996.

[85] S. Haykin, *Adaptive Filter Theory*, 4th ed., T. Kailath, Ed. Prentice Hall, 2001.

[86] G. P. Chen and O. P. Malik, "Tracking constrained adaptive power system stabiliser," *IEE Proceedings-Generation, Transmission and Distribution*, vol. 142, no. 2, pp. 149–156, 1995.

[87] D. Rai, R. Gokaraju, and S. O. Faried, "Model reference adaptive control of FACTS," in 16^{th} *National Power System Conference, Hyderabad, India,*, Dec 15-17, 2010.

[88] M. M. Chansarkar and U. B. Desai, "A robust recursive least squares algorithm," *IEEE Transactions on Signal Processing*, vol. 45, no. 7, pp. 1726–1735, 1997.

[89] R. Gokaraju, "Beyond gain-type scheduling controllers: New tools of identification and control for apdaptive PSS," Ph.D. dissertation, Department of Electrical and Computer Engineering, University of Calgary, Calgary, Alberta, May 2000.

[90] P. C. Krause, O. Wasynczuk, and S. D. Sudhoff, *Analysis of Electric Machinery and Drive Systems*, 2nd ed. Wiley-Interscience, 2002.

[91] A. Gole, S. Filizadeh, and P. Wilson, "Inclusion of robustness into design using optimization-enabled transient simulation," *Power Delivery, IEEE Transactions on*, vol. 20, no. 3, pp. 1991 – 1997, july 2005.

[92] J. C. Lagarias, J. A. Reeds, M. H. Wright, and P. E. Wright, “Convergence properties of the Nelder-Mead simplex method in low dimensions,” *SIAM Journal on Optimization*, vol. 9, no. 1, pp. 112 – 47, 1998.

[93] W. H. Press, S. A. Teukolsky, W. T. Vetterling, and B. P. Flannery, *Numerical Recipes in Fortran 90: The Art of Parallel Scientific Computing*, 2nd ed. Cambridge University Press, 1977.

[94] J. M. Gers and E. J. Holmes, *Protection of Electricity Distribution Networks*, 2nd ed. Institution of Engineering and Technology, 2004.

[95] P. Forsyth and R. Kuffel, “Utility applications of a RTDS® Simulator,” in *Proc. Int. Power Engineering Conf. IPEC 2007*, 2007, pp. 112–117.

[96] R. Chassaing and R. Donald, *Digital Signal Processing and Applications with the TMS320C6713 and TMS320C6416 DSK*. Wiley-Interscience, 2008.

[97] Spectrum Digital Inc., “TMS320C6713 DSK module technical reference,” Tech. Rep. 506735-0001 Rev. A, May 2003.

[98] S. S. Haykin, *Communication systems*. New York: Wiley, 2001.

[99] *IEEE Recommended Practice for Excitation System Models for Power System Stability Studies*, Std. IEEE Std 421.5-1992, 1992.

[100] “IEEE recommended practice for excitation system models for power system stability studies,” 1992, IEEE Std 421.5-1992.

[101] W. H. Press, B. P. Flannery, S. A. Teukolsky, and W. T. Vetterling, *Numerical Recipes in C: The Art of Scientific Computing*, 2nd ed. Cambridge University Press, 1992.

APPENDIX A

Estimation Algorithms

A.1 Phasor Evaluation Using Low-pass Filter Based Algorithm

Any single-phase signal $e(t)$ can be expressed in terms of average value and rotating phasor as [65]:

$$e(t) = E_{av} + Re\left[\vec{E}\ e^{j\omega_0 t}\right] \tag{A.1}$$

where E_{av} is average dc component, $\vec{E} = E_R + jE_I$ is the phasor component, Re represents the real component of the phasor, and ω_0 is the frequency of the signal. The Eq. (A.1) can also be expressed as:

$$e(t) = E_{av} + \frac{1}{2}\vec{E}\ e^{j\omega_0 t} + \frac{1}{2}\vec{E^*}\ e^{-j\omega_0 t} \tag{A.2}$$

where $\vec{E^*}$ represents the complex conjugate of phasor $\vec{E}$. The average dc component, real part of the phasor and the imaginary part of the phasor can be easily extracted from the Eq. (A.2). The rough estimate of the dc component, real and imaginary phasors can be obtained as:

$$\hat{x_{av}} = e(t) - \frac{1}{2}\vec{E}\ e^{j\omega_0 t} - \frac{1}{2}\vec{E^*}\ e^{-j\omega_0 t} \tag{A.3}$$

$$\hat{x_R} = Re\left\{e^{-j\omega_0 t}\left[2(e(t) - E_0) - \frac{1}{2}\vec{E^*}\ e^{-j\omega_0 t}\right]\right\} \tag{A.4}$$

$$\hat{x_I} = Im\left\{e^{-j\omega_0 t}\left[2(e(t) - E_0) - \frac{1}{2}\vec{E^*}\ e^{-j\omega_0 t}\right]\right\} \tag{A.5}$$

Since the average dc value, real and imaginary parts of the phasor varies slowly (almost dc values), the low pass filter can be used to smooth the values in Eqns. (A.3)-(A.5) to achieve actual estimates $\hat{E_{av}}$, $\hat{E_R}$ and $\hat{E_I}$.

A.2 Tracking Constrained Recursive Least Square Estimation

The system parameter weight vector, $\theta(t)$ can be estimated using the following extended recursive least square (RLS) equations algorithm [54]:

$$\hat{\theta}(t) = \hat{\theta}(t-1) + K(t)\left[y(t) - \Psi(t)^T\hat{\theta}(t-1)\right] \tag{A.6a}$$

$$K(t) = \frac{P(t-1)\Psi(t)}{\lambda(t) - \Psi(t)^T P(t-1)\Psi(t)} \tag{A.6b}$$

$$P(t) = \frac{1}{\lambda(t)}\left[P(t-1) - K(t)\Psi^T(t)P(t-1)\right] \tag{A.6c}$$

where $\lambda(t)$ is the time varying forgetting factor, $P(t)$ is the covariance matrix, and $K(t)$ is the gain vector. The forgetting factor $\lambda(t)$ is calculated as:

$$\lambda(t) = \lambda_0\lambda(t-1) + (1-\lambda_0) \tag{A.7}$$

where λ_0 is a positive value between 0 and 1. During the transients, the identified power system model may shift from one operating state to another, and the identified plant parameters may vary significantly. To limit such large deviations in parameters, a simple tracking constraint term $\beta(t)$ can be introduced in the update algorithm Eq. (A.6a) as given below:

$$\hat{\theta}(t) = \hat{\theta}(t-1) + K(t)\left[y(t) - \Psi(t)^T\hat{\theta}(t-1)\right]\beta(t) \tag{A.8}$$

where $\beta(t)$ is calculated in each sampling time interval as follows:

$$\beta(t) = \begin{cases} 1.0 & \text{if } N_2/N_1 \le \beta_0 \\ \beta_0/N_2 & \text{if } N_2/N_1 > \beta_0 \end{cases} \tag{A.9}$$

where,

$$\begin{aligned} N_1 &= \|\hat{W}(t)\|_2 \\ N_2 &= \|K(t)[y(t) - \Psi(t)^T\hat{W}(t-1)]\|_2. \end{aligned}$$

$\|.\|_2$ is the norm of the corresponding vector, and β_0 is a positive constant which determines the rate of parameter update.

A.3 Damping Estimation using Prony Analysis

The Prony Analysis can be used directly to estimate the dominant frequency, damping, magnitude, and relative phase of the modal components present in a time domain information, such as power oscillation response [82, 83]. It is suitable for parametric studies for power system damping analysis and is used as a tool to estimate damping provided by a TCSC in the real power system application [81].

Equation (A.10) represents the equally spaced sample of $y(t)$ by the Prony approximation $\hat{y(t)}$ where A_i is amplitude, σ_i is damping component, ω_i is frequency, and ϕ_i is phase component of a Prony component [83].

$$\hat{y}(t) = \sum_{i=1}^{N} A_i e^{\sigma_i t} \cos(\omega_i t + \phi_i) \tag{A.10}$$

A.4 Modal Speed Calculation

System I modal speed calculation data:

$$\Delta\omega_m = \begin{bmatrix} \Delta\omega_0 & \Delta\omega_1 & \Delta\omega_2 & \Delta\omega_3 & \Delta\omega_4 \end{bmatrix}^T$$

$$\Delta\omega = \begin{bmatrix} \Delta\omega_{HP} & \Delta\omega_{IP} & \Delta\omega_{LPA} & \Delta\omega_{LPB} & \Delta\omega & \Delta\omega_{EXC} \end{bmatrix}^T$$

$$Q = \begin{bmatrix} 1 & -0.7770 & -0.1099 & 1 & 0.8638 & -0.7874 \\ 1 & -0.5837 & 0.0646 & 0.3422 & -0.0437 & 1 \\ 1 & -0.3424 & 0.0150 & -0.2297 & -0.5027 & -0.1133 \\ 1 & 0.1117 & -0.0395 & -0.0945 & 1 & 0.0211 \\ 1 & 0.3731 & -0.0374 & 0.1660 & -0.6205 & -0.0045 \\ 1 & 1 & 1 & -0.2525 & 0.3768 & 0.0009 \end{bmatrix}$$

System II modal speed calculation data:

Generator 1:

$$\Delta\omega_m = \left[\begin{array}{cccc} \Delta\omega_0 & \Delta\omega_1 & \Delta\omega_2 & \Delta\omega_3 \end{array}\right]^T$$

$$\Delta\omega = \left[\begin{array}{cccc} \Delta\omega_{HP} & \Delta\omega_{LP} & \Delta\omega & \Delta\omega_{EXC} \end{array}\right]^T$$

$$Q_1 = \left[\begin{array}{cccc} 0.5 & -0.6306 & 0.8959 & -0.0005 \\ 0.5 & -0.1629 & -0.2514 & 0.0012 \\ 0.5 & 0.4611 & 0.1872 & -0.0097 \\ 0.5 & 0.6026 & 0.3148 & 1 \end{array}\right]$$

Generator 2:

$$\Delta\omega_m = \left[\begin{array}{ccc} \Delta\omega_0 & \Delta\omega_1 & \Delta\omega_2 \end{array}\right]^T$$

$$\Delta\omega = \left[\begin{array}{ccc} \Delta\omega_{HP} & \Delta\omega_{LP} & \Delta\omega \end{array}\right]^T$$

$$Q_2 = \left[\begin{array}{ccc} -0.9333 & -0.6592 & 0.5774 \\ 0.3499 & -0.3872 & 0.5774 \\ -0.0808 & -0.6446 & 0.5774 \end{array}\right]$$

Appendix B

Calculations - Model Validation

B.1 SSSC validation

B.1.1 Steady-state sending/receiving end power calculation

Analytical calculation:

<u>At $x_{SSSC} = j26\,\Omega$ (1.0 $p.u.$ inductive)</u>

$$
\begin{aligned}
I_{Line} &= \frac{V_s - V_r}{Z_{Line}} = \frac{230\angle 20^o - 230\angle 0^o}{j129.68 - j26} \\
&= 0.770\angle 10^o\ kA \\
S_s &= V_s I^*_{Line} = 230\angle 20^o \times (0.770\angle 10^o)^* \\
&= 174.409 + j30.753\ MVA \\
S_r &= V_r I^*_{Line} = 230\angle 0^o \times (0.770\angle 10^o)^* \\
&= 174.409 - j30.753\ MVA
\end{aligned}
$$

<u>At $x_{SSSC} = -j26\,\Omega$ (-1.0 $p.u.$ capacitive)</u>

$$
\begin{aligned}
I_{Line} &= \frac{230\angle 20^o - 230\angle 0^o}{j129.68 + j26} \\
&= 0.513\angle 10^o\ kA \\
S_s &= V_s I^*_{Line} = 230\angle 20^o \times (0.513\angle 10^o)^* \\
&= 116.197 + j20.488\ MVA \\
S_r &= V_r I^*_{Line} = 230\angle 0^o \times (0.513\angle 10^o)^* \\
&= 116.197 - j20.488\ MVA
\end{aligned}
$$

B.1.2 Steady-state DC capacitor voltage calculation

Considering the equivalent impedance of the coupling transformer is in secondary side and neglecting the presence of the magnetising branch as shown in the Fig. B.1.

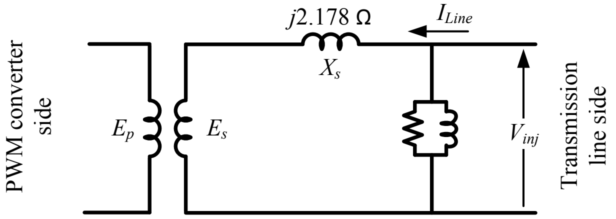

Figure B.1: Coupling transformer equivalent circuit.

The fundamental voltage component of the twelve-pulse PWM converter is given as:

$$V_0 = m_a V_{dc}/\sqrt{2}$$

where m_a is the modulation index and V_{dc} represents the dc capacitor voltage. The dc voltage of the capacitor can be calculated as:

At $x_{SSSC} = j26\Omega$ (1.0 $p.u.$ inductive)

$$\begin{aligned} I_{Line} &= 0.513\angle 10^o\ kA \\ V_{inj} &= x_{sssc}\ I_{Line} = j26 \times 0.513\angle 10^o\ = 13.34\angle 100^o\ kV \\ E_s &= V_{inj} + I_{line}X_s = 13.34\angle 100^o - 0.513\angle 10^o j2.178 = 12.22\angle 100^o \\ |E_p| &= \frac{11}{33}12.22 = 4.07\ kV \\ V_{dc} &= \frac{\sqrt(2)}{m_a}|E_p| = \frac{\sqrt(2)}{0.99}4.07 = 5.81\ kV \end{aligned}$$

At $x_{SSSC} = -j26\Omega$ (-1.0 $p.u.$ capacitive)

$$\begin{aligned} I_{Line} &= 0.770\angle 10^o\ kA \\ V_{inj} &= -j26 \times 0.77\angle 10^o\ = 20.02\angle -80^o\ kV \\ E_s &= 20.02\angle -80^o - 0.77\angle 10^o j2.178 = 21.69\angle -80^o \\ |E_p| &= \frac{11}{33}21.69 = 7.23\ kV \\ V_{dc} &= \frac{\sqrt(2)}{0.99}7.23 = 10.33\ kV \end{aligned}$$

Appendix C

System Data - SSR Studies

C.1 IEEE First Benchmark Model for SSR Studies

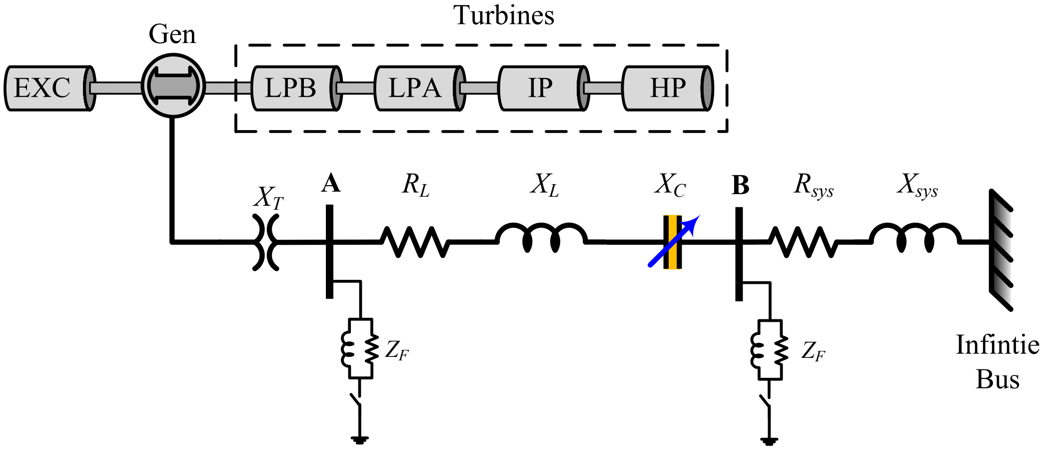

Figure C.1: IEEE first benchmark model for SSR studies.

<u>*Generator data:*</u> 892.4 MVA, 26 kV, $x_d = 1.79\ p.u.$, $x_q = 1.71\ p.u.$, $x'_d = 0.169\ p.u.$, $x'_q = 0.288\ p.u.$, $x''_d = 0.135\ p.u.$, $x''_q = 0.20\ p.u.$, $T'_{d0} = 4.3\ s$, $T''_{d0} = 0.032\ s$, $T'_{q0} = 0.85\ s$, $T''_{q0} = 0.05\ s$.

Table C.1: IEEE FBM shaft inertia and spring constants.

Mass	Inertia Constant, H (s)	Shaft Section	Spring Constant, K ($p.u.$)
HP turbine	0.092897	HP-IP	19.303
IP turbine	0.155589	IP-LPA	34.929
LPA turbine	0.858670	LPA-LPB	52.038
LPB turbine	0.884215	LPB-GEN	70.858
Generator	0.868495	GEN-EXC	2.822
Exciter	0.0342165	-	-

Table C.2: IEEE FBM network impedances.

Parameter	Positive Sequence ($p.u.$)	Zero Sequence ($p.u.$)
R_L	0.02	0.50
X_L	0.50	1.56
X_{sys}	0.06	0.06

C.2 IEEE Second Benchmark Model for SSR Studies

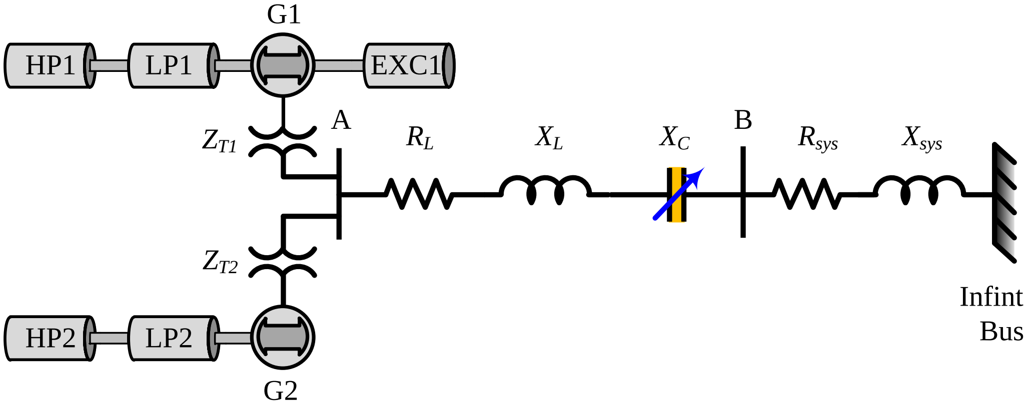

Figure C.2: IEEE second benchmark model for SSR studies.

Generator G_1 data: 600 MVA, 22 kV, $r_a = 0.0045$, $x_l = 0.14$, $x_d = 1.65$, $x_q = 1.59$, $x_d = 0.25$, $x_q = 0.46$, $x_d = 0.20$, $x_q = 0.20$, $T_{d0} = 4.5\ s$, $T_{d0} = 0.04\ s$, $T_{q0} = 0.67\ s$, $T_{q0} = 0.09\ s$.

Generator G_2 data: 700 MVA, 22 kV, $r_a = 0.0045$, $x_l = 0.12$, $x_d = 1.54$, $x_q = 1.50$, $x_d = 0.23$, $x_q = 0.42$, $x_d = 0.18$, $x_q = 0.18$, $T_{d0} = 3.70\ s$, $T_{d0} = 0.04\ s$, $T_{q0} = 0.43\ s$, $T_{q0} = 0.06\ s$.

Table C.3: IEEE SBM network impedances (on 100 MVA, 500 kV base).

Parameter	Positive Sequence ($p.u.$)	Zero Sequence ($p.u.$)
R_L	0.0052	0.0120
X_L	0.0540	0.120
R_{sys}	0.0014	0.0014
X_{sys}	0.03	0.03

C.3 SSR supplementary controller parameters

C.3.1 First Benchmark Model

Table C.4: FBM: SSR supplementary controller parameters.

Modes (i)	K_i	$T_{a,i}$	$T_{b,i}$
0	2	0.0750	0.0375
1	20	0.0071	0.0143
2	-15	0.0111	0.0055
3	5	0.0088	0.0044
4	10	0.0069	0.0034

C.3.2 Second Benchmark Model

Table C.5: SBM: SSR supplementary controller parameters.

Gen.	Modes (i)	K_i	$T_{a,i}$	$T_{b,i}$
G1	0	5	0.1125	0.0375
G2		3	0.1125	0.0562
G1	1	15	0.0129	0.0032
G2		15	0.0129	0.0032
G1	2	10	0.0069	0.0034
G2		5	0.0050	0.0025
G1	3	5	0.0044	0.0022

Appendix D

System Data - Low Frequency Oscillation Studies

D.1 Local Oscillation Damping Studies

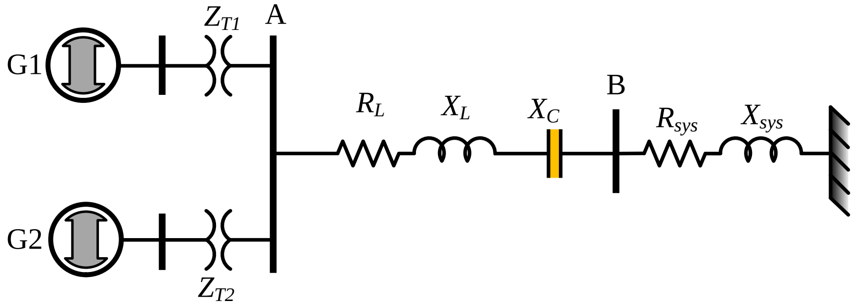

Figure D.1: Two machine infinite bus system used for local oscillation damping studies.

Machines data: $H(G_1) = 22680.96\ kg\ m^2/rad$, $H(G_2) = 34357.624\ kg\ m^2/rad$.

Generator steady state data: G_1: V=1.03$\measuredangle 0^0$ $p.u.$, G_2: 700 MW, V=1.01 $p.u.$, G_3: 720 MW, V=1.01 $p.u.$, G_4:700 MW, V=1.01 $p.u.$, G_5:800 MW, V=1.02 $p.u.$, G_6:780 MW, V=1.01 $p.u.$

D.2 Inter-Area Oscillation Damping Studies

D.2.1 Three-area, Six-machine System

Generator data: 900 MVA, 20 kV, $r_a = 0.0025$, $x_l = 0.2$, $x_d = 1.8$, $x_q = 1.7$, $x'_d = 0.3$, $x'_q = 0.55$, $x''_d = 0.25$, $x''_q = 0.25$, $T_{d0} = 8\ s$, $T''_{d0} = 0.03\ s$, $T'_{q0} = 0.4\ s$, $T''_{q0} = 0.05\ s$, $H(G_1\&G_2) = 6.5\ s$, $H(G_3\&G_4) = 6.175\ s$, $H(G_5) = 5.5\ s$, $H(G_6) = 5\ s$.

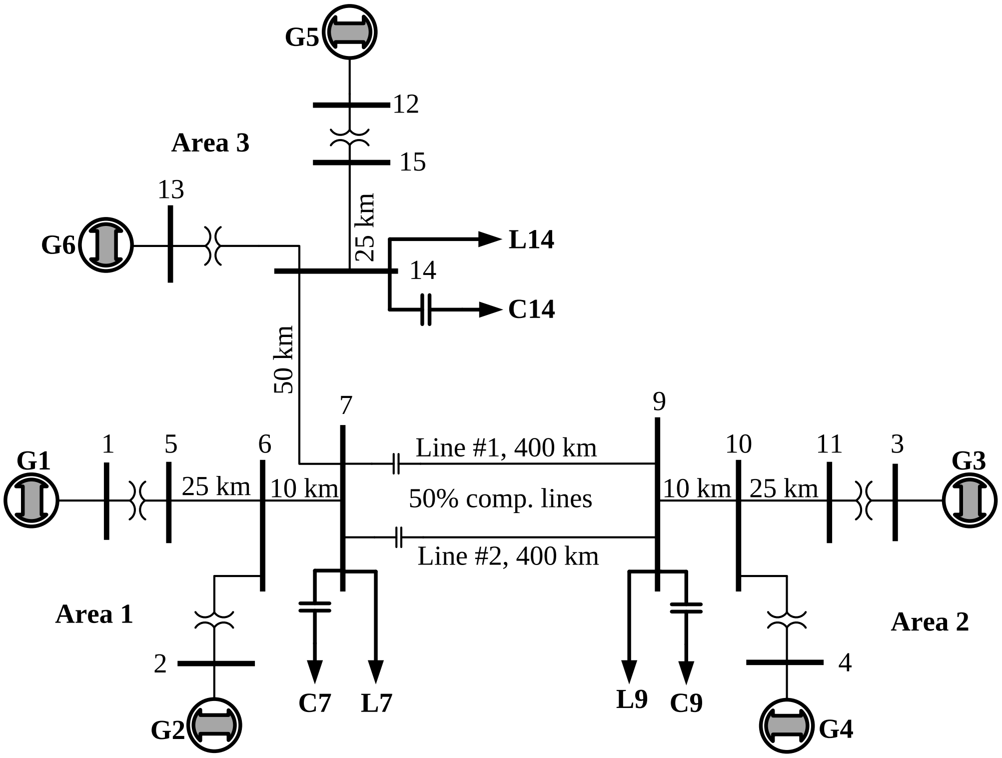

Figure D.2: Three-area test system used for inter-area oscillation damping studies.

Table D.1: Three-area system: load data (MVA, MVAR) for different study cases.

Case	Bus 7 (L_7, C_7)	Bus 9 (L_9, C_9)	Bus 14 (L_{14}, C_{14})
A, B, E	$1400 + j100$, $-j350$	$1800 + j100$, $-j500$	$1200 + j100$, $-j220$
C	$1400 + j100$, $-j260$	$1600 + j100$, $-j350$	$1450 + j100$, $-j220$
D	$1755 + j100$, $-j260$	$1200 + j100$, $-j350$	$1200 + j100$, $-j240$

Generator steady state data: G_1: V=1.03$\measuredangle 0^0$ $p.u.$, G_2: 700 MW, V=1.01 $p.u.$, G_3: 720 MW, V=1.01 $p.u.$, G_4: 700 MW, V=1.01 $p.u.$, G_5: 800 MW, V=1.02 $p.u.$, G_6: 780 MW, V=1.01 $p.u.$

Transmission line data: $r = 0.053\ \Omega/km$, $X_L = 0.53\ \Omega/km$

Exciter data: IEEE type ST1A exciter, $T_r = 0.01\ s$, $T_C = 1\ s$, $T_B = 10\ s$, $K_A = 50$, $V_{MAX} = 9\ p.u.$, $V_{MIN} = -9\ p.u.$.

Steam governor data: GE mechanical-hydraulic controls, Droop $(R) = 0.04\ p.u$, Speed relay lag time constant (TC) $(T_1) = 0.1\ s$, Gate servo TC $(T_3) = 0.25\ s$.

Steam turbine data (in p.u.): IEEE type 2 thermal turbine, $K_1 = 0.0$, $K_3 = 0.25$, $K_5 = 0.0$,

$K_7 = 0.0$, $K_2 = 0.25$, $K_4 = 0.5$, $K_6 = 0.0$, $K_8 = 0.0$, Steam chest TC (T_4) = 0.42 s, Reheater TC (T_5) = 4.25 s, Reheater/cross-over TC (T_6) = 0.72 s.

TCSC Parameters: $kB_{ref} = 1.75$, $C_{TCSC} = 87.76\ \mu F$, $L_{TCSC} = 12.8\ mH$, PI controller: $K_P = 10$, $T_C = 0.05\ s$.

D.2.2 Lead-lag Controller Parameters (Three-area, Six-machine system)

A. Chapter 4 - Inter-area Oscillation Damping Studies

TCSC PSD Controller: $K_{D1} = -2$, $K_{D2} = 2$, $T_W = 1\ s$, $T_{ca} = T_{cc} = 0.2$, $T_{cb} = T_{cd} = 0.1$

SSSC PSD Controller: $K_{D1} = -0.35$, $K_{D2} = 0.35$, $T_W = 1\ s$, $T_{ca} = T_{cc} = 1.2$, $T_{cb} = T_{cd} = 0.1$

B. Chapter 5 - Inter-area Oscillation Damping Studies

Simplex-optimized lead-lag supplementary controller (Balanced TCSC): $T_w = 1\ s$, $T_1 = T_3 = 3.2925\ s$, $T_2 = T_4 = 0.17072\ s$, $K_P = 0.0114$.

Simplex-optimized lead-lag supplementary controller (Balanced SSSC): $T_w = 1\ s$, $T_1 = T_3 = 0.20\ s$, $T_2 = T_4 = 0.4090\ s$, $K_P = 0.5$.

Simplex-optimized lead-lag supplementary controller (Hybrid TCSC): $T_w = 1\ s$, $T_1 = T_3 = 0.425\ s$, $T_2 = T_4 = 0.010\ s$, $K_P = 0.536$.

Simplex-optimized lead-lag supplementary controller (Hybrid SSSC): $T_w = 1\ s$, $T_1 = T_3 = 0.2\ s$, $T_2 = T_4 = 0.4\ s$, $K_P = 0.5$.

Power system stabilizer parameters: IEEE type PSS1A power system stabilizer, $T_w = 1s$, $T_1 = 4.597s$, $T_3 = 3.131s$, $T_2 = 2.082s$, $T_4 = 3.173s$, $K_P = 0.21$.

D.2.3 IEEE 12-bus System

Table D.2: IEEE 12-bus system: Bus data.

Bus	Nominal voltage, kV	Specified voltage, kV	Load, MVA	Shunt capacitor, $MVAr$	Generation, MW
1	230				
2	230		$280 + j200$		
3	230		$320 + j240$		
4	230		$320 + j240$	160	
5	230		$100 + j60$	80	
6	230		$440 + j300$	180	
7	345				
8	345				
9	22	1.04			
10	22	1.02			500
11	22	1.01			200
12	22	1.02			300

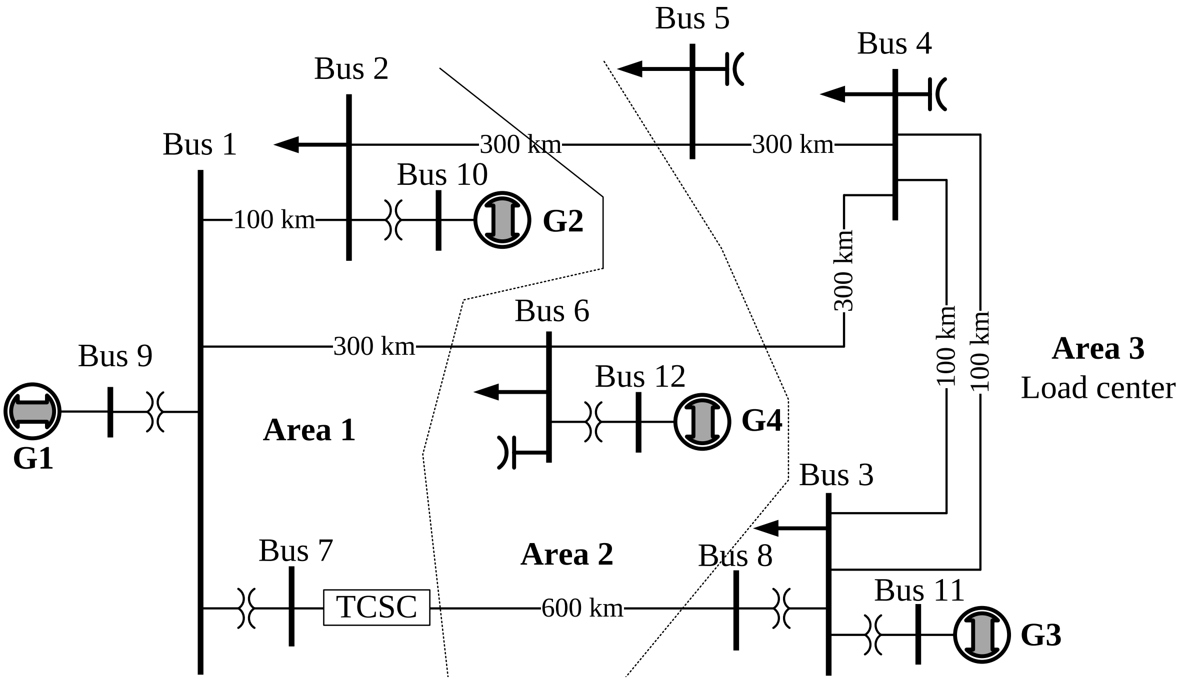

Figure D.3: IEEE 12-bus test system used for inter-area oscillation damping studies.

Table D.3: IEEE 12-bus system: Branch data, system base: 100 MVA.

Line	Voltage, *kV*	Length, *km*	R, *p.u.*	X, *p.u.*	B, *p.u.*	Rating, *MVA*
1-2	230	100	0.01144	0.09111	0.18261	250
1-6	230	300	0.03356	0.26656	0.55477	250
2-5	230	300	0.03356	0.26656	0.55477	250
3-4(1)	230	100	0.01144	0.09111	0.18261	250
3-4(2)	230	100	0.03356	0.09111	0.18261	250
4-5	230	300	0.03356	0.26656	0.55477	250
4-6	345	300	0.03356	0.26656	0.55477	250
7-8	345	600	0.01595	0.17214	3.28530	500

D.2.4 Controller parameters (IEEE 12-bus system)

Simplex-optimized lead-lag supplementary controller (TCSC): $T_w = 1\ s$, $T_1 = 0.97\ s$, $T_2 = 0.26\ s$, $T_3 = 0.49\ s$, $T_4 = 0.23\ s$, $K_P = 0.1$.

Appendix E

System Data - Experimental Studies

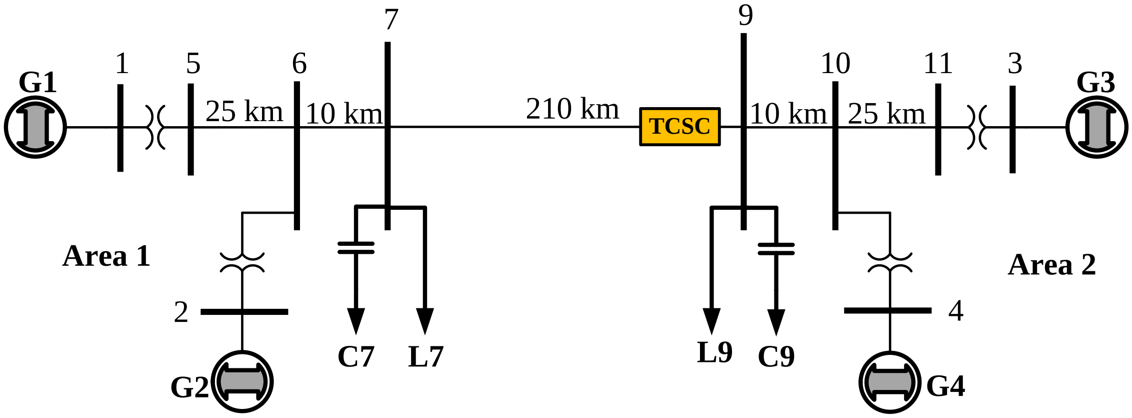

Figure E.1: Two-area test system used for experimental studies.

Generator data: 700 MVA, 20 kV, $r_a = 0.0025$, $x_l = 0.2$, $x_d = 1.8$, $x_q = 1.7$, $x'_d = 0.3$, $x'_q = 0.55$, $x''_d = 0.25$, $x''_q = 0.25$, $T_{d0} = 8\ s$, $T''_{d0} = 0.03\ s$, $T'_{q0} = 0.4\ s$, $T''_{q0} = 0.05\ s$, $H(G_1\&G_2) = 6.5\ s$, $H(G_3\&G_4) = 6.175\ s$, $H(G_5) = 5.5\ s$, $H(G_6) = 5\ s$.

Transmission line data: $x_l = 0.001\ p.u./km$, $r_l = 0.0001\ p.u./km$

Transformer data: 900 MVA, $V_1/V_2 = 230/20\ kV$, $r = 0$, $x = 0.15\ p.u.$

Exciter data: IEEE type ST1A exciter, $T_r = 0.01\ s$, $T_C = 1\ s$, $T_B = 10\ s$, $K_A = 50$, $V_{MAX} = 5.7\ p.u.$, $V_{MIN} = -4.9\ p.u.$, $K_c = 0.175$, $K_f = 0.0$, $T_f = 1.0\ s$.

Governor and Turbine data: IEEE type 1 governor/turbine, $K = 20$, $T_1 = 1\ s$, $T_2 = 1\ s$, $T_3 = 0.25\ s$, $T_4 = 0.20\ s$, $K_1 = 0.30$, $K_2 = 0$, $T_5 = 5.0$, $K_3 = 0.70\ s$.

TCSC Parameters: $X_{TCSC} = 22.2\ \Omega$, $C_{TCSC} = 176\ \mu F$, $L_{TCSC} = 9.0\ mH$, PI controller: $K_P = 4.0$, $T_C = 0.008\ s$.